EUROPEAN COMMISSION

Community research

PEBS

(Contract Number: FP7 249681)

PROYECT DERIVERABLE 3.5-1: Report on integration of available data for bentonites from different scales and scaling laws and extrapolation for long-term analyses for clay barriers

Author(s):

Javier Samper, Alba Mon, Bruno Pisani, Luis Montenegro

University of Coruña
Spain

Reporting period: **01/03/10 – 28/02/14**

Date of issue of this report: **09/2011**

Start date of project: **01/03/10** Duration: **48** Months

Project co-funded by the European Commission under the Seventh Euratom Framework Programme for Nuclear Research &Training Activities (2007-2011)		
Dissemination Level		
PU	Public	**PU**
RE	Restricted to a group specified by the partners of the [acronym] project	
CO	Confidential, only for partners of the [acronym] project	

EURATOM

DISTRIBUTION LIST

Name	Number of copies	Comments

Integration of available data for bentonites from different scales and scaling laws and extrapolation for long-term analysis for clay barrier.

Summary

The disposal of high-level radioactive waste in deep geological repositories is based on a combination of engineered barriers made of unsaturated compacted bentonite. A large number of hydrodynamic, geochemical and thermal data have been collected for compacted bentonites during the last 30 years to characterize their properties and evaluate the feasibility of compacted bentonite for the Engineered Barrier System (EBS) of a high level radioactive waste repository. Various laboratory and in situ heating and hydration experiments have been performed within European Projects such as FEBEX I and II, and NFPRO (ENRESA, 2001; 2006a). Such experiments have been modeled previously by several groups, including mainly the UPC team using THM models (Villar et al, 2008b) and the UDC group using THC models (Samper et al., 2008; Zheng and Samper 2008; Zheng et al., 2010; 2011). Experiments have a wide range of time and space scales within the Their durations range from a few months in the case of the CT cells to more than 14 years in the case of the FEBEX mock up and in situ tests. The size of the experiments ranges from 10 cm in CT cells to more than 10 m in the in situ test. An integrated analysis of the hydrodynamic, thermal and chemical data from several space and time scales has been performed. Such integrated analysis has been made in terms of dimensionless variables.

The following activities have been performed:

1) The compilation of available hydrodynamic, thermal and hydrochemical data from reported and on-going heating and hydration experiments performed on FEBEX bentonite.

2) The analysis and filtering of data.

3) The dimensional analysis of key hydrodynamic, thermal and chemical variables, including the definition of: 1) The characteristic times and volumes and 2) Dimensionless water uptake, water content, temperature and solute concentration.

4) The integrated analysis of water content, water uptake, temperatures, chemical concentrations of bentonite pore water data from experiments performed at different space-time scales by means of dimensionless variables.

5) The development of an analytical solution for bentonite hydration based on the Green-Ampt method

A novel Green-Ampt analytical solution has been developed and used to compare the water uptake for radial and parallel flow. Such comparison reveals that the analytical solutions are markedly different. Such differences should be taken into account when translating the results obtained in laboratory cells, where the conditions are of parallel flow, to the in situ test where heating and hydration are radial. The water uptake for parallel flow has been computed for the following cases: 1) Same volume and thickness; 2) Same hydration surface and thickness; 3) Same volume and hydration surface; and 4) For optimized thickness, volume and hydration surface. The best fit is obtained with the optimized values. The case of the same volume and hydration surface gives the second best approximation. It can be concluded that the water uptake of radial and parallel flow are comparable when the dimensions and the conditions are correctly selected. Measured water uptake data from CG cells having durations from 0.5 to 7.5 years fit well to the Green-Ampt analytical solution for an apparent hydraulic conductivity K slightly greater than that corresponding to 25ºC and the initial bentonite porosity. The analytical Green-Ampt solutions for radial and parallel flow reproduce well the numerical solutions by using an apparent hydraulic conductivity slightly larger than that corresponding to 25ºC and the initial bentonite porosity.

The main conclusions of the integrated analysis of water uptake data include:

1) Water hydration in CT and CG cells is mostly one dimensional and parallel to the axis of the cell. Hydration in the mock up and in situ tests, on the other hand, occurs from the outer surface and has a radial distribution. Therefore, there is a clear difference in the geometry of the hydration of the lab cells and the mock up and in situ tests.

2) Measured water uptake data contains uncertainties. For CG cells the water uptake data may have an uncertainty of about 15%. The final water uptake determined with the on line measurements (from changes in the weight of the water tank) is 15% larger than the water uptake estimated from the difference in the weight of the bentonite sample at the end and at the beginning of the test. Water uptake data

from the mock up test may also contain uncertainties, especially for the most recent data because the flow rate is becoming very low.

3) The dimensionless analysis of measured water uptake data shows that the water uptake data from the CT and CG cells and the mock up test cannot be scaled up. There are large differences at early times due to spurious effects such as electric shutdown and the filling of block joints. Such differences, however, decrease with time. Measured data from most of the tests converge for dimensionless times greater than 0.04. The water uptake of the CT cell is slightly larger than that of the mock up test.

4) The computed water uptake with the numerical model for parallel flow is larger than that computed for radial flow.

Our integrated analysis assumes that the volume and density are constant. Therefore, changes in porosity, temperature and permeability are not accounted for.

The integrated analyses of water content data leads to the following conclusions:

1) Water content data for the CT cell are much smaller than the water content data from other tests. Water content data for the mock up test are the largest for all the tests for dimensionless times smaller than 0.04. For large times ($t_D > 0.04$), the curves of the water content versus radial distance for the CG cells, the mock up and in situ tests have similar slopes.

2) There are differences in water content data among the tests which could be due to differences in:

   - The initial flooding. The joins and gaps of the mock up test were flooded at the beginning of the test. This explains why the water content data for the mock up test are always the largest.

   - The geometric configuration of the water flow and heat transfer. Water flow is radial in the mock and in situ tests while it is parallel for CT and CG cells.

   - The thermal gradient. The temperatures at the boundaries are similar in most tests (100ºC near the heater and from 12 to 20 ºC at the hydration boundary). However, the thickness of the bentonite ranges from 10 cm (CT cells) to 75 cm in the in situ test. It should be taken into account that water evaporates near

the heater. Vapour diffuses away from the heater and condensates at some distance. This process retards the hydration of the bentonite buffer.

- The internal boundary condition at the heater-bentonite interface. The bentonite is directly in contact with the heater in the CT and CG cells as well as in the mock up test, whereas in the in situ test there is a metallic liner with a gap between the heater and the liner.

Temperatures reach quasi steady values quickly. Therefore, our analysis of temperature data has focused on in its spatial distribution along the bentonite buffer. The temperature decreases from the heater to the hydration boundary. The curves of temperature versus distance from the heater show two main parts: 1) Near the heater where the thermal gradient is large and 2) Near the hydration boundary where the gradient is smaller. Dimensionless measured temperature profiles show a slope of 0.7 which is similar for all the tests. This slope is similar to that of the computed temperatures.

Obtaining reliable chemical data for the bentonite pore water is a difficult task. Most often, the chemical composition of the bentonite is derived from aqueous extract tests which must be interpreted numerically with inverse geochemical models. This adds a difficulty to the integrated analysis of chemical data. Here, the analysis has focused on chloride, Cl^-, a conservative species. Chemical data cannot be monitored in time. Therefore, they are determined at the end of the heating and hydration during the dismantling of the bentonite barrier. Therefore, our analysis of the chemical data has dealt with the spatial distribution of the Cl^- concentration along the bentonite buffer at different times. In general, Cl^- concentrations are smallest near the hydration boundary and increase near the heater due to evaporation. In the central sections of the buffer, the concentration of Cl^- is constant for early and intermediate times. The integrated analysis of dimensionless Cl^- concentrations show that: 1) The Cl^- concentrations in the CT cell are much smaller than those of other tests; and 2) There are significant differences in the Cl^- concentrations of several sections of the dismantled heater 1 of the in situ test. Available data do not allow drawing clear conclusions regarding the consistency between aqueous extract and squeezing data. Preliminary analyses of pH data show that data from CG cells and in situ test are consistent. However, the pH data from CT cells and from section 29 of the in situ test are markedly different from the rest of the data. Possible reasons for the differences in chemical data among the tests include: 1) The method used to measure the chemical variables. This is the case for exchanged cations which in some tests were determined with the Chapman's method and in other tests were measured with the

$CsNiO_3$ method; 2) The chemistry of the hydration water. There are differences in the chemical composition of the hydration waters of the mock up and in situ tests; 3) Geometric configuration of the flow: radial versus parallel; 4) Thermal gradient which may affect water evaporation, vapour condensation and the evapo-concentrantion near the heater; and 5) Differences in the experimental conditions. There are heterogeneities in the barrier and in the granitic rock in the in situ test.

The integrated analysis presented here could be extended by:

1) Accounting for water redistribution in the Green-Ampt solution.
2) Developing analytical solutions for other variables such as temperature and concentration of dissolved species.
3) Including laboratory tests performed on very small bentonite samples.
4) Performing the integrated analysis of chemical data for reactive species such as Ca^{2+}, Mg^{2+}, Na^{+}, K^{+}, sulfate and bicarbonate.

Data from different space-time scales cannot be integrated and therefore there is no possibility for extrapolation in time from available data. Such extrapolation is most likely to be feasible my means of coupled THMC models.

Integración de los datos disponibles de bentonita usando diferentes escalas y análisis de la extrapolación a largo plazo para las barreras de arcilla

Resumen

La gestión final de los residuos radiactivos de alta actividad contempla el almacenamiento geológico profundo (AGP) que se basa en la utilización de una barrera de ingeniería compuesta de materiales arcillosos no saturados. Son numerosos los ensayos de laboratorio realizados en muestras de diferentes tamaños, con diferentes duraciones, con hidratación en flujo paralelo y radial. También se han desarrollado en los últimos años sofisticados modelos que se han calibrado con datos de ensayos de escalas espaciales y temporales menores que las de la barrera de ingeniería de un AGP real. Para evaluar hasta qué punto los datos disponibles se pueden extrapolar en el espacio y a largo plazo en el tiempo, se han recopilado los resultados disponibles sobre la hidratación de la bentonita FEBEX en ensayos de hidratación y calentamiento realizados en celdas de 12 y 60 cm de longitud y del ensayo en maqueta a escala casi real. Estos datos se han analizado de forma integrada mediante la adimensionalización del volumen y del tiempo. Se han desarrollado soluciones analíticas para la hidratación de la arcilla en condiciones de flujo paralelo y flujo radial mediante el método de Green-Ampt. Las soluciones analíticas para la hidratación con flujo paralelo y radial muestran diferencias importantes. Las soluciones analíticas permiten reproducir las curvas de hidratación de la bentonita calculadas con un modelo numérico de flujo no isotermo multifásico mediante el ajuste de la conductividad hidráulica aparente. Los datos de volumen de agua en función del tiempo para los ensayos realizados en las celdas CT (12 cm de longitud), las celdas CG (60 cm) de duraciones comprendidas entre 6 meses y 7.5 años y los del ensayo de la maqueta (a escala real y con una duración de 14 años) muestran diferencias grandes para tiempos adimensionales pequeños, pero en general presentan una coherencia global entre sí.

Los principales objetivos del análisis integral incluyen:

1) La recopilación de los datos disponibles hidrodinámicos, térmicos, y hidroquímicos de ensayos de calentamiento e hidratación en curso y los realizados en la bentonita FEBEX.
2) El análisis y filtrado de datos.
3) El análisis dimensional de las variables hidrodinámicas, térmicas y químicas, mediante la definición de los tiempos y volúmenes característicos, y la adimensionalización de los datos de consumo de agua, temperatura y concentración de soluto.
4) El análisis integrado de los datos de contenido de agua, entrada de agua, temperatura, concentraciones químicas del agua intersticial de los datos de bentonita de los experimentos realizados a diferentes escalas espacio-temporales.
5) El desarrollo de una solución analítica para la hidratación de la bentonita basada en el método de Green-Ampt.

Se ha desarrollado una solución analítica para la hidratación mediante el método de Green-Ampt. Se ha utilizado para comparar la entrada de agua del flujo radial y paralelo. La comparación revela que las soluciones analíticas son marcadamente diferentes. Estas diferencias se deben tener en cuenta al comparar los resultados obtenidos en celdas de laboratorio, donde las condiciones son de flujo paralelo, con las del ensayo in situ, en el que el calentamiento y la hidratación son radiales. La entrada de agua para flujo paralelo se ha calculado para los siguientes casos: 1) Mismo volumen y espesor, 2) Misma superficie de hidratación y espesor, y 3) Mismo volumen y la superficie de hidratación, y 4) Valores optimizados de espesor, volumen y superficie de hidratación. El mejor ajuste se obtiene con los valores optimizados. Se puede concluir que la entrada de agua de flujo radial y paralelo son comparables cuando las dimensiones y las condiciones se seleccionan correctamente. Los datos medidos de entrada de agua de las celdas CG de varios períodos, que van desde 0.5 a 7.5 años, se aproximan muy bien a la solución analítica Green-Ampt de una conductividad hidráulica aparente, K, ligeramente mayor que la correspondiente a 25 º C y la porosidad inicial de la bentonita. La solución analítica de Green-Ampt para flujo radial y paralelo reproducen bien las soluciones numéricas con una conductividad hidráulica aparente un poco más mayor que el correspondiente a 25 º C y la porosidad inicial de la bentonita.

Las principales conclusiones del análisis integrado de la entrada de agua incluyen:

1) La hidratación de las celdas CT y CG se produce en la parte inferior de las celdas y es esencialmente unidimensional y paralela al eje de la celda. La hidratación en la maqueta e in situ, por el contrario, se produce desde la superficie exterior y tiene una distribución radial. Por lo tanto, existe una clara diferencia en la geometría de la hidratación de las celdas de laboratorio y los ensayos de maqueta e in situ.

2) Los datos medidos de entrada de agua tienen incertidumbres. Para las celdas CG los datos de entrada de agua pueden tener una incertidumbre de aproximadamente el 15%. La entrada de agua final determinada con las mediciones en línea (a partir de la variación de peso del aparato) es un 15% mayor que la entrada de agua estimada a partir de la diferencia en el peso de la columna de bentonita al final y al inicio del ensayo. Los datos de entrada de agua de la maqueta también puede contener algunas incertidumbres, sobre todo para los datos más recientes debido a que el caudal es cada vez más bajo.

3) El análisis adimensional de los datos entrada de agua muestran que los datos de las celdas CT y CG y de la maqueta muestra una coherencia global. Hay grandes diferencias en los tiempos iniciales debido a efectos espurios tales como cortes eléctricos, relleno de juntas de los bloques de bentonita y otros. Estas diferencias, sin embargo, disminuyen con el tiempo. Los datos de la mayoría de los ensayos convergen para tiempos adimensionales superiores a 0,04. La entrada de agua de la celda CT es un poco más grande que la de la maqueta.

4) La entrada de agua calculada con el modelo numérico para flujo paralelo, como el de la celda la CT23, es mayor que la calculada para la maqueta (flujo radial).

5) El presente análisis integrado supone que el volumen y la densidad son constantes. Por lo tanto no se contabilizan los cambios en la porosidad, en la permeabilidad y en la temperatura.

El análisis integrado de datos de contenido de humedad conduce a las siguientes conclusiones:

1) El contenido de humedad de las celdas CT es menor que el contenido de humedad de los otros ensayos. Los datos de la maqueta son los más grandes de todos para tiempos adimensionales menores de 0,04. Para los tiempos altos (T_D> 0,04), la forma general de la curva de contenido de humedad en función de la distancia son similares para las celdas CG, maqueta e in situ.

2) Hay diferencias en los datos de contenido de humedad entre los ensayos debidos a:

   - La inundación inicial de la maqueta. Entre bloques de la bentonita de la maqueta se inundaron en el inicio del ensayo. Por ello, el contenido de humedad de la maqueta es el mayor de todos los ensayos.

   - La configuración geométrica del flujo. El flujo de agua es radial en la maqueta y en el ensayo in situ, mientras que es paralelo en las celdas CT y CG.

   - Gradiente térmico. Las temperaturas en los contornos son similares en la mayoría de los ensayos (100 º C, cerca del calentador y de 12 a 20 º C en el borde de hidratación). Sin embargo, el espesor de la bentonita oscila entre 10 cm (celdas CT) y 75 cm en el ensayo in situ. El agua se evapora cerca del calentador. El vapor se difunde lejos del calentador y se condensa a cierta distancia. Este proceso retarda la hidratación de la zona intermedia de bentonita.

   - La condición de borde en la interfaz de calentador-bentonita. La bentonita está directamente en contacto con el calentador en las celdas CT y GC, así como en la maqueta, mientras que en el ensayo in situ hay un revestimiento metálico que crea un vacío hueco entre el calentador y la bentonita.

Las temperaturas alcanzan valores casi constantes rápidamente. Por lo tanto, el análisis de la temperatura se ha concentrado en su distribución espacial en la bentonita. La temperatura disminuye desde el calentador hacia la zona de hidratación. La distribución radial de la temperatura muestra dos partes principales: 1) Cerca del calentador donde el gradiente térmico es grande y 2) Cerca del borde de hidratación donde la pendiente es menor. Los perfiles adimensionales de la temperatura muestran una pendiente de 0.7 que es similar para todos los ensayos. Esta pendiente es similar a la de las temperaturas calculadas numéricamente.

La obtención de datos fiables químicos para el agua intersticial de la bentonita es una tarea difícil. Por lo general, la composición química de la bentonita se obtiene mediante ensayos de extractos acuosos, que deben ser interpretados numéricamente con modelos geoquímicos inversos. Esto impone una restricción en el análisis integrado de los datos químicos. El análisis se ha centrado en cloruro, Cl^-, una especie conservativa. Los datos químicos no pueden ser medidos en el tiempo durante el ensayo. Se determinan al final del ensayo, después del desmantelamiento de la barrera de bentonita. Por lo tanto, el análisis de los datos químicos se ha centrado en la distribución espacial en la bentonita de la concentración de Cl^- en diferentes tiempos. En general, la concentración de Cl^- es el más pequeña cerca de la zona de hidratación y aumenta cerca del calentador debido a la evaporación. En las zonas centrales, la concentración de Cl^- se mantiene constante durante los tiempos iniciales. El análisis integrado de las concentraciones adimensionales de Cl^- muestra que: 1) Las concentraciones de Cl^- en la celda CT son mucho menores que los de otros ensayos, y 2) Existen diferencias significativas en las concentraciones de Cl^- cerca del calentador en varias secciones del ensayo in situ. Los datos disponibles no permiten obtener conclusiones claras sobre la similitud entre el extracto acuoso y los datos de "estrujamiento". Los análisis preliminares de los datos de pH indican que los datos de las celdas CG e in situ son consistentes. Sin embargo, los datos de pH de las celdas CT y de la sección 29 del ensayo en situ son muy diferentes a los del resto de los datos. Las posibles razones de las diferencias en los datos químicos entre los ensayos son: 1) El método utilizado para medir las variables químicas. Este es el caso de los cationes de intercambio, que en algunos ensayos se determinaron con el método de Chapman y en otros midieron con el método del $CsNiO_3$, 2) La composición química del agua de hidratación, que es diferente en la mayoría de los ensayos, 3) La configuración geométrica del flujo: radial y paralelo, 4) El gradiente térmico, que puede afectar a la evaporación del agua, la condensación del vapor y a la evapo-concentración cerca del calentador, y 5) Las diferencias en las condiciones experimentales. En el ensayo in situ podría haber heterogeneidades a lo largo de la barrera de arcilla y a lo largo de la roca granítica.

El trabajo aquí presentado se puede mejora mediante:

1) La ampliación de la solución Grenn-Ampt para tener en cuenta la redistribución del agua.

2) El desarrollo de soluciones analíticas para otras variables como, la temperatura y la concentración de especies disueltas.

3) La consideración de ensayos de laboratorio realizados en muestras muy pequeñas de bentonita cuyos datos no pudieron ser recopilados para este estudio.

4) Completar el análisis integrado de los datos químicos de las especies reactivas tales como, Ca^{2+}, Mg^{2+}, Na^{+}, K^{+}, sulfato y bicarbonato.

Content

List of Figures

List of Tables

1. Introduction

1.1. Objectives

A large number of hydrodynamic, geochemical and thermal data have been collected for compacted bentonites during the last 30 years to characterize their properties and evaluate the feasibility of compacted bentonite for the Engineered Clay Barrier (EBS) of a high level radioactive waste repository. Various laboratory and in situ heating and hydration experiments were performed within FEBEX and NFPRO Projects (ENRESA, 2001; 2006a). Such experiments were modeled previously by several groups, including mainly the THM models of the UPC team (Villar et al, 2008b) and the THC models performed by the UDC group (Samper et al., 2008; Zheng and Samper 2008; Zheng et al., 2010; 2011). There is a wide range of time and space scales within the experiments. Their durations range from a few months in the case of the CT cells to more than 14 years in the case of the FEBEX mock up and in situ tests. The size of the experiments ranges from 10 cm in CT cells to more than 10 m in the in situ test. The need to extrapolate from laboratory experiments to the long-term conditions of the actual barrier motivates the need to compile, analyze and integrate the data from the heating and hydration experiments performed on FEBEX bentonite.

The main objectives of this study include:

1) The compilation of available hydrodynamic, thermal, and hydrochemical data from reported and ongoing heating and hydration experiments performed on FEBEX bentonite
2) The analysis and filtering of such data
3) The dimensional analysis of hydrodynamic, thermal and chemical variables, including the definition of
    - The characteristic times and volumes
    - Dimensionless water uptake, water content, temperature and solute concentration
4) The integration of water content, water uptake, temperature and chemical concentration data from experiments performed at different space-time scales by means of dimensionless variables

5) The development of an analytical solution for bentonite hydration based on the Green-Ampt method

1.2. Scope

Chapter 2 describes the reference concept of the Spanish repository in granitic rock and presents a description of its expected early time evolution with an indication of the most relevant time and space scales of the engineered barrier. The compilation of available data from FEBEX bentonite is presented in Chapter 3. Chapter 4 describes the dimensionless analysis of the flow equation and the formulation of the main variables such as time, water inflow, radial distance, temperature, water content and chemical composition. Chapter 5 presents the integrated analysis of hydration data. The use of the Green-Ampt method to derive analytical solutions for bentonite hydration in radial and parallel flow conditions is described in Chapter 6. Chapters 7, 8 and 9 describe the integrated analysis of the water content, temperature and chemical data, respectively. Finally, Chapter 10 contains the main conclusions.

2. Reference concept and time and space scales of the EBS

2.1. Introduction

High-level radioactive waste disposal (HLW) in deep geological formations is based on a multi barrier concept which includes natural and engineered barriers. The natural barrier is the host rock while the engineered barriers include the waste form, the canister, and the bentonite buffer. This chapter describes the reference concept for the Spanish HLW repository in granitic rock and presents a description of its expected early time evolution with an indication of the most relevant time and space scales of the engineered barrier. This description is based on the ENRESA performance assessment project, named ENRESA 2000 (ENRESA, 2000b) and the results of the FEBEX project (ENRESA 2000a, 2006a).

2.2. Spanish reference concept for radioactive waste disposal

The repository concept in granite is based on the disposal of spent fuel in carbon steel canisters in long horizontal disposal drifts. Canisters are surrounded by high-density bentonite. Access is accomplished by means of "main drifts" which are perpendicular to the disposal drifts. The main drifts meet at a central area, which includes the required underground infrastructure. Communications between the surface and the central underground area are accomplished by means of 3 access shafts and a ramp. Figure 1 shows a view of the underground installations.

The canister measures 4.54 m in length and 0.90 m in diameter, and contains 4 PWR or 12 BWR fuel elements in a subcritical configuration. The thickness of the wall of the canister is 0.10 m at the cylindrical wall and 0.12 m at the ends, and is capable of withstanding the pressures to which it is subjected under disposal conditions and of providing a minimum period of containment of one thousand years. After being unloaded from the reactor, the fuel elements are temporarily stored for their thermal power to decay to a level at which they may be disposed of with a total thermal power of 1,220 W per canister. A total of 3,600 canisters will be required for the final waste inventory of spent fuel estimated for the Spanish nuclear power programme.

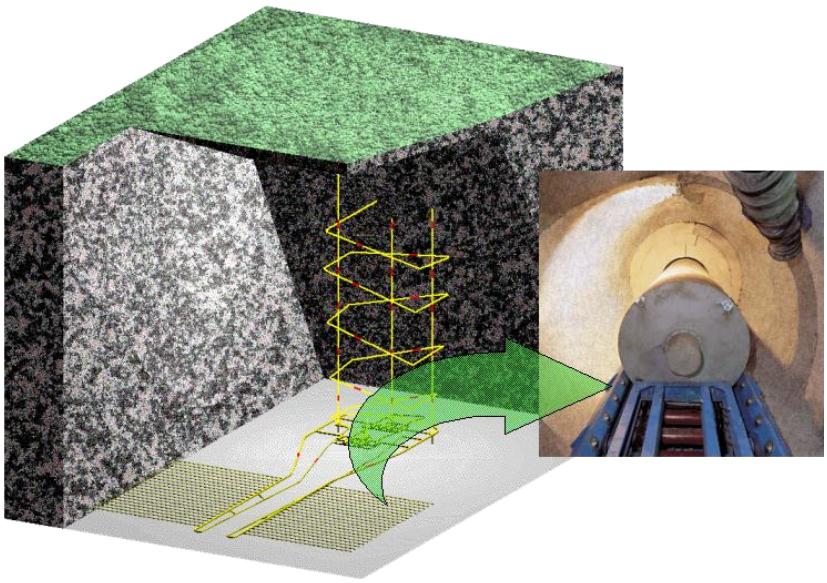

Figure 1. ENRESA repository concept. Underground installations.

Canisters are disposed in cylindrical disposal cells, constructed with blocks of precompacted bentonite. Pre-compacted bentonite blocks, of 1,700 kg/m^3 dry density (in order to achieve a final dry density of 1,600 kg/m^3), are used. The blocks are initially unsaturated with a degree of saturation of 66%. The disposal drifts of 500 m in length and 2.4 m in diameter (see Figure 2) are located at a depth of 500 m in the host rock formation. The separation between canisters is determined mainly by thermal constraints. Separations of 2.0 m between canisters and 35 m between disposal drifts have been established, in order not to exceed a temperature of 100 ºC in the bentonite. Actual separation is a function of the properties of the host rock. The thermal calculations have been made for a reference generic site. The detailed dimensions of an individual "cell" are shown in Figure 3.

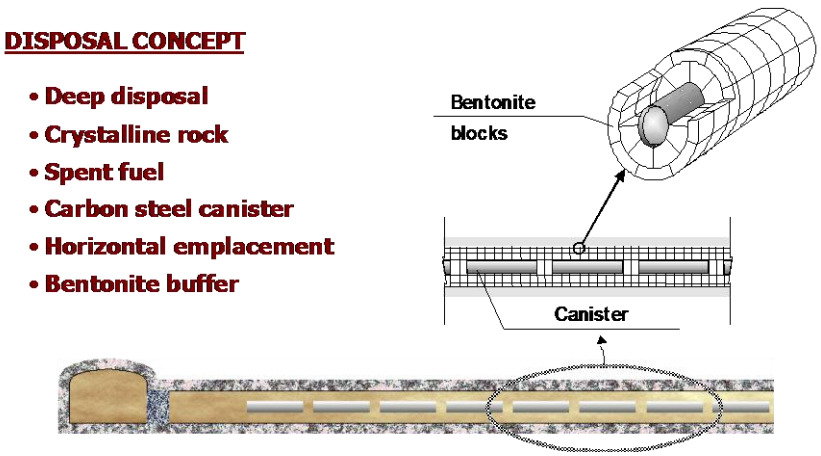

Figure 2. Longitudinal section of a disposal drift.

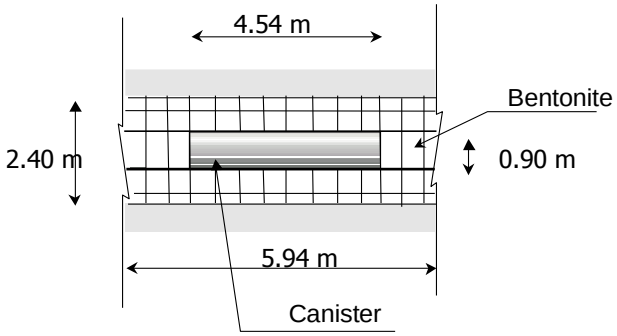

Figure 3. Dimensions of an individual disposal cell.

Once a disposal drift is completed, it is sealed with a 6 m long seal made of bentonite blocks and closed with a concrete plug at its entry. After completion of all the disposal drifts, main drifts, ramp, shafts and other remaining rock cavities will be backfilled with a mixture of bentonite and natural sand or an appropriate crushed material. The backfilling material will consist of 10 % bentonite (increasing up to 20 % at the top of the drifts) and suitably graded sand.

2.3. Relevant transient stages in a HLW repository

Knowing the estimated duration of the relevant transient stages of the repository is required to study the bentonite buffer of the engineered barrier. This section on the relevant transient stages of the EBS is based on a Technical Note of the PEBS Project (Samper et al., 2010).

The estimated duration of the water saturation will be from 50 to 100 years. The approximate duration of the pressure equilibration will be 200 years. Thermal gradients within the EBS are expected to dissipate after around 1000 years. The thermal pulse will last longer. Geochemical transient stages include: 1) Those associated with the thermal and hydrodynamic transient, 2) The geochemical transient stage associated with solute diffusion through the EBS outer interface, 3) The stage associated with the geochemical evolution of the major aqueous chemical species within the EBS, 4) The stage associated with the interactions of corrosion products and the bentonite, 5) The stage of interactions of concrete and bentonite, and 6) The stage associated with the transport and sorption of the radionuclides (Samper et al., 2010).

2.4. Lab and in situ experiments of the PEBS project

The available experiments for PEBS come from earlier projects such as FEBEX project (Full scale engineered barrier experiment) (ENRESA, 200a, 2006a). The large scale experiments include the in situ FEBEX experiment at Grimsel, the mock up test at Ciemat with similar dimensions, and the geochemical mock up experiment (GAME).

The laboratory experiments include the heating and hydration experiments on CT cells (Fernández et al., 1999), the large column experiments from Ciemat (CG) (Villar et al, 2008a), and the laboratory experiments to study the interfaces. Medium size experiments were made to study the canister-bentonite and the bentonite-concrete interfaces. New experiments are being performed within PEBS on small samples to study the combination of the two interfaces: canister-bentonite-concrete.

2.5. Stages of the HLW repository studied with each experiment

Large scale experiments aim at studying the EBS water saturation and the pressure equilibration transients. The large column experiments from Ciemat were designed to study the EBS water saturation and pressure equilibration transients. The geochemical mock up experiments (GAME) aim at the studying the geochemical transient stages. Other laboratory experiments are intended to study the interactions of the concrete and the bentonite, and the interactions of the corrosion products with the bentonite (Samper et al., 2010).

2.6. Uses of the test for modeling

2.6.1 Use of the ongoing tests

Large scale experiments will be used to test the THM model. Large column experiments from Ciemat will be used to test the THCm model. The use of the geochemical mock up experiments (GAME) will depend on the outcome of the feasibility report. If they are feasible, these tests will be used for THMC model testing. Laboratory experiments of the interfaces will be used to improve the model of corrosion products and the concrete-bentonite interactions, and to calibrate model parameters (Samper et al., 2010).

2.6.2 Use of the new tests

The new tests aim at reproducing the repository conditions for a time window from 1000 to 3000 years. The time window was selected because (Samper et al., 2010): 1) Reported performance assessment projects consider such time window for the failure of stainless-steel canister; 2) The time needed for solute out diffusion from bentonite into granite is on the order of a few thousands of years; 3) Both hydrodynamic and thermal gradients are dissipated after 3000 years.

The new tests aim at studying simultaneously the two interfaces canister-bentonite and bentonite-concrete and theirs possible interactions. They will be useful for: 1) Model testing; 2) Bounding model hypotheses; 3) Testing current PA models such as those used within NFPRO and evaluating if they can reproduce the new tests.

3. Available data for FEBEX bentonite

3.1. Description of the FEBEX project

FEBEX (Full-scale Engineered Barrier Experiment) was a demonstration and research project for the engineered barrier of high level radioactive waste repository. FEBEX was based on the Spanish reference concept for radioactive waste disposal in crystalline rock according to which canisters are emplaced in horizontal drifts and surrender by a compacted bentonite clay barrier (Samper et al., 2008). The main objectives of the FEBEX project were: 1) Demonstration of handling and constructing an engineered barrier system; 2) Study and modeling of the thermo-hydro-mechanic (THM) processes in the near field; 3) Study and modeling of the thermo-hydro-geochemical (THG) processes in the near field. The project includes two main large-scale tests which started in February, 1997: the in situ full-scale test performed at Grimsel, Switzerland, and the mock-up test operating at Ciemat facilities in Madrid, Spain (ENRESA, 2006a; ENRESA, 2006b). Numerous lab tests, with different sizes, durations and heating and wetting conditions, were also performed. The project was initially planned to last 7 years (1994 to 2001) and its performance was divided into four successive stages. The stages were: pre-operational (planning, design, characterisation of the clay, installation, and modelling); dismantling (extraction, inspection, sampling, and study of the materials); and final evaluation of the results and verification of the models. Then, it was extended from 2000 to 2004.

3.2. FEBEX tests

3.2.1 Lab tests

Heating and hydration lab tests include those performed in the CT and CG cells. Experiments on CT cells are performed on single a bentonite block measuring 13 cm in height and 15 cm in diameter. Compacted bentonite at a dry density similar to that of the barrier in a repository is heated at the top at 100ºC while it is simultaneously hydrated with distilled or granitic water at the bottom. At the end of the test, the effect produced in the bentonite was studied (Fernández et al., 1999; Zheng et al., 2010). The bentonite bolck is covered by a stainless steel cell with dimensions, 15.05 cm in internal diameter, 22.2 cm in external diameter, 14.6 cm in height and 3.5 cm in wall thickness. Distilled water is injected at a

pressure of 1 MPa at the bottom of the cell through a porous stone. At the top of the cell a heating system is used to impose a temperature of 100ºC (Figure 4).

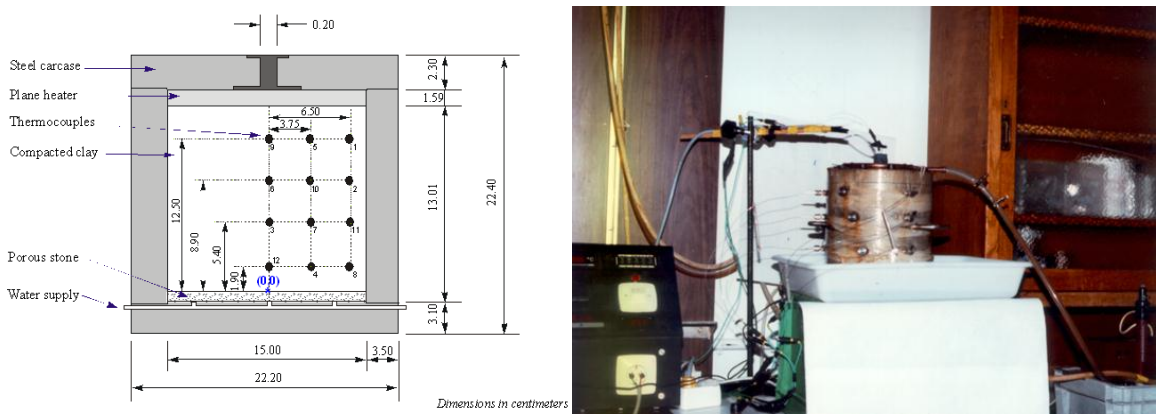

Figure 4. Schematic design of the CT cells and cell in the laboratory (Fernández et al.,1999).

Infiltration tests in large-scale cells were performed on CG cells during FEBEX I (Villar et al., 2008a). They lasted from 0.5 to 7.6 years. These cells are made of Teflon inside and steel outside to prevent lateral heat conduction and avoid the deformation of the cell by bentonite swelling. The dimensions of the bentonite cell are 7 cm in diameter and 60 cm in length. The bentonite sample is made of smaller blocks of FEBEX bentonite 10 cm long and 7 cm diameter. At the bottom part of the cell, a flat stainless steel heater imposed a temperature of 100ºC. Hydration with granitic water took place through the upper surface at an injection pressure of 1.2 MPa. Seven tests were performed in these cells: two of them with a duration a 0.5 years, two with a duration of 1 year, two with a duration of 2 years and another one with a duration of 7.6 years (Villar et al., 2008b). Two tests were performed for each duration, the FQ test which was used for post-mortem determination of hydro-mechanical and geochemical properties, and the HI test which was used for post-mortem determination of geochemistry and extraction of pore water. The longest test, CG3, was used for both types of post-mortem determinations (Figure 5).

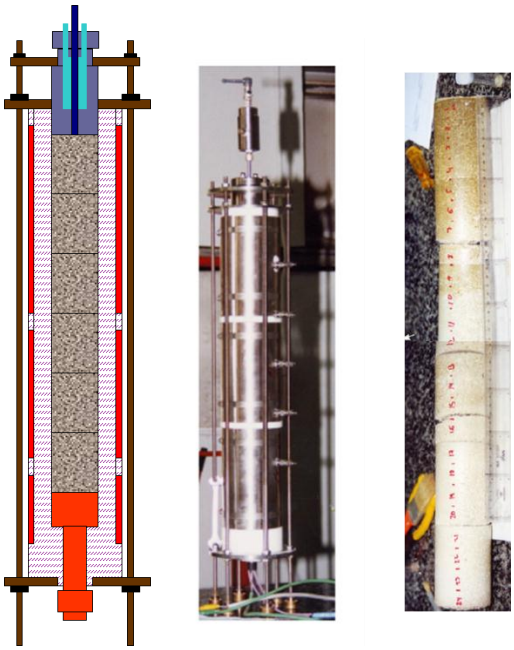

Figure 5. Laboratory CG cell and bentonite column in the post-mortem analysis (Martin et al.,2006).

3.2.2 Large scale tests

The mock up test replicates at almost full scale the EBS of the Spanish reference concept for radioactive waste disposal in granite. The components are two electric heaters, the clay barrier, the instrumentation, the automatic control heating system, and a data acquisitions system. The bentonite buffer is confined in a steel structure which ensures a uniform temperature and water pressure around the external surface of the bentonite (Zheng and Samper, 2008; ENRESA, 2000, 2006b). The clay barrier is made up of highly compacted benonite blocks. The total bentonite mass installed was 22.5 t. The heating and hydration stage commenced in February 1997. The hydration of the mock up test started by filling all the joins and gaps with an initial flooding of six days. Once joins were closed, bentonite hydration took place at a pressure of 700kPa. The temperature of the heaters inside was controlled initially at a temperature of 100ºC (Figure 6).

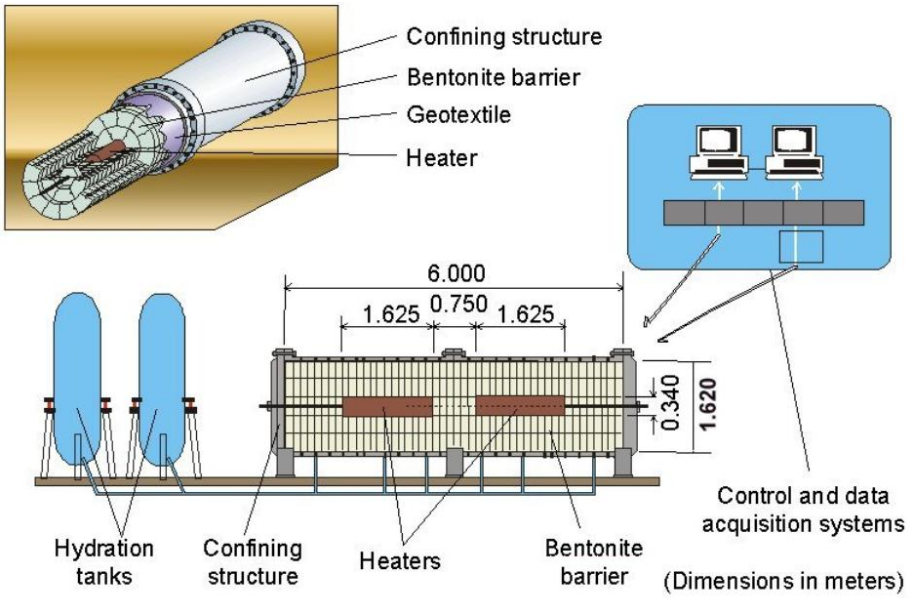

Figure 6. Schematic design of the mock up test (Martin et al.,2006).

The in situ test is being performed in a gallery excavated in granite in the underground research laboratory of Grimsel operated by NAGRA in Switzerland. The test includes the heating system, the clay barrier and the instrumentation, monitoring and control system. The drift is 70.4 m long and 2.28 m in diameter (ENRESA, 2000). The test zone is located in the last 17.4 m of the drift where heaters, bentonite and instrumentation were installed. The heaters are separated by 1m. They are designed to maintain a maximum temperature of 100ºC at the steel liner bentonite interface. The bentonite barrier is made of blocks of highly compacted bentonite. The test began on February 1997. Heater 1 was switched-off in February 2002 (Figure 7).

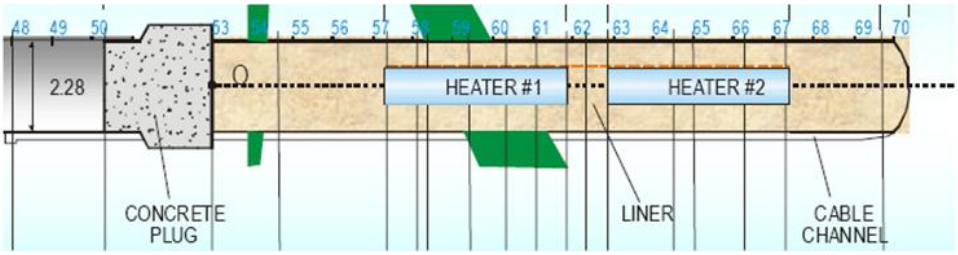

Figure 7. Scheme of the FEBEX in situ test. Vertical lines show the location of the sampling sections (Samper et al., 2008).

3.3. Water inflow data

Water inflow data are available for the following tests:

- CT22, CT23
- FQ1/2 (CG1), HI1/2 (CG1), FQ2 (CG2), CG3
- Mock up

3.4. Water content data

Water content is measured with different methods. For the CT and CG cells the Gravimetric water content are available. In the mock up test, relative humidity is monitored. Volumetric water content is available for the in situ test. Water content data are available for the following tests:

- CT22, CT23, CT24
- FQ1/2 (CG1), HI1/2 (CG1), FQ2 (CG2), CG3
- Mock up
- In situ

3.5. Temperature data

Most of the tests have installed thermocouples which measure the temperature evolution. Temperature data are available for the following tests:

- CT22, CT23, CT24
- FQ1/2 (CG1), HI1/2 (CG1), FQ2 (CG2), HI2 (CG4), FQ1 (CG5), HI1(CG6)
- Mock up
- In situ

3.6. Chemical concentration data

Pore water chemistry of the bentonite has been measured with 1:4 aqueous extract, and squeezing methods. Chemical data are available for the following tests:

- CT22, CT23
- FQ1/2 (CG1), HI1/2 (CG1), FQ2 (CG2), HI2 (CG4), FQ1 (CG5), HI1(CG6), CG3
- In situ

3.7. Summary of available data

Table 1 shows a summary of the available data for all the tests. It includes the type of test, the duration and the thickness of the bentonite barrier. Laboratory cells are smaller and shorter than the mock up and in situ tests. The geometry of the tests is cylindrical. The hydration of the in situ and mock up tests takes place at the external lateral surface. Heating was applied at the internal surface. On the other hand, the cells were heated at the top (CT cells) or the bottom (CG cells) and hydrated from the bottom or top sides. Therefore, the flow is radial in the mock up and in situ tests, and parallel in the CT and CG cells.

Table 1. Summary of the available data selected in FEBEX tests.

Test	Duration (days)	Bentonite thickness (m)	Available data			
			Hydration	Water content	Temperature	Chemical
CT-22	26	0.12	Yes	Yes	Yes	Yes
CT-23	183	0.12	Yes	Yes	Yes	Yes
CT-24	168	0.12	No	No	Yes	No
FQ1/2 (CG1)	188	0.60	Yes	Yes	Yes	Yes
HI1/2 (CG1)	214	0.60	Yes	Yes	Yes	Yes
FQ2 (CG2)	762	0.60	Yes	Yes	Yes	Yes
CG3	2775	0.60	Yes	Yes	No	Yes
HI2 (CG4)	747	0.60	No	No	Yes	Yes
FQ1 (CG5)	370	0.60	No	No	Yes	Yes
HI1(CG6)	440	0.60	No	No	Yes	Yes
MOCK UP	5076	0.79 (no heater) 0.62 (heater)	Yes	Yes	Yes	No
IN SITU	4839	1.14 (heater) 0.66 (no heater)	No	Yes	Yes	Yes

3.8. Location of sensors and sampling sections

Figure 8 shows the location of the sampling sections used for the water content and chemical data determination for the CT cells.

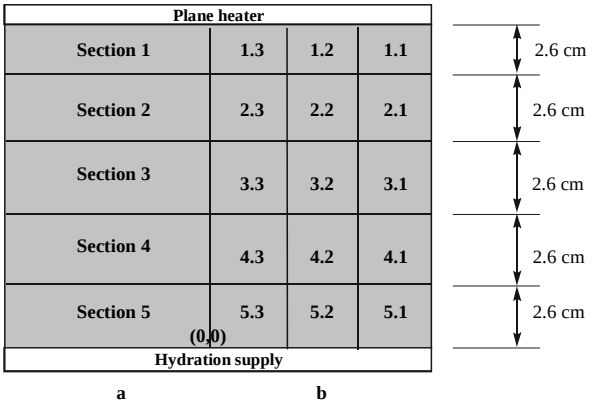

Figure 8. Location of samplings sections for water content data chemical data for CT cell (Fernández et al., 1999).

Figure 9 shows the location of the thermocouple sensors Ch103, Ch106 and Ch109 used to measure temperature for the CT cells. Figure 10 shows the location of the sections used to measure water content and chemical data for CG cells. Figure 11 shows the layout and the location of the sensors used in the mock up test. Sensors A4 and A6 were used to measure relative humidity. Sensors A2, A5 and A8 were used for temperature.

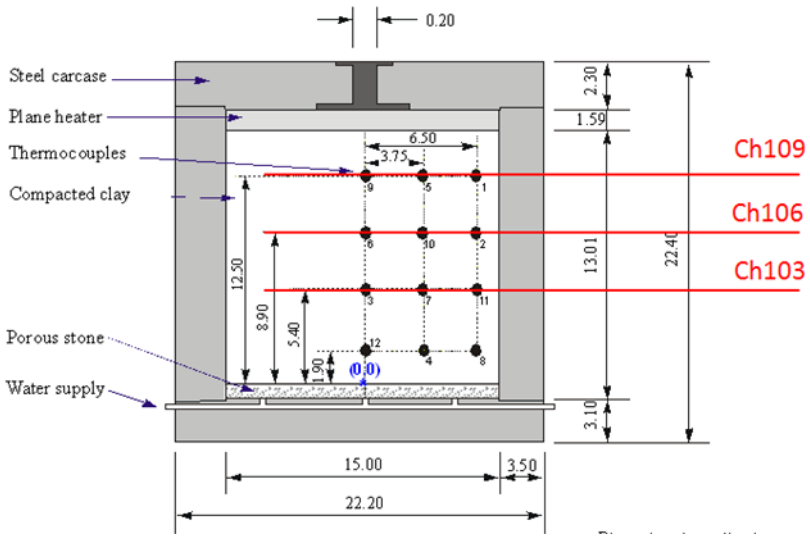

Figure 9.Location of temperature thermocouples Ch103, Ch106 and Ch109 for CT cell (Fernández et al., 1999).

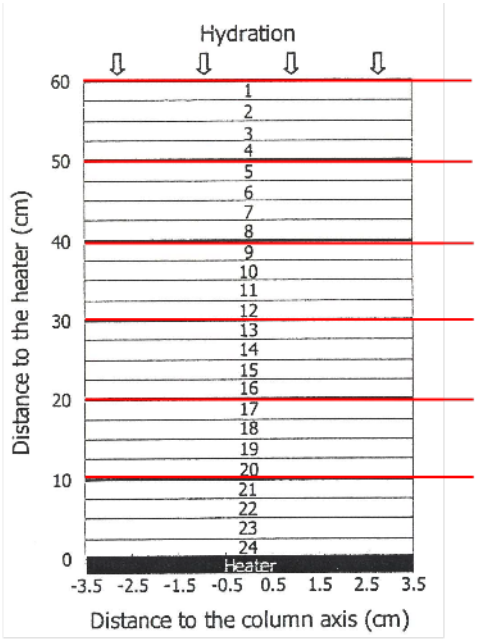

Figure 10. Location of sampling sections for water content and chemical data for CG cells (Villar et al, 2008).

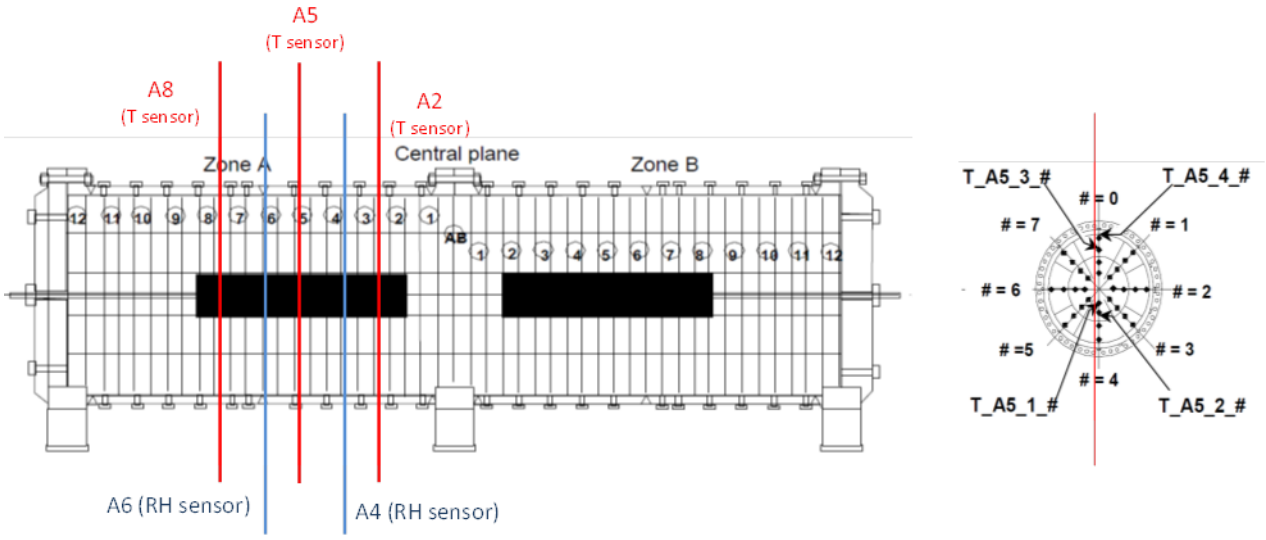

Figure 11. Layout and location of relative humidity (A4 and A6) and temperature (A2,A5 and A8) sensors for the mock up test (Martín et al., 2005).

Figure 12 shows the layout and the location of water content and temperature sensors for the in situ test. Sections M1 and M2 were used to measure water content data. Sensors D1, G, I and D2 were used to measure temperature. Figure 13 shows the location of the sections 19, 28, 29 and 31 used to determinate water content and chemical data during the post-mortem analysis.

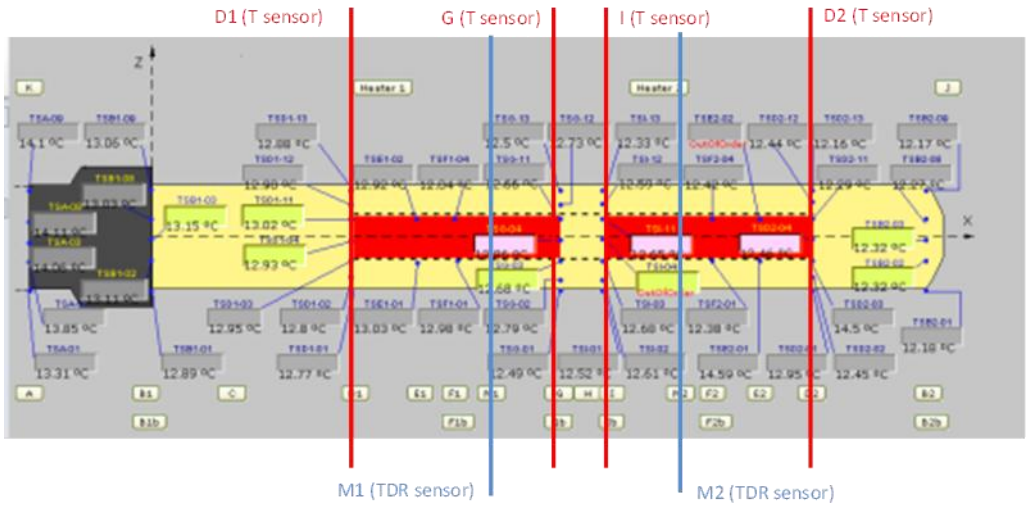

Figure 12. Layout and location of the water content (M1 and M2) and temperature (D1, G, I and D2) sensors for the in situ test (Aitemin, FEBEX database).

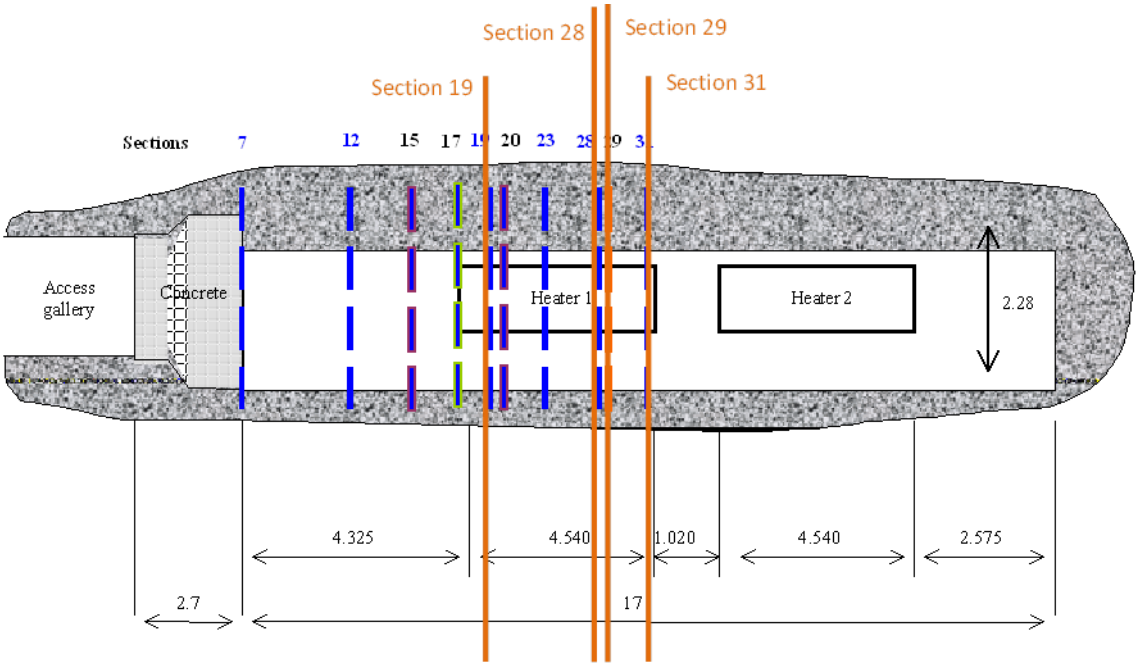

Figure 13. Layout and location of 19, 28, 29 and 31 sections for water content and chemical data for the in situ test (Samper et al., 2008).

4. Dimensional analysis

4.1. Introduction

The tests have different geometries, dimensions and durations. The flow applied is parallel for the lab cells and radial for the mock up and in situ tests. For this reason, the integrated analysis of the data is made in terms of dimensionless variables. The dimensional analysis is a tool to find or check the relations among physical quantities by using their dimensions. The dimension of physical quantities is the combination of the basic physical dimension (such as mass, length, time, temperature…) which describes it. First, a dimensionless analysis of the flow equation is performed to obtain the dimensionless variables. Then, other variables such as temperature, water content, and concentrations are studied.

4.2. Dimensional analysis of the flow equation

The mass balance equation is given by (Navarro and Alonso, 2000):

$$\frac{D_s m^w}{Dt} + m^w \nabla \cdot v^s + \nabla \cdot (\rho^l X_l^w q^l + \rho^g X_{gl}^v q^g + j^v) = 0 \quad (1)$$

where:

- D_s/Dt is the derivative with respect to the solid particles which move with the velocity vector, V^s.
- ρ^l and ρ^g are the liquid and gas densities, respectively
- X^w_l and X^v_g are the mass fraction of the water in the liquid and of the vapour in the gas, respectively
- q^l, q^g, j^v, are the liquid flow, gaseous and diffusive flux, respectively

The water mass per unit volume of porous medium is:

$$m^w = \phi(\rho^l X_l^w S^l + \rho^g X_{gl}^v (1 - S^l)) \quad (2)$$

where:

- Ø is the porosity
- S^l is the saturation degree

The flux of the liquid and the gas are obtained from the constitutive equations (Zheng et al., 2010):

$$q^l = -\frac{k^{il}k^{rl}}{\mu^l}(\nabla p^l + \rho^l g \nabla z) - k_T \nabla T + \sigma \frac{k^{il}k^{rt}}{\mu^l}\nabla \pi_h \tag{3}$$

$$q^g = -\frac{k^{ig}k^{rg}}{\mu^g}(\nabla p^g + \rho^g g \nabla z) \tag{4}$$

The diffusive flow of the vapour is defined by Fick's law according to:

$$j^v = -\rho^g D^v \nabla X_g^v \tag{5}$$

where:

- k^{il}, k^{rl}, k^{ig}, k^{rg}, are the intrinsic and relative permeabilities of the liquid and gas, respectively
- z is the elevation
- K_T is the thermo-osmotic permeability
- π_h is the osmotic pressure
- σ is the reflexion coefficient
- D^v is the dispersion tensor

To simplify our analysis, the terms involving gas, osmosis and the velocity derivative are ignored. The resulting equations are:

$$\frac{D_s m^w}{Dt} + \nabla \cdot (\rho^l X_l^w q^l) = 0 \tag{6}$$

$$m^w = \phi(\rho^l X_l^w S^l) \tag{7}$$

$$q^l = -\frac{k^{il}k^{rl}}{\mu^l}(\nabla p^l + \rho^l g \nabla z) \tag{8}$$

Introducing Equations (7) and (8) into the balance Equation (6), one obtains:

$$\frac{D_s(\phi(\rho^l X_l^w S^l))}{Dt}+\nabla\cdot\left[\rho^l X_l^w\left(-\frac{k^{il}k^{rl}}{\mu^l}(\nabla p^l+\rho^l g\nabla z)\right)\right]=0 \tag{9}$$

$$\frac{(\rho^l X_l^w S^l)D_s(\phi)}{Dt}-\frac{k^{il}k^{rl}}{\mu^l}\rho^l X_l^w\nabla\cdot(\nabla p^l+\rho^l g\nabla z)=0 \tag{10}$$

The dimensional analysis is made by defining the following dimensionless variables

$$t_D=\frac{t}{t_*},x_D=\frac{x}{L},z_D=\frac{z}{H},p_D^l=\frac{p^l}{P},\phi_D=\frac{\phi}{\phi_t} \tag{11}$$

where the sub index D denotes dimensionless variable.

Operating and re-arranging Equation (10), one obtains:

$$\rho^l X_l^w S^l\frac{\phi}{t_*}\frac{\partial\phi_D}{\partial t_D}-\frac{k^{il}k^{rl}}{\mu^l}\rho^l X_l^w\left(\frac{P}{L^2}\frac{\partial^2 p_D}{\partial {x_D}^2}+\frac{\rho^l gH}{L^2}\frac{\partial^2 z_D}{\partial {x_D}^2}\right)=0 \tag{12}$$

$$\frac{L^2 S^l\phi}{t_*}\frac{\partial\phi_D}{\partial t_D}=\frac{k^{il}k^{rl}}{\mu^l}\left(P\frac{\partial^2 p_D}{\partial {x_D}^2}+\rho^l gH\frac{\partial^2 z_D}{\partial {x_D}^2}\right) \tag{13}$$

$$\frac{L^2 S^l\phi\mu^l}{t_* k^{il}k^{rl}P}\frac{\partial\phi_D}{\partial t_D}=\left(\frac{\partial^2 p_D}{\partial {x_D}^2}+\frac{\rho^l gH}{P}\frac{\partial^2 z_D}{\partial {x_D}^2}\right) \tag{14}$$

Therefore, the dimensionless time t_D is given by:

$$t_D=\frac{t}{t_*}=\frac{k^{il}k^{rl}Pt}{L^2 S^l\phi\mu} \tag{15}$$

Let K is the saturated hydraulic conductivity which is given by:

$$K=\frac{k^{il}\rho^l g}{\mu^l} \tag{16}$$

Substituting (16) into (15), one obtains:

$$t_D=\frac{k^{rl}PK}{L^2 S\phi\rho^l g}t \tag{17}$$

We recall here the flow equation in porous media for saturated flow:

$$K\frac{\partial^2 h}{\partial x^2}+w=S_S\frac{\partial h}{\partial t} \tag{18}$$

The dimensionless time in this case is given by:

$$t_D=\frac{tK}{S_S L^2} \tag{19}$$

Other authors have proposed other dimensionless times. Table 2 shows a compilation of dimensionless times. The dimensionless time includes always a conductivity divided by the square of a length, the dynamic viscosity and the compressibility.

Table 2. Comparison of different dimensionless times.

Paper	Calculation characteristics	Dimensionless time	Comparison
Cox and Pruess, 1990	Convection cells experiments	$t_D=\frac{Kt}{Kx^2\mu\phi\beta}$ $\beta=\frac{1}{\rho}\frac{d\rho}{dP}$	$t_D=\frac{k^{il}k^{rl}P}{L^2S^l\phi\mu}$ $x^2=L^2$ $K\approx\frac{k^{il}k^{rl}}{S^l},(S^l)^3=k^{rl}$ $\beta=\frac{1}{P}$
Yu-Shu Wu and Pruess, 1999	Radial system, constant permeability	$t_D=\frac{kt}{r^2\mu\phi C_T}$ $C_T=\frac{1}{\phi}\frac{d\phi}{dP}$	$t_D=\frac{k^{il}k^{rl}P}{L^2S^l\phi\mu}$ $r^2=L^2$ $K\approx\frac{k^{il}k^{rl}}{S^l},(S^l)^3=k^{rl}$ $C_T=\frac{1}{P}$
Yu-Shu Wu, et al., 2004	Triple porosity media (matrix, large fracture, short fractures) and steady state flow	$t_D=\frac{k_F t}{r_w^2\mu(\phi_m C_m+\phi_f C_f+\phi_F C_F)}$ $C_T=\frac{1}{\phi}\frac{d\phi}{dP}$ M=matrix, f=short fracture, F=large fracture	$t_D=\frac{k^{il}k^{rl}P}{L^2S^l\phi\mu}$ $r^2=L^2$ $K\approx\frac{k^{il}k^{rl}}{S^l},(S^l)^3=k^{rl}$ $C=\frac{1}{P}$ $\phi_M+\phi_f+\phi_F=\phi$

4.3. Dimensional analysis of hydration data

4.3.1 Cumulative volume

Dimensionless water uptake is defined as follow:

$$V_D = \frac{4V}{\pi D^2 L \Delta\theta} \tag{20}$$

It can be seen that V_D is equal to the water uptake V divided by the volume of water that the system can take which is equal to the volume of the medium $\pi D^2 L/4$ times $\Delta\theta$, where $\Delta\theta$ is the difference between the porosity and the initial water content.

4.3.2 Time

Based on the Equation (17) and (19) the dimensionless time is defined as:

$$t_D = \frac{K}{\rho g \alpha L^2} t \tag{21}$$

where α is the bentonite compressibility.

4.4. Dimensional analysis of the geometric variables

Figure 14 and Figure 15 show the scheme of the tests, indicating the dimensions and the method used to calculate dimensionless distances.

Here:

- R_e and R_i are the external and internal radii, respectively
- L is the total length of bentonite
- Ø is the diameter of the cells
- r_i is the distance measured from the heater in the bentonite column and the distance measured the axis of the gallery for the mock up and in situ tets
- z* is the dimensionless distance

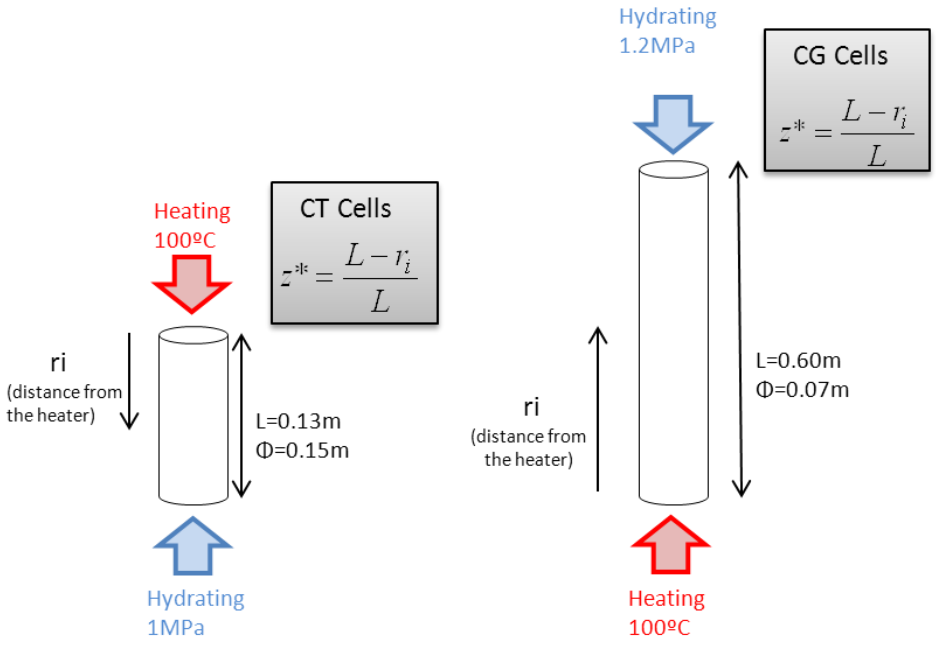

Figure 14. Schematic geometry and conditions of the cell.

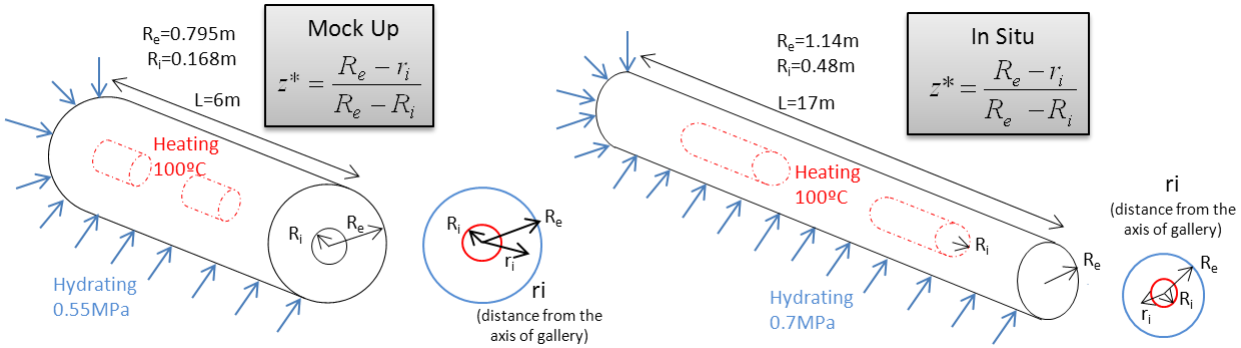

Figure 15. Schematic geometry and conditions of the mock up and in situ tests.

4.5. Dimensionless water content

Water content data are available for different types of tests and for several sensors. The dimensionless volumetric water content θ_D, is defined as:

$$\theta_D = \frac{\theta - \theta_i}{\theta_{sat} - \theta_i} \tag{22}$$

where θ_i is the initial volumetric water content, and θ_{sat} is the saturated volumetric water content, which is equal to the porosity.

4.6. Dimensionless temperature

The dimensionless temperature, T_D is defined as:

$$T_D = \frac{T - T_b}{T_h - T_b} \tag{23}$$

where T_b is the temperature at the hydration boundary and T_h is the temperature at the heater.

4.7. Dimensionless concentrations

Chemical data are available for different test and for different chemical components. The dimensionless concentration, c_D, is defined as follow.

$$c_D = \frac{c - c_b}{c_i - c_b} \tag{24}$$

where c_b is the concentration of the chemical species in the hydration water and c_i is the initial concentration of the pore water.

4.8. Summary of dimensionless variables

Table 3 presents a summary of the dimensionless variables used for the integrated analysis of water uptake, water content, temperature and chemical concentration.

Table 3. Summary of dimensionless variables.

Variable	Dimensionless variable

Water uptake	$V_D = \frac{4V}{\pi D^2 L \Delta\theta}$
Time	$t_D = \frac{Kt}{\rho g \alpha L^2}$
Water content	$\theta_D = \frac{\theta - \theta_i}{\theta_{sat} - \theta_i}$
Temperature	$T_D = \frac{T - T_b}{T_h - T_b}$
Contentration	$c_D = \frac{c - c_b}{c_i - c_b}$

5. Integrated analysis of hydration data

5.1. Introduction

The cumulative water uptake is calculated as the cumulative volume of the water that enters into the bentonite from the beginning of the test. The difference between radial and parallel flow is studied in terms of dimensionless volume and time.

5.2. Available water uptake

Water uptake data are available for the CT22 and CT23 small cells, the CG cells, FQ1/2 (CG1), HI1/2 (CG1), FQ2 (CG2) and CG3, and the mock up test. The main hydration characteristics of these tests are listed in Table 4. The following notation has been defined to shorten the names of the CG tests. The test on CG cell with a duration of 0.5 years are denoted as CG0.5 for FQ1/2(CG1) and CG0.5b for HI1/2(CG1). The test on CG cells with a duration of 1 year are denoted as CG1 for FQ1 (CG5) and CG1b for HI1 (CG6). The test on CG cells with a duration of 2 years are denoted as CG2 for FQ2(CG2) and CG2b for HI2(CG4). Finally, the CG3 cell is denoted as CG7.5.

Table 4. Summary of the key hydration parameters of the CT and CG cells and the mock up test.

Parameters	Test name						
	CT22	CT23	CG0.5	CG0.5b	CG2	CG7.5	Mock up
Flow type	parallel	parallel	parallel	parallel	parallel	parallel	radial

Duriation (d)	26	183	188	214	762	2775	5110
Total water uptake (l)	0.275	0.486	0.171	0.128	0.280	0.461	1120
Joints volume (l)	0.136	0.136	0.06	0.06	0.06	0.06	650
Characteristic water volume (l)	0.486	0.486	0.4837	0.4476	0.4776	0.461	1294
Diameter (m)	0.15	0.15	0.07	0.07	0.07	0.07	1.59
Length (m)	0.12	0.12	0.6	0.6	0.6	0.6	0.625
Porosity	0.39	0.39	0.4	0.4	0.4	0.4	0.41
Initial volumetric water content	0.226	0.226	0.216	0.232	0.219	0.226	0.351
Injection pressure (kPa)	1000	1000	1200	1200	1200	1200	550
Hydraulic conductivity (m/s)	$3 \cdot 10^{-14}$	$3 \cdot 10^{-14}$	$3.2 \cdot 10^{-14}$	$3.2 \cdot 10^{-14}$	$3.2 \cdot 10^{-14}$	$3.2 \cdot 10^{-14}$	$2.78 \cdot 10^{-14}$
Apparent density (g/cm^3)	1.65	1.65	1.64	1.67	1.66	1.64	1.65
Bentonite compressibility (Pa^{-1})	$2.3 \cdot 10^{-8}$	$2.3 \cdot 10^{-8}$	$2.3 \cdot 10^{-8}$	$2.3 \cdot 10^{-8}$	$2.3 \cdot 10^{-8}$	$2.3 \cdot 10^{-8}$	$2.3 \cdot 10^{-8}$
Characteristic time (d)	$1.25 \cdot 10^{4}$	$1.25 \cdot 10^{4}$	$2.93 \cdot 10^{4}$	$2.93 \cdot 10^{4}$	$2.93 \cdot 10^{4}$	$2.93 \cdot 10^{4}$	$3.66 \cdot 10^{4}$

5.2.1 Water uptake data for CT cells

Figure 16 shows the cumulative water uptake for CT cells. Hydration data were measured for cells CT22 and CT23.

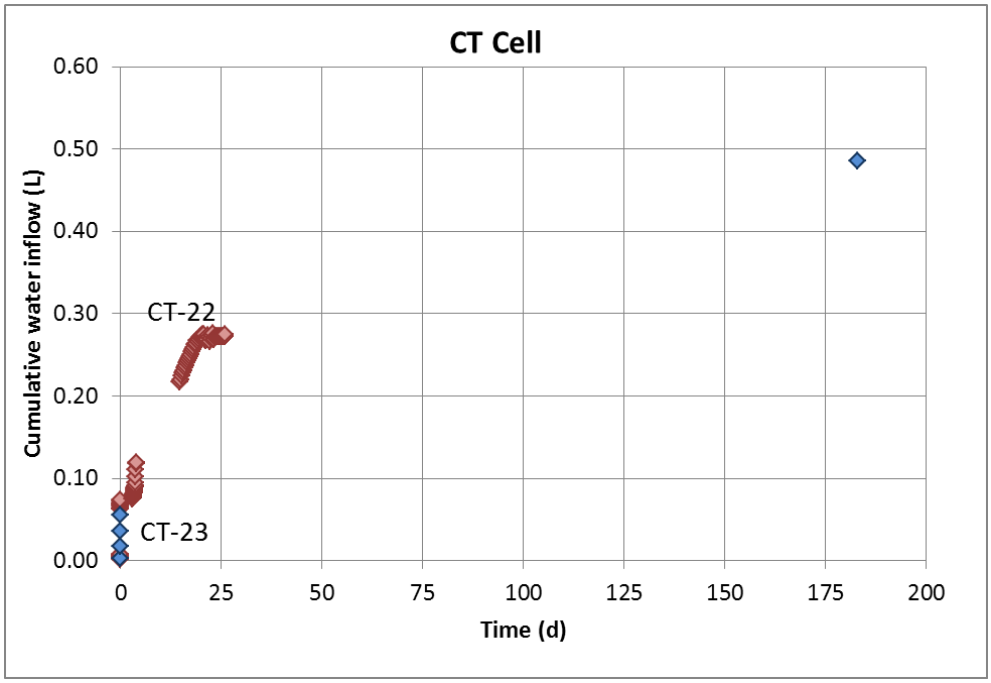

Figure 16. Cumulative water uptake for CT cells versus time.

5.2.2 Water uptake data for CG cells

Figure 17 shows the cumulative water uptake data for CG cells. CG7.5 cell has the largest water uptake of 0.45 L. These data were obtained from the water uptake online measurements during the tests. The water intake calculated from the difference between the final and initial bentonite weights is 15% smaller. Therefore, the online water uptake data were corrected by a factor of 0.85 (see Table 2 of Villar et al., 2008.)

Figure 18 shows the corrected cumulative water uptake for CG cells. The corrected curve of water uptake is lower than the original water uptake data.

Figure 19 shows the compilation of the corrected cumulative water uptake for CG cells.

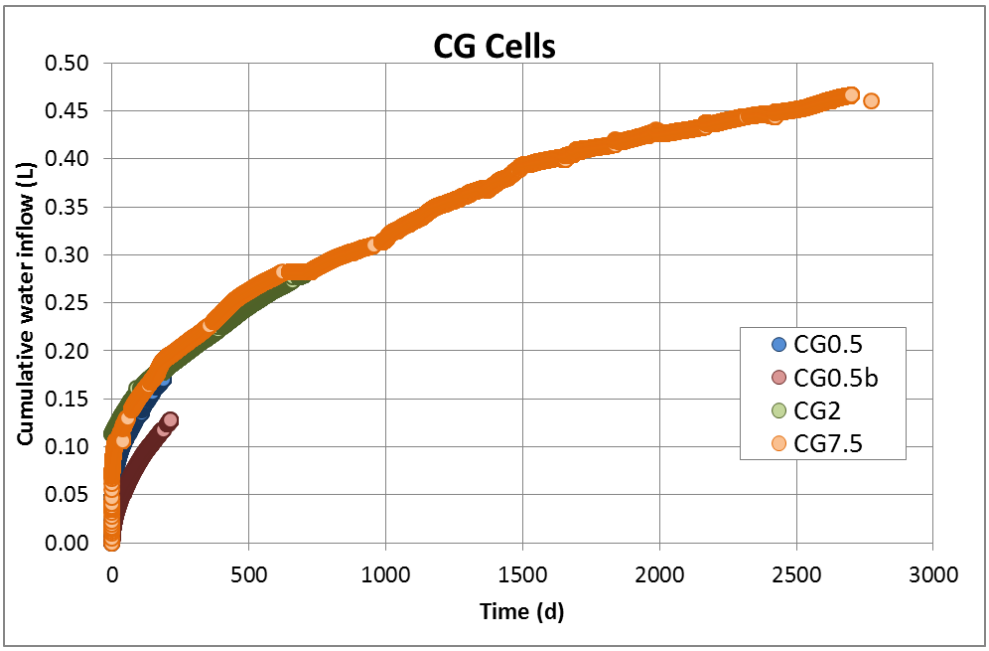

Figure 17. Raw cumulative water uptake for CG cells versus time.

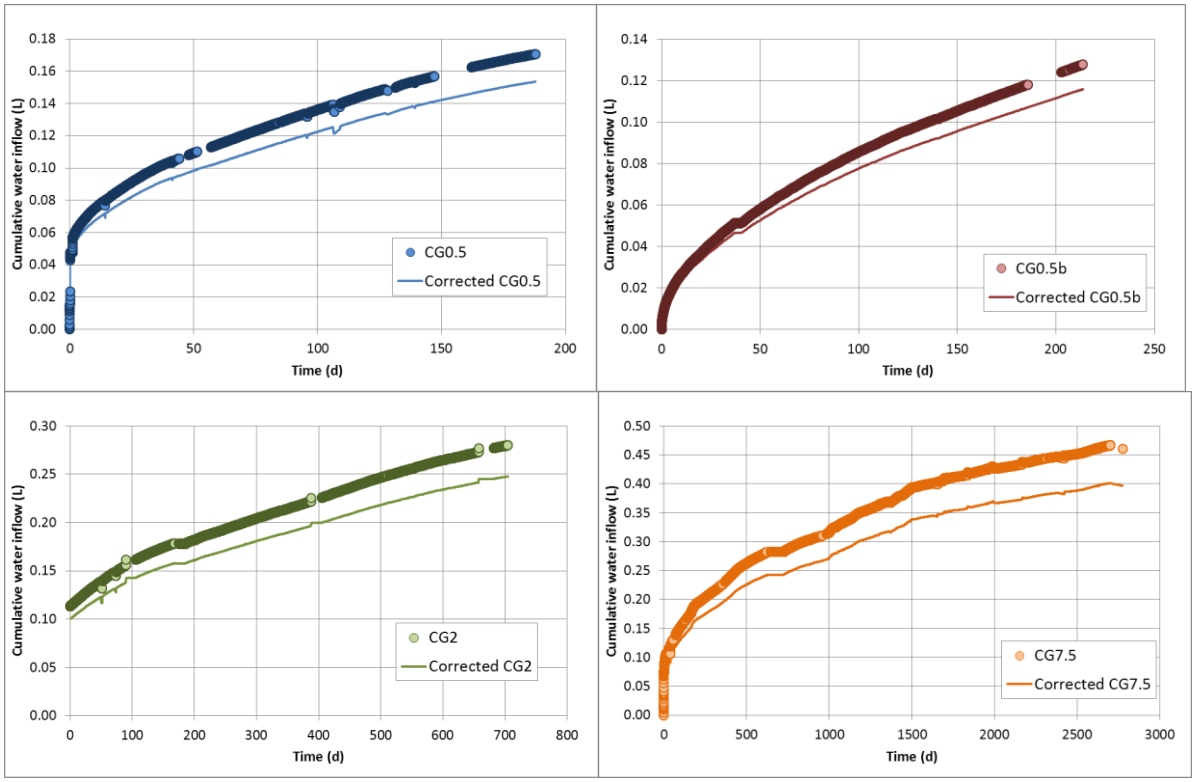

Figure 18. Raw and corrected cumulative water uptake for CG cells.

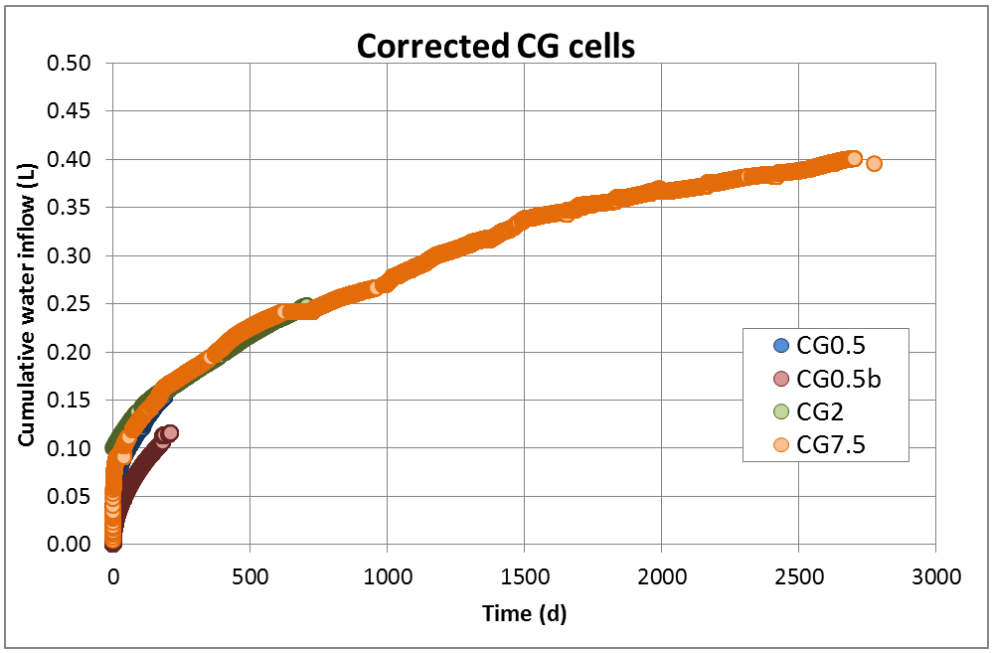

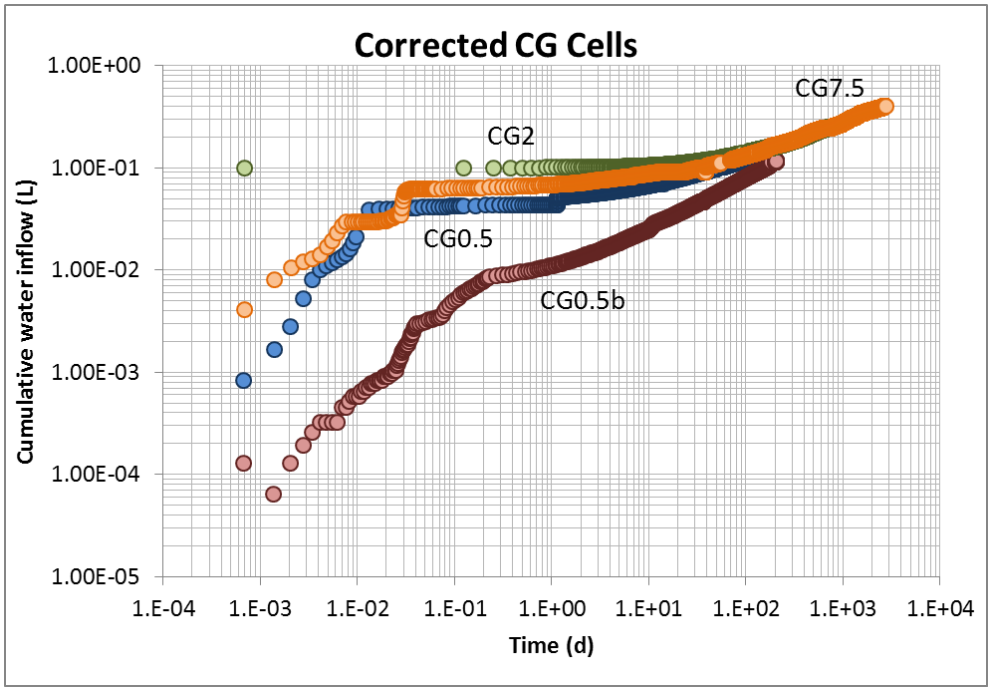

Figure 19. Corrected cumulative water uptake for CG cells (natural scale and log-log plots).

5.2.3 Water uptake data for the mock up test

Figure 20 shows the cumulative water uptake data for the mock up test. The mock test has been operating for more than 5000 days. Its water uptake is larger than that of the lab cells. The measured water uptake data for the mock up test is measured as the loss of water in the water injection tanks. The mass of bentonite in the mock up is about 1000 times larger than that of the cells.

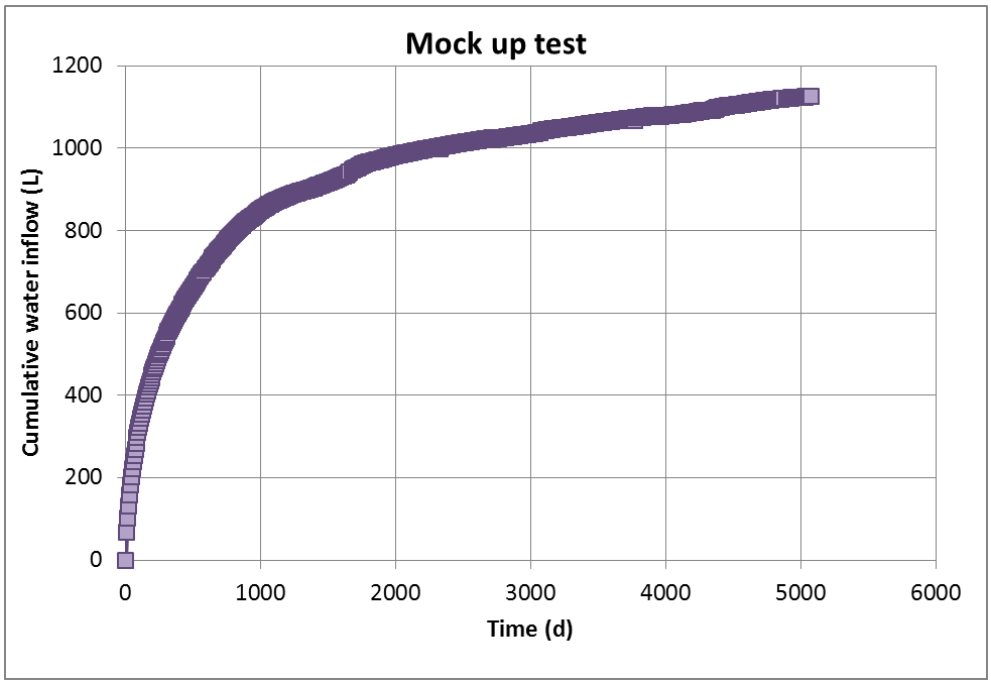

Figure 20. Cumulative water uptake for the mock up test versus time.

5.3. Integrated analysis of raw water uptake data

Figure 21 shows the cumulative water uptake data for CT and CG cells. The CT and CG cells have parallel flow. Figure 22 shows the cumulative water uptake for CT and CG cells and the mock up test. The cumulative water uptake data for the mock up test is several orders of magnitude larger than that of the CT and CG cells. Therefore, a dimensionless analysis of the water uptake versus time is needed.

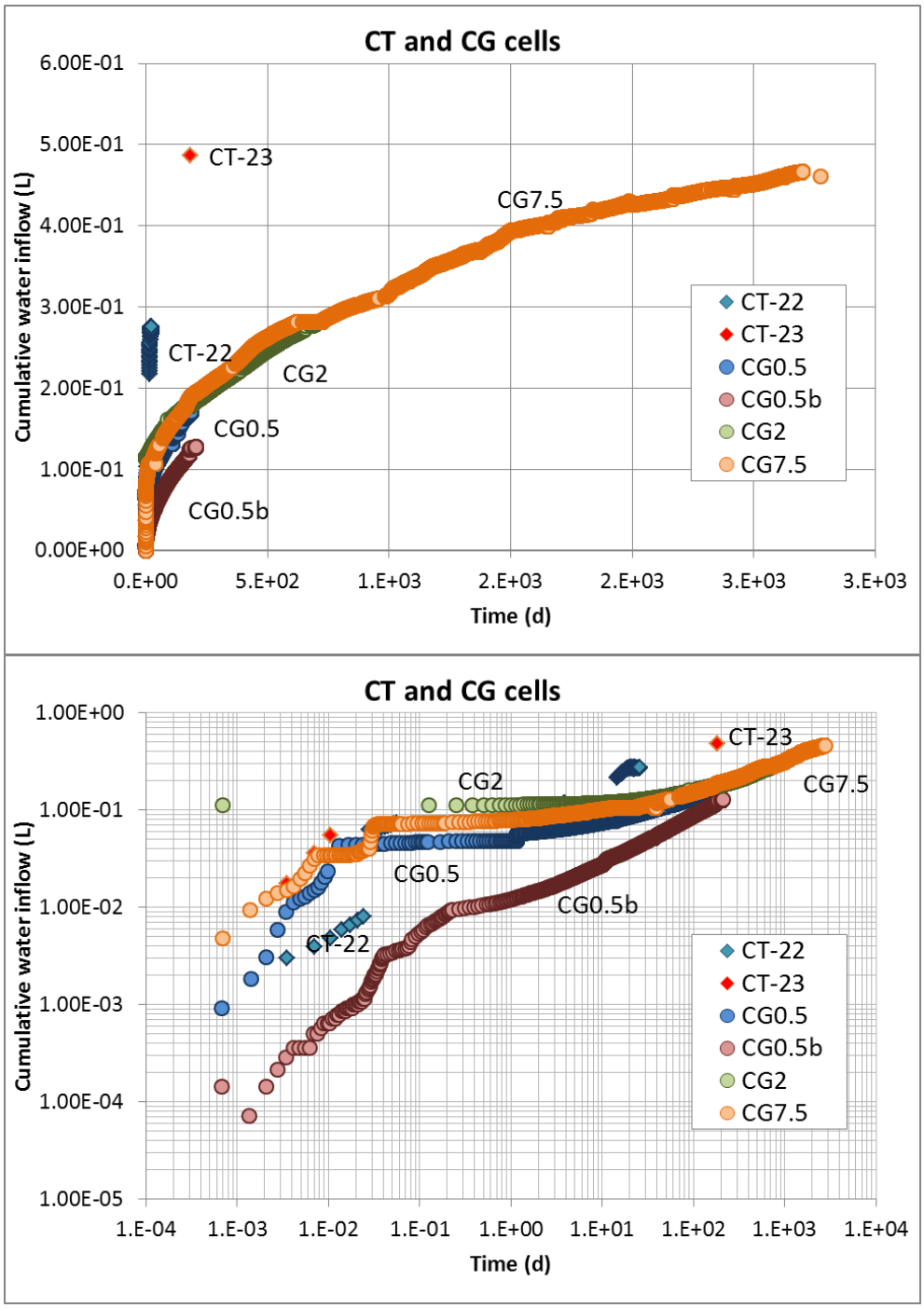

Figure 21. Cumulative water uptake data for CT and CG cells.

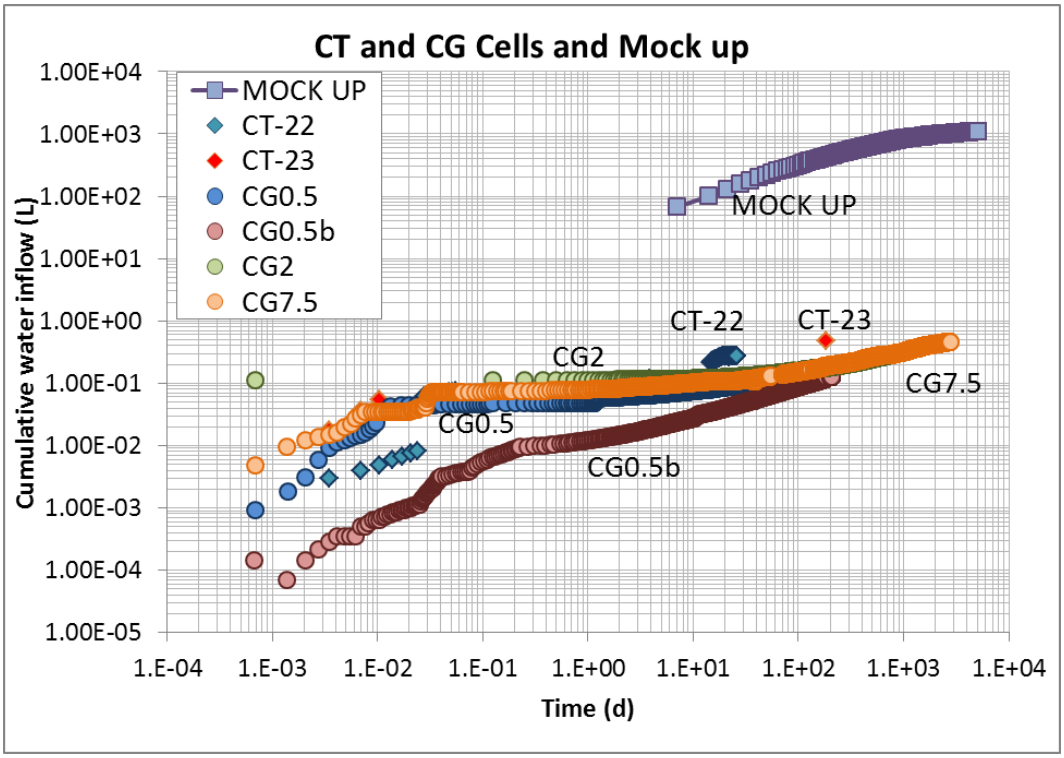

Figure 22. Cumulative water uptake data for CT and CG cells and mock up test.

5.4. Dimensionless integrated analysis

Dimensionless water uptakes are calculated by dividing the cumulative water uptake by the characteristic volumes listed in Table 4. The characteristic volume was calculated as the total volume of water that can enter into the bentonite which is equal to the difference between the water volume at saturation and the initial water volume. An additional volume is considered, the volume needed to fill the gaps and the joints between bentonite blocks. The dimensionless time is calculated by dividing the time by the characteristic time of each test (see also Table 4). Our dimensionless analysis assumes the porosity, the density and other bentonite parameters do not change during the test. For instance, the swelling of the bentonite deformed the Teflon walls of the CG7.5 cell, and the diameter of the bentonite column increased 3.5% near the hydration (Villar et al., 2008a).

Figure 23 shows the dimensionless water uptake versus dimensionless time, in natural and logarithmic scales for CT and CG cells and the mock up test. In natural scale the behaviour is similar for all the tests for dimensionless times $t_D < 0.04$. For $t_D > 0.04$, cells CT and CG and the mock up show a different behaviour. The water uptake of cell CG7.5 is larger than that of the mock up for the same dimensionless time for $t_D > 0.06$. In logarithmic

scale it can be seen that the data show a large scatter at early times due to spurious effects such as electric shutdowns and the fillings of the gaps between bentonite blocks.

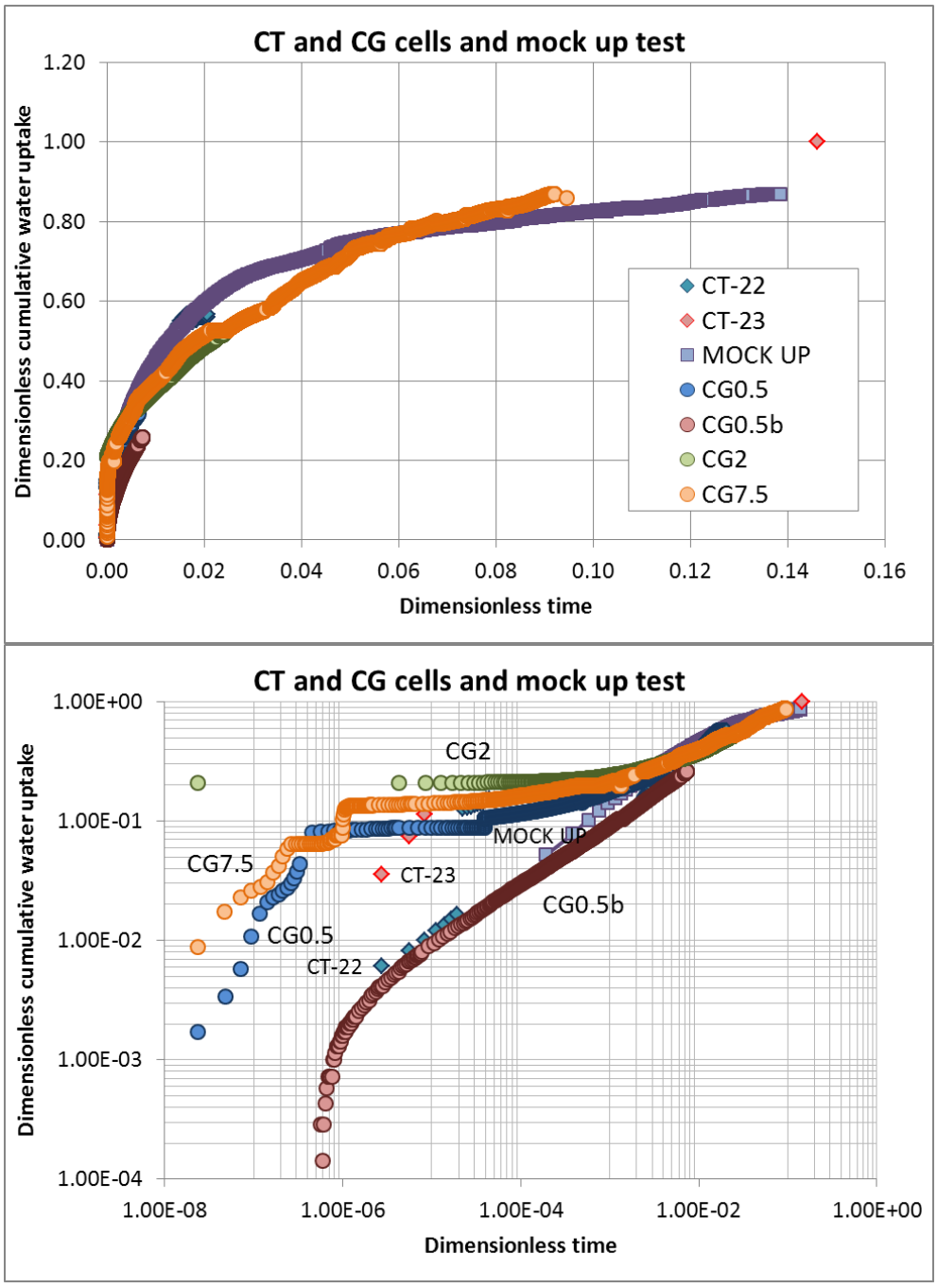

Figure 23. Dimensionless water uptake versus dimensionless time for CT and CG cells and the mock up test.

5.5. Differences caused by differences in geometry.

The hydration surface for radial flow is $2\pi R_e L$, where R_e is the external radius of the mock up test. The surface where the flow is applied in radial flow is equal to 29.9 m^2. However, in the case of parallel flow, water flows from the bottom through a smaller surface. The surface is 0.017 m^2 for CT cell and 0.004 m^2 for CG cells. The differences in water uptake can also be due to the initial flooding of the mock up test, where the joints were flooded initially with 600 L of water.

5.6. Comparison in terms of numerical solutions

Coupled THMC models of the mock up test and the CT cells have been performed with INVERSFADES2 by Zheng and Samper (2008) and Zheng et al. (2010). The mock up test considered the initial injection of water. Here, we performed also a model without this hydration. The model of the CT cell considered a porous stone used to facilitate the water uptake. Here, we performed a model without the porous stone. Figure 24 shows the comparison of the cumulative water uptake for the mock up model and without the initial hydration. Figure 25 shows the comparison of the computed water uptake with and without porous stone. It can be seen that the computed hydration curves, without the porous stone is smoother than that computed with the porous stone.

The computed dimensionless water uptake for the mock up without the initial hydration and the CT cell without the porous stone are compared in Figure 26. There are differences between the CT cell (parallel flow) and the mock up test (radial flow) in the initial and boundary conditions, the temperatures, the water and the gas pressure. However, in terms of dimensionless variables their hydration curves are similar, although hydration in parallel flow is faster than in radial flow. This result of the numerical models is consistent with the observation of the measured data (Figure 22).

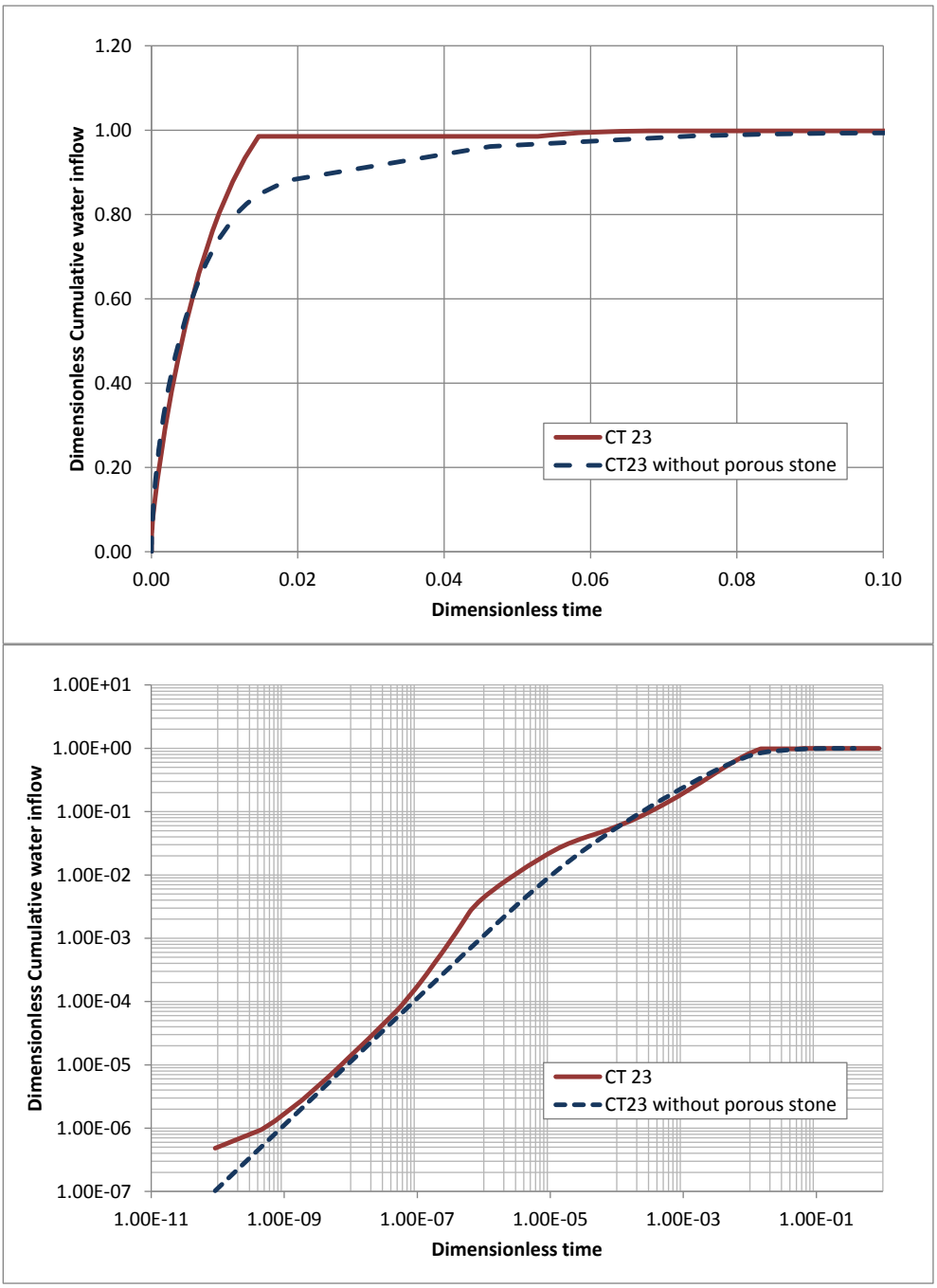

Figure 24. Computed dimensionless cumulative water uptake in the CT23 cell with and without porous stone.

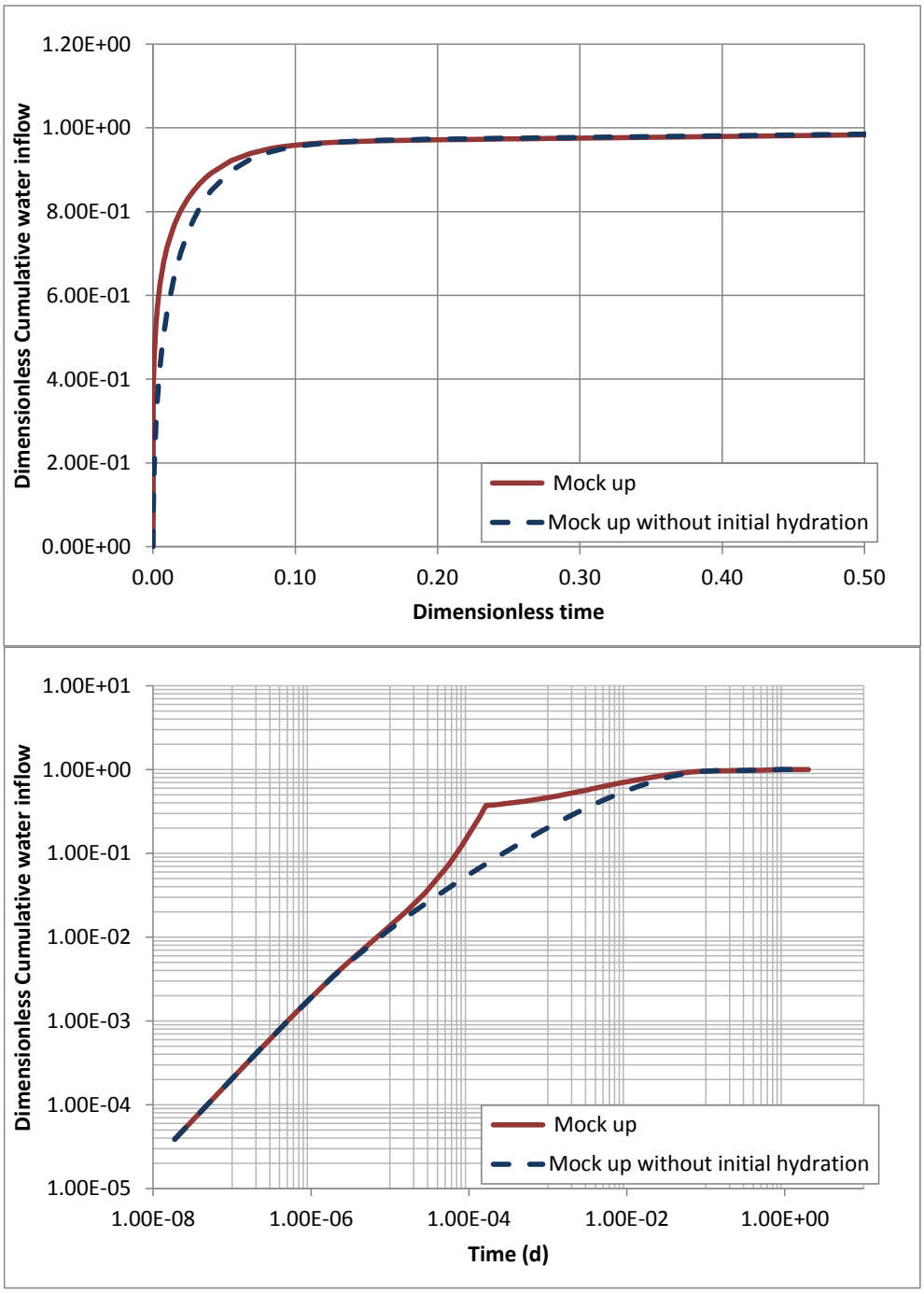

Figure 25. Computed dimensionless cumulative water uptake of the mock up test with and without the initial flooding of the joints.

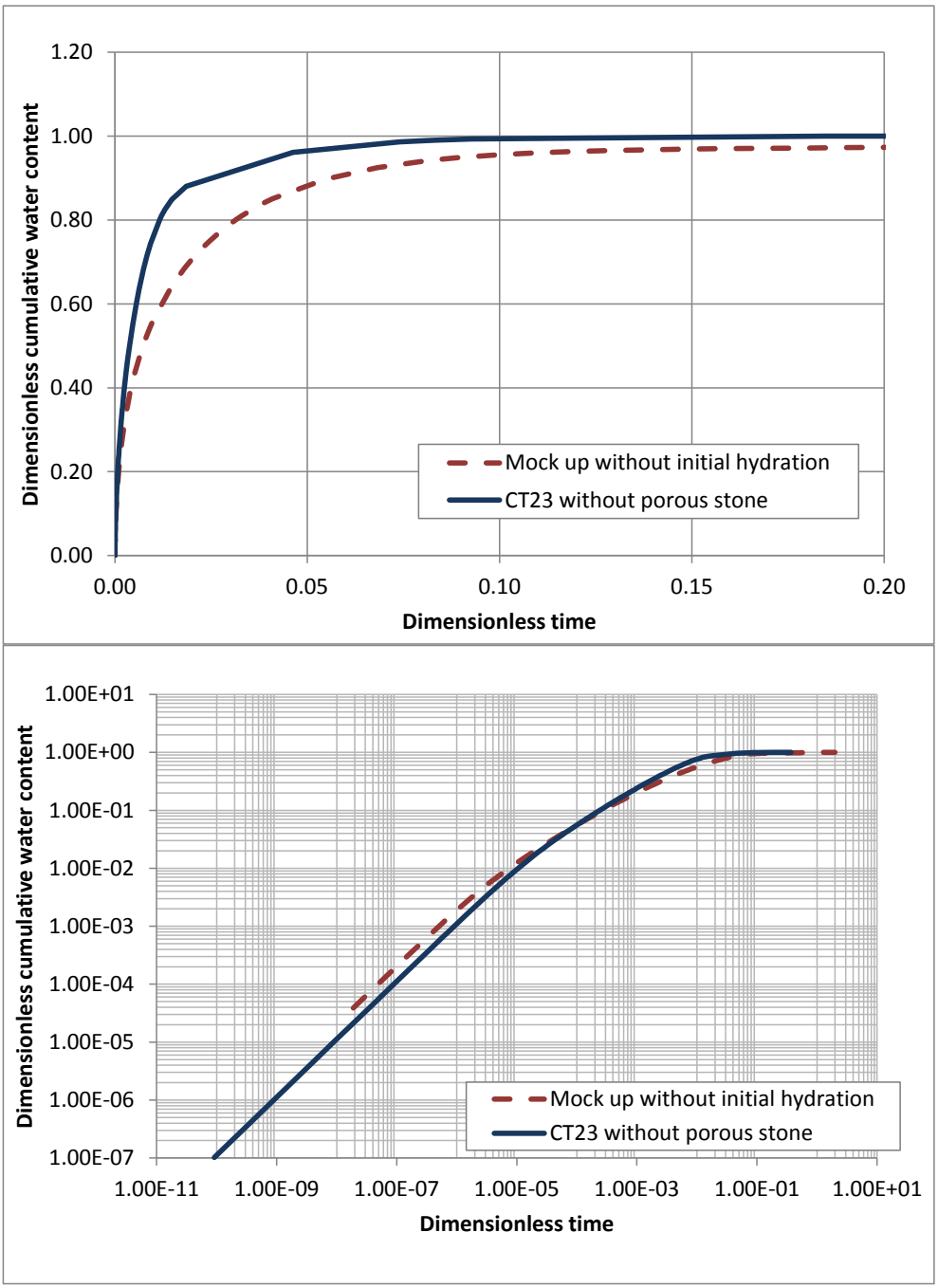

Figure 26. Computed dimensionless water uptake versus dimensionless time for CT23 cell without porous stone and the mock up without initial flooding.

5.7. Conclusion

The main conclusions of the integrated analysis of water uptake data include:

1) Water hydration in CT and CG cells take place at the bottom of the cells and is essentially one dimensional and parallel to the axis of the cell. Hydration in the mock up and in situ tests, on the other hand, occurs from the outer surface and has a radial distribution. Therefore, there is a clear difference in the geometry of the hydration of the lab cells and the mock up and in situ tests.

2) Water uptake measured data contains uncertainties. For CG cells the water uptake data may have an uncertainty of about 15%. The final water uptake determined with the on line measurements (from changes in the weight of the water tank) is 15% larger than the water uptake estimated from the difference in the weight of the bentonite column at the end and at the beginning of the test. Water uptake data from the mock up test may also contain some uncertainties, especially for the most recent data because the flow rate is becoming very low.

3) The dimensionless analysis of measured water uptake data shows that the water uptake data from CT and CG cells and the mock up test show cannot be scaled up. There are large differences at early times due to spurious effects such as electric shutdown and the filling of block joints. Such differences, however, decrease with time. Data of most of the tests converge for dimensionless times greater than 0.04. The water uptake of the CT cell is slightly larger than that of the mock up test.

4) The computed water uptake with the numerical model for parallel flow is larger than that computed for radial flow.

5) Our integrated analysis assumes that the volume and density are constant. Therefore, changes in porosity, temperature and permeability are not accounted for.

6. Green-Ampt analytical solution for water inflow

6.1. Introduction

Infiltration is the process by which water moves into a soil from the ground surface. Infiltration depends on the surface and soil properties (porosity and hydraulic conductivity) and the initial water content, θ_i. The Green-Ampt method provides an approximate way to calculate water infiltration. The saturation front marks the boundary between the dry soil with an initial water content θ_i, and the saturated soil with θ_s. Water ponds on the ground surface with a constant depth H. At a time t, the front is at a depth z (Figure 27).

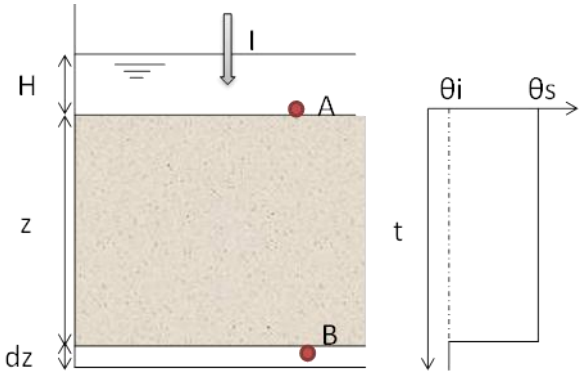

Figure 27. Scheme of soil infiltration with the Green-Ampt method.

We consider a soil column of unit surface area. The increase of water content between the initial data and saturation, is defined by, $\Delta\theta = \theta_s - \theta_i$. From the continuity equation, in a differential time dt, that the infiltrated volume (qdt) is given by:

$$qdt = dz\Delta\theta \tag{25}$$

where dz is the advance of the saturation front in a time dt. Applying Darcy's law, between points A and B in Figure 27, one has:

$$q = K_s \frac{H - (-z - \psi)}{z} \tag{26}$$

where K_s is the saturated soil hydraulic conductivity, H is the water pond height on the surface and ψ is the soil suction in the dry zone. Substituting Equation (25) into (26) and integrating one has:

$$\frac{K_s}{\Delta\theta}t = z - (H+\psi)\left[\ln(1+\frac{z}{H+\psi})\right] \tag{27}$$

This equation can be solved with an iterative method.

6.2. Green-Ampt solution for parallel flow in the bentonite buffer

The Green-Ampt method has been used to obtain approximate solutions for the parallel and radial hydration of bentonite (Samper et al., 2011). For parallel flow we consider a bentonite column with a cross section area A, which is hydrated at a pressure head H (Figure 28). The hydration rate or specific flux, q, takes place at the bottom of the bentonite column. The continuity equation is:

$$A\text{qdt}=\text{A}\Delta\theta\text{dz} \tag{28}$$

Darcy's law is applied to points A and B. Since the injection pressure head, H, and the initial suction, ψ, are much larger than the penetration z, the flux is given by:

$$q = K_S\,\frac{(H+\psi)}{z} \tag{29}$$

Substituting this equation into Equation (28) and integrating the resulting differential equation, one obtains the following expression for the penetrating depth z:

$$z^2 = 2\text{K}\,\frac{(\text{H}+\psi)}{\Delta\theta}t \tag{30}$$

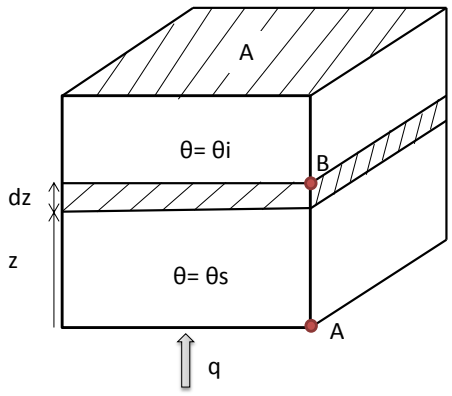

Figure 28. Scheme of soil infiltration used in the Green-Ampt method for parallel flow.

Substituting z into Equation (29), one obtains the solution of the specific flux:

$$q = \sqrt{\frac{K(\mathrm{H}+\psi)\Delta\theta}{2t}} \tag{31}$$

The cumulative water uptake, V, is obtained by integrating in time the flux q along the hydration boundary:

$$V = A\int_0^t \mathrm{q}(\tau)\mathrm{d}\tau = A\sqrt{2K(\mathrm{H}+\psi)\Delta\theta t} \tag{32}$$

6.3. Green-Ampt solution for radial flow in the bentonite buffer

The Spanish reference concept for radioactive waste disposal in a crystalline rock foresees a cylindrical bentonite barrier with an inner radius R_i and a outer radius R_e. Bentonite hydrates under radial flow conditions (Figure 29).

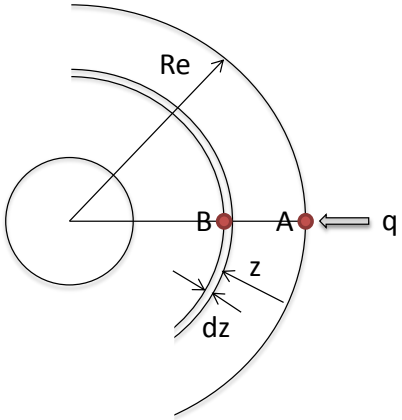

Figure 29. Scheme of bentonite hydration according to the Green-Ampt method for radial flow.

Applying the continuity equation, the water stored inside a crown of thickness dz is equal to the volume of water injected in a time dt:

$$2\pi \mathrm{R}_e\, qdt = 2\pi(R_e - z)\Delta\theta dz \tag{33}$$

Applying Darcy's law between point A at the outer surface of the barrier and the point B located at the dry side of the saturation front, one obtains Equation (29). Substituting Equation (29) into Equation (33) and integrating the resulting differential equation between (0,0) and (t,z), one obtains:

$$z^2\left(1-\frac{2z}{3R_e}\right)=2\mathrm{K}\ \frac{(\mathrm{H}+\psi)}{\Delta\theta}t \tag{34}$$

This is a cubic equation in z, that can be solved in several ways. One can the time, t, for a given value of z. The second method relies on the analytical solution to the cubic equation based on a change of variables according to the Cardano equation (Angulo, 1996). Once the values of z are known, q can be calculated from Equation (28). Finally, the cumulative volume is obtained by integrating numerically the flow rate q.

The analytical solutions for radial and parallel flow show differences. They are similar for small values of time. The differences become more important when the time increases. Difference in radial and parallel flow are analysed in terms of dimensionless variables which are defined as (Samper et al., 2011):

$$V_D=\frac{V}{V_c}=\frac{4V}{\pi D^2 L\Delta\theta} \qquad \textit{for parallel flow} \tag{35}$$

$$V_D=\frac{V}{V_c}=\frac{V}{\pi(R_e^2-R_i^2)L\Delta\theta} \quad \textit{for radial flow} \tag{36}$$

$$t_D=\frac{t}{t_c}=\frac{t}{\frac{\Delta\theta L^2}{K(H+\psi)}}=\frac{K(H+\psi)t}{\Delta\theta L^2} \tag{37}$$

where:

- L is a characteristic length
- V_D is the dimensionless volume
- t_D is the dimensionless time

The characteristic volume is equal to the volume of water needed to saturated the bentonite.

6.4. Comparison of analytical and numerical solutions

Water flow in CT and CG cells is parallel. The numerical solution has been compared to the Green-Ampt analytical for parallel flow. The numerical solution for CT23 cell has been

obtained with INVERSFADES2 (Zheng et al, 2010) with the properties, parameters and the initial and boundary conditions indicated in Chapter 3. Figure 30 shows the comparison of the numerical and Green-Ampt analytical solutions for the CT23 cell. The analytical solution has the same slope as the final part of the numerical solution in the log-log scale. The analytical solution for dimensionless water uptake is larger than the numerical solution.

Water flow in the mock up test shows radial symmetry. Figure 31 shows the comparison of the numerical and the analytical solutions for the radial flow. The analytical solution is slightly larger than the numerical solution. There are significant differences between the analytical and numerical solutions because the analytical solution predicts full saturation after $t_D < 0.02$. The numerical solution, on the other hand, does not reach saturation even for $t_D > 0.08$.

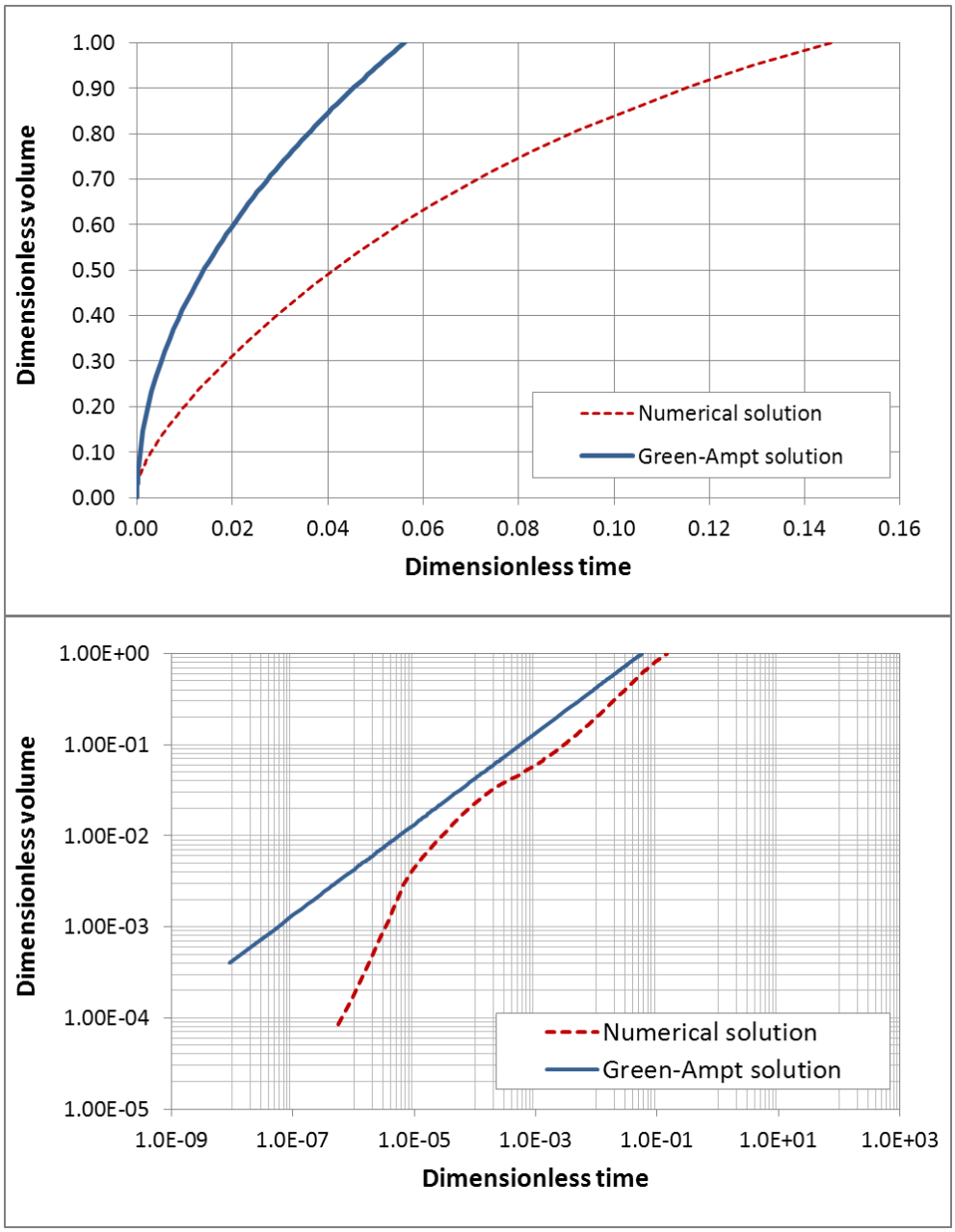

Figure 30. Comparison of the numerical and analytical solutions for parallel flow (CT23 cell).

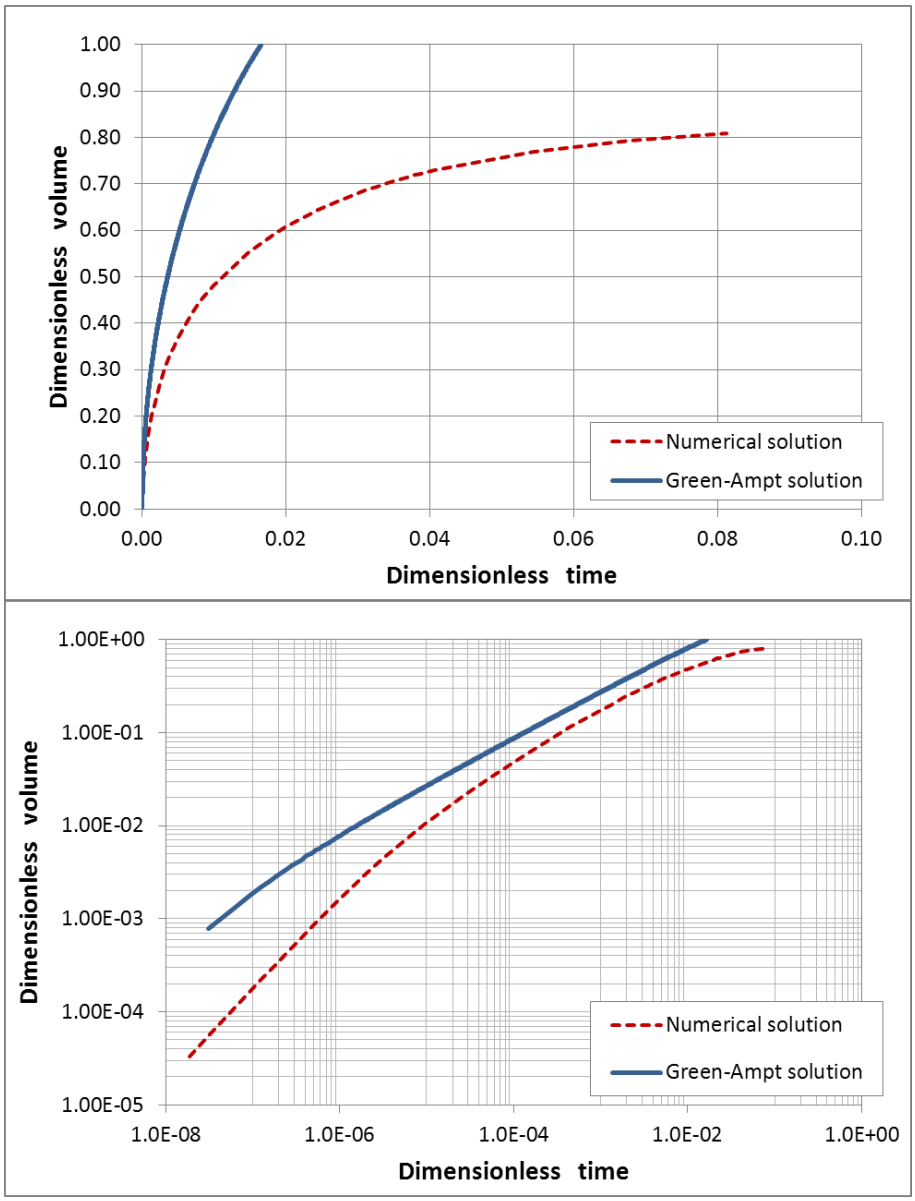

Figure 31. Comparison of the numerical solution and analytical solutions for radial flow (mock up test).

6.5. Comparison of analytical solution and measured data

Figure 32 shows the comparison of the measured water uptake data for CG cells and the Green-Ampt analytical solution for parallel flow. Figure 33 shows the comparison of the dimensionless measured water uptake of the mock up test and the Green-Ampt solution for radial flow. The measured data are smaller than the water uptake predicted by the analytical solution.

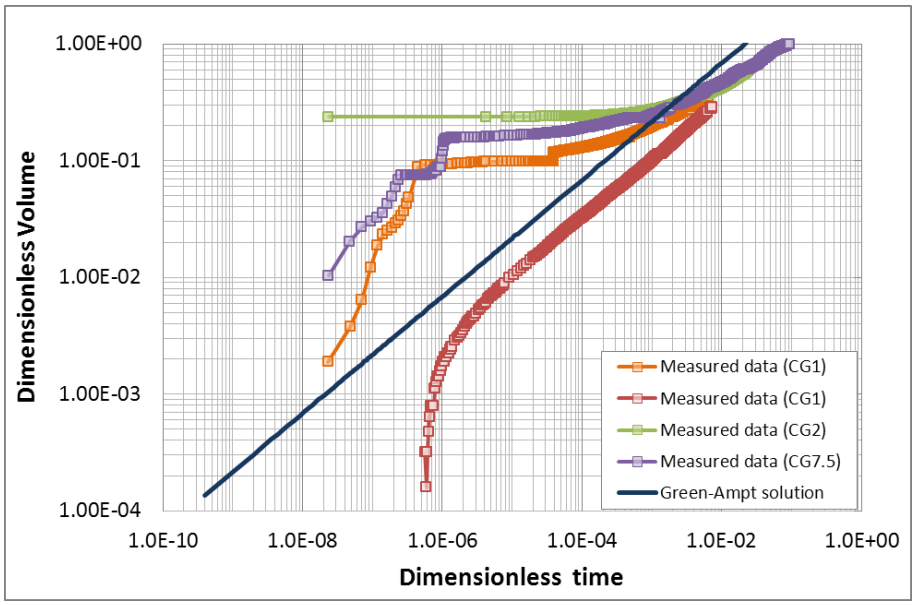

Figure 32. Comparison of the measured water uptake data for the CG cells and Green-Ampt solution for parallel flow.

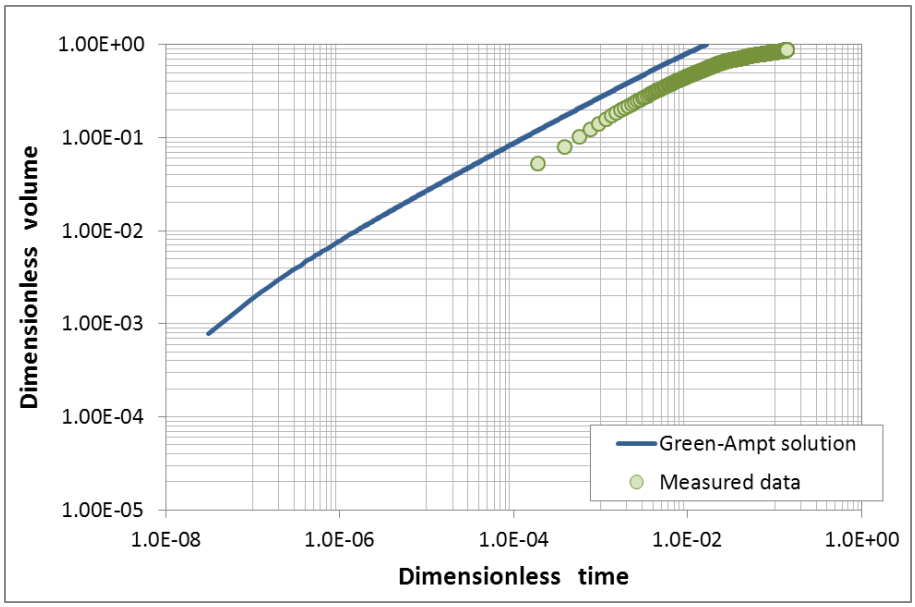

Figure 33. Comparison of the measured water uptake data for the mock up test and the Green-Ampt solution for radial flow.

6.6. Apparent hydraulic conductivities

The analytical solution of water uptake is slightly larger than the numerical (Table 5). The hydraulic conductivity of the analytical solution has been calibrated so that the analytical solution reproduces the final part of the numerical solution. The apparent hydraulic conductivity, K, is smaller than the assumed K by a factor of about 2.5.

Table 5. Values of the hydraulic conductivity and permeability used in the analytical solutions of the CT, CG cells and the mock up test.

Parameter	CT cell	CG cell	Mock up
Permeability (m^2)	$2.75 \cdot 10^{-21}$	$3.28 \cdot 10^{-21}$	$3.51 \cdot 10^{-21}$
Hydraulic conductivity(m/s)	$2.68 \cdot 10^{-14}$	$3.20 \cdot 10^{-14}$	$2.78 \cdot 10^{-14}$
Calibrated permeability (m^2)	$1.10 \cdot 10^{-21}$	$1.49 \cdot 10^{-21}$	$1.17 \cdot 10^{-21}$
Calibrated hydraulic conductivity (m/s)	$1.07 \cdot 10^{-14}$	$1.45 \cdot 10^{-14}$	$9.27 \cdot 10^{-15}$

Figure 34 and Figure 35 show that the Green-Ampt solutions with the calibrated K reproduce the numerical results better than the original Green-Ampt solution. This could be due to the fact that the Green-Ampt solution does not take into account changes in temperature, and assumes that all the parameters such as K are constant. In spite of the simplicity of the Green-Ampt solution, the analytical solution is capable to reproduce the numerical solution. Figure 36 and Figure 37 show the dimensionless measured water uptake and for the Green-Ampt solutions for the original and calibrated hydraulic conductivity.

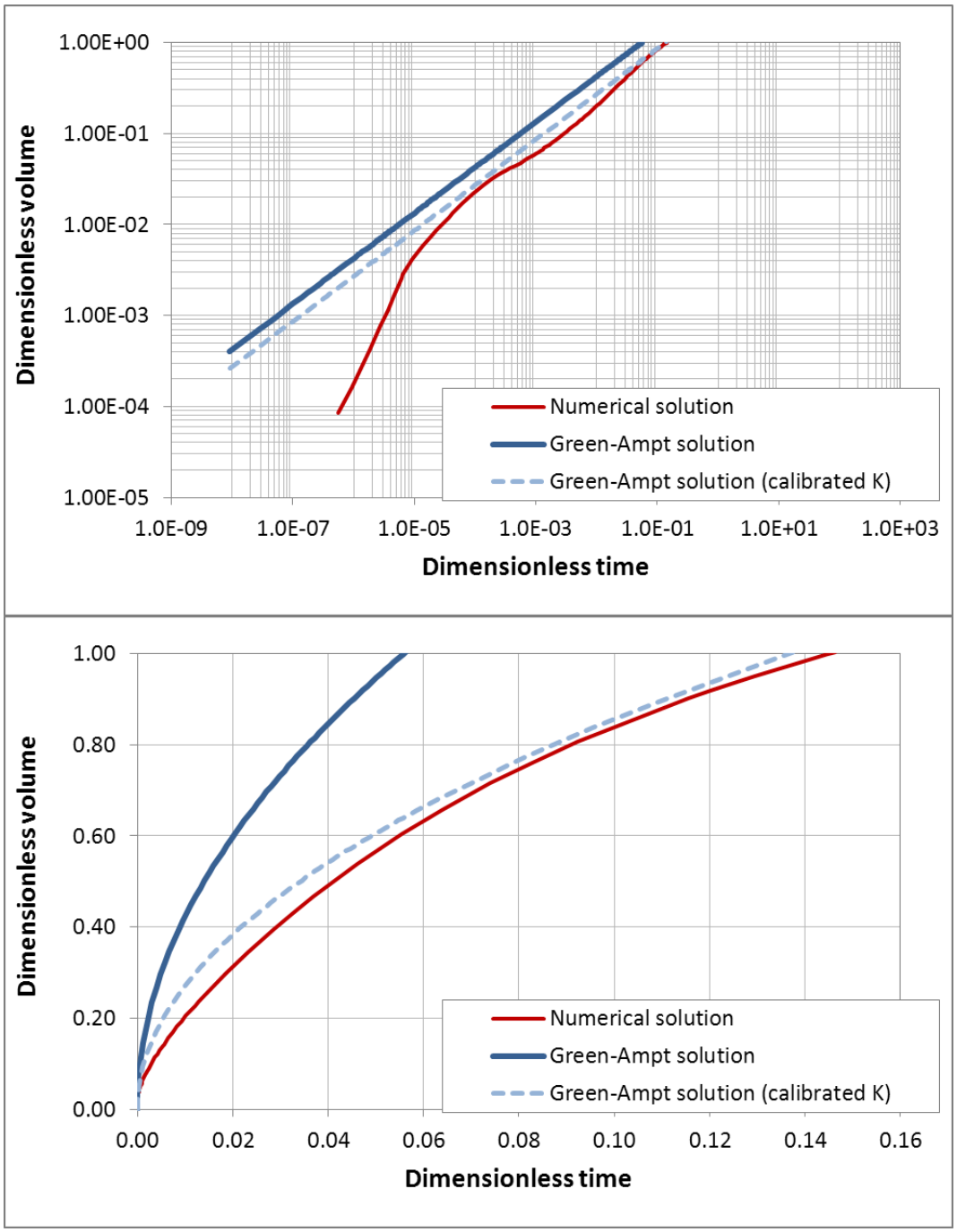

Figure 34. Comparison of the numerical and the analytical solution for the CT23 cell (log-log scale above and natural scale below).

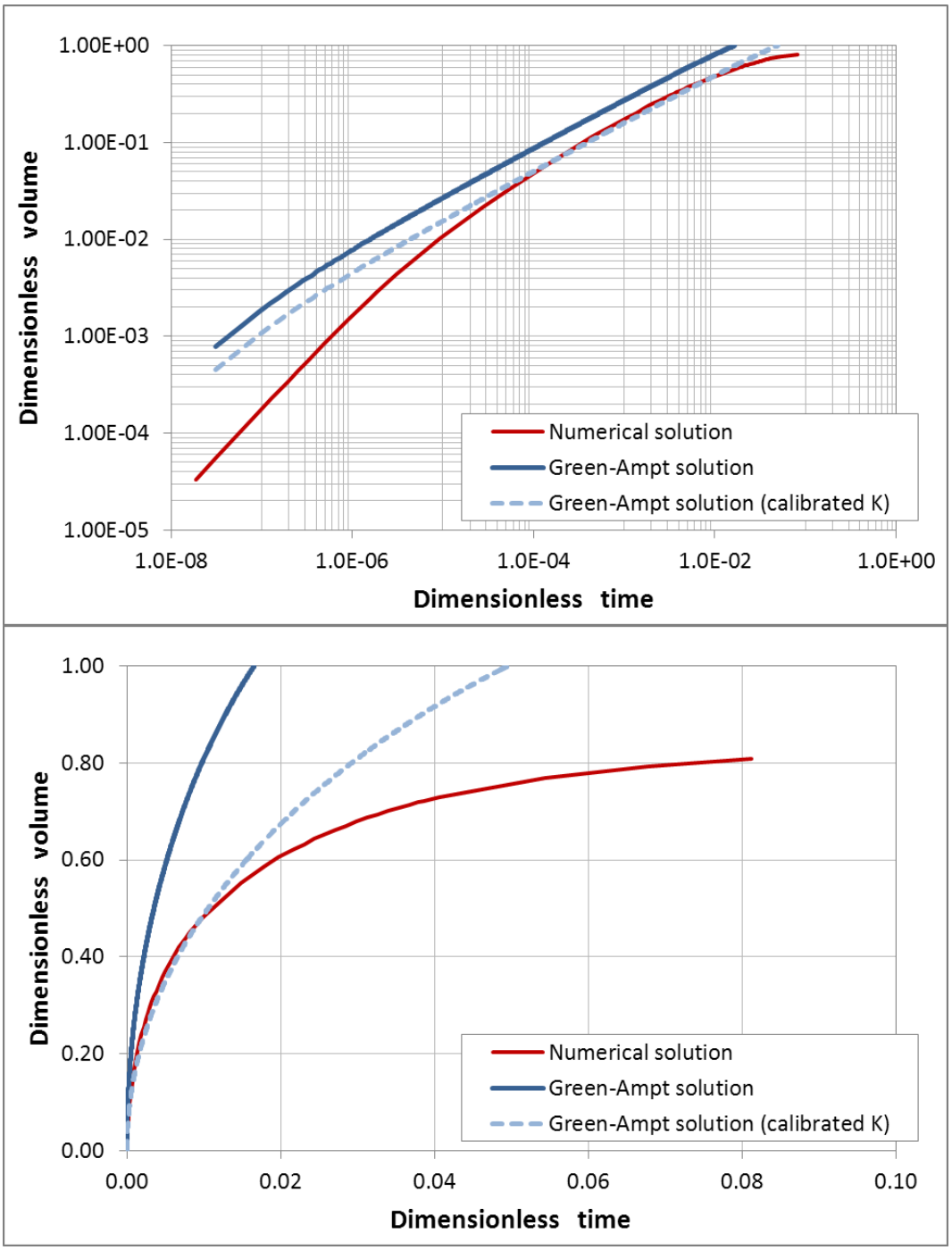

Figure 35. Comparison of the numerical and the analytical solution for the mock up test (log-log scale above and natural scale below).

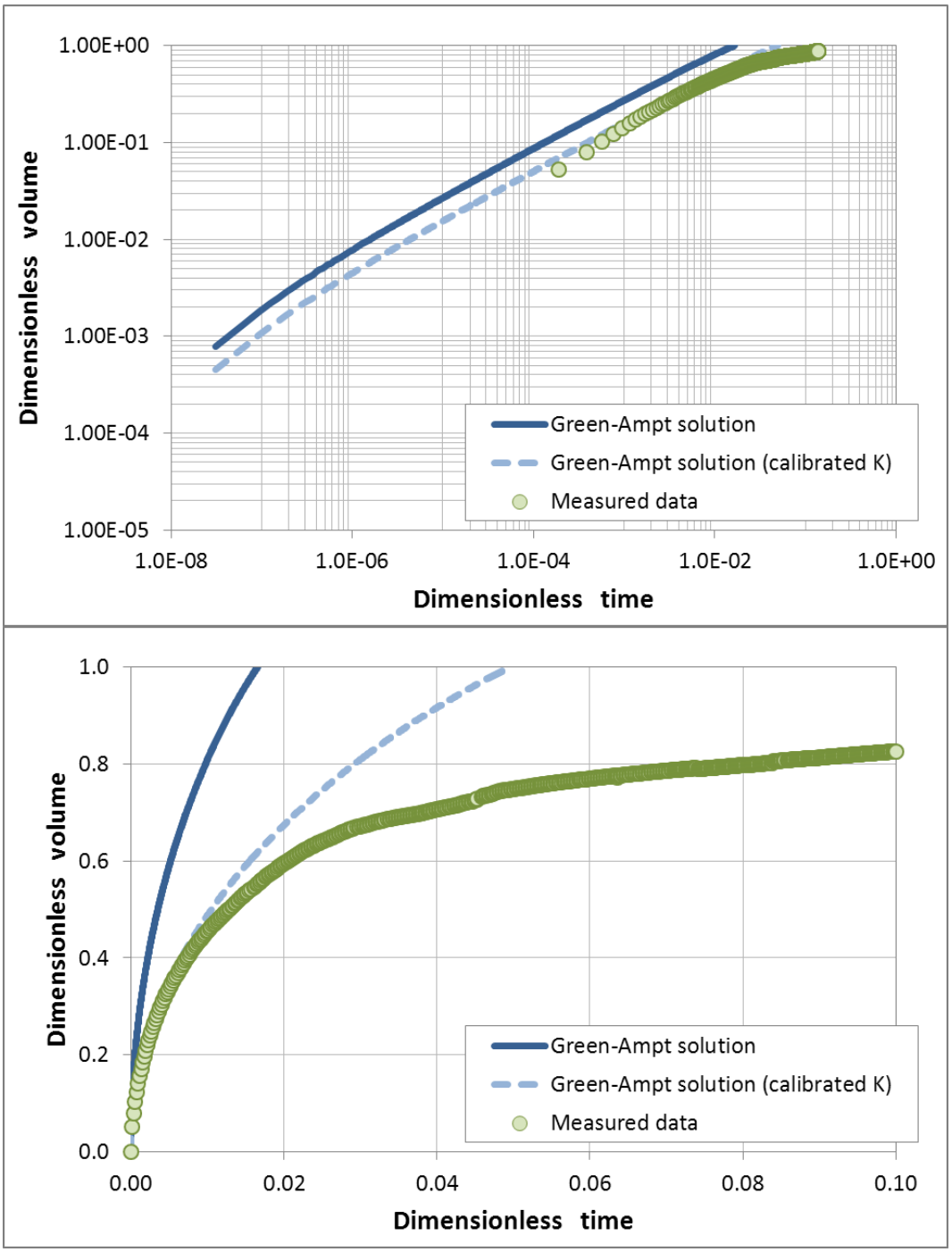

Figure 36. Comparison of the measured data and the analytical solution for the mock up test (log-log scale above and natural scale below).

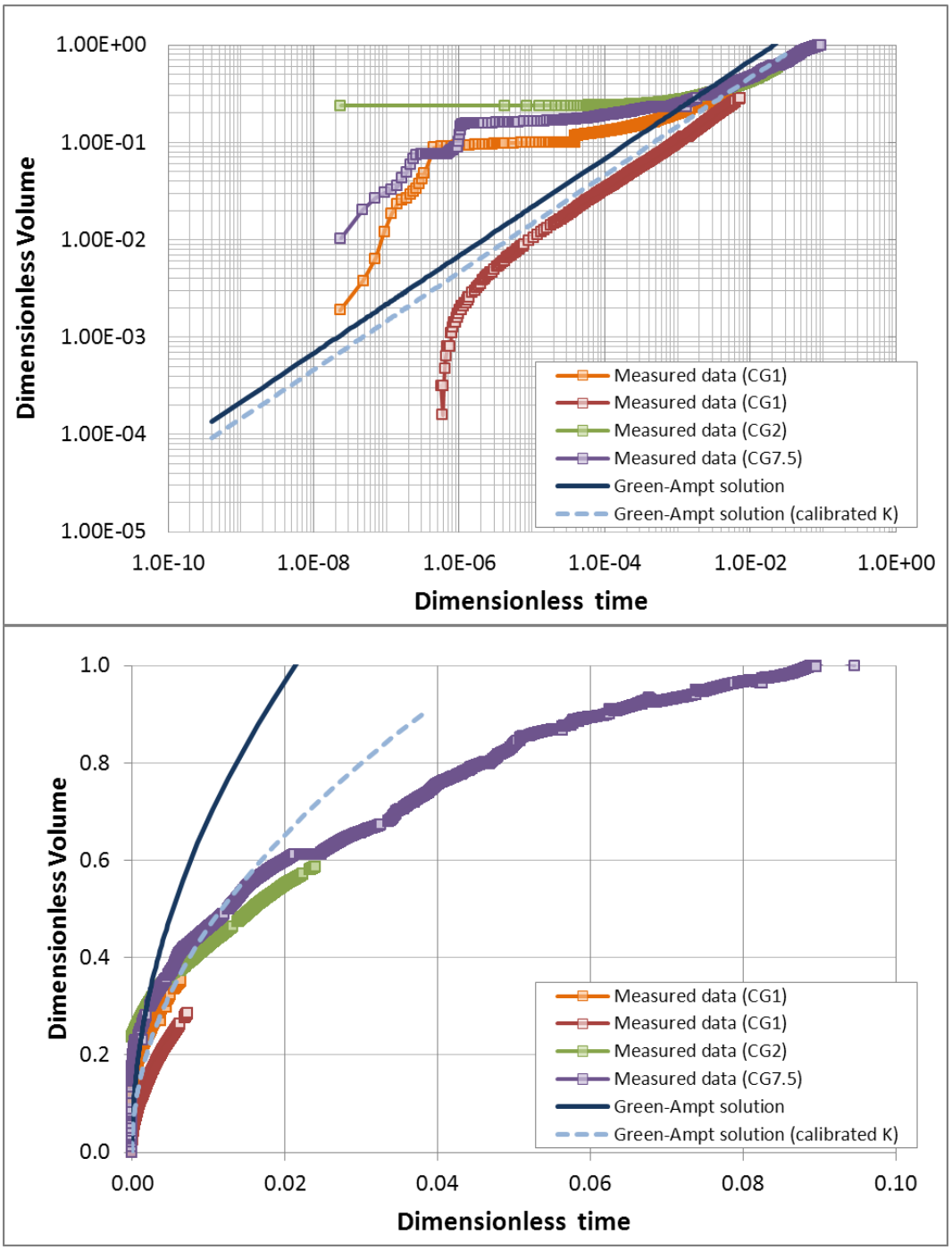

Figure 37. Comparison of the measured data and the analytical solution for the CT cell (log-log scale above and natural scale below).

6.7. Comparison of the Green-Ampt analytical solutions for radial and parallel water flow

The domains of the CT and CG cells and that of the mock up test are all cylindrical. However, the mock up test is hydrated from the lateral surface of the cylinder. In the cells water is injected from one of the bases of the cylinder. The main parameters and the initial and boundary conditions are listed in

Table 6. Figure 38 shows the geometry and configuration of the radial flow. A prismatic geometry is used for the Green-Ampt solution (Figure 39). The following variables are used to define the geometry of the problem:

- q is the water flow per unit surface (m/s)
- L is the length of the test (m)
- R_e is the hydration radius (m)
- R_i is the internal radius (m)
- b is bentonite thickness (m)
- a is the width of the test (m)

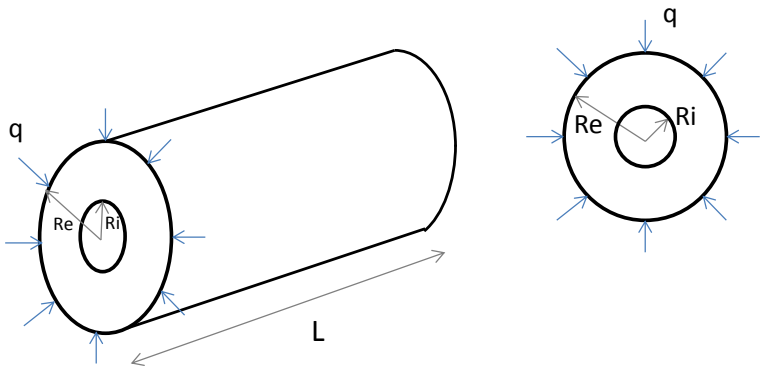

Figure 38. Geometry of radial flow.

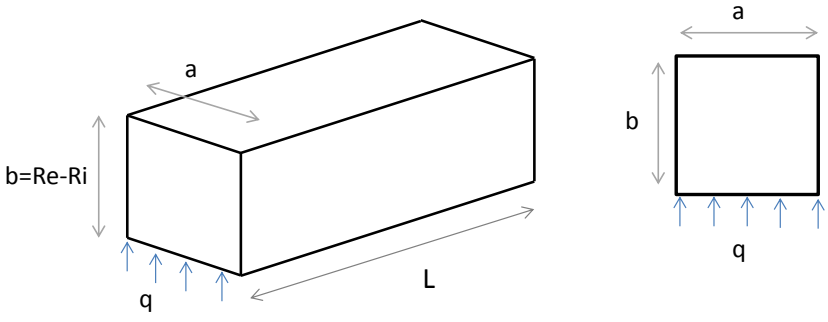

Figure 39. Geometry of for parallel flow.

Table 6. Main hydrodynamic and geometric parameters of CT and CG cells and the mock up test.

Parameters and dimensions	CT cells	CG cells	Mock up
K_s Hydraulic conductivity (m/s)	$2.68 \cdot 10^{-14}$	$3.20 \cdot 10^{-14}$	$2.78 \cdot 10^{-14}$
H Hydraulic pressure (m)	100	120	70
Ψ Suction (m)	$1.12 \cdot 10^{4}$	$1.12 \cdot 10^{4}$	$1.13 \cdot 10^{4}$
$\Delta\theta$ water content ($\Delta\theta = \theta_s - \theta_i$)	0.193	0.177	0.181
L bentonite thickness/length (m)	0.13	0.60	0.625
R_e Hydration radius (m)	-	-	0.795
R_i Internal radius (m)	-	-	0.168
Hydration surface (m^2)	0.017	0.004	29.9

The differences in the parallel and radial flow are analysed by using the analytical Green-Ampt solution. The comparison is made by using the conditions and parameters of the mock up test for radial flow.

6.7.1 Same thickness and volume

Figure 40 shows the comparison of the advance of the hydration front, z, for parallel and radial flow. The values of z are similar for radial and parallel flow at early times. Later, the advance of the saturation front for radial flow is larger than that of the parallel flow. The values z_{radial} and $z_{parallel}$ satisfy:

$$\frac{z_{parallel}}{z_{radial}} = 1 - \frac{2z_{radial}}{3R_e}$$

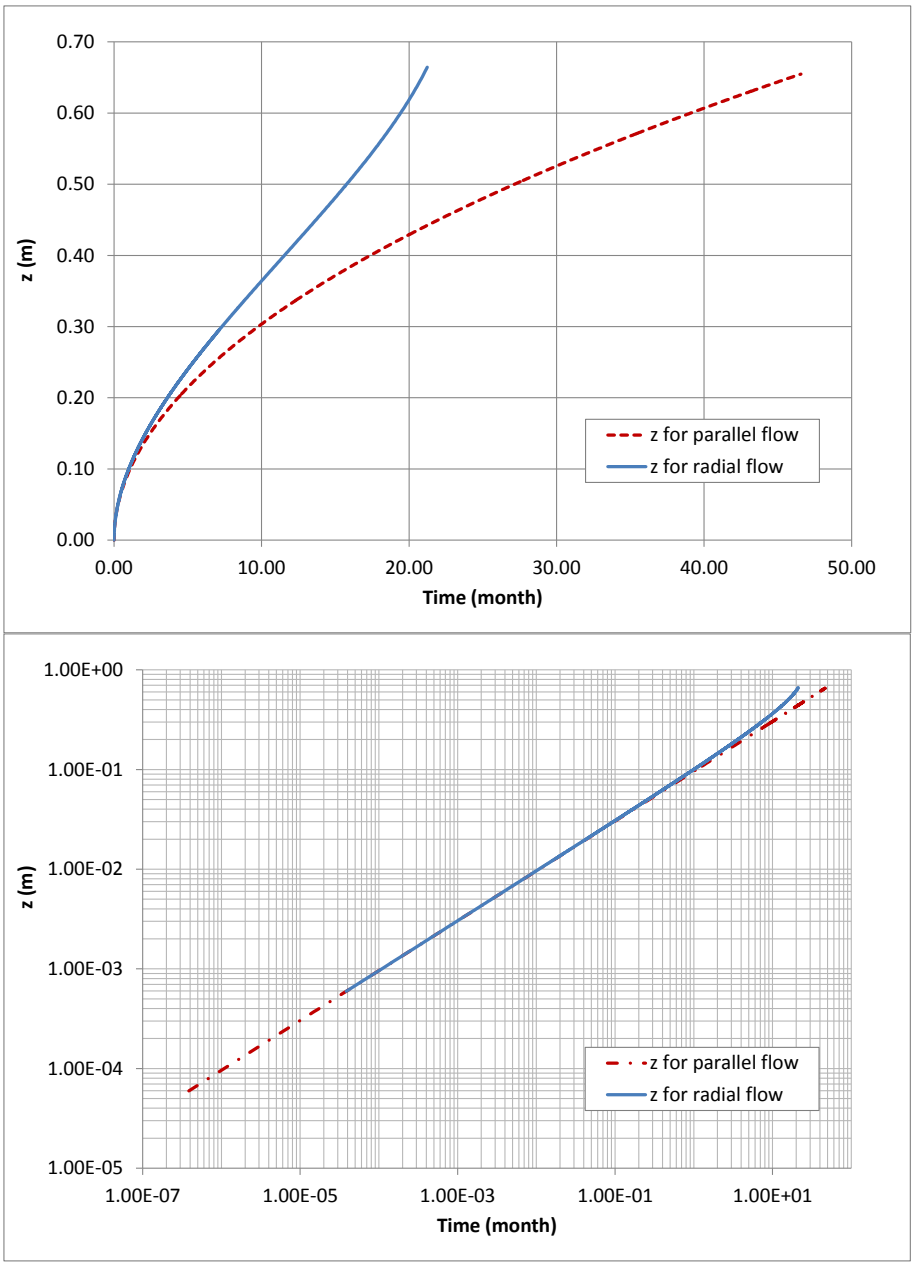

Figure 40. Comparison of the computed advance of the hydration front, z, for parallel and radial flow (natural scale above and logarithmic scale below).

The specific flux q is calculated with the Darcy´s law (Equation (31)). Figure 41 shows the specific flux q in semi log and log-log scales. The flux for parallel flow is larger than that of parallel flow. They are related through:

$$\frac{q_{parallel}}{q_{radial}} = \frac{z_{radial}}{z_{parallel}} \geq 1$$

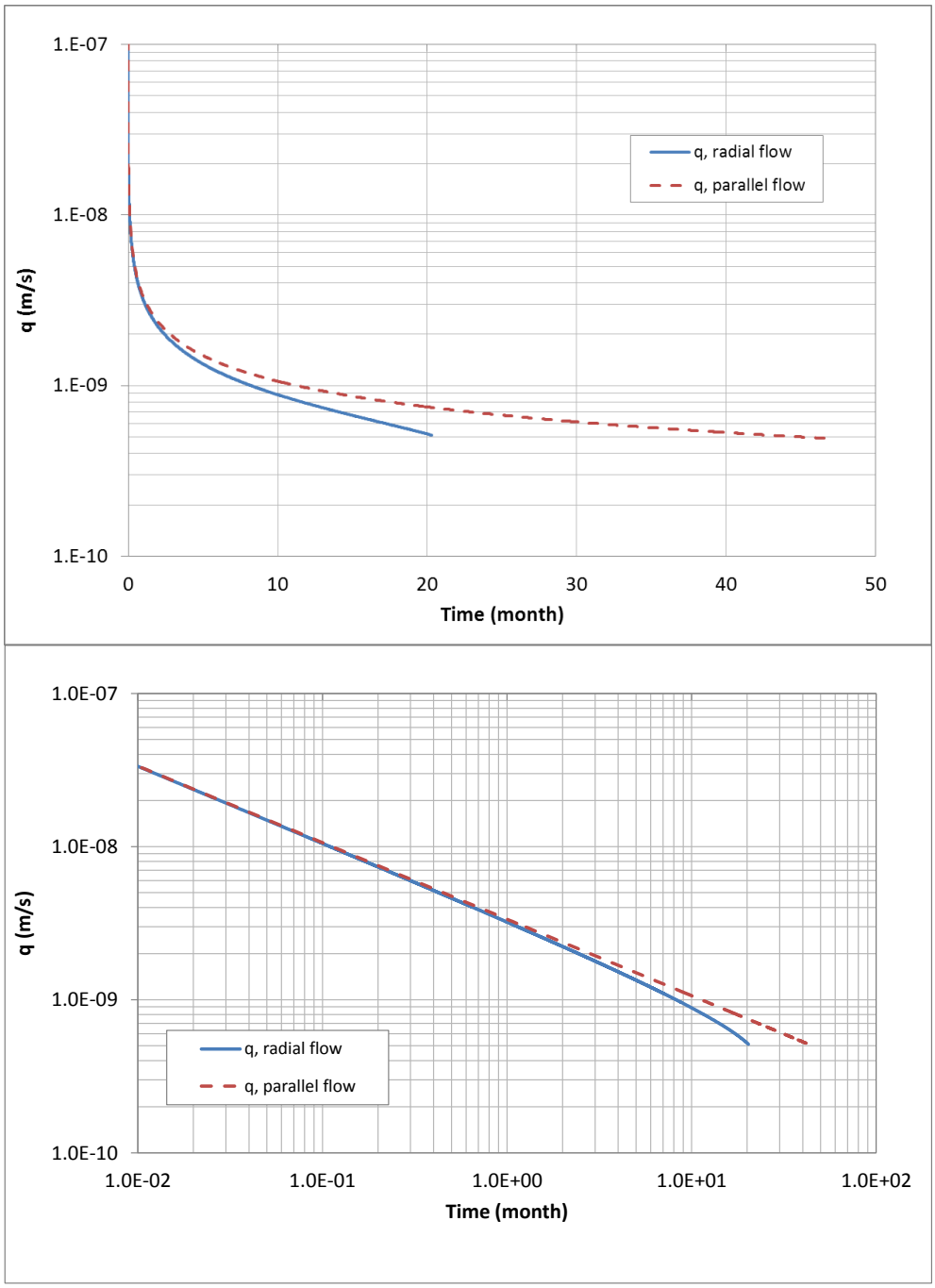

Figure 41. Specific flux, q(m/s) for parallel and radial flow (semi log above and logarithmic scale below).

The water flux, Q, is calculated by multiplying the specific flux, q, by the hydration surface through which water flows. The hydration surface, S_h, for radial flow is given by $S_h = 2\pi R_e L$ (see Figure 38):

For parallel flow, S_h is given by $S_h = aL = 2\pi\left(\frac{R_e + R_i}{2}\right)L$ (Figure 39).

For the same volume and thickness of bentonite, the hydration surface is larger of radial flow than that of parallel flow. Then, the radial flow Q_r is also larger than the parallel flow Q_p. Figure 42 shows the time evolution of Q_r and Q_p.

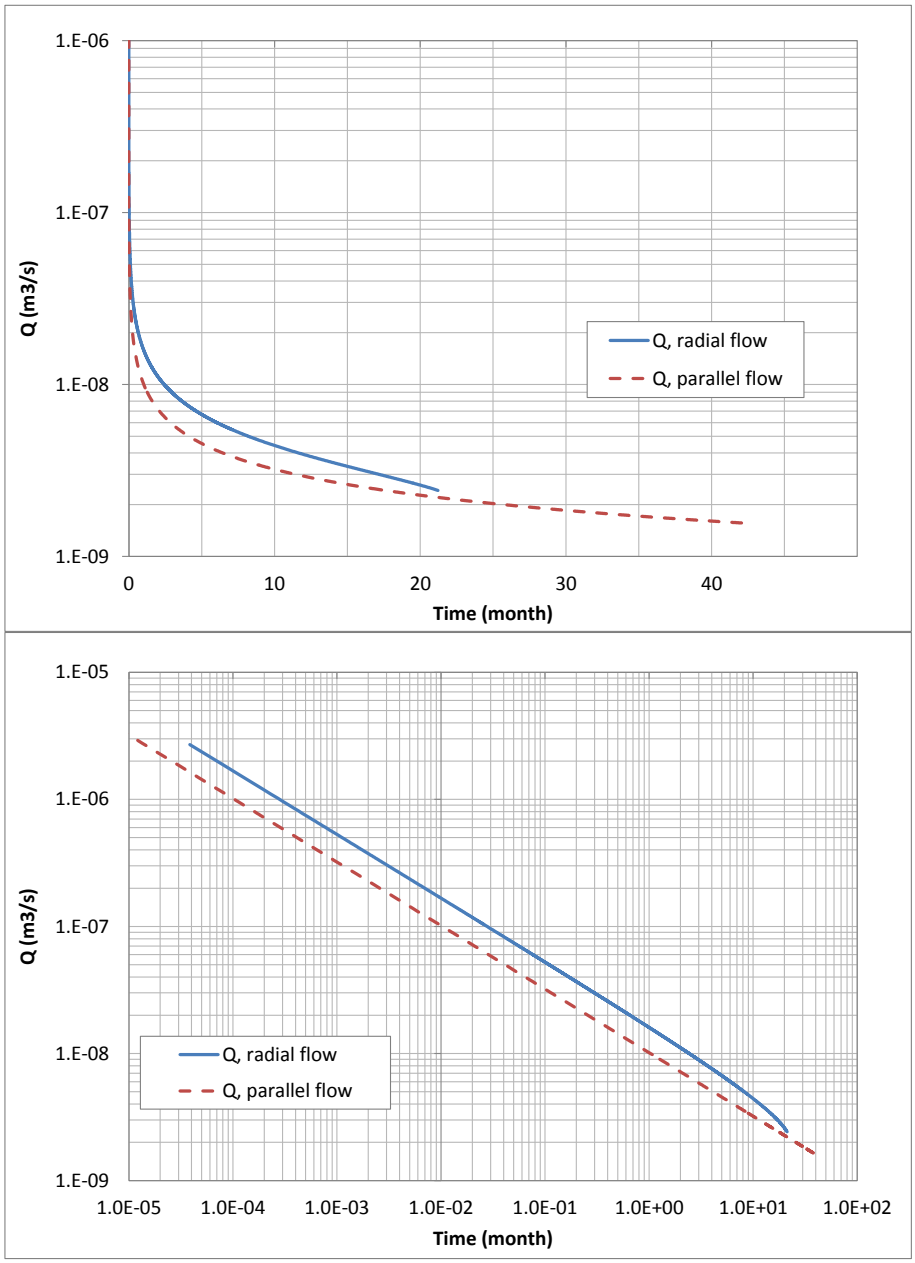

Figure 42. Water flux for parallel and radial flow (semi log scale above and log-log scale below).

Figure 43 shows the comparison of the cumulative water uptake, V, for radial and parallel flow. The cumulative water uptake of the radial flow is larger than that of parallel flow. Figure 44 shows the time evolution of the dimensionless volume versus the dimensionless time for radial and parallel flow. The time evolution of the dimensionless cumulative water uptake is different for radial and parallel flow because the hydration surface for radial flow is larger than that of parallel flow.

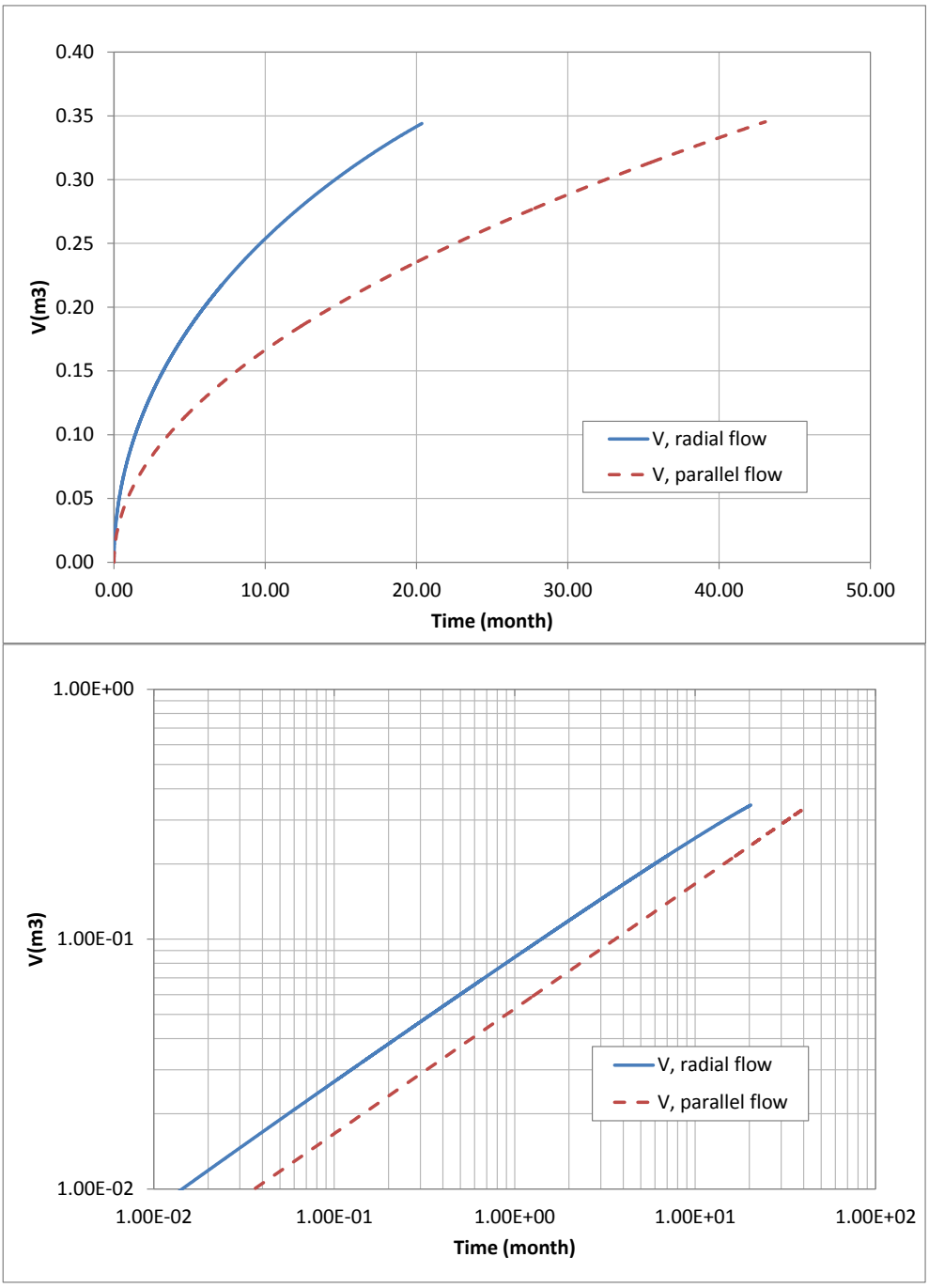

Figure 43. Cumulative water uptake for parallel and radial flow (natural scale above and log-log scale below).

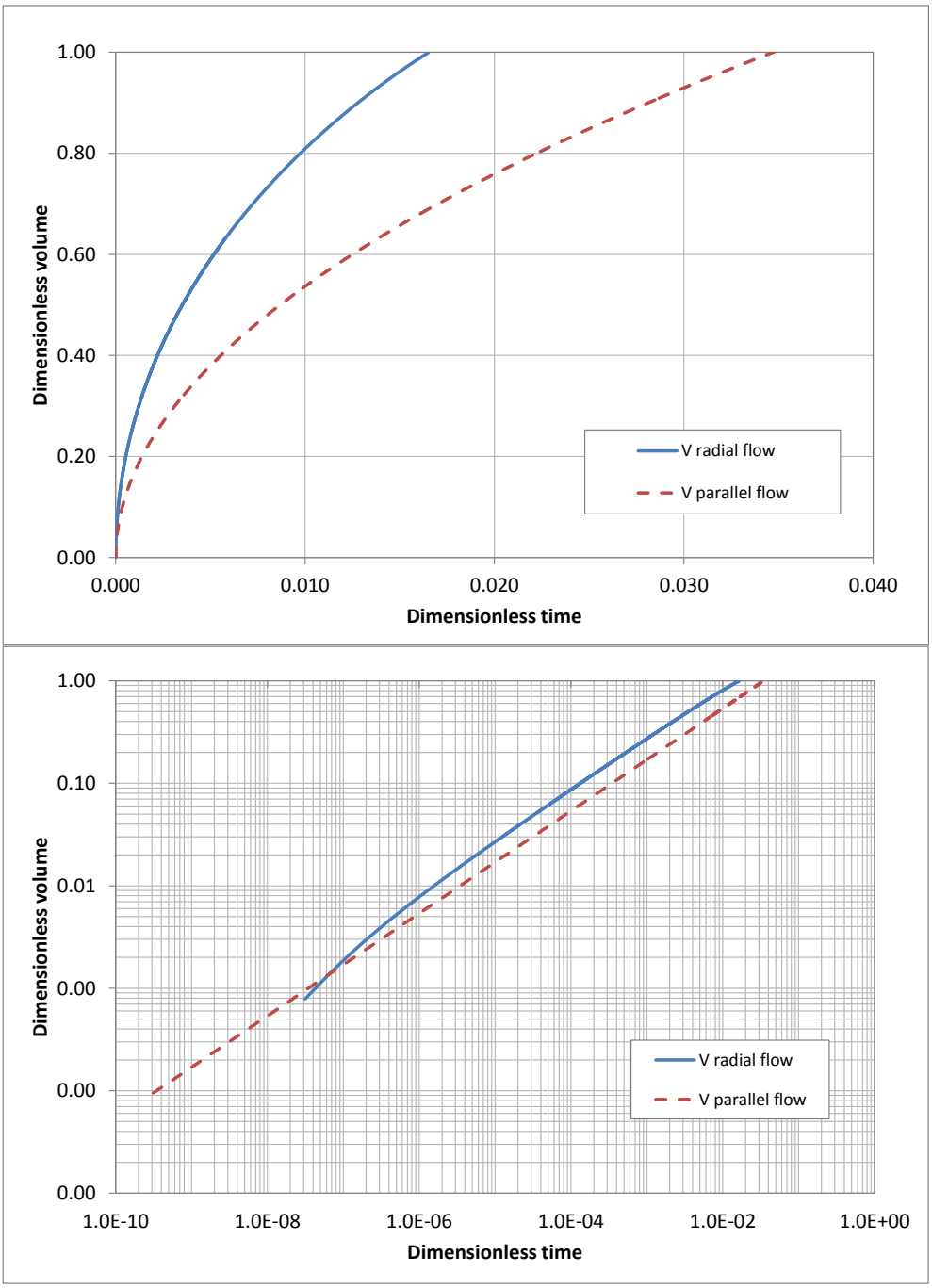

Figure 44. Dimensionless cumulative water uptake versus dimensionless time for parallel and radial flow (natural scale above and log-log scale below).

6.7.2 Same thickness and hydration surface

The water flow and the cumulative water uptake have been calculated for the same thickness and hydration surface for parallel flow. The dimension a in Figure 39 is taken equal to $2\pi R_e L$ so that the hydration surface for parallel flow is equal to that of the radial flux. Figure 45 shows the water flow (m^3/s) for radial and parallel flow when the thickness and the hydration surface are the same. One can see that the flow for parallel flow Q_p is larger than Q_r. Figure 46 shows the dimensionless water uptake for radial and parallel flow. The final volume of the parallel flow is larger than that of the radial flow. The results of the two previous cases show that the water uptake for parallel flow is different than that of radial flow.

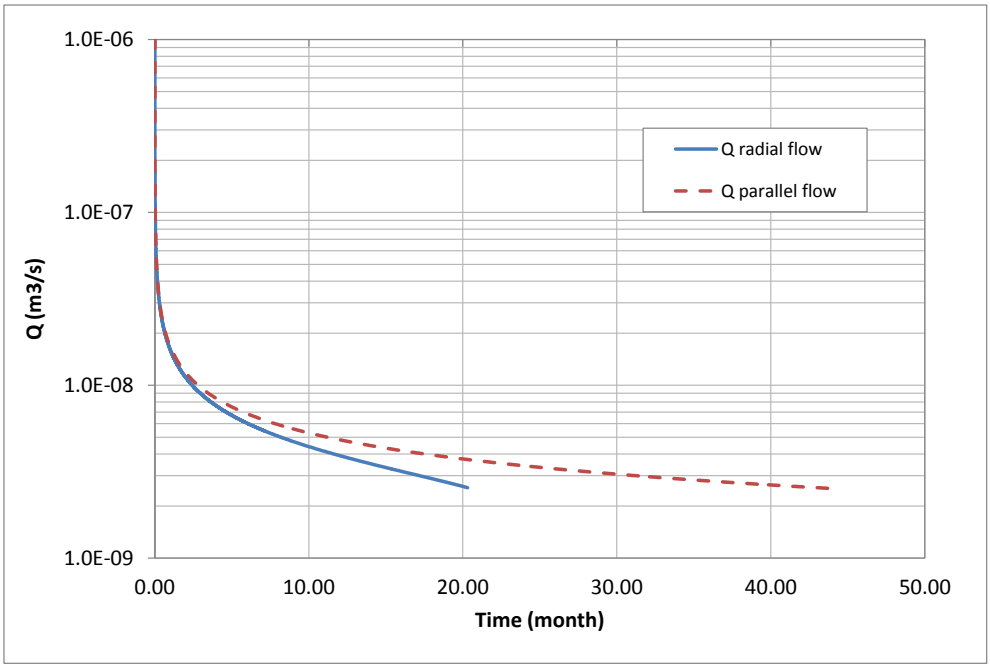

Figure 45. Water uptake for parallel and radial flow.

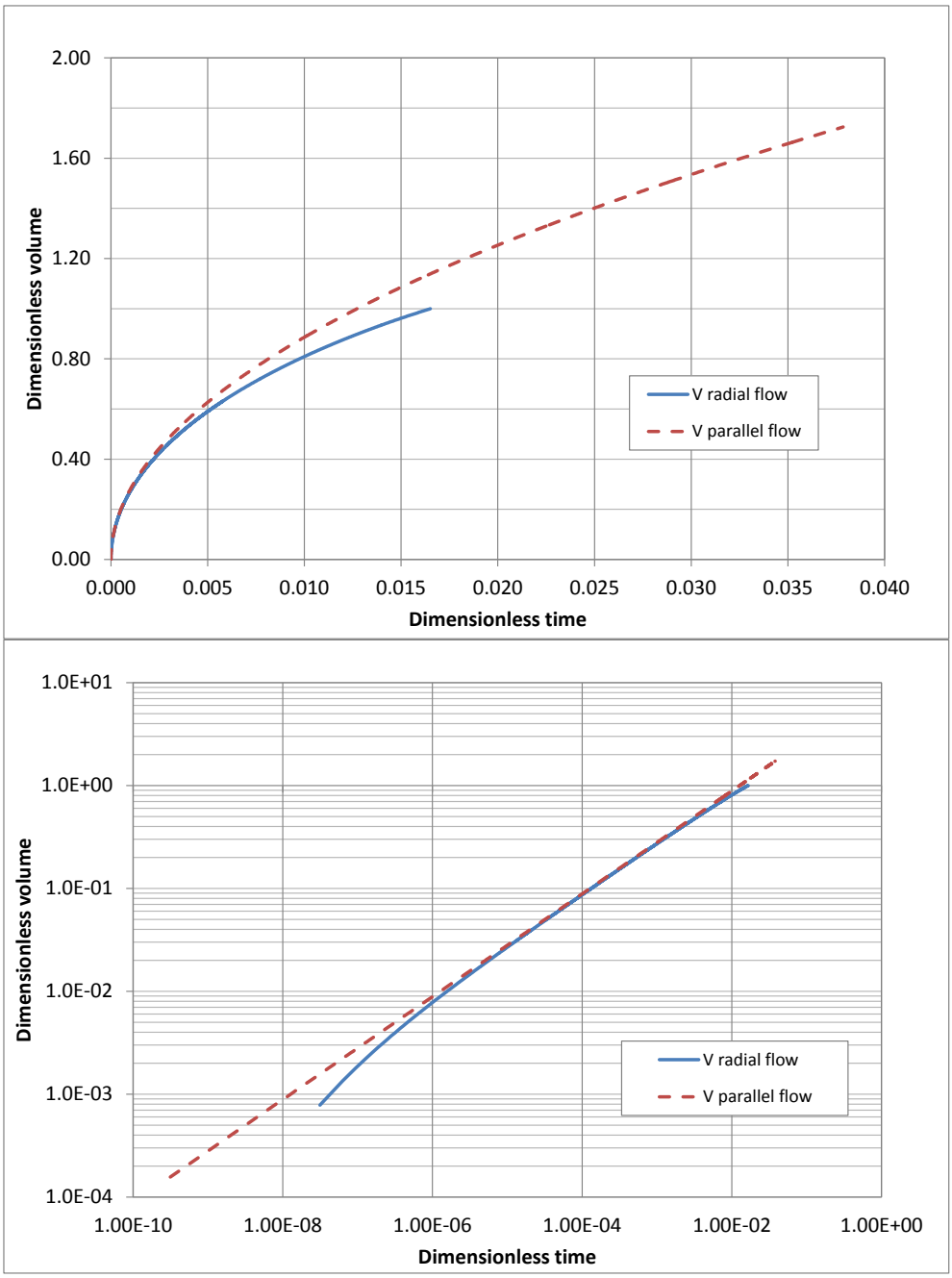

Figure 46. Dimensionless cumulative water uptake versus dimensionless time for parallel and radial flow (natural scale above and log-log below).

6.7.3 Same volume and hydration surface

We investigate an intermediate case in which the volume and hydration surface are the same. The dimensions a (hydration surface) and b (thickness) in Figure 39 are calculated so that the volume and the hydration surface of parallel and a radial flow are the same. The

volumes of radial and parallel flow, V_r and V_p, respectively coincide when $b = \frac{(R_e^2 - R_i^2)}{2R_e}$.

On the other hand, the hydration surfaces coincide when $a = 2\pi R_e$.

When the hydration surface and the volume are the same for radial and parallel flow, the bentonite thickness for the parallel flow is smaller than that of the radial flow. Figure 47 shows the water uptake of radial and parallel flow. Although the differences are smaller than in the previous cases, there are still clear differences between both solutions.

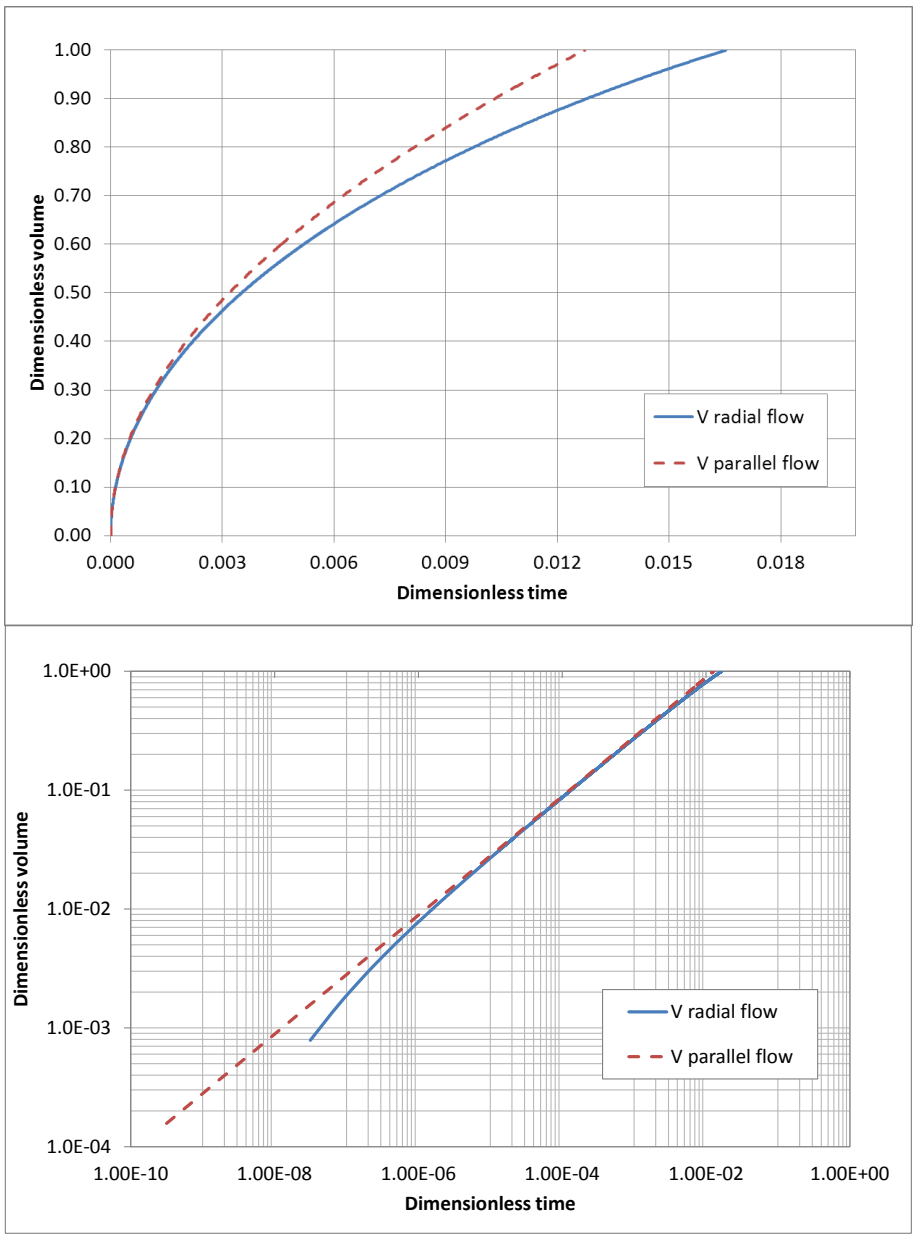

Figure 47. Dimensionless cumulative water uptake versus dimensionless distance for parallel and radial flow (natural scale above and log-log scale below).

6.7.4 Optimization of the thickness, volume and hydration surface

The values of and b for parallel flow were calibrated to reproduce the cumulative water uptake of the radial flow. Parameter a was varied within the range of previous cases while b was calculated by imposing the condition $V_r = V_p$. Which is full filled when $b = \frac{\pi(R_e^2 - R_i^2)}{a}$. The optimum value of a was found to be 0.4215 m which is smaller than those of previous cases. Figure 48 shows the dimensionless cumulative water uptake for the calibrated values of a and b. It can be seen that both curves are very close to each other.

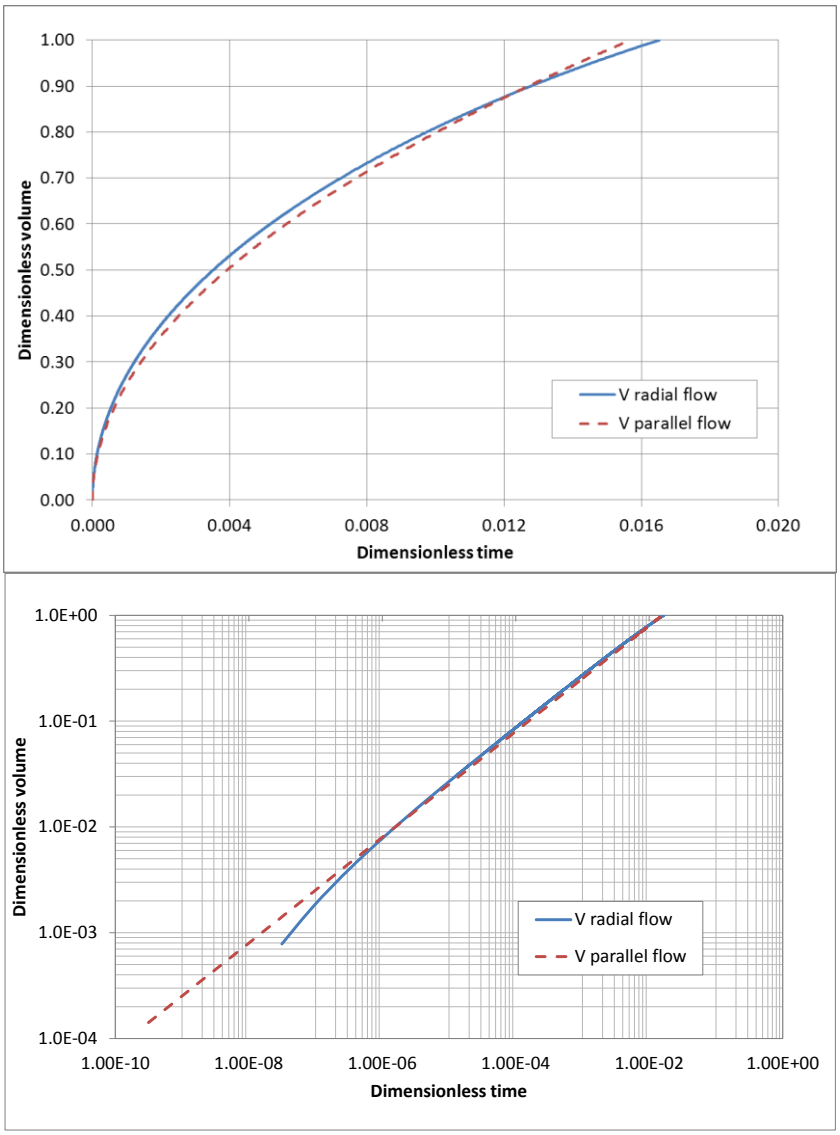

Figure 48. Dimensionless cumulative water uptake versus dimensionless time for parallel and radial flow (natural scale above and log-log scale below).

6.7.5 Conclusions

Figure 49 shows the comparison of the solution corresponding to: the same thickness and volume, same thickness and hydration surface, same volume and hydration surface, and the calibration values of thickness and hydration surface.

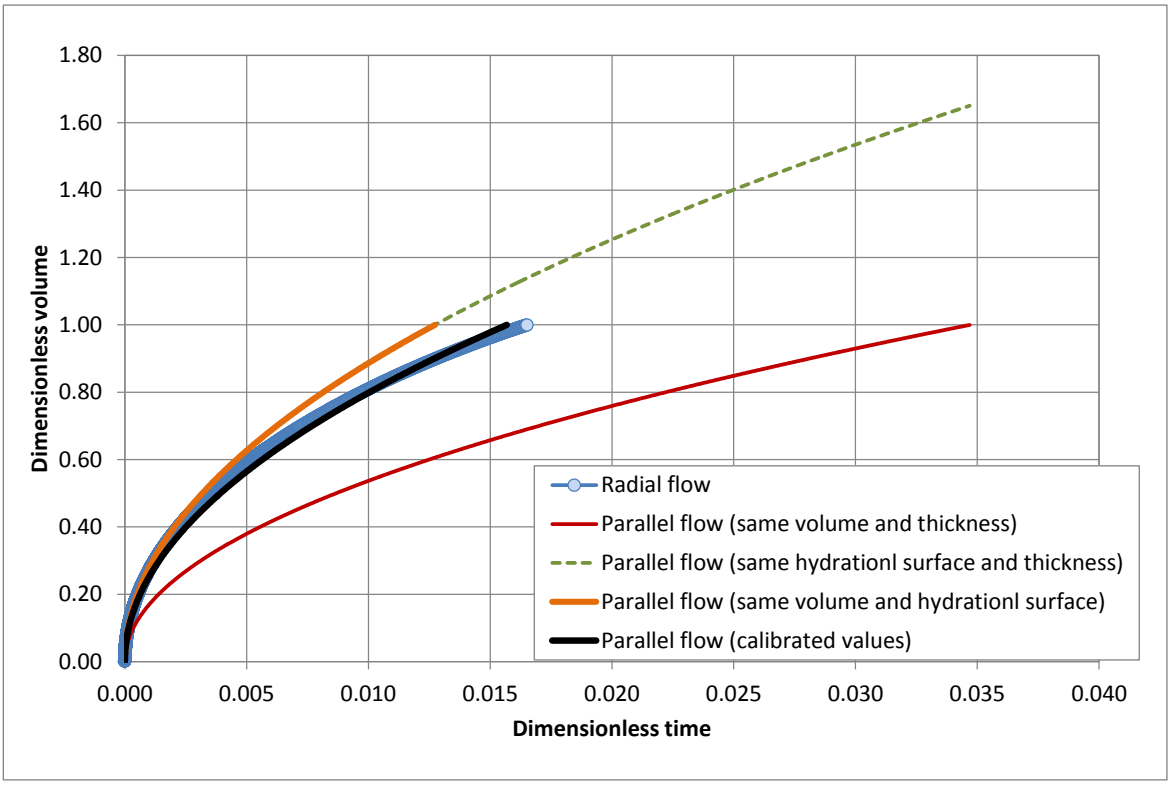

Figure 49. Dimensionless cumulative water uptake versus dimensionless time for radial and parallel flow.

Table 7 presents a summary of all the cases. It includes the values of q, Q, V, the advance of the front z, the hydration surface S_h, and the thickness of bentonite b. The advance z for parallel flow is smaller than that of radial flow. q for radial flow is smaller than the parallel flow.

Table 7. Values of z, q ,S_h, b, Q and V for radial and parallel flow.

Case	z (advancing depth)	q (unit volume)	S_h (hydration surface)	b (thickness)	Q (total flow)	V (cumulative water uptake)
Same volume and thickness	$z_{radial} \geq z_{parallel}$	$q_{radial} \leq q_{parallel}$	$S_{radial} \geq S_{parallel}$	$b_{radial} = b_{parallel}$	$Q_{radial} \geq Q_{parallel}$	$V_{radial} = V_{parallel}$
Same hydration surface and thickness	$z_{radial} \geq z_{parallel}$	$q_{radial} \leq q_{parallel}$	$S_{radial} = S_{parallel}$	$b_{radial} = b_{parallel}$	$Q_{radial} \leq Q_{parallel}$	$V_{radial} \leq V_{parallel}$
Same volume and hydration surface	$z_{radial} \geq z_{parallel}$	$q_{radial} \leq q_{parallel}$	$S_{radial} = S_{parallel}$	b calculated	$Q_{radial} \leq Q_{parallel}$	$V_{radial} = V_{parallel}$
Calibrated values	$z_{radial} \geq z_{parallel}$	$q_{radial} \leq q_{parallel}$	S_h calibrated	b calibrated	$Q_{radial} \leq Q_{parallel}$	$V_{radial} = V_{parallel}$

6.8. Comparison of the geometry of the cells and the mock up applied to Green-Ampt method

The analysis of parallel flow presented so far corresponds to prismatic geometry (Figure 39). However, CT and CG cells have a cylindrical cross section. Figure 50 shows the geometry and the dimensions used for prismatic and cylindrical parallel flow.

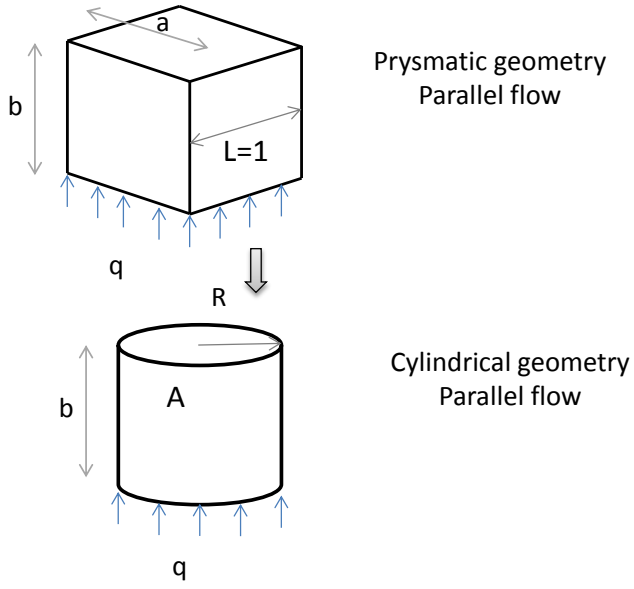

Figure 50. Scheme of the prismatic and cylindrical geometries used for parallel flow.

Table 8 shows a summary of the values of the radius and the thickness of the cylinder for parallel flow.

Table 8. Dimensions of the cylinder for parallel flow.

Case	Radius, R	Thickness, b
Same volume and thickness	$R = \sqrt{(R_e - R_i)L}$	$b = R_e - R_i$
Same hydration surface and thickness	$R = \sqrt{2R_eL}$	$b = R_e - R_i$
Same volume and hydration surface	$R = \sqrt{2R_eL}$	$b = \frac{R_e^2 - R_i^2}{2R_e}$
Calibrated values	R calibrated	$b = \frac{(R_e^2 - R_i^2)L}{R^2}$

The results obtained for prismatic and cylindrical geometries for parallel flow are similar. They only differ in the shape of the cross section.

6.9. Comparison of the numerical solutions for radial and parallel flow

The mock up test has been modelled with a numerical model using INVERSFADES2 (Zheng and Samper, 2005). The mesh of the model is a 2D axisymmetric mesh, which takes into account axial symmetry (Zheng and Samper, 2008). The model simulates radial flow with a water flow from the hydration surface. Another model of the mock up has been constructed, using the same characteristic, parameters, heating and hydrating, but the mesh, the model and the water flow is 1D parallel flow with the same volume and hydration surface as the mock up test. The computed water uptake for parallel flow is larger than that of radial flow (Figure 51). This result is consistent with the results obtained with the analytical solution (Figure 47).

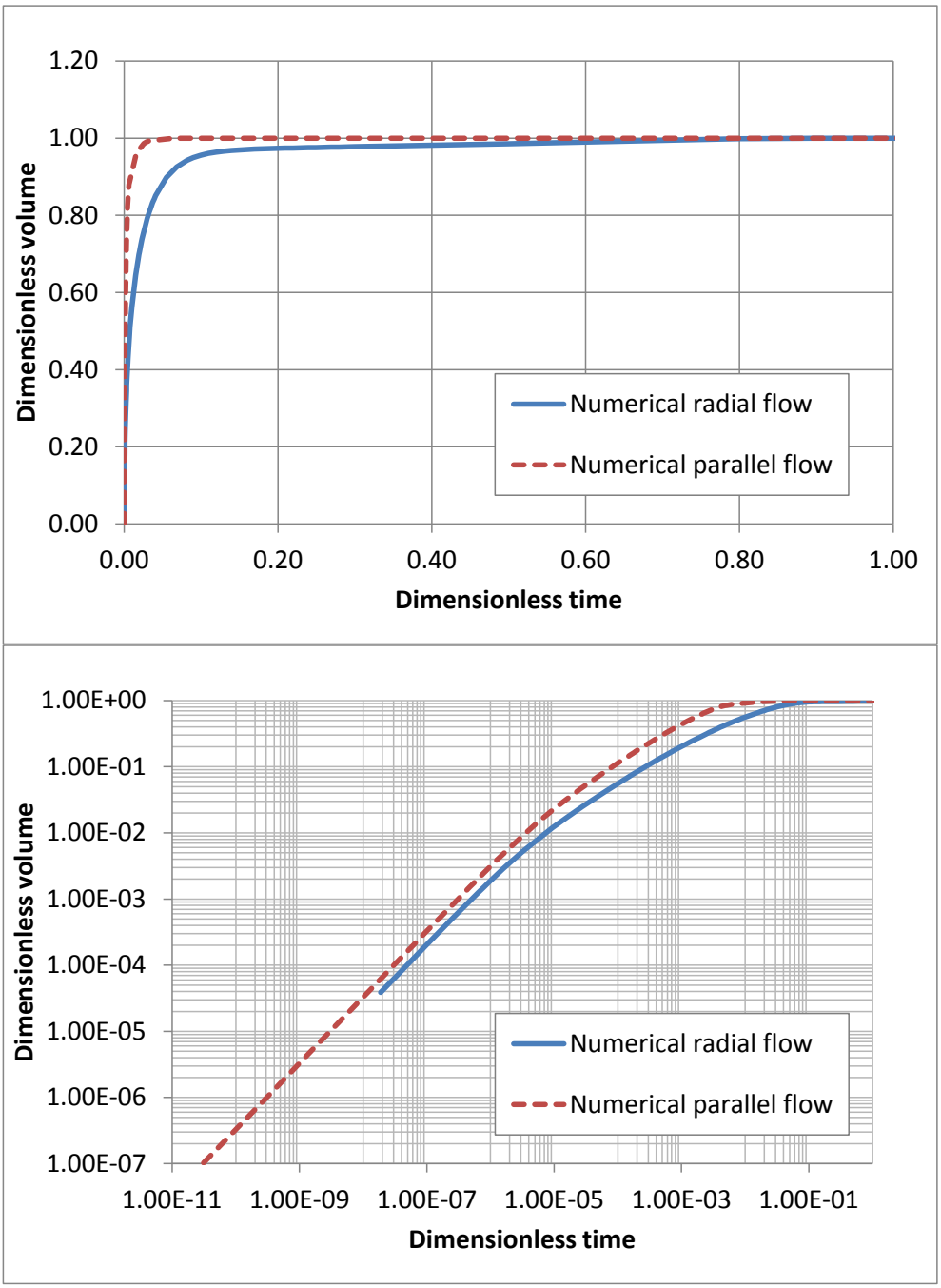

Figure 51. Comparison of the numerical solutions for the radial and parallel flow for the conditions of the mock up test.

6.10. Conclusion

The Green-Ampt analytical solution has been used to compare the water uptake for radial and parallel flow. Such comparison reveals that the analytical solutions are markedly different. Such differences should be taken into account when translating the results obtained in laboratory cells, where the flow parallel, to the in situ test where water flow is radial. The water uptake for parallel flow has been computed for the following cases: 1) Same volume and thickness; 2) Same hydration surface and thickness; 3) Same volume and hydration surface; and 4) For optimized thickness, volume and hydration surface. The best fit was obtained with the optimized values. The case of the same volume and hydration surface gives the second best approximation. It can be concluded that the water uptake for radial and parallel flow are comparable only when the dimensions and the conditions are correctly selected. Measured water uptake data from CG cells for several durations ranging from 0.5 to 7.5 years fit well to the Green-Ampt analytical solution for an apparent hydraulic conductivity K slightly greater than that corresponding to 25ºC and the initial bentonite porosity. The analytical Green-Ampt solution for radial and parallel flow reproduce well the numerical solutions by using an apparent hydraulic conductivity slightly larger than that corresponding to 25ºC and the initial bentonite porosity (Samper et al., 2011).

7. Integrated analysis of water content data

7.1. Introduction

This chapter presents the integrated analysis of water content data from various tests performed on FEBEX bentonite. Available water content data come from several heating and hydration tests including CT cells, CG cells, mock up and in situ tests. Data are first compiled. Then, anomalous values are filtered. "Clean" data are then integrated in terms of dimensionless variables. Dimensionless water content data are integrated as a function of dimensionless distance for several dimensionless times. Then, the computed data were analyzed and integrated for lab cells, and the mock up and in situ tests.

7.2. Available water content data from heating and hydration tests

Water content data are available for CT cells (CT22, CT23 and CT24), and for CG cells (FQ1/2(CG1), HI1/2(CG1), FQ2 (CG2) and CG3). These data were obtained at the end of the tests from bentonite samples in which the gravimetric water content was measured. For the mock up test, the available data include relative humidity data. Such data have been transformed into volumetric water content. For the in situ test, bentonite water content data are available from TDR and relative humidity sensors from heater 1 and 2. There are also many gravimetric water content data from the dismantling of the heater 1.

A summary of the water content data, the initial volumetric water content, the initial dry density and the characteristic times for the selected tests are listed in Table 9.

Table 9. Summary of the initial volumetric water content, duration, characteristic time, type of analysis and dry density.

Type of test	Test	Duration (d)	Characteristic time (d)	Analysis	Initial ρ_d (g/cm^3)	Initial Volumetric Water content
CT cell	CT22	26	$1.25 \cdot 10^4$	Post-mortem analysis	1.65	0.22

	CT23	183	$1.25 \cdot 10^4$	Post-mortem analysis	1.65	0.22
	CT24	168	$1.25 \cdot 10^4$	Post-mortem analysis	1.65	0.43
CG cell	FQ1/2(CG1)	188.76	$2.93 \cdot 10^4$	Post-mortem analysis	1.64	0.21
	HI1/2(CG1)	213.95	$2.93 \cdot 10^4$	Post-mortem analysis	1.67	0.23
	FQ1(CG5)	370	$2.93 \cdot 10^4$	Post-mortem analysis	1.67	0.23
	HI1(CG6)	440	$2.93 \cdot 10^4$	Post-mortem analysis	1.67	0.23
	FQ2(CG2)	762	$2.93 \cdot 10^4$	Post-mortem analysis	1.66	0.22
	HI2(CG4)	747	$2.93 \cdot 10^4$	Post-mortem analysis	1.67	0.23
	CG3	2775	$2.93 \cdot 10^4$	Post-mortem analysis	1.64	0.22
Mock up	Heater 1	5076	$3.66 \cdot 10^4$	V_A4 Rh sensor	1.65	0.30
	Heater 1	5076	$3.66 \cdot 10^4$	V_A6 Rh sensor	1.65	0.30
In situ	Heater 1	1948	$4.24 \cdot 10^4$	WT-M1 TDR sensor	1.70	0.20
	Heater 2	2862	$4.24 \cdot 10^4$	WT-M2 TDR sensor	1.70	0.20
	Heater 1	1948	$4.24 \cdot 10^4$	Post-mortem analysis	1.70	0.18

7.2.1 Water content data from CT and CG cells

The bentonite water content in cells CT and CG was measured at the end of the tests in the post-mortem analysis of the samples. Available data for CT and CG cells include gravimetric water content, *w*. These data can be transformed into volumetric water content θ, by multiplying *w* by the dry density, ρ_d.

7.2.2 Relative humidity from the mock up test

Bentonite water content in the mock up test is monitored with relative humidity, RH, sensors. Relative humidity can be related to the suction, $\psi = P_l - P_g$, through the following equation:

$$P_l - P_g = ln(RH)\frac{\rho_l RT}{M_w} \tag{36}$$

where:

- P_l is the liquid pressure (kPa)
- P_g is the gas pressure (kPa)
- R is the gas constant (8314 J/mol/ºK)
- T is the temperature (ºK)
- ρ_l is the liquid density (kg/L)
- M_w is the molecular mass of water (0.018 kg/mol)

The suction is related to the liquid saturation degree, S_l, through the retention curve:

$$S_l = \left(1 - \psi / 1100000\right)^{1.1} \Big/ \left[\left(1 + 5 \cdot 10^{-5} \psi\right)^{1/0.82}\right]^{0.18} \quad (37)$$

Figure 52 and Figure 53 show the relative humidity, saturation degree and volumetric water content of the sensors in sections VA4 and VA6 of the mock up test. The water content is largest in the external surface due to the hydration of the bentonite. The relative humidity measured in the sensor A6 reaches the value of 100%. Sensor A4 does not reach the saturation. The relative humidity measurements do not take into account changes in bentonite porosity and water salinity. Therefore, bentonite near the sensor A4 is saturated but measured data are smaller than 100%.

Data in sensor A4 are available for 5000 days for radial distances of 0.22, 0.55 and 0.7 m. The sensor located at r = 0.37m has data until 3000 days. The sensors located in section A6 for radial distances of 0.22, 0.37 and 0.55 m have data until 5000 days. The most external sensor in section A6 has data for 3000 days. The external sensors measure a larger relative humidity data because they are near the hydration boundary. The internal sensors register the smallest relative humidity values. Humidity data for early times decrease from the initial value due to water evaporation.

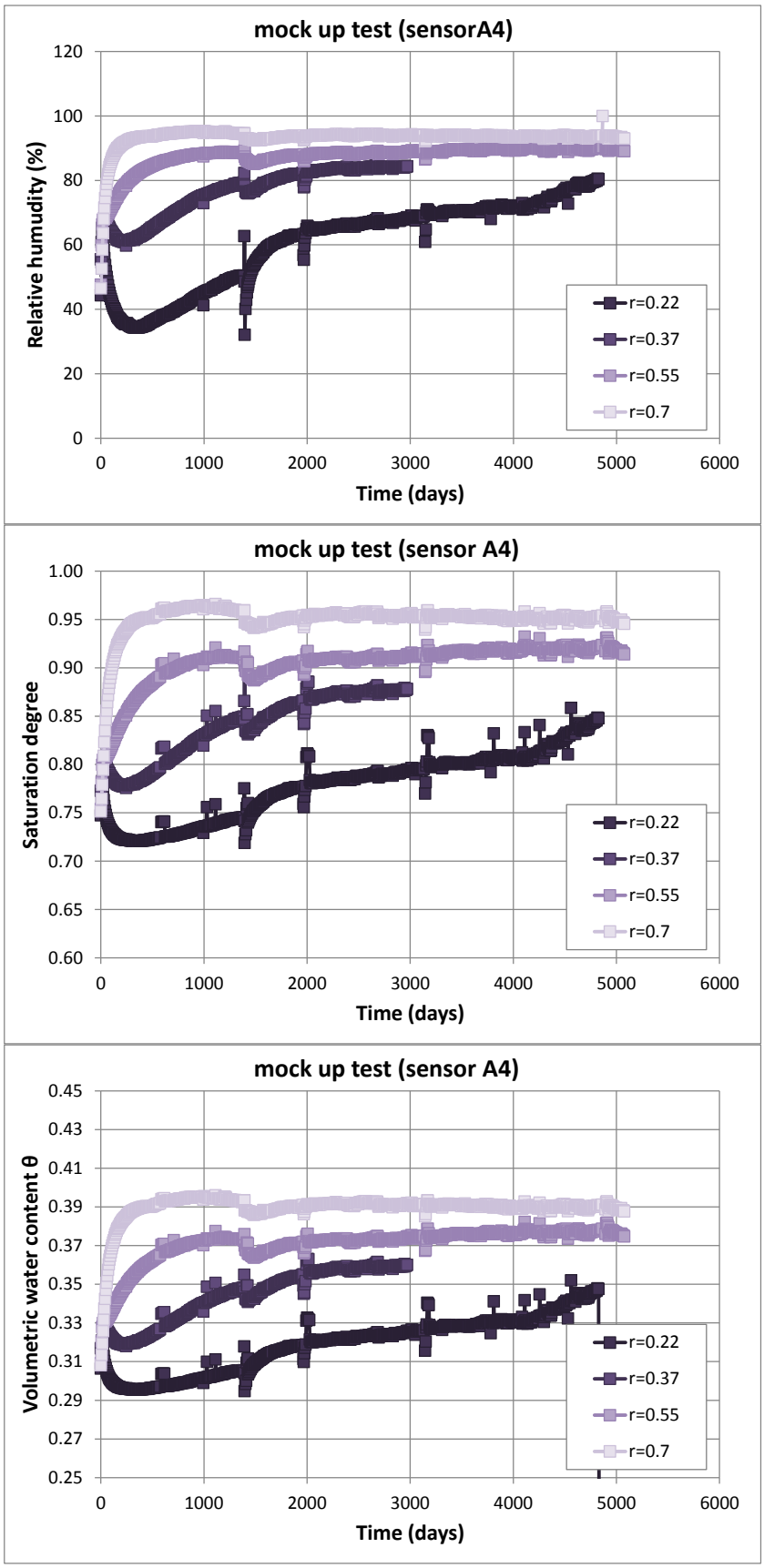

Figure 52. Raw relative humidity (top), saturation degree (intermediate) and volumetric water content data (bottom) in section A4 of the mock up test.

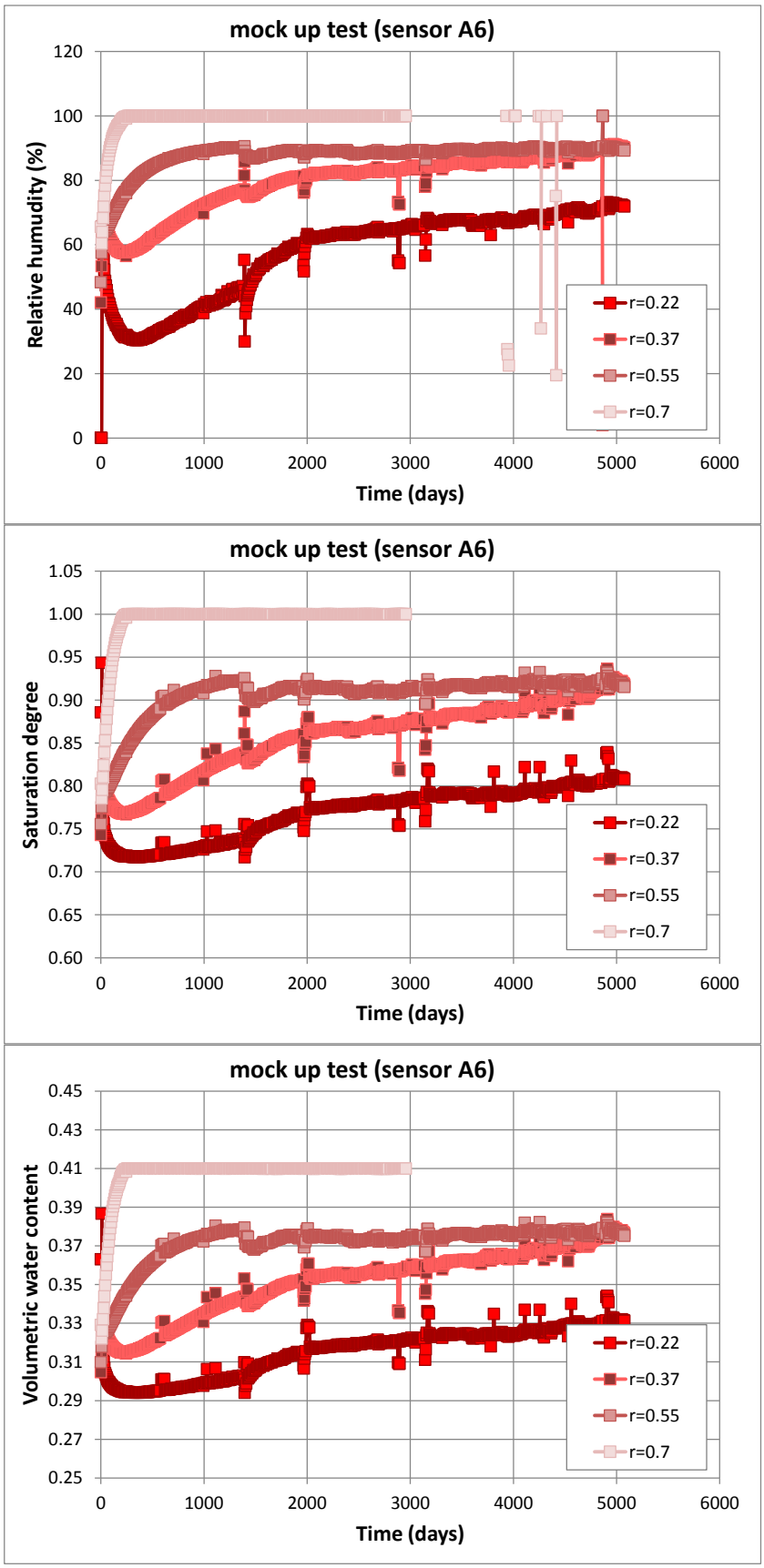

Figure 53. Raw relative humidity (top), saturation degree (intermediate) and volumetric water content data (bottom) in section A6 of the mock up test.

7.2.3 Water content data for the in situ test

Water content data in the in situ test is monitored with capacitive sensors which measure relative humidity and TDR sensors which provide directly the bentonite water content data. Figure 54 shows the time evolution of the volumetric water content in the sensors located in sections M1 and M2 of the in situ test. The section M1 corresponds to the heater 1, which was dismantled after 1948 days of heating in June 2000. The section M2 corresponds to the heater 2. Water content data are available for 5000 days. The water content data of the section M1 do not reach bentonite saturation. The maximum data measured in section M1 is 0.32 at a radial distance of 0.867 m. This value is similar to the measured data in section M2 at a radial distance of 0.74 m. External sensors in section M2 reach smaller bentonite saturation. The slope of the measured water content data is lower than that of the external sensors.

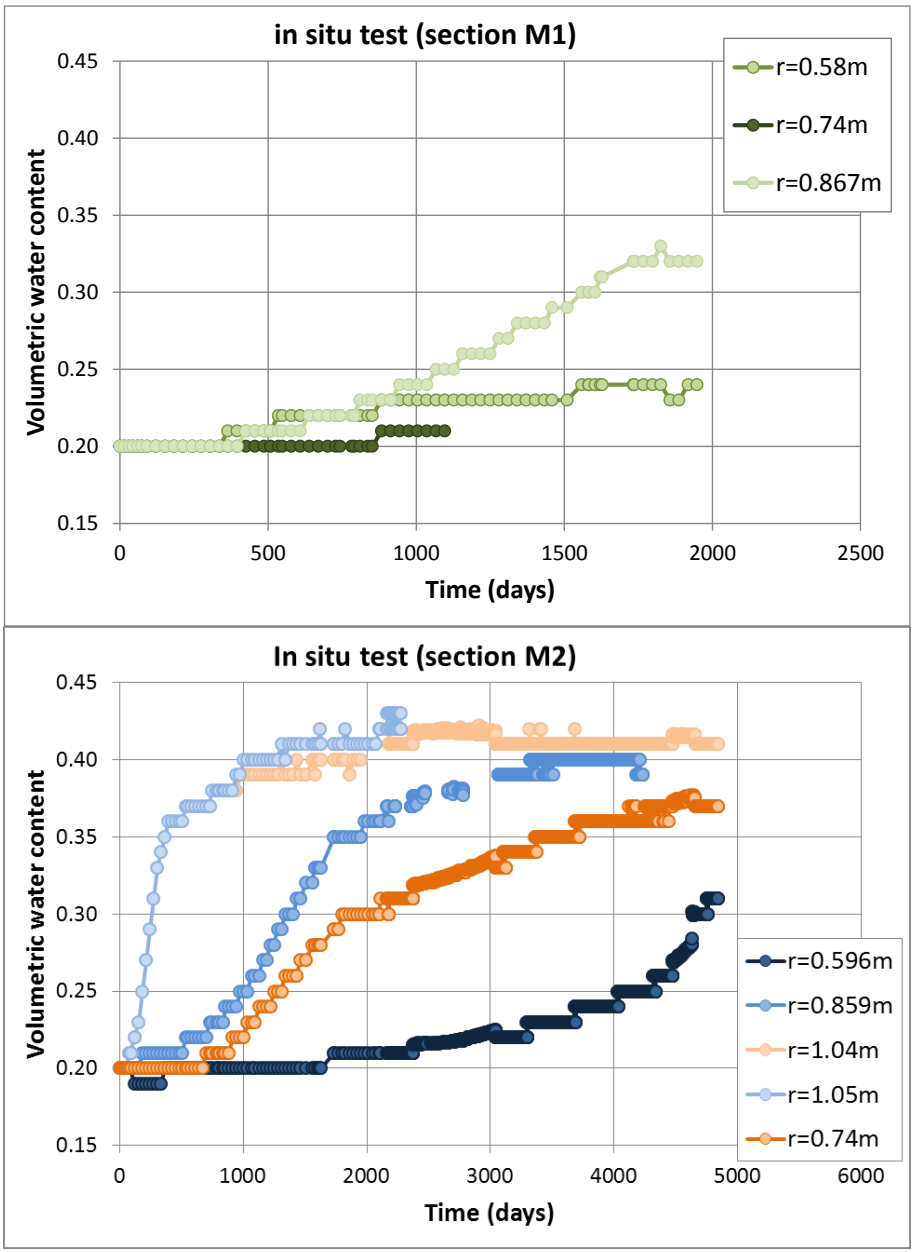

Figure 54. Volumetric water content in sections M1 and M2 of the in situ test.

7.3. Data analysis and filtering

Measured water content data show some anomalous values which are due to errors in the measurement of the relative humidity sensors. The values which do not follow the general trend of the water content have been filtered. Figure 55 shows the filtered water content data for sections A4 and A6 of the mock up test. Most sensors show a sudden decrease of water after about 1500 days. This anomalous behaviour was caused by an overheating period (ENRESA, 2006).

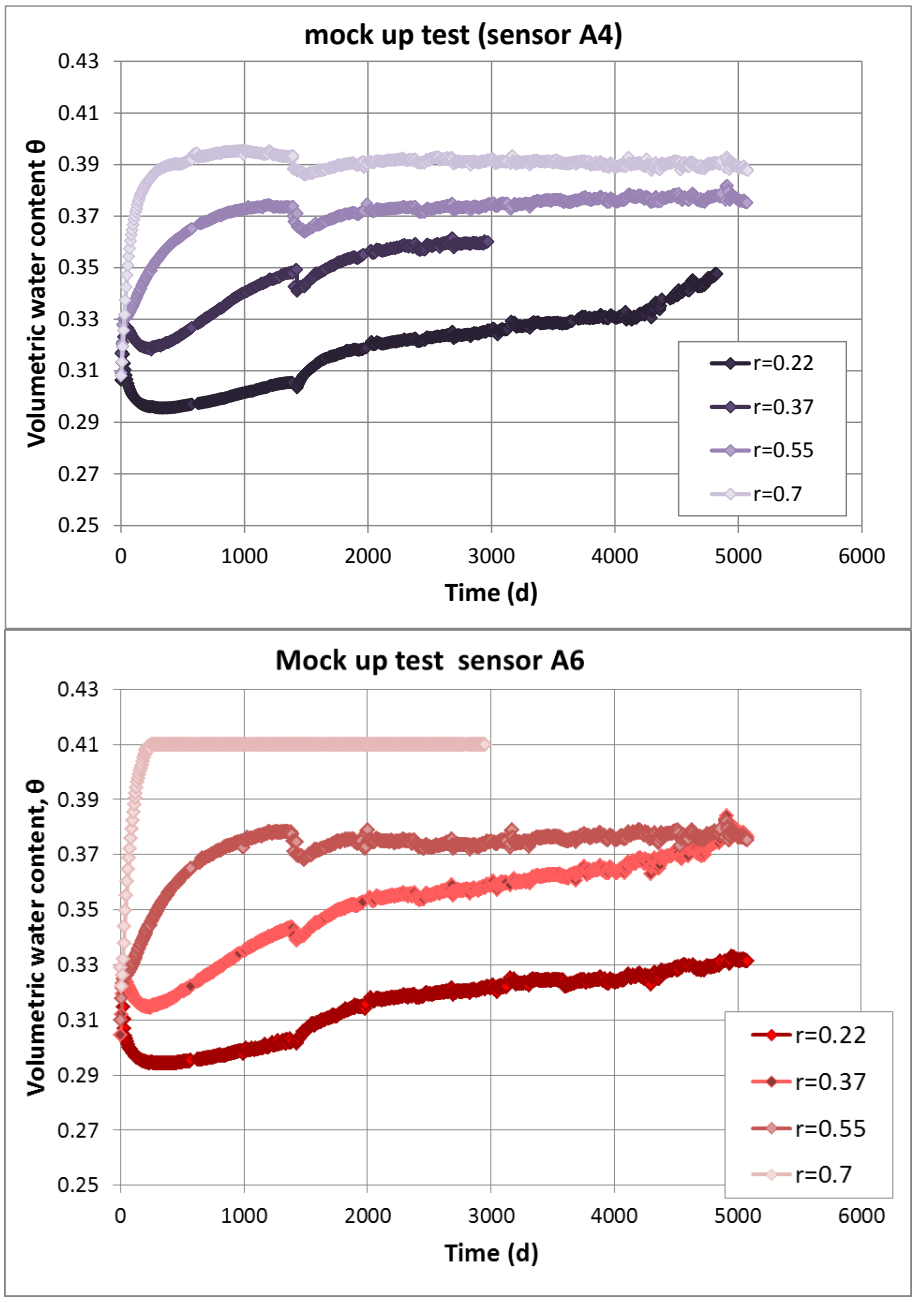

Figure 55. Filtered volumetric water content for sections A4 and A6 of the mock up test.

Figure 56 shows the filtered volumetric water content data for the sections M1 and M2 of the in situ test. The data measured in the in situ sensors are spaced, thus water content data show broken curves.

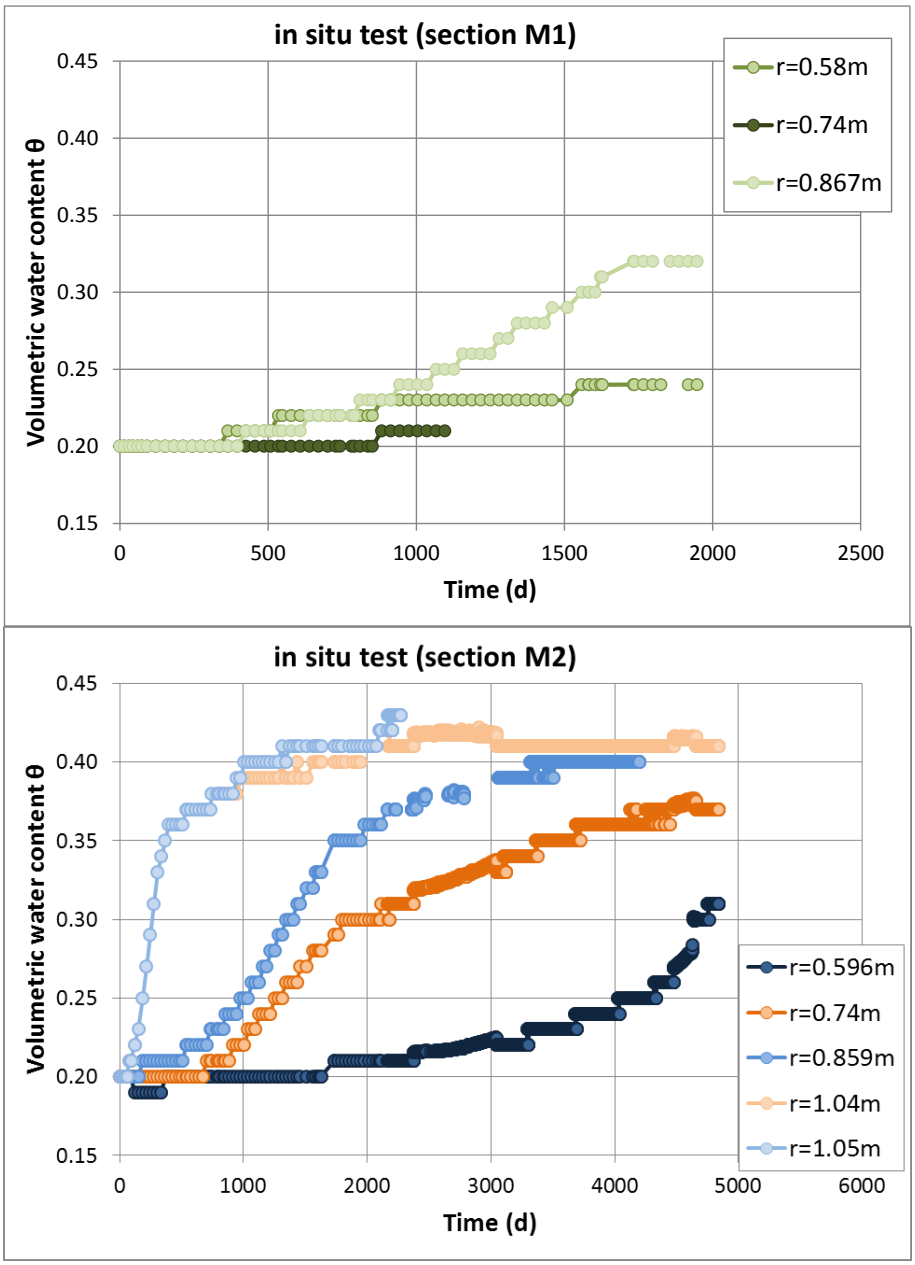

Figure 56. Filtered volumetric water content for the sections M1 and M2 of the in situ test.

7.4. Integrated analysis

Water content data for section M2 of the in situ test are considered for the integrated analysis. The data of the section A6 of the mock up test are selected for the analysis. Figure 57 shows the integration of the water content data for the mock up and in situ tests. The initial water content of the mock up test is larger than that of the in situ test. The mock up test was hydrated initially to fill the gaps by flooding the bentonite barrier. Therefore, the integrated analysis of their data requires working with dimensionless variables.

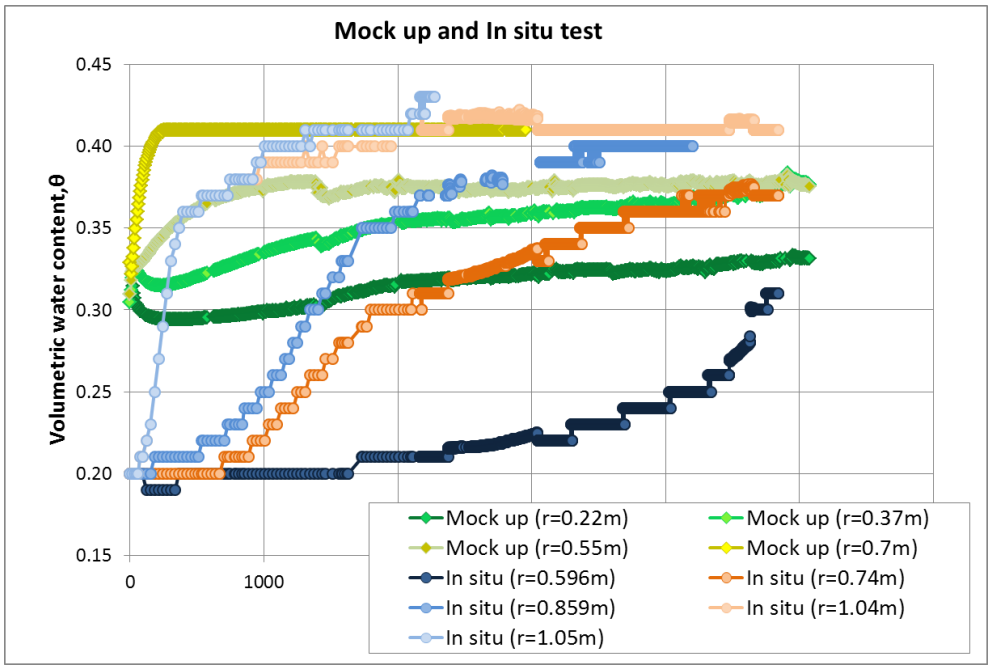

Figure 57. Integrated analysis of water content data for the mock up and in situ tests.

7.5. Dimensionless analysis of the time evolution of the water content

The dimensionless time is calculated by dividing the time by the characteristic time indicated in Table 9. The dimensionless volumetric water content is calculated according to Equation (23). The dimensionless distance is calculated by dividing the distance measured from the hydration zone by the bentonite thickness. A dimensionless distance of 0 corresponds to the hydration boundary and a value of 1 to the heater-bentonite interface. Figure 58 shows the dimensionless water content for the sensors located near the hydration boundary for the mock up and in situ tests. Water content data measured near the hydration boundary are larger than those near the heater. Dimensionless water content data of the mock up reaches plateaus values before those of the in situ. The dimensionless time needed for the saturation of the in situ test is about ten times larger than the time of saturation required in the mock up test.

Water content data for the sensors located close to the heater are shown in Figure 59. The dimensionless water content for the mock up becomes negative due to the evaporation. The curves of dimensionless water content data for the in situ and mock up tests show some differences. The increase of the water content in the intermediate zone of the mock up tests is slower than in the in situ test.

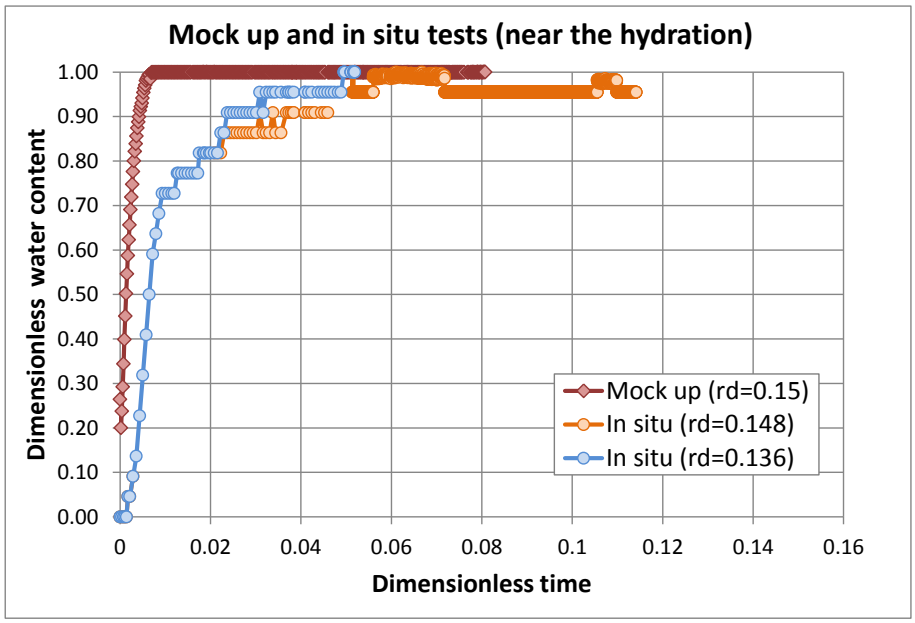

Figure 58. Integrated analysis of the dimensionless water content data from the sensors located near the hydration boundary for the in situ and mock up tests.

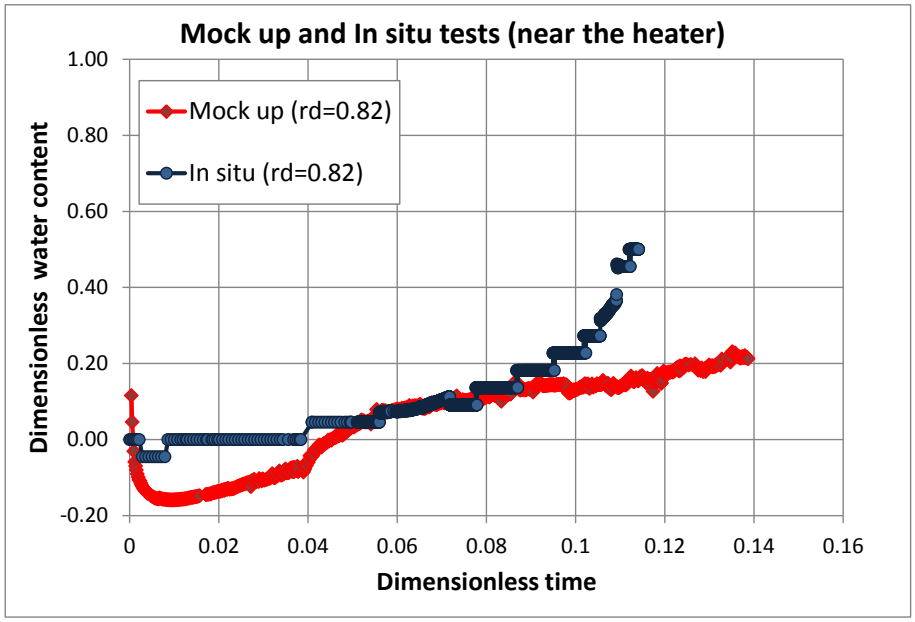

Figure 59. Integrated analysis of the dimensionless water content data from the sensors located near the heater for the in situ and mock up tests.

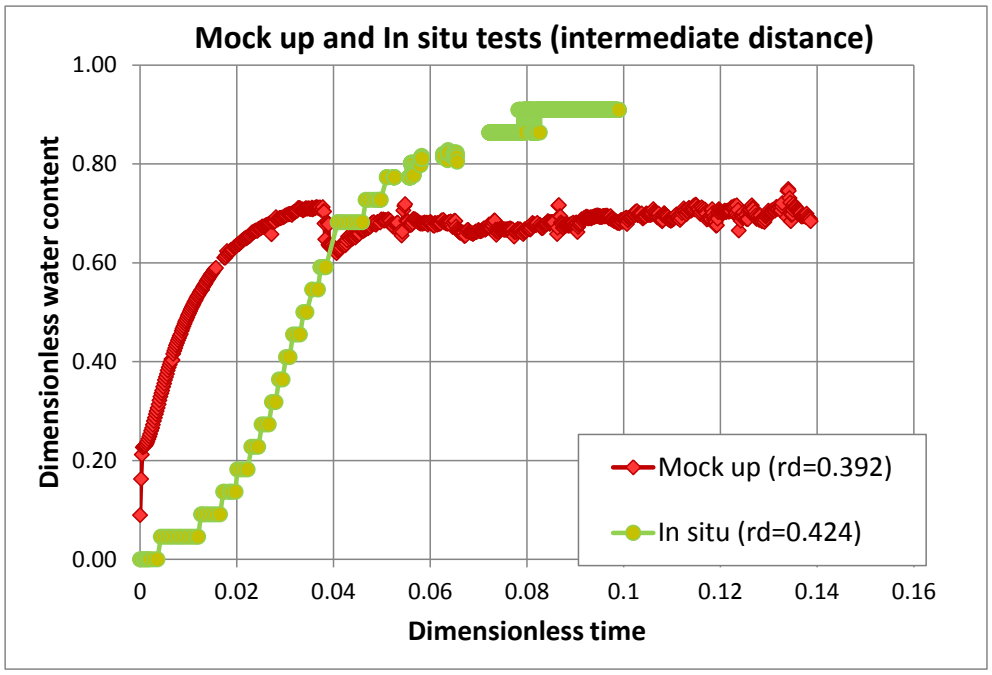

Figure 60. Integrated analysis of the dimensionless water content data from the sensors located in intermediate distances of 0.4 for the in situ and mock up tests.

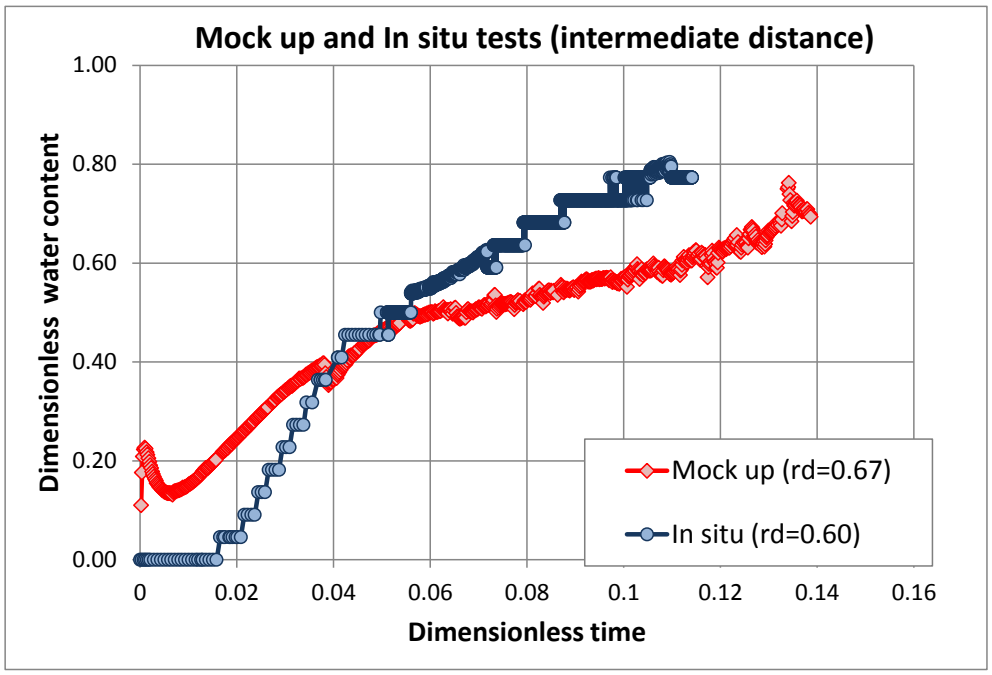

Figure 61. Integrated analysis of the dimensionless water content data from the sensors located in intermediate distances of 0.6 for the in situ and mock up tests.

Figure 60 and Figure 61 show the dimensionless water content for the dimensionless distance of 0.4 for the mock up and in situ tests. The water content curve of the in situ test is larger than that of the mock up for dimensionless times larger than 0.06.

Evaporation in the early times is shown in the mock up sensor data. Evaporation is more prominent in the sensors located near the heater. The sensors of in situ test do not show the effect of the evaporation. The dimensionless water content increase fast, reaching a quasi-constant value. The initial slope for the mock up is larger than the slope of the in situ test. The increase of the water content for the in situ is slow. The dimensionless water content for larger times ($t_d \sim 0.1$) for the in situ test is larger than that of the mock up data.

7.6. Analysis of water content in terms of t/r^2

In this chapter is analyzed the dependence of the water content to the factor time dividing by the squared distance (t/r^2), where t is the time and r is the radial distance. Figure 62 shows the water content versus the factor t/r^2 for the sensors A4 and A6 for the mock up test. The water content curve is similar for the same radial distance. Figure 63 shows the water content versus the factor t/r^2 for the sections M1 and M2 for the in situ test. The water content slope increases with the radial distance. Near the hydration boundary the water content is larger than that near the heater.

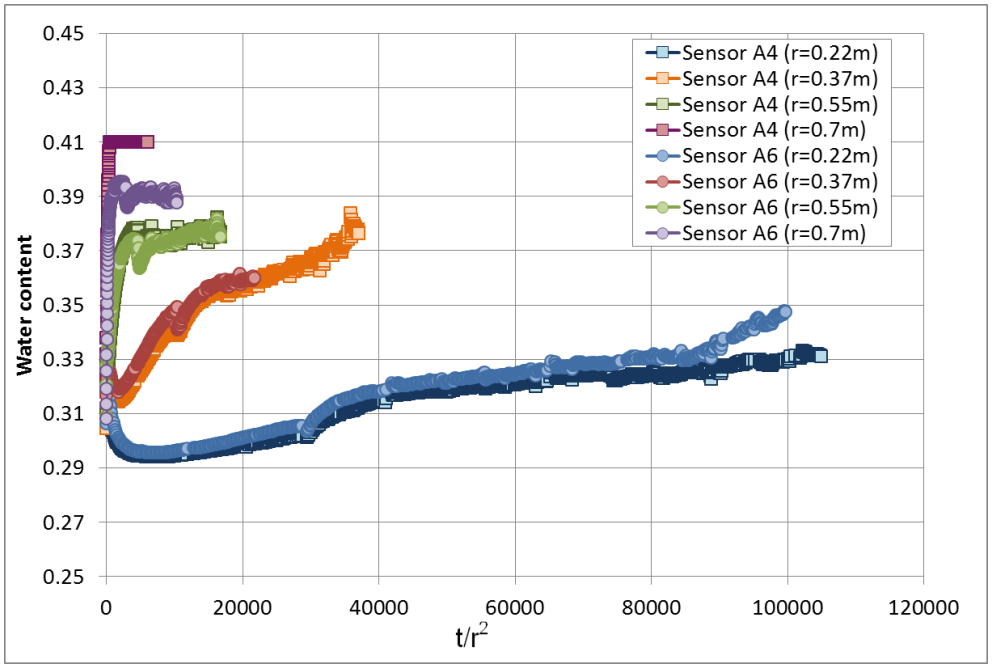

Figure 62. Water content data versus t/r^2 for the sensors A4 and A6 for the mock up test.

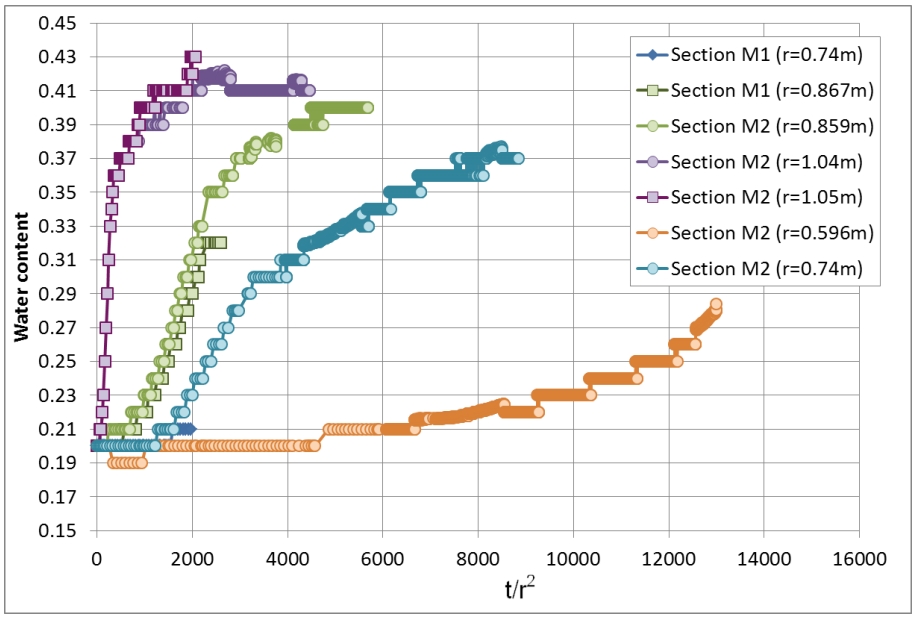

Figure 63. Water content data versus t/r^2 for the sections M1 and M2 for the in situ test.

The factor t_D/r_D^2 was calculated using the dimensionless time t_D, and the dimensionless distance r_D. Figure 64 shows dimensionless water content versus t_D/r_D^2 for the sensor located close to the hydration boundary for the mock up tests and in situ tests. Figure 65 shows the dimensionless water content for the sensor located near the heater for the mock up and in situ tests. Water content decreases at early times and then it increases similar for both cases.

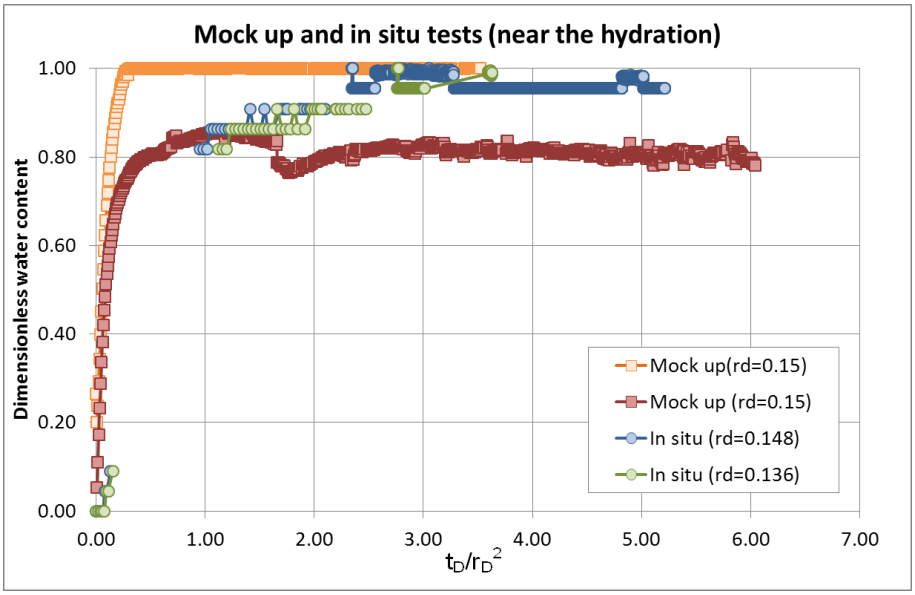

Figure 64. Dimensionless water content data versus t_D/r_D^2 from the sensors located near the hydration boundary for the mock up and in situ tests.

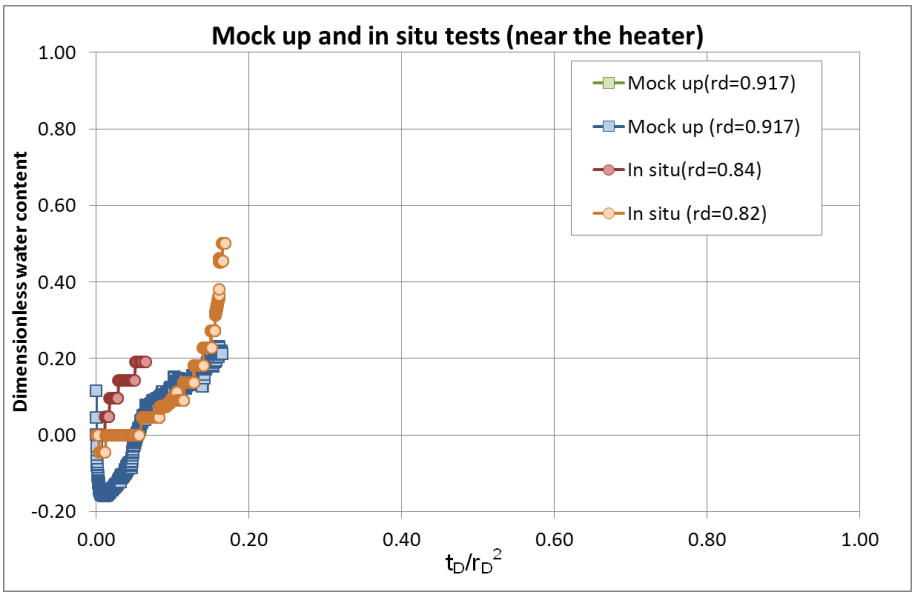

Figure 65. Dimensionless water content data versus t_D/r_D^2 from the sensors located near the heater for the mock up and in situ tests.

Figure 72 and Figure 73 shows the dimensionless water content for the dimensionless distances of 0.4 and 0.6 versus t_D/r_D^2 for the mock up and the in situ tests. The water content curves for the in situ test are larger than those of the mock up for the dimensionless distance of 0.4. For the dimensionless distance of 0.6 the water content curves have the same slope for the mock up ant in situ tests.

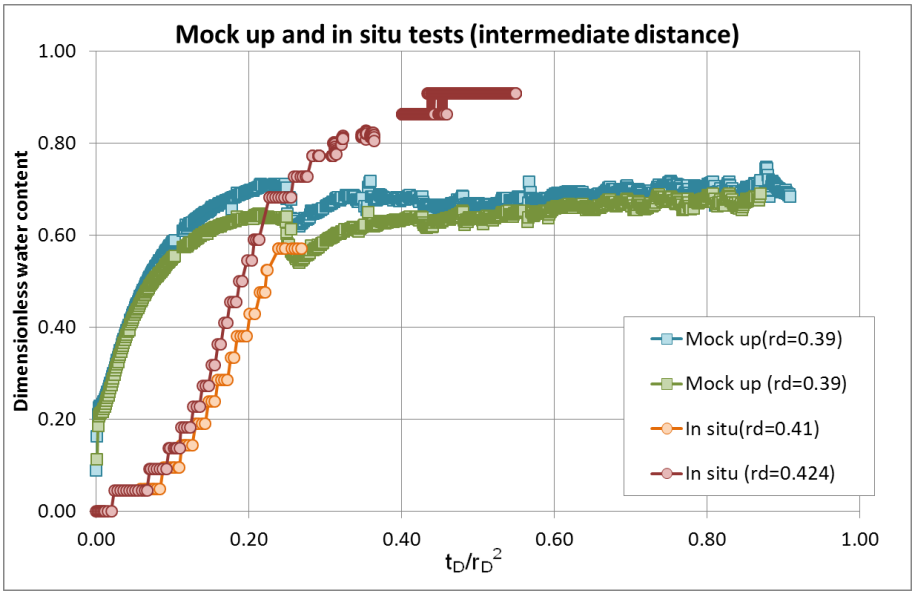

Figure 66. Dimensionless water content data versus t_D/r_D^2 from the sensors located in intermediate distances of 0.4 for the mock up and in situ tests.

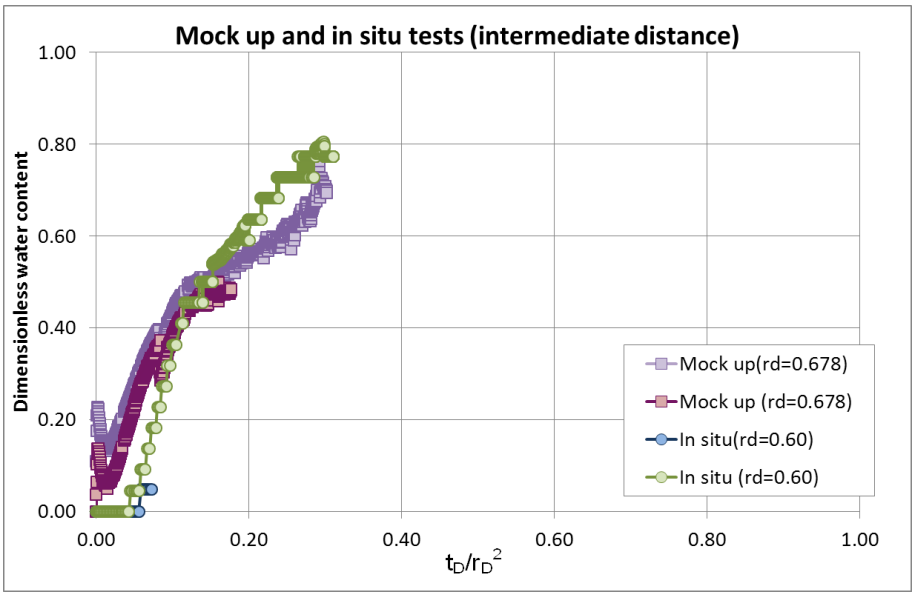

Figure 67. Dimensionless water content data versus t_D/r_D^2 from the sensors located in intermediate distance of 0.6 for the mock up and in situ tests.

7.7. Spatial distribution of the gravimetric water content at different times

Only the final distribution of gravimetric water content, *w*, is available for laboratory test. The spatial distribution of w at different times is analysed in this section. Figure 68 shows the dimensionless water content data of CT22, CT23 and CT24 cells. The profile of CT24 is nearly constant because this test was performed without hydration. The dimensionless water content increases with time as attested by comparing the data of cells CT23 (t_D = 0.015) and CT22 (t_D = 0.0021).

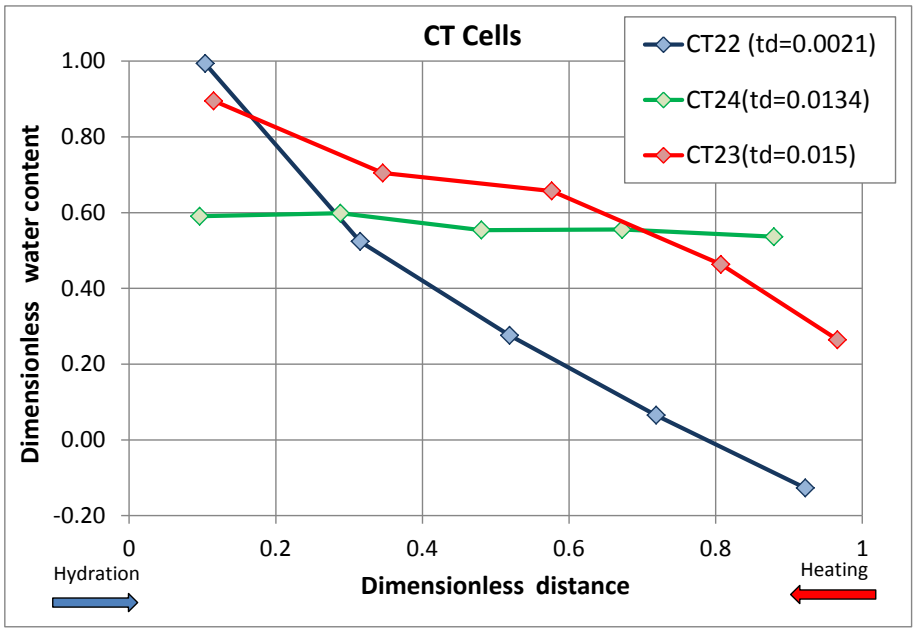

Figure 68. Dimensionless gravimetric water content versus dimensionless distance for CT cells.

Figure 69 shows the spatial distribution of dimensionless gravimetric water content for CG cells. Dimensionless water content increases from the shortest test (FQ1/2) to the largest one (CG3). CG3 test has the largest water content data because this test lasted 14 times more than the shortest one. The dimensionless water content is negative near the heater because the water content decreases below the initial water content.

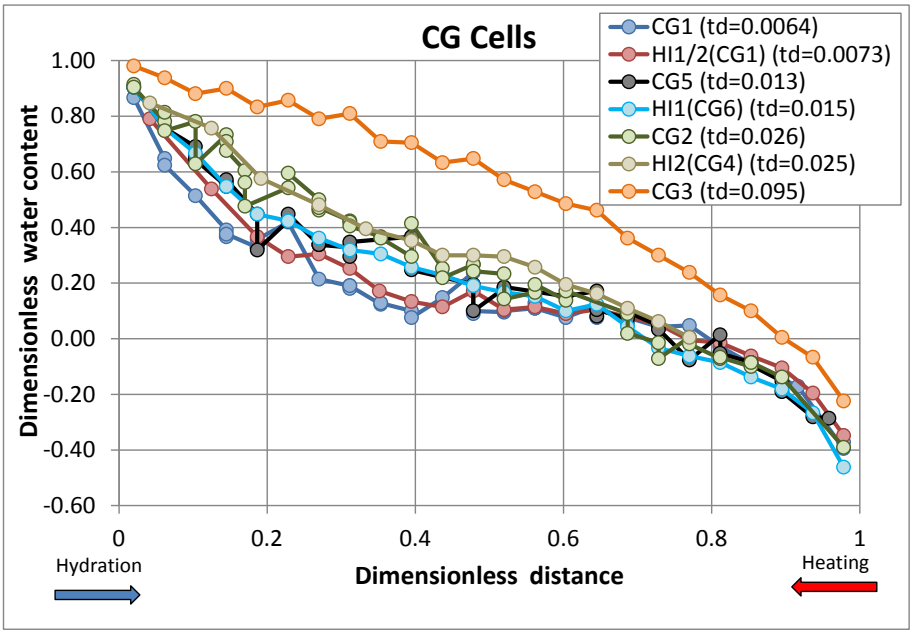

Figure 69. Dimensionless gravimetric water content versus dimensionless distance for CG cell.

Figure 70 shows the dimensionless gravimetric water content data for several times and the data from the post-mortem analysis of heater 1 for in situ test. The data of the sections 19 and 29 for a dimensionless time of 0.05 are larger than the data measured in the sensors. The data measured in the sensors increases with time. Figure 71 shows the spatial distribution of the dimensionless water content of the mock up test. The dimensionless water content is taken from the sensors in the section A6. The dimensionless water content is similar for all the sensors and shows a small increase with dimensionless time.

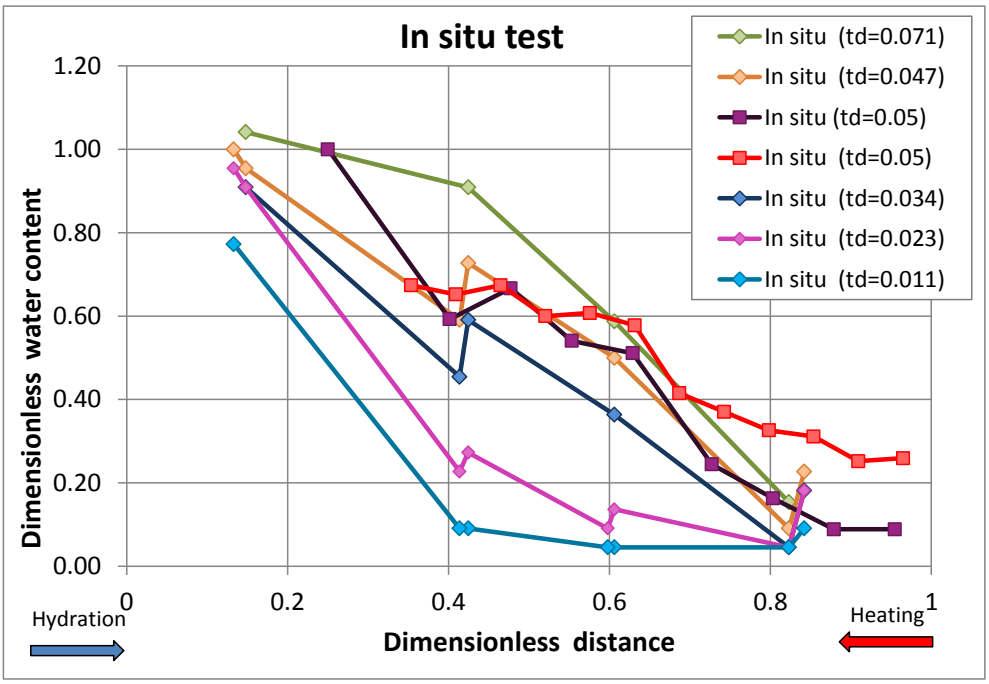

Figure 70. Dimensionless water content versus dimensionless distance for the in situ test for several dimensionless times corresponding to the dismantling of heater 1 (t_D =0.05) and TDR data at severals times.

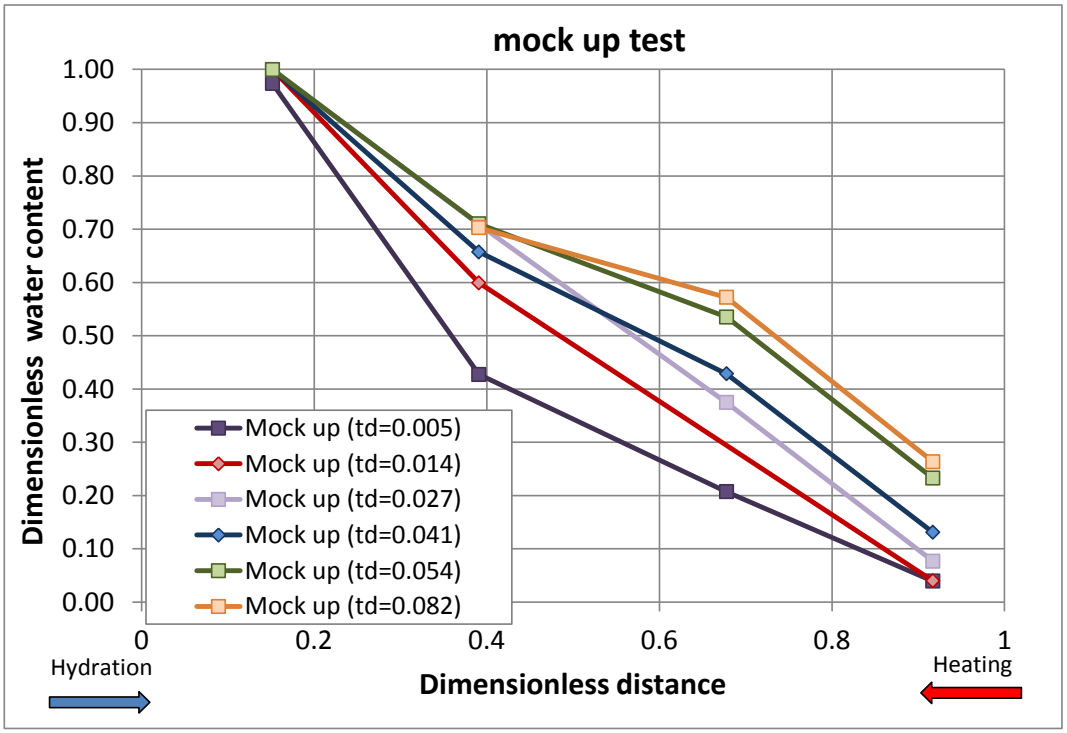

Figure 71. Dimensionless gravimetric water content versus dimensionless distance for the mock up test for several dimensionless times.

7.8. Dimensionless analysis of the spatial distribution of the water content

7.8.1 Dimensionless analysis of water content for CT and CG cells

Figure 72 shows the dimensionless water content versus the dimensionless distance for the laboratory cells for several dimensionless times. The average water content of the CG cells having the same duration (CG0.5, CG1, CG2 and CG7.5) has been plotted. The general behaviour of the dimensionless water content for CT and CG cells is similar. The dimensionless water content of CT22 cell for a dimensionless time of 0.0013 shows a steeper profile than the shortest CG test (CG1, t_D = 0.0064).

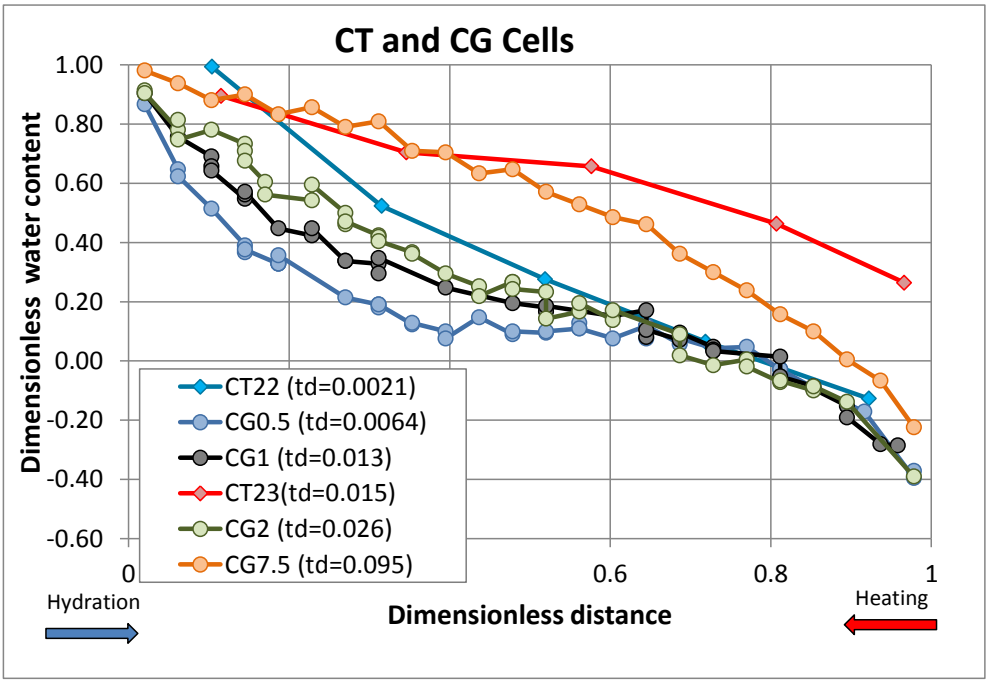

Figure 72. Dimensionless water content versus dimensionless distance for the CT and CG cells for several dimensionless times.

7.8.2 Dimensionless analysis of water content of the mock up and in situ tests

Figure 73 shows the dimensionless water content for a dimensionless time of 0.05 for the mock up and in situ tests. The slope of the dimensionless water content for the in situ test is larger. The water content in the in situ test decreases more than the data from the mock up test with the dimensionless distance. Figure 74 shows the dimensionless water content for a dimensionless time of 0.08 for the mock up and in situ tests. Figure 75 shows the

dimensionless water content for dimensionless times ranging 0.011 to 0.034 for the mock up and in situ tests. In general the dimensionless water content in the mock up test is larger than that of the in situ test. The decrease of the dimensionless water content with dimensionless distance for the in situ test is larger than that for the mock up test.

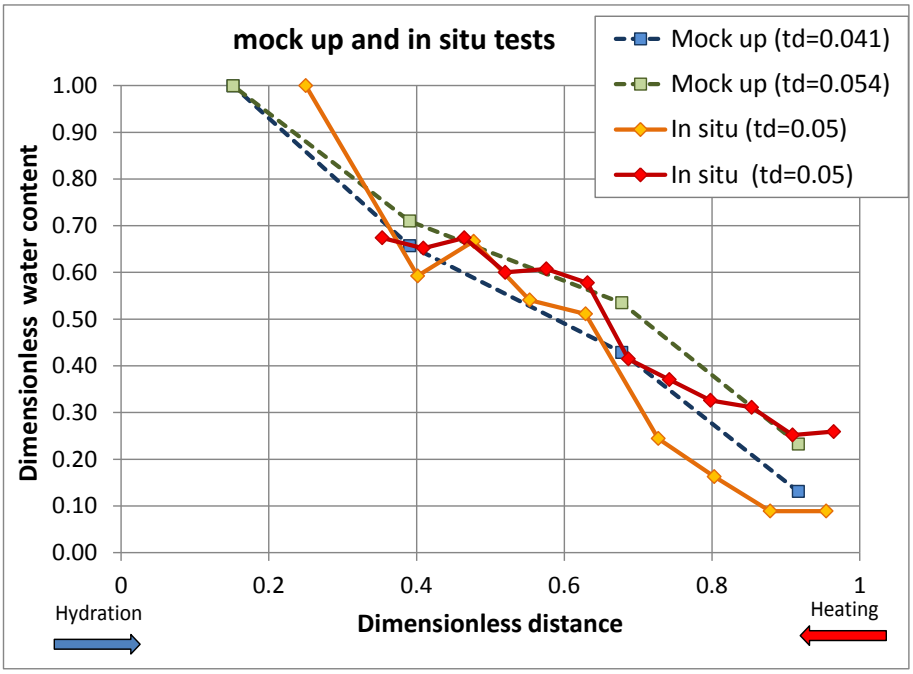

Figure 73. Dimensionless water content versus dimensionless distance for the mock up and in situ tests for a dimensionless time of about 0.05.

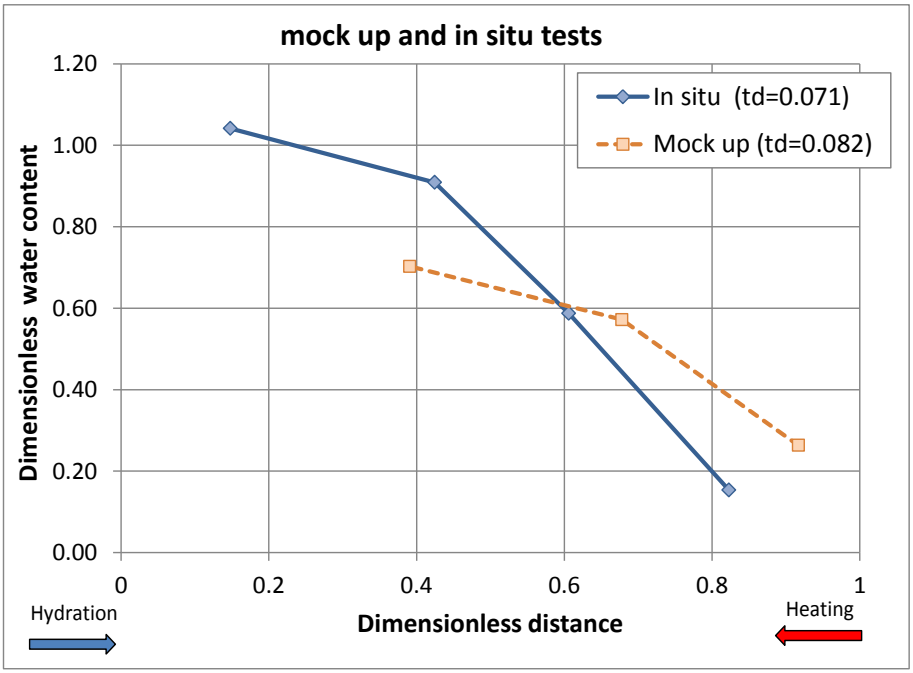

Figure 74. Dimensionless water content versus dimensionless distance for the mock up and in situ tests for a dimensionless time of about 0.08.

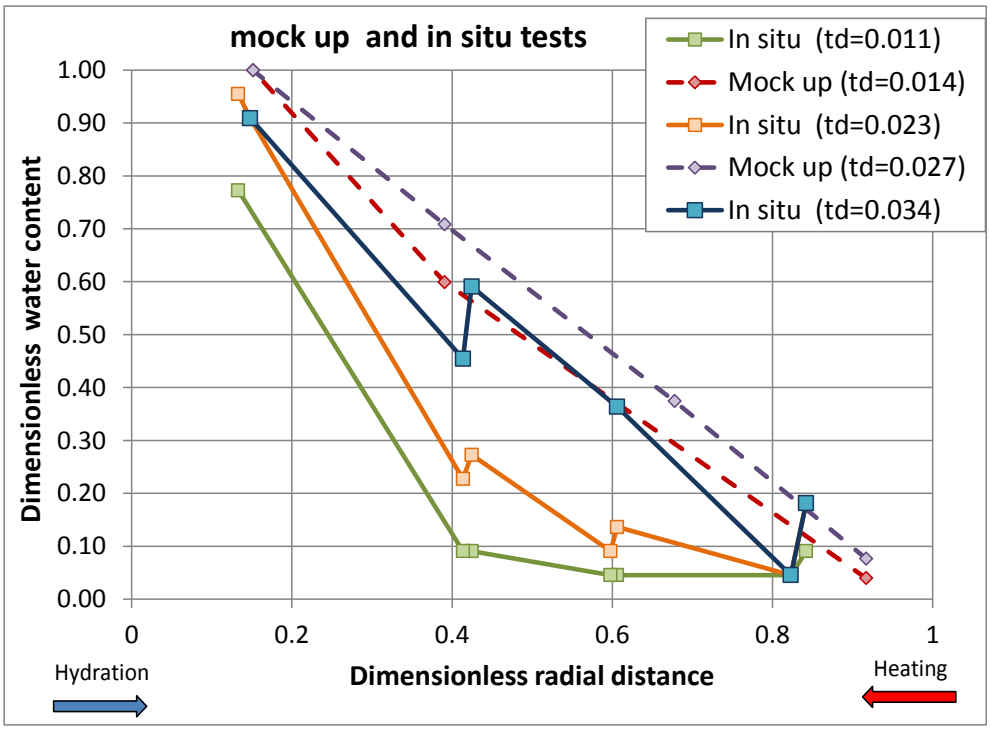

Figure 75. Dimensionless water content versus dimensionless distance for the mock up and in situ tests for dimensionless times ranging 0.01 to 0.034.

7.8.3 Dimensionless analysis of water content for CT and CG cells, mock up and in situ tests.

Figure 76 shows the dimensionless water content for the lab cells, and the mock up and in situ tests for dimensionless times ranging from 0.0064 to 0.015. The dimensionless water content for the CG cells is larger than those of the rest of the test. Data from CT cells cannot be compared with those of the other tests. Their trends do not correspond with those of other tests. Figure 77 shows the dimensionless water content versus dimensionless distance for dimensionless time of about 0.025. CG cells test registered the lowest water content data near the heater due to the evaporation. The dimensionless water content curves for the CG cells and the in situ for the dimensionless time of about 0.025 have the same slope.

Figure 78 shows the dimensionless water content for the mock up and the in situ test for dimensionless times ranging from 0.041 to 0.05. The average slope of the dimensionless water content is the same for both tests.

Figure 79 shows the dimensionless water content for the lab cells, and the mock up and in situ tests for dimensionless times ranging from 0.071 to 0.095. The dimensionless water content data are similar in all of them for large dimensionless times.

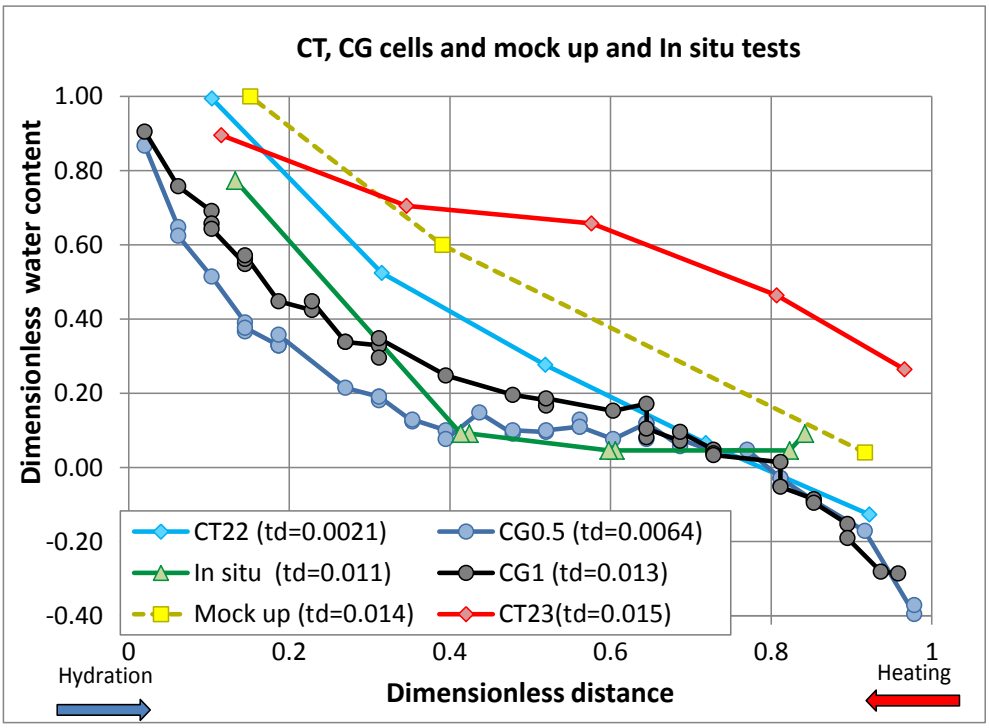

Figure 76. Dimensionless water content versus dimensionless distance for the CT and CG cells and the mock up and in situ lab tests for dimensionless times ranging from 0.0064 to 0.015.

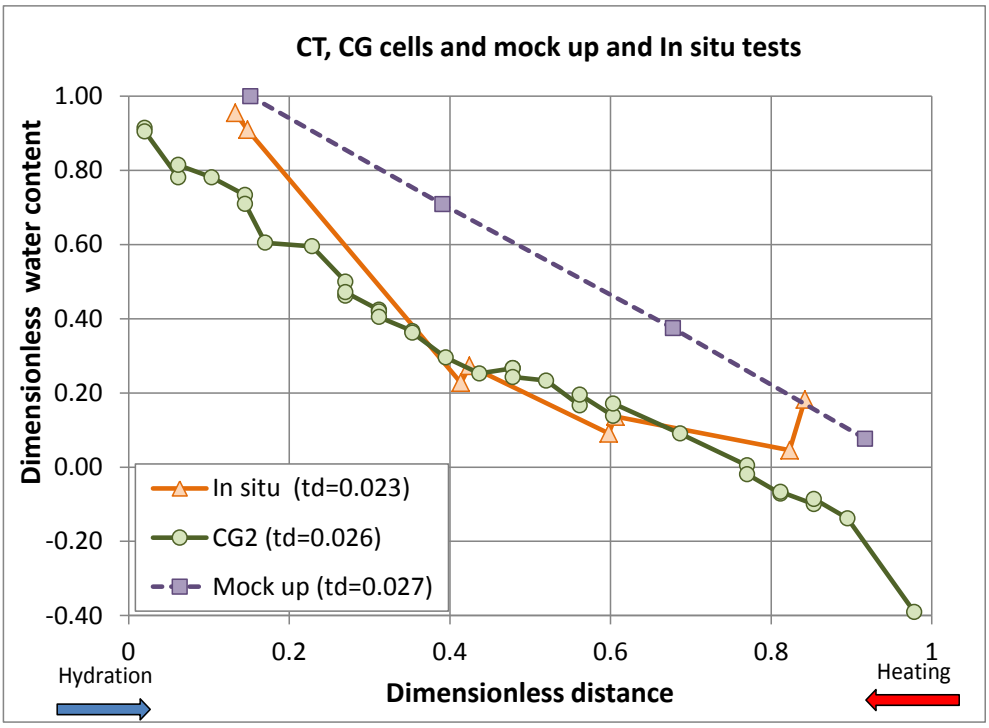

Figure 77. Dimensionless water content versus dimensionless distance for the CT and CG cells and the mock up and in situ lab tests for a dimensionless time of about 0.025.

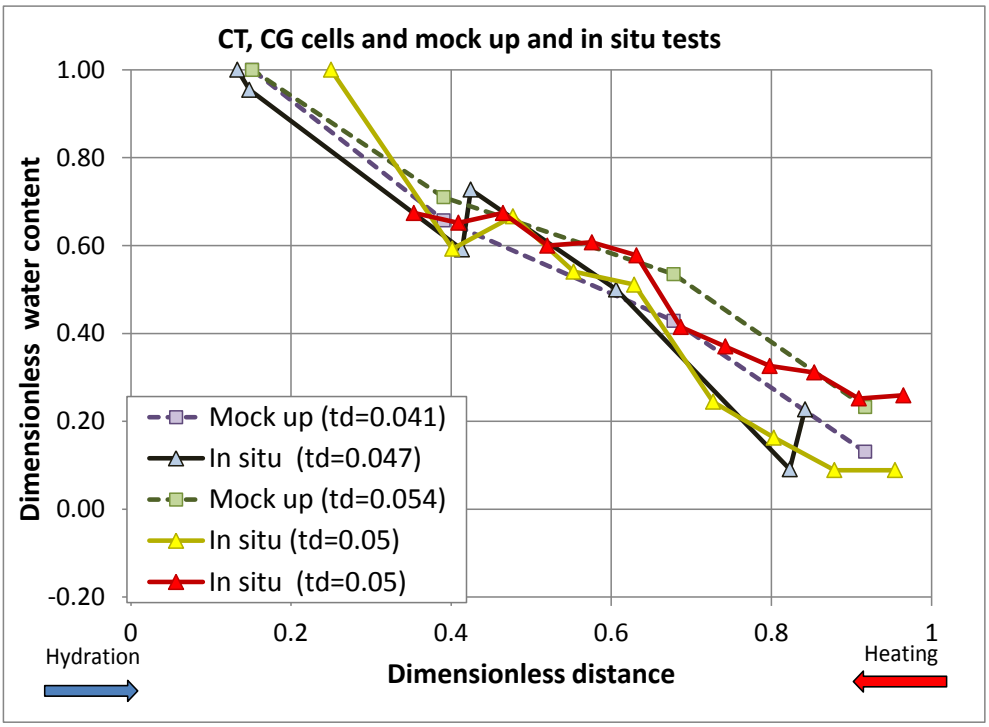

Figure 78. Dimensionless water content versus dimensionless distance for the CT and CG cells and the mock up and in situ lab tests for dimensionless times ranging from 0.041 to 0.05.

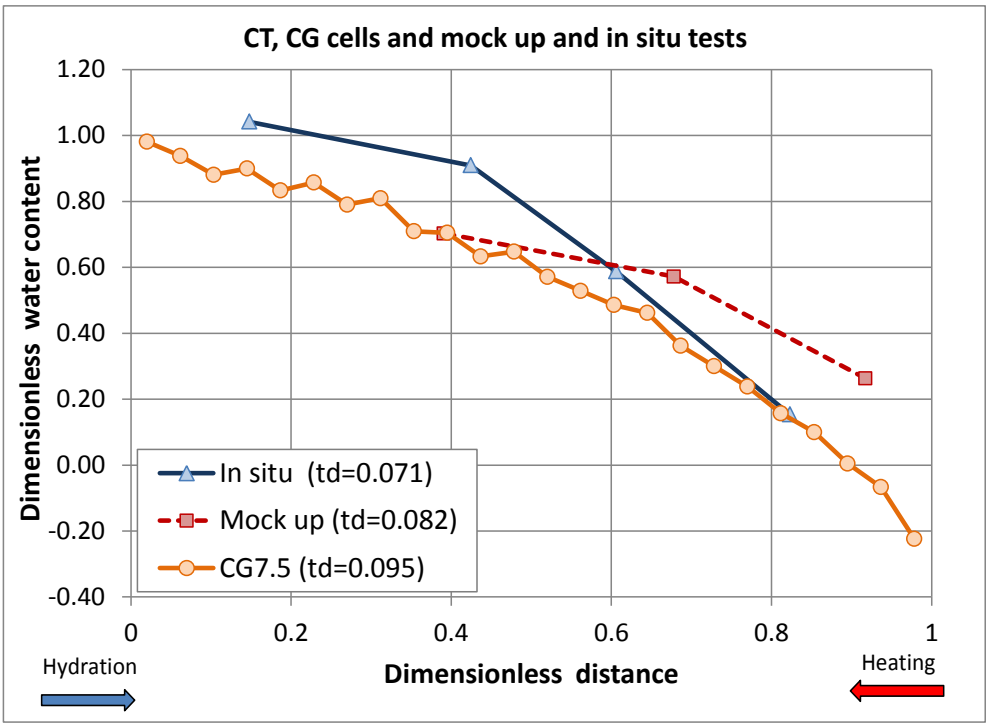

Figure 79. Dimensionless water content versus dimensionless distance for the the CT and CG cells and mock up and in situ lab tests for dimensionless times ranging from 0.071 to 0.095.

7.9. Integrated analysis of computed water content

The computed volumetric water content has been obtained from the models performed with INVERSFADES2 (Zheng and Samper, 2008; Samper et al., 2008) for the CT23 cell, mock up and the in situ tests.

Figure 80 shows the numerical results for the dimensionless water content versus dimensionless time for CT23, the mock up and the in situ tests for a dimensionless distance of 0.04. The computed dimensionless water content are almost equal in all cases. The in situ test needs more time to reach saturation. Figure 81 shows the time evolution of the dimensionless water content for CT23, the mock up and the in situ test for the dimensionless distance of 0.95. The dimensional water content presents a decrease due to the evaporation. Dimensionless water content is largest for the CT23 cells for $t_D > 0.0025$.

Figure 83 shows the time evolution of the dimensionless water content data for a dimensionless distance of 0.3 for CT23 cell, the mock up and the in situ tests. The rate of the increase of water content data is slow for the mock up test. Figure 82 shows the computed dimensionless water contents for dimensionless distance of 0.6.

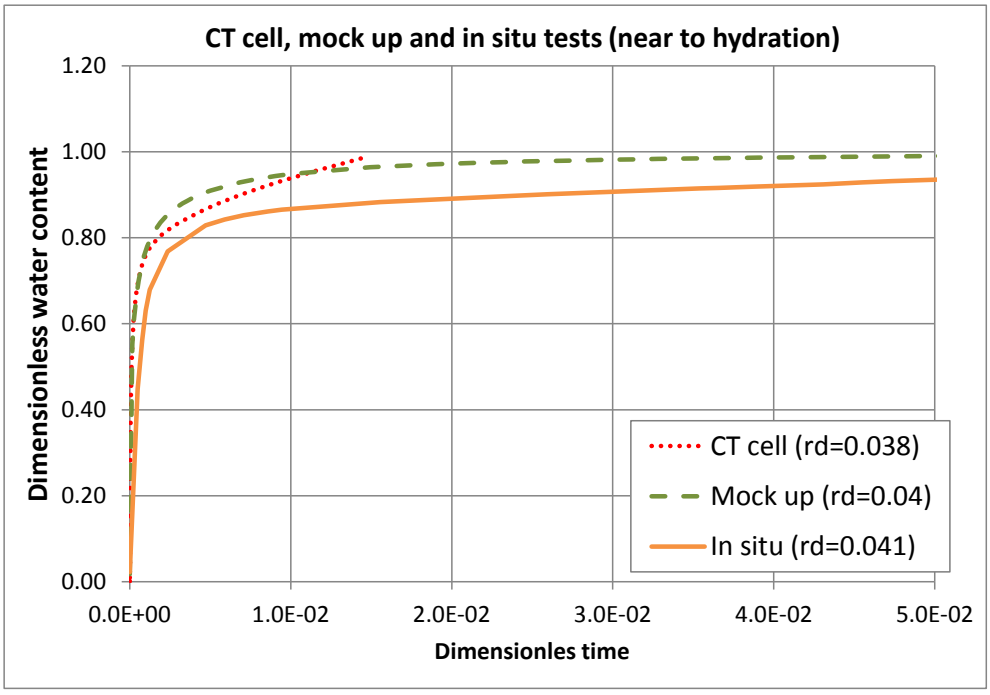

Figure 80. Computed dimensionless water content versus dimensionless time for a dimesionless distance of about 0.04 which corresponds to a point close to the hydration boundary for CT cell, and mock up and in situ tests.

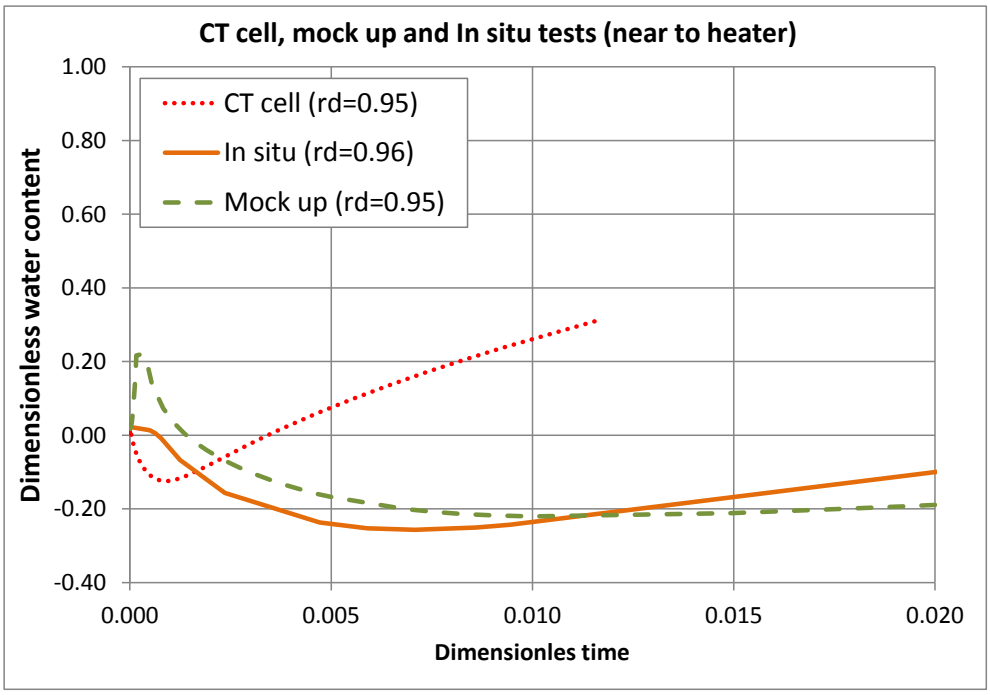

Figure 81. Computed dimensionless water content versus dimensionless time for a dimesionless distance of about 0.95 which corresponds to a point close to the hydration boundary for CT cell, and mock up and in situ tests.

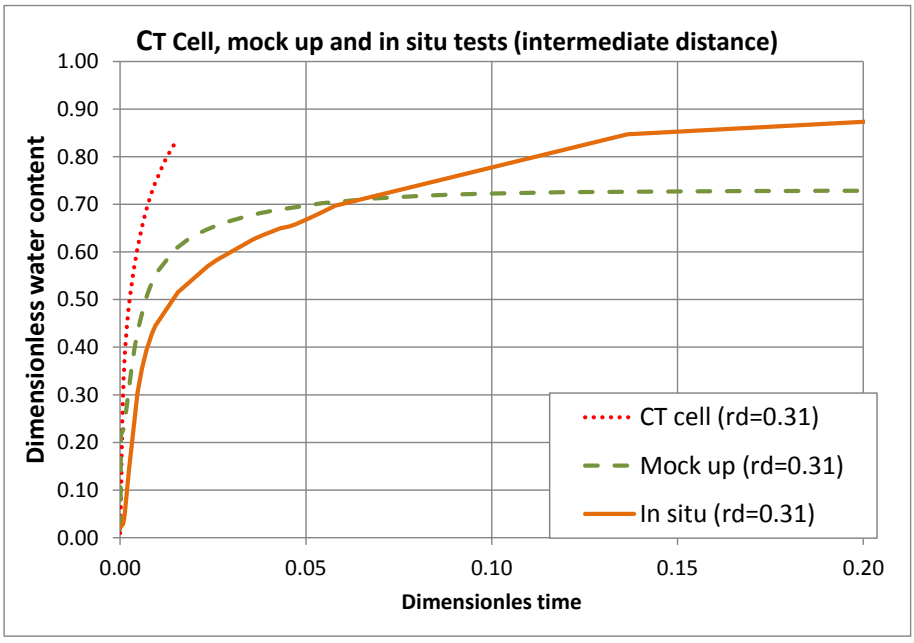

Figure 82. Computed dimensionless water content versus dimensionless time for a dimesionless distance of about 0.31 which corresponds to a point close to the hydration boundary for CT cell, and the mock up and in situ tests.

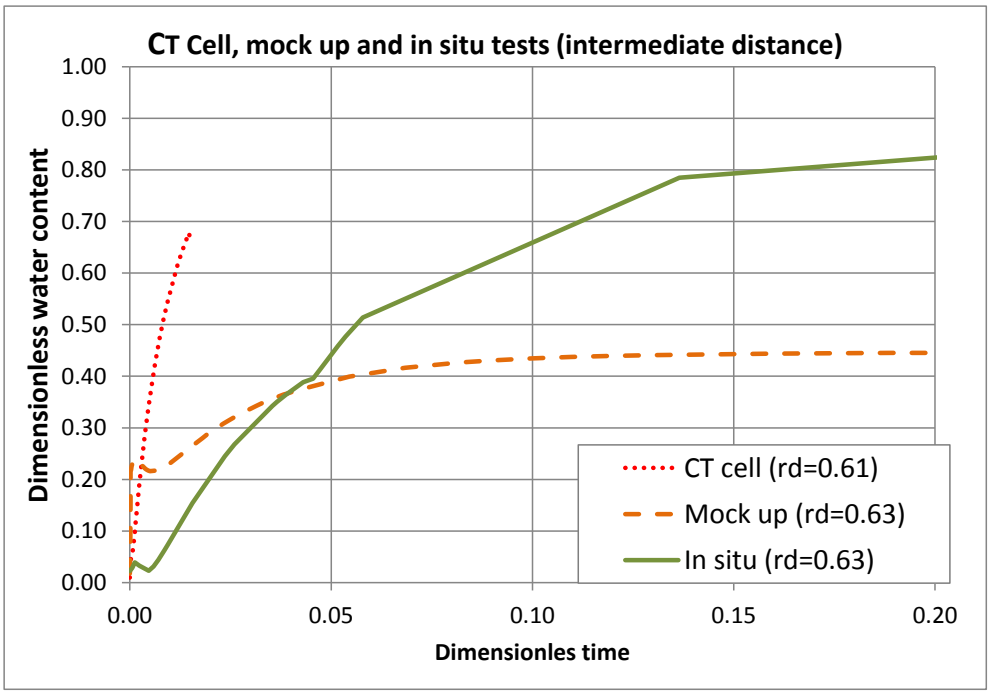

Figure 83. Computed dimensionless water content versus dimensionless time for a dimesionless distance of about 0.31 which corresponds to a point close to the hydration boundary for CT cell, and the mock up and in situ tests.

7.10. Conclusions

The main conclusions of the integrated analyses of water content data include:

1) Water content data for the small CT cell are much smaller than the water content data from other tests. Water content data for the mock up test are the largest for all the tests for dimensionless times smaller than 0.04. For large times (>0.04), the general slope of the water content data are similar for the CG cell, and mock up and in situ tests.

2) Possible reasons for the differences in water content data among the tests include:

   - The initial flooding of the mock up test. The joins and gaps of the barrier of the mock up test were flooded at the beginning of the test. This explains why the water content data for the mock up test are the largest for all the tests small dimensionless times.

   - Geometric configuration of the flow. Water flow is radial in the mock and in situ tests while it is parallel for CT and CG cells.

- Thermal gradient. The temperatures at the boundaries are similar in most tests (100ºC near the heater and from 12 to 20 ºC at the hydration boundary). However, the thickness of the bentonite ranges from 10 cm (CT cells) to 75 cm in the in situ test. Water evaporates near the heater. Vapour diffuses away from the heater and condensates at some distance. This process retards the hydration of the bentonite buffer.
- The internal boundary condition at the heater-bentonite interface. The bentonite is directly in contact with the heater in the CT and CG cells as well as in the mock up test, while in the in situ test there is metallic liner which creates void gap between the heater and the bentonite.

8. Integrated analysis of temperature data

8.1. Introduction

This chapter presents the integrated analysis of temperature data. There are available temperature data at several sensors which provide temperature versus time at several distances. A dimensionless analysis of temperature versus distance has been made.

8.2. Available temperature data

Temperature data are available for, CT cells, CG cells, the mock up and in situ tests. Temperature data are available from thermocouples installed in the tests. The temperature data are expressed in ºC. Temperature data show oscillations due to changes in the external ambient temperature. Anomalous temperature data have been deleted. Table 10 shows the details of the tests, the thermal sensors we have used, the test duration, the distance from the heater, the dimensionless distance, and the average temperature, maximum and minimum temperature.

Table 10. Temperature data and parameters of the tests.

Test	Thermal sensor	Duration (d)	Characteristic time (d)	Average Temperature (ºC)	Maximum temperature (º)	Minimum temperature (ºC)
CT22	Ch10	26.06	$1.25 \cdot 10^4$	48.55	79.92	29.81
CT23	Ch10	181.31	$1.25 \cdot 10^4$	37.84	48.99	28.36
FQ1/2(CG1)		188.76	$2.93 \cdot 10^4$	28.64	54.47	20.51
HI1/2(CG1)		213.95	$2.93 \cdot 10^4$	28.08	54.39	16.61
FQ2(CG2)		762.70	$2.93 \cdot 10^4$	27.71	53.43	14.36
HI2(CG4)		748.82	$2.93 \cdot 10^4$	28.39	54.53	14.41
FQ1(CG5)		369.86	$2.93 \cdot 10^4$	30.37	52.63	16.66
HI1(CG6)		440.15	$2.93 \cdot 10^4$	30.00	41.89	18.40
Mock up	T_A5	5076	$3.66 \cdot 10^4$	58.75	93.02	22.42
Mock up	T_A2	5076	$3.66 \cdot 10^4$	51.09	82.63	23.11
Mock up	T_A8	5076	$3.66 \cdot 10^4$	48.23	79.57	21.26
In situ	TSG	4841	$4.24 \cdot 10^4$	41.33	103.86	12.51
In situ	TSD1	1938	$4.24 \cdot 10^4$	47.71	88.03	12.73
In situ	TSI	4841	$4.24 \cdot 10^4$	54.21	96.67	12.34
In situ	TSD2	4841	$4.24 \cdot 10^4$	51.88	99.39	12.734

8.2.1 Temperature data for CT cells

Figure 84 shows the time evolution of temperature in CT cells CT22 and CT23.

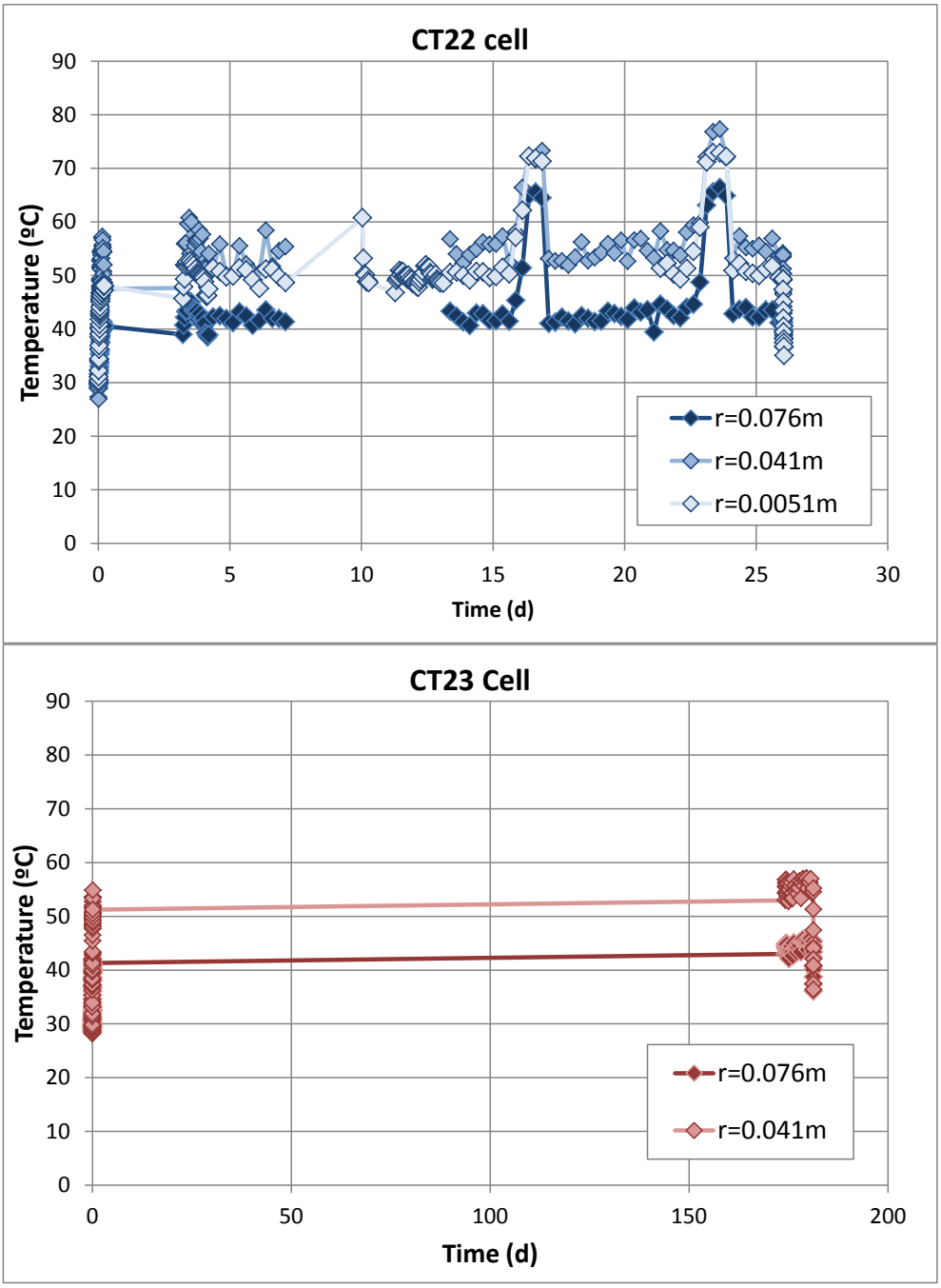

Figure 84. Time evolution of temperatures at CT cells at several distances.

8.2.2 Temperature data for CG cells

Figure 85 shows the time evolution of temperature data of CG cells measured at several thermocouples located at distances of 10, 20, 30, 40 and 50 cm from the heater.

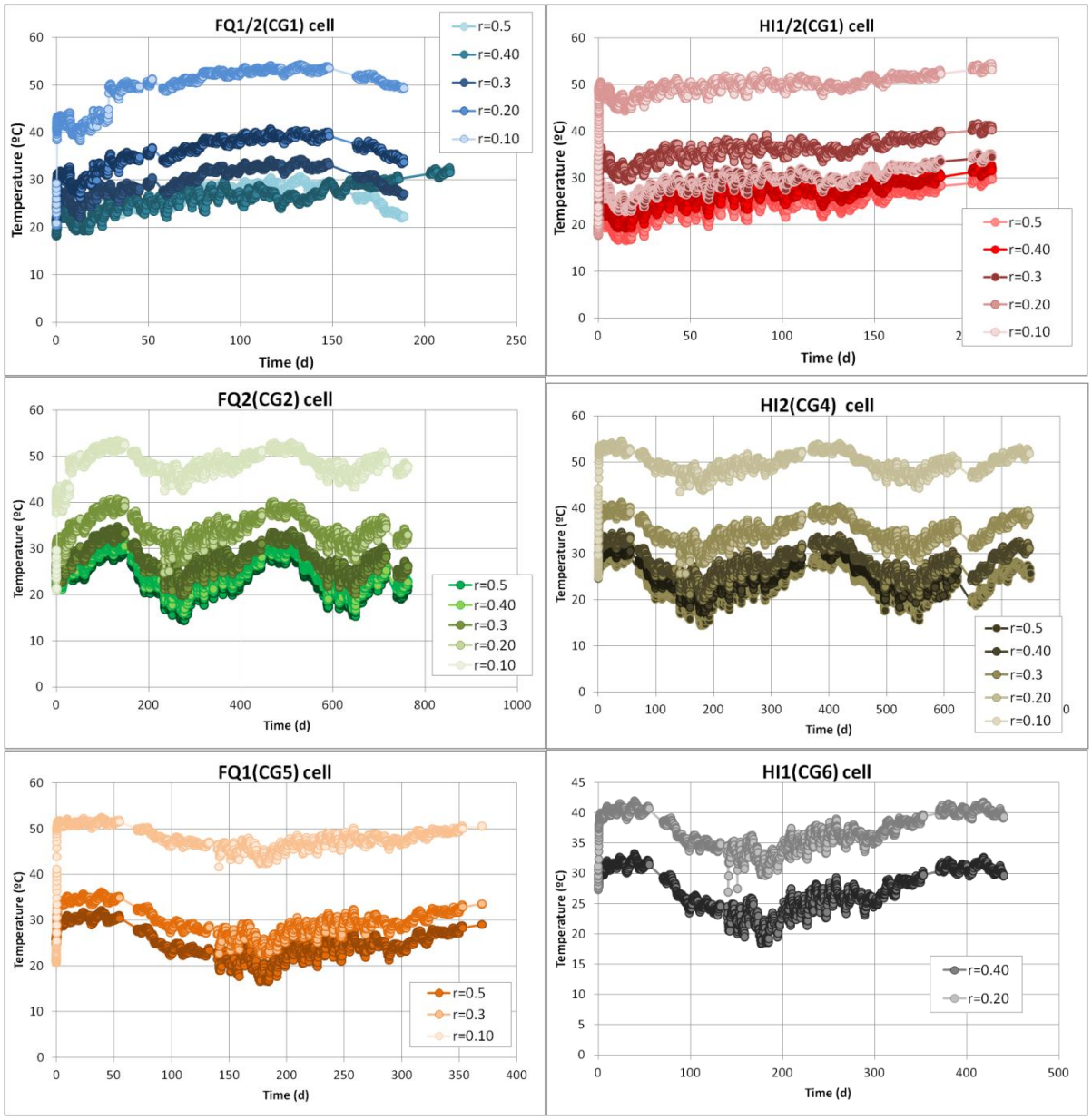

Figure 85. Time evolution of temperatures at the CG cells at several distances.

8.2.3 Temperature data for the mock up test

Figure 86 shows the time evolution of temperature data at the mock up test, at four radial distances. It can seen that the temperature oscillations are smaller than those of other

tests shown above. Sensors A2 and A8 are located in the ends of the heater, and the sensor A5 is located in the central section, where the temperatures are slightly higher than the temperature in the other sensors.

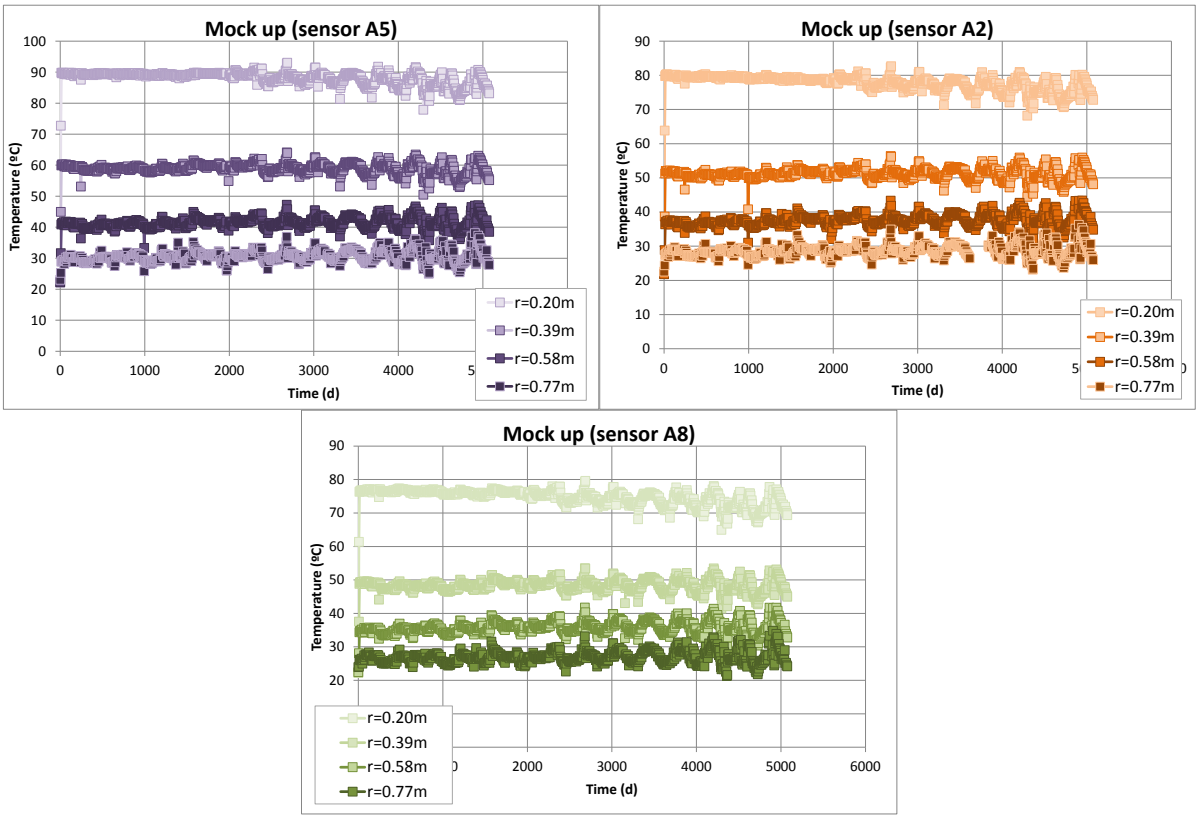

Figure 86.Time evolution of temperatures in the sensors A5, A2 and A8 of the mock up test.

8.2.4 Temperature data for the in situ test

Figure 87 shows the temperature data measured during 5000 days in the situ test. The behaviour is different from others test. The temperature was almost constant during 2000 days, then the heater 1 was switched off and the temperature decreased. Temperature data from sensors located on heater 2 are almost constant.

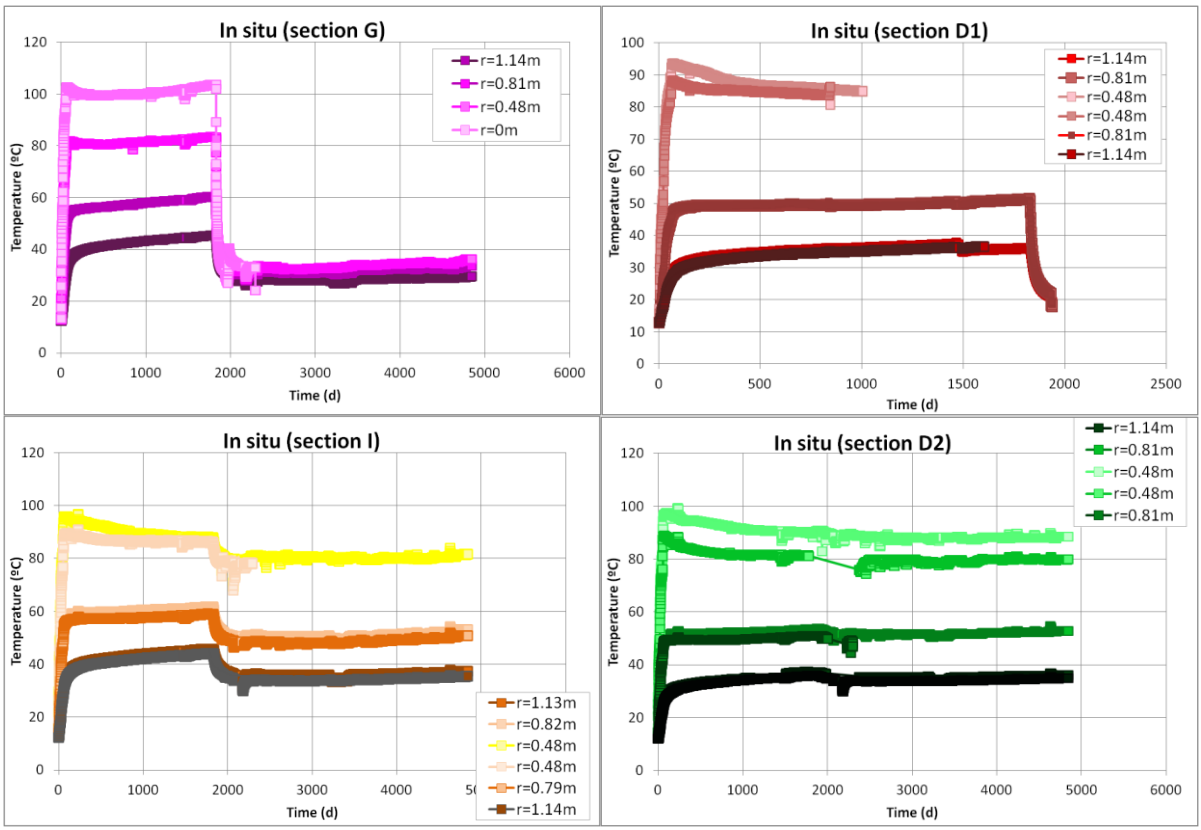

Figure 87. Time evolution of temperatures for sensors of sections G and D1 of heater 1 and sensors of section I and D2 of heater 2 of the in situ test.

8.3. Analysis of the spatial distribution of temperature data

Temperatures reach steady values quickly. Therefore, their spatial distribution has been studied in terms of dimensionless distance which is calculated by dividing the distance from the hydration boundary divided by the bentonite thickness.

Figure 88 shows the average temperature data versus the dimensionless distance for CT cells. Temperature data are shown as the average temperature and the error bars which are equal to standard deviation.

Figure 89 shows the average temperatures and theirs deviations for the CG cells. It can be seen that temperatures of the CG cells are similar.

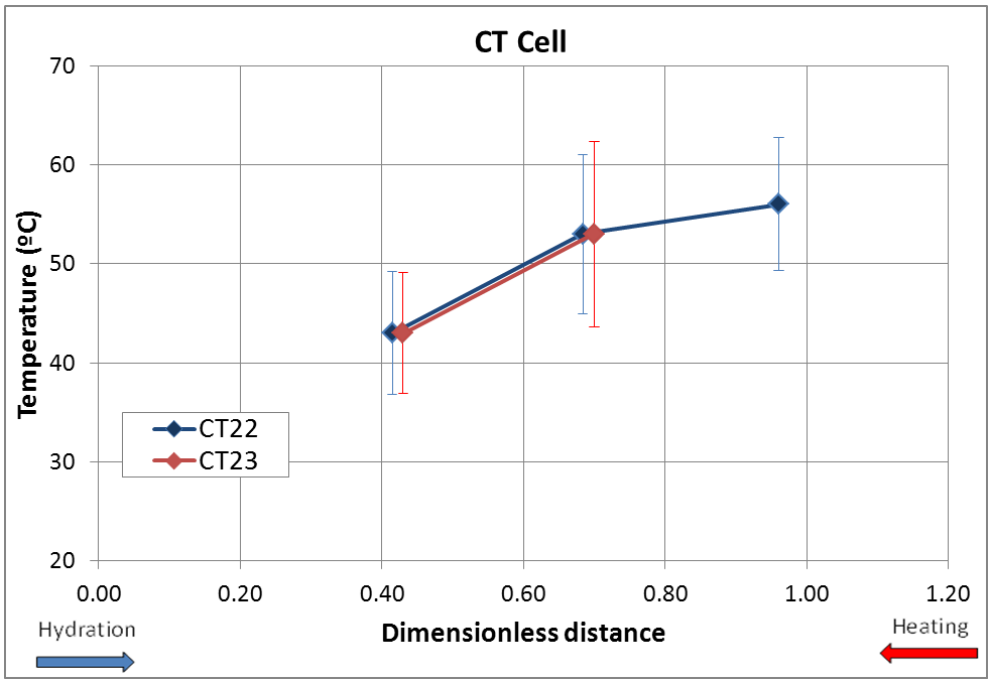

Figure 88. Average temperature versus distance for CT cells. Line bars indicate the range of temperature fluctuations.

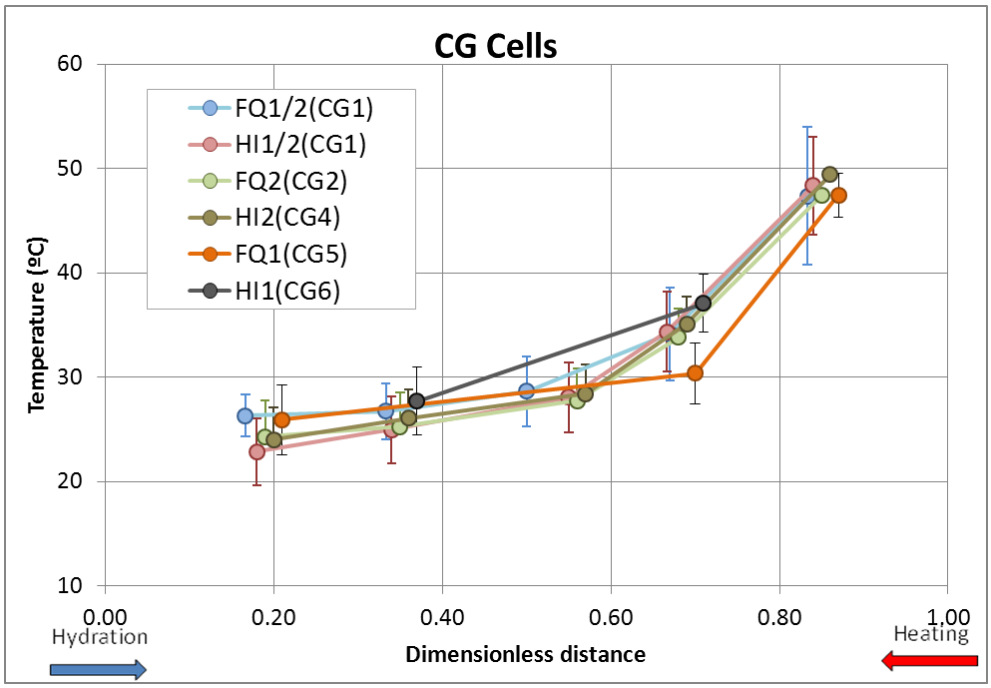

Figure 89. Average temperature versus distance for CG cells. Line bars indicate the range of temperature fluctuations.

Figure 90 shows the average temperatures for the mock up test. The largest temperatures were monitored in sensor A5 located in the centre of the heater. Figure 91 shows

the averages temperatures and errors bars for the section D2 and I, of the heater 2 of the in situ test.

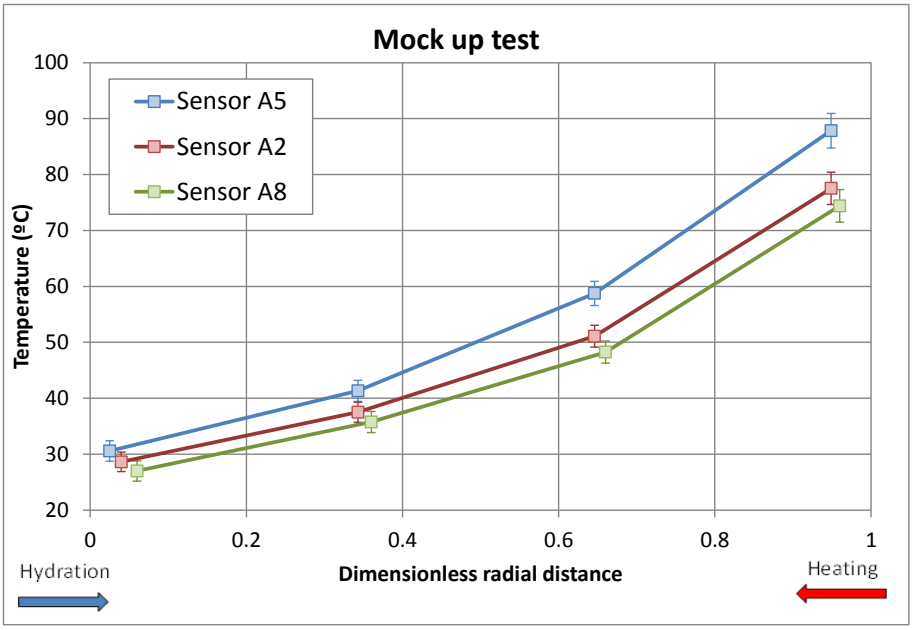

Figure 90. Average temperature versus distance for the mock up test. Line bars indicate the range of the temperature fluctuations.

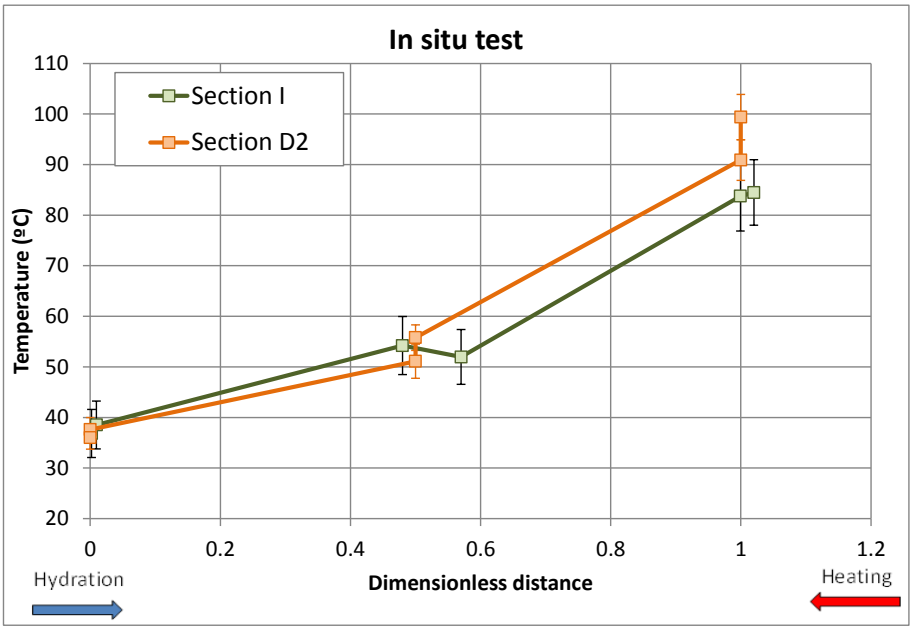

Figure 91. Average temperature versus distance for the in situ test. Line bars indicate the range of the temperature fluctuations.

8.4. Integrated analysis of the spatial distribution of temperature data

Figure 92 shows the average temperatures for CT and CG cells. The temperature is largest near the heater and lowest near the hydration boundary. The temperatures of the CT cells are larger than those of CG cells.

Figure 93 shows the average temperatures for the mock up and in situ tests. The distribution of temperatures is similar in both tests.

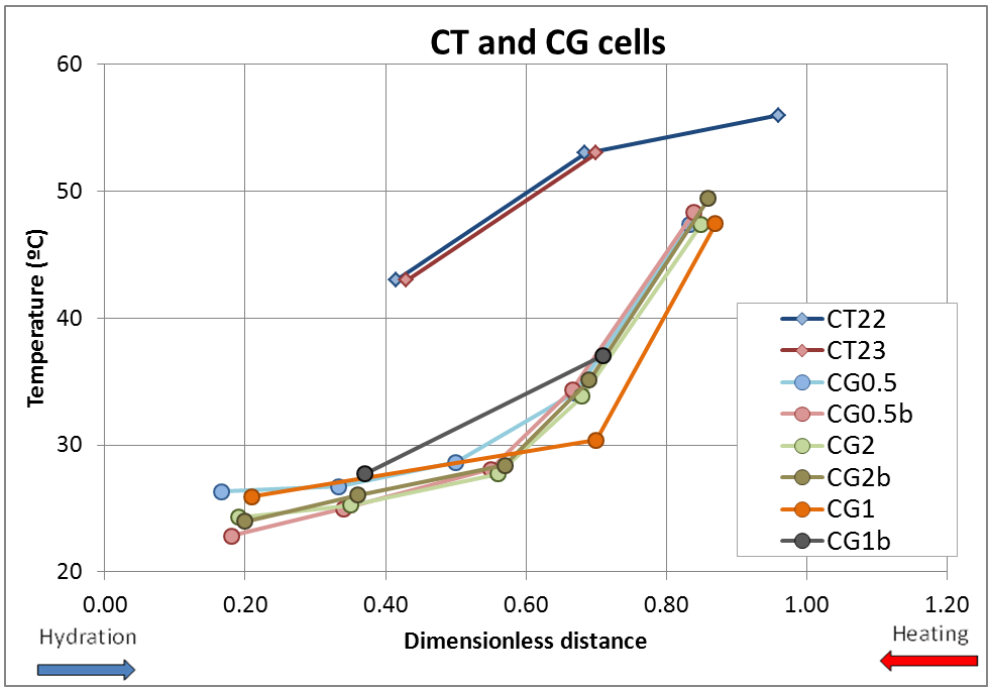

Figure 92. Average temperature versus dimensionless distance for CT and CG cells.

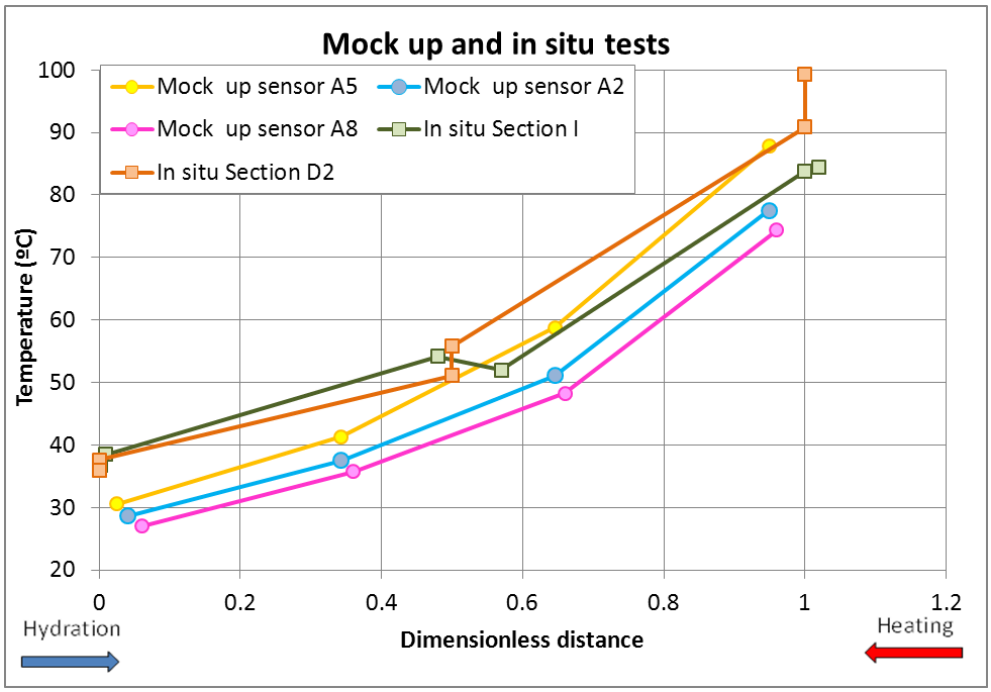

Figure 93. Average temperature versus dimensionless distances for the mock up and in situ tests.

Figure 94 shows the comparison of the average temperature versus the dimensionless distance for CT and CG cells, the mock up and the in situ tests. There are two cells with the same duration for CG cells. The average temperature of the two cells has been plotted in Figure 94. Section D2 and I which are located in heater 2 are selected for the in situ test. For dimensionless distances between 0 and 0.6 the slope of the temperature curve is similar for most tests. This slope is approximately equal to (20/0.6) ºC. For dimensionless distances between 0.6 and 1 (near the heater) the slope is (30/0.4) ºC.

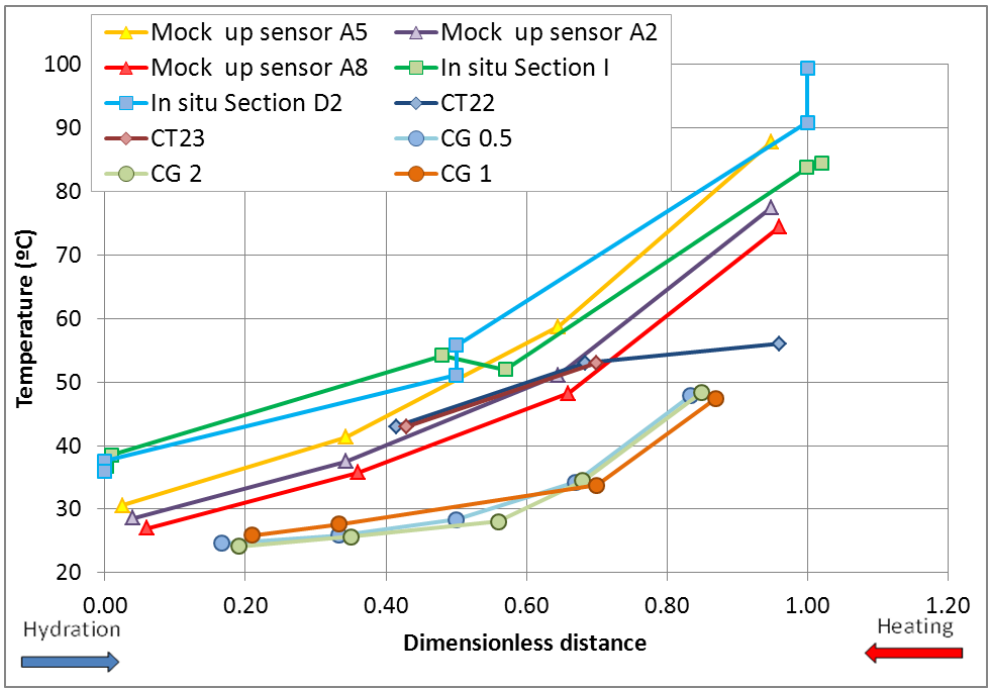

Figure 94. Average temperature versus dimensionless distance for CT and CG cells and the mock up and in situ tests.

8.5. Dimensionless analysis of the spatial distribution of temperature data

Tests have different thermal and hydration conditions. Therefore, their integrated analysis requires the definition of dimensionless temperatures. For a given experiment, the temperature ranges from the value at the hydration boundary, T_b, to the temperature at the heater side, T_h. The expected range of temperatures is therefore equal to (T_h-Tb). Dimensionless temperatures T_D are calculated by means of:

$$T_d = \frac{T - T_b}{T_h - T_b}$$

In this way, the dimensionless temperature T_D is equal to 1 at the heater and zero at the hydration boundary. T_b is equal to the temperature of the hydration water for CT and CG cells and the mock up test. For the in situ test, however, T_b is equal to the mean temperature of the granitic rock sufficiently far from the FEBEX gallery which is about 12 º C.

Figure 95 shows the dimensionless temperature for the dimensionless distance for CT and CG cells, mock up and in situ tests. The average slope of the increase of temperature data to the heater zone is more or less 0.7 approximately.

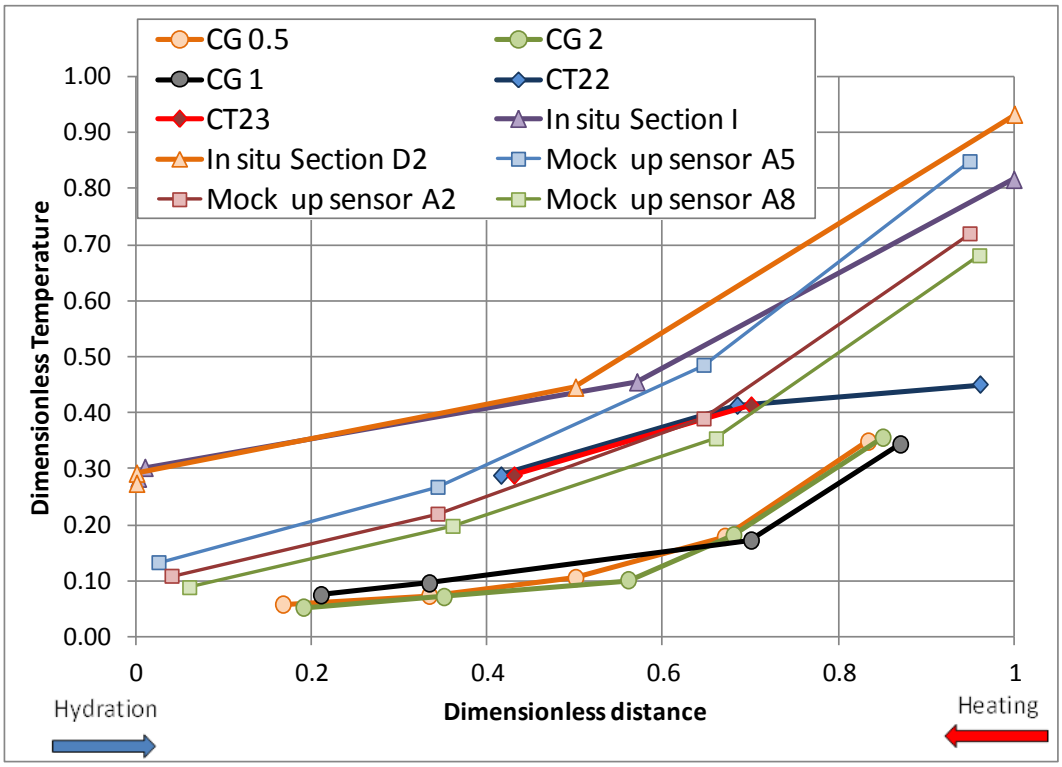

Figure 95. Dimensionless temperature for dimensionless distance for CT and CG cells and mock up and in situ test.

8.6. Spatial distribution of computed temperatures

Numerical models of the CT 23 cell (Zheng et al., 2010), the mock up test (Zheng and Samper, 2008) and the in situ test (Zheng et al., 2011) have been made with INVERSFADES2 (Zheng, Samper, 2005). The models consider the initial and boundary conditions, the parameters and the specific pressure and flow condition for each test. Figure 96 shows the dimensionless temperatures versus the dimensionless distance. The slope of the temperature increase to the heater is equal to 0.7 more or less. The dimensionless temperature curve of the in situ test is larger than that of CT23 cell and the mock up test because the heat conduction into the rock. The dimensionless temperature curve for CT23 cell is larger than that of the mock up test due to the porous stone conducts some heat. The temperature curves are different due to the differences in thermal, hydration and boundary conditions.

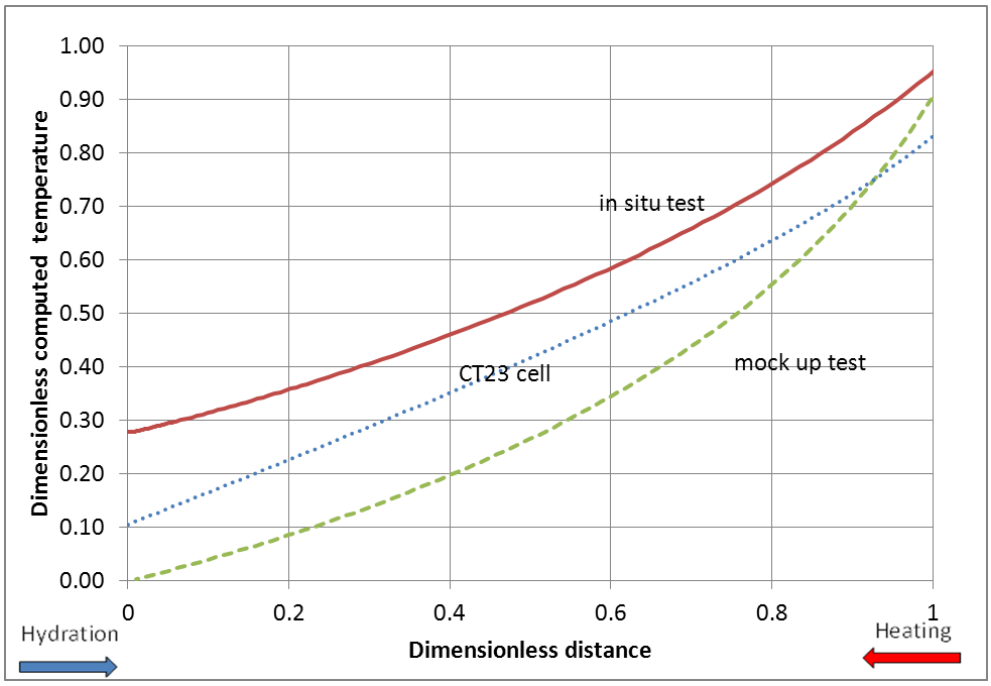

Figure 96. Computed dimensionless temperatures for CT23 cell (Zheng, et al.2010), the mock up test (Zheng and Samper, 2008) and the in situ test (Zheng et al 2011).

8.7. Conclusions

Temperatures reach quasi steady values quickly. Therefore, the analysis has been concentrated in its spatial distribution along the bentonite buffer. The temperature decreases from the heater to the hydration boundary. The curves of temperature versus distance from the heater shows two mains parts: 1) Near the heater, where the thermal gradient is large and 2) Near the hydration boundary where the gradient is smaller. Dimensionless measured temperature profiles show a slope of 0.7 which is similar for all the tests. This slope is similar to that of the computed temperatures.

9. Integrated analysis of chemical data

9.1. Introduction

This chapter presents the integrated analysis of chemical data from CT and CG cells and the in situ test. The dimensionless analysis is performed first on the concentration of chloride Cl^- of aqueous extracts. Then, the inferred Cl^-concentration data are analysed.

9.2. Available chemical data

9.2.1 Compilation of data and experimental methods

Chemical data are available for the CT and CG cells and the in situ test. The chemical composition of the bentonite pore water was obtained with the squeezing and the aqueous extract methods. The aqueous extract method is used to quantify the total content of soluble salts of a clay sample. An 1:R aqueous extract consists on adding to a mass M_s of powdered clay sample a mass of distilled water equal to R times M_s (Zheng et al, 2008). The solid-liquid ratio for CT and CG cells is 1:4 (10 g of clay in 40 ml of water). The clay sample and water are stirred for two days, thus allowing the equilibration of water and clay samples. Squeezing was used for some bentonite samples. The squeezing involves the expulsion of the interstitial pore water from a nearly saturated sample of bentonite. The volume of water extracted depends on the water content, the squeezing pressure and the squeezing time. There are also available data for exchanged cations for the CT and CG cells and the in situ test. The available chemical data are listed in Table 11.

Table 11. Summary of the available chemical data.

Test	Duration (d)	Characteristic time	Available chemical data		
			Aqueous extract	Squeezing	Exchanged cations
CT-23	183	$1.25 \cdot 10^4$	Yes	Yes	Yes
FQ1/2 (CG1)	188	$2.93 \cdot 10^4$	Yes	No	Yes
FQ1 (CG5)	370	$2.93 \cdot 10^4$	Yes	No	Yes
FQ2 (CG2)	762	$2.93 \cdot 10^4$	Yes	No	Yes
HI1/2 (CG1)	214	$2.93 \cdot 10^4$	Yes	Yes	Yes
HI1 (CG6)	440	$2.93 \cdot 10^4$	Yes	Yes	Yes
HI2 (CG4)	747	$2.93 \cdot 10^4$	Yes	Yes	Yes
CG3	2775	$2.93 \cdot 10^4$	Yes	No	Yes
In situ	1948	$3.66 \cdot 10^4$	Yes	No	Yes

9.2.2 Aqueous extract data

Aqueous extract data are analysed first. The concentration of the soluble salts is expressed in mol/l. Figure 97 shows the spatial distribution of the measured aqueous extract data for CT23 cell. The data show a large variability. The largest variations near the heater zone.

Figure 98 shows the spatial distribution of pH, SO_4^{2-} , HCO_3^- , K^+, Na^+, Ca^{2+}, Mg^{2+} and Cl^- for CG cells. The aqueous extract data are represented by the average concentration data for the cells that have the same duration. The aqueous extract data for CG3 cells shows values larger than those of the other of the CG cells. In general the concentrations are smaller in the hydration boundary and larger in the heater. There are several measured data with values out of range.

Figure 99 shows the aqueous extract for the sections 19, 28, 29 and 31 of the in situ test. The data are similar for the sections 19, 28, 29 and 31. The concentrations in the in situ test are larger in the central zone and smaller in the hydration and heating boundary for several cases such Ca^{2+}.

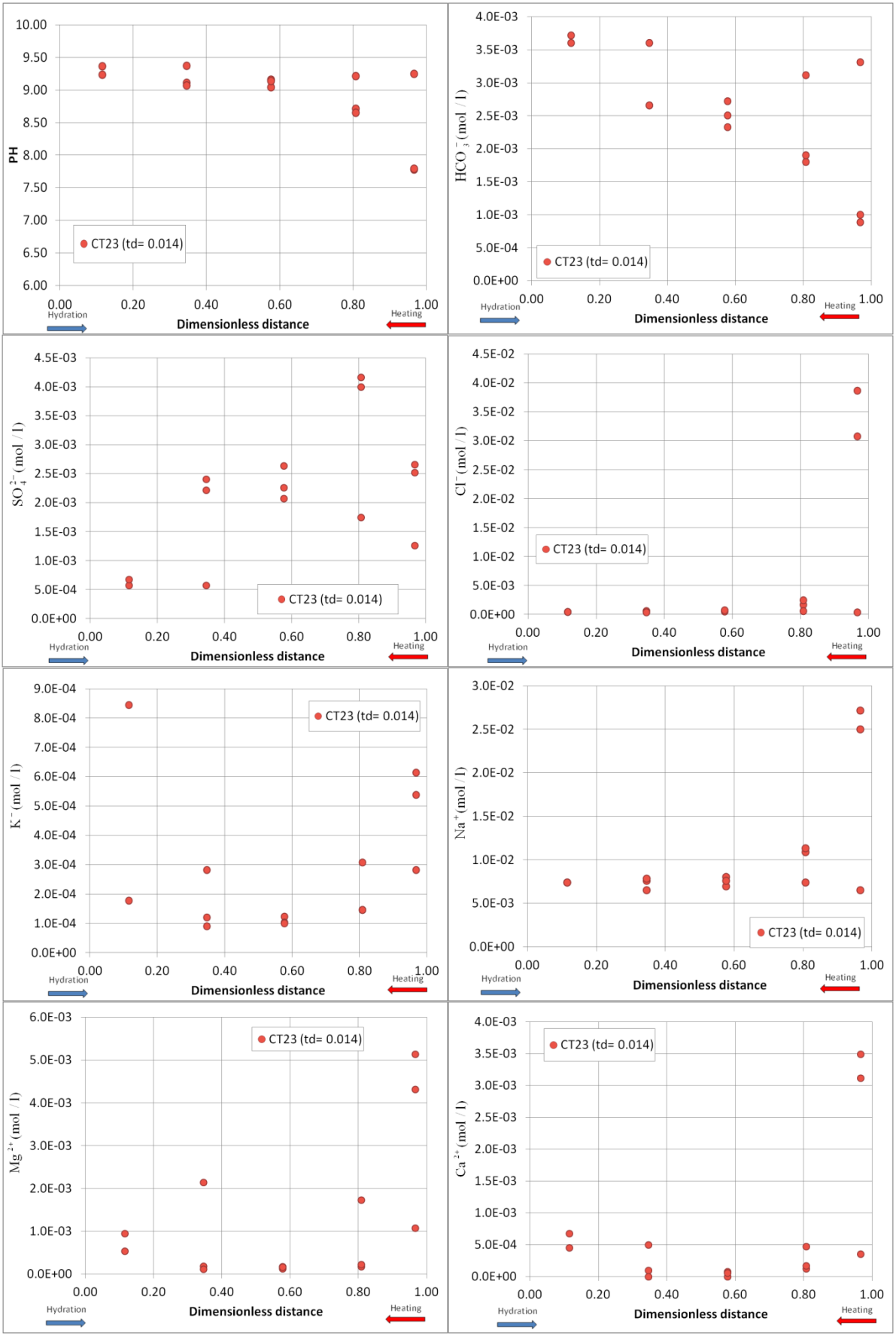

Figure 97. Measured aqueous extract data from the CT23 cell (Fernández et al., 1999).

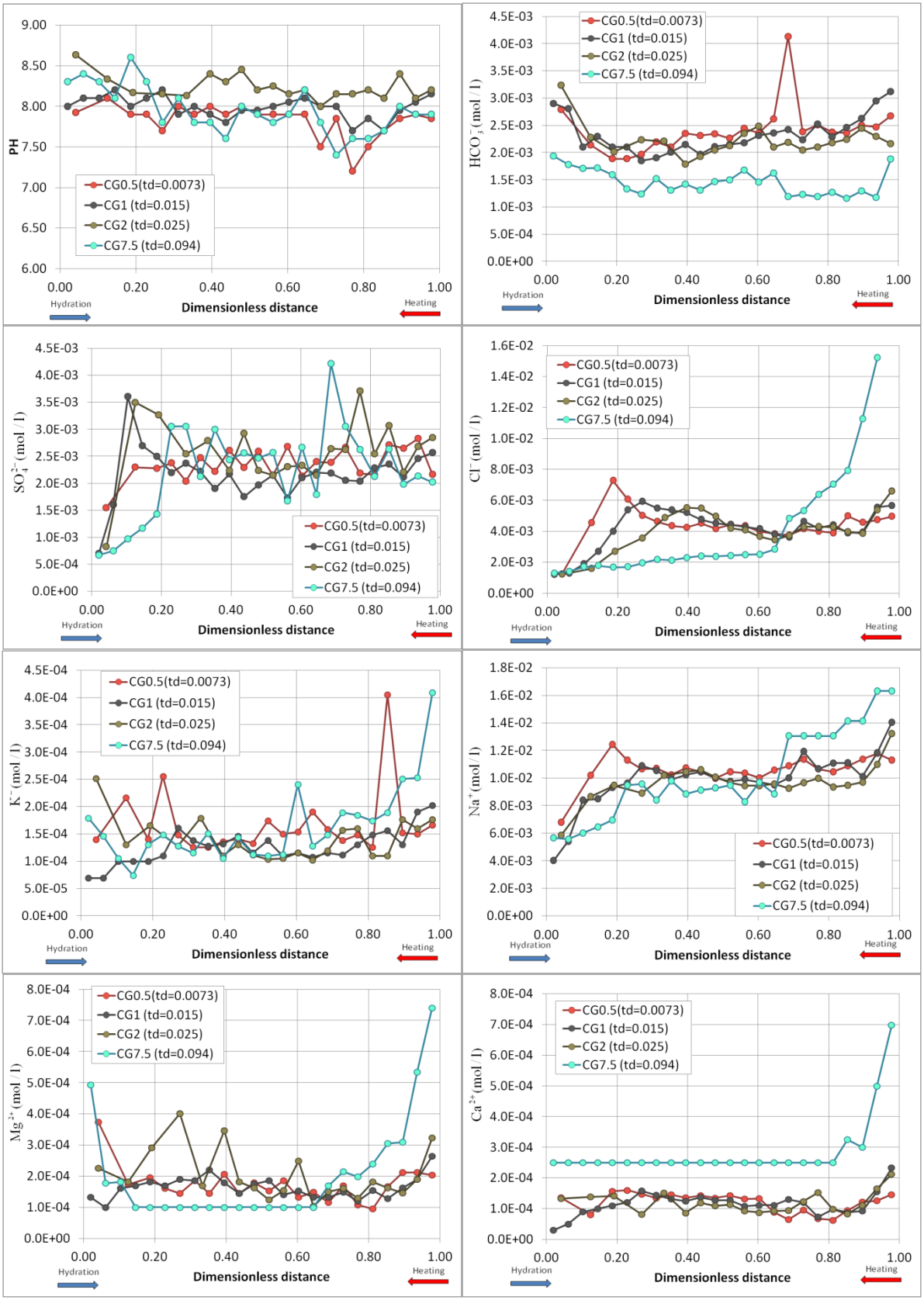

Figure 98. Measured aqueous extract data from CG cells (Fernández and Villar, 2010).

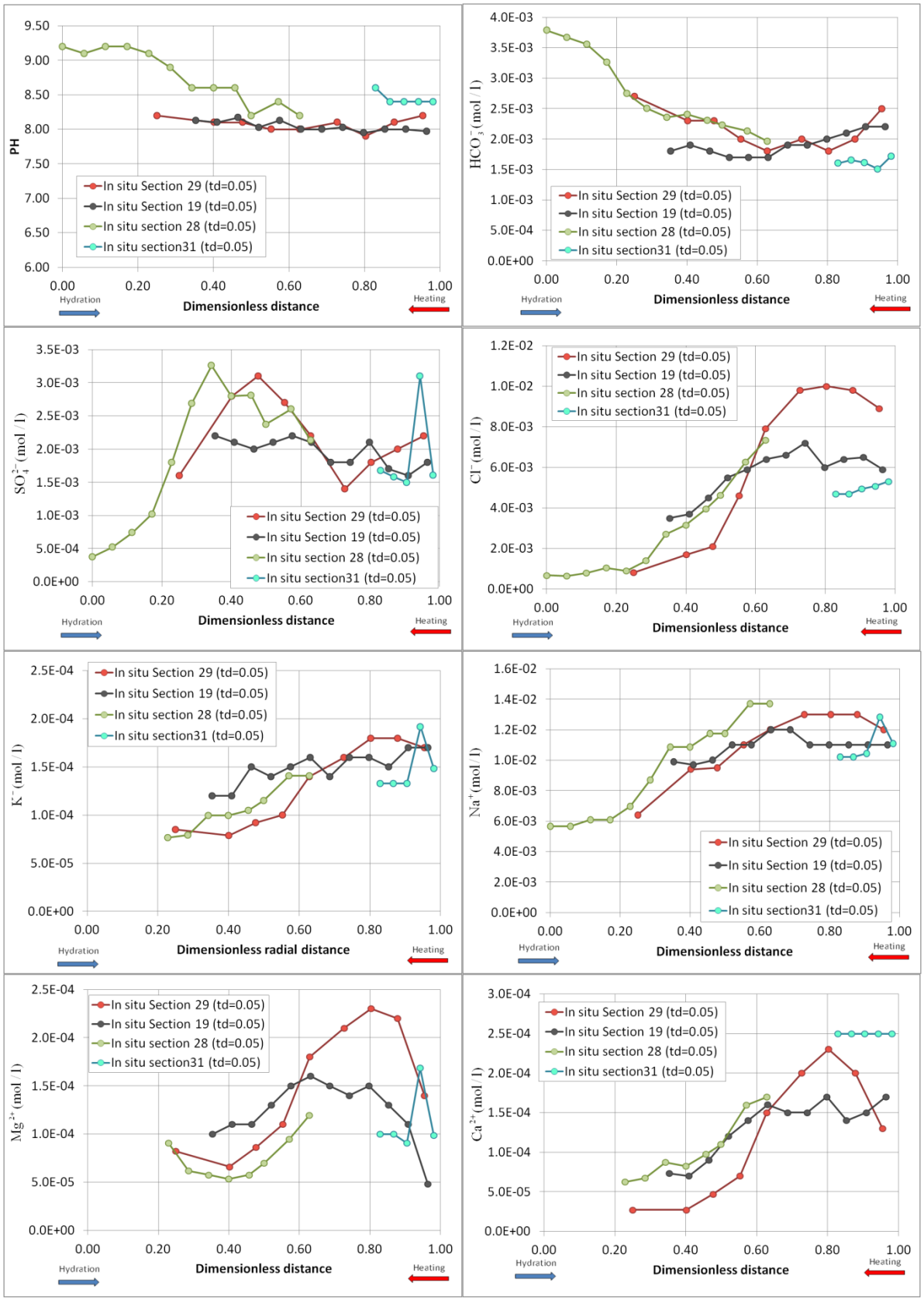

Figure 99. Measured aqueous extract data from sections 19, 28, 29 and 31 after dismantling the heater 1 of the in situ test (ENRESA, 2006).

9.2.3 Squeezing data

Figure 100 shows the measured squeezing data for CT23 cell. There are four measured data, the smaller values are near the hydration boundary and larger in the heater. Squeezing data from CG cells are available near the hydration zone.

Figure 101 shows the CG cells squeezing data. Aqueous extract data cannot be compared directly to those of the squeezing method because aqueous extract concentrations must be transformed into the concentration of pore water using inverse models such as that used by Zheng et al (2008). The squeezing data for CG cells increase more in a dimensionless distance of 0.4 than that of CT23 cell.

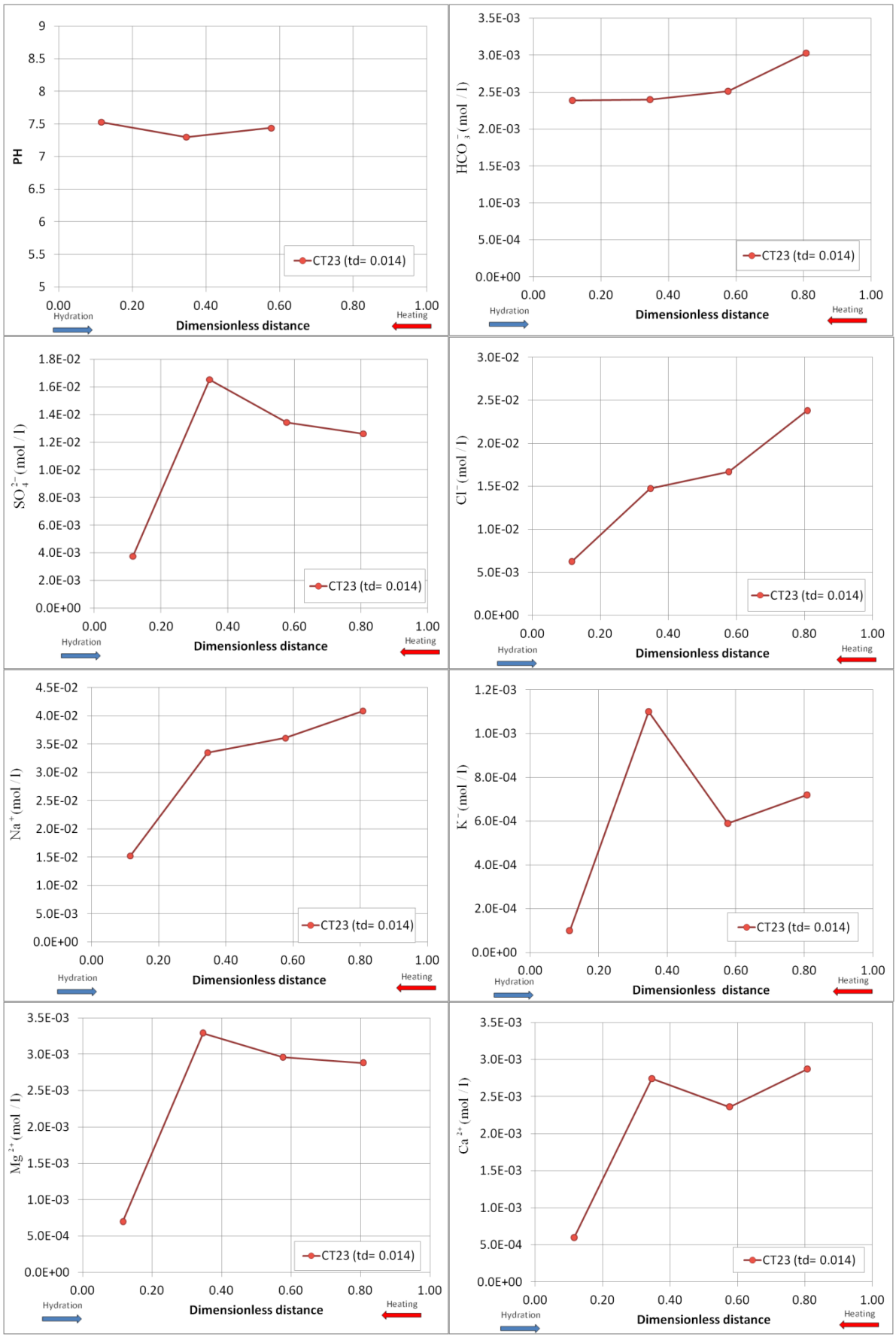

Figure 100. pH, SO_4^{2-}, HCO_3^-, K^+, Na^+, Ca^{2+}, Mg^{2+} and Cl^- squeezing data for CT23 Cell (Fernández et al., 1999).

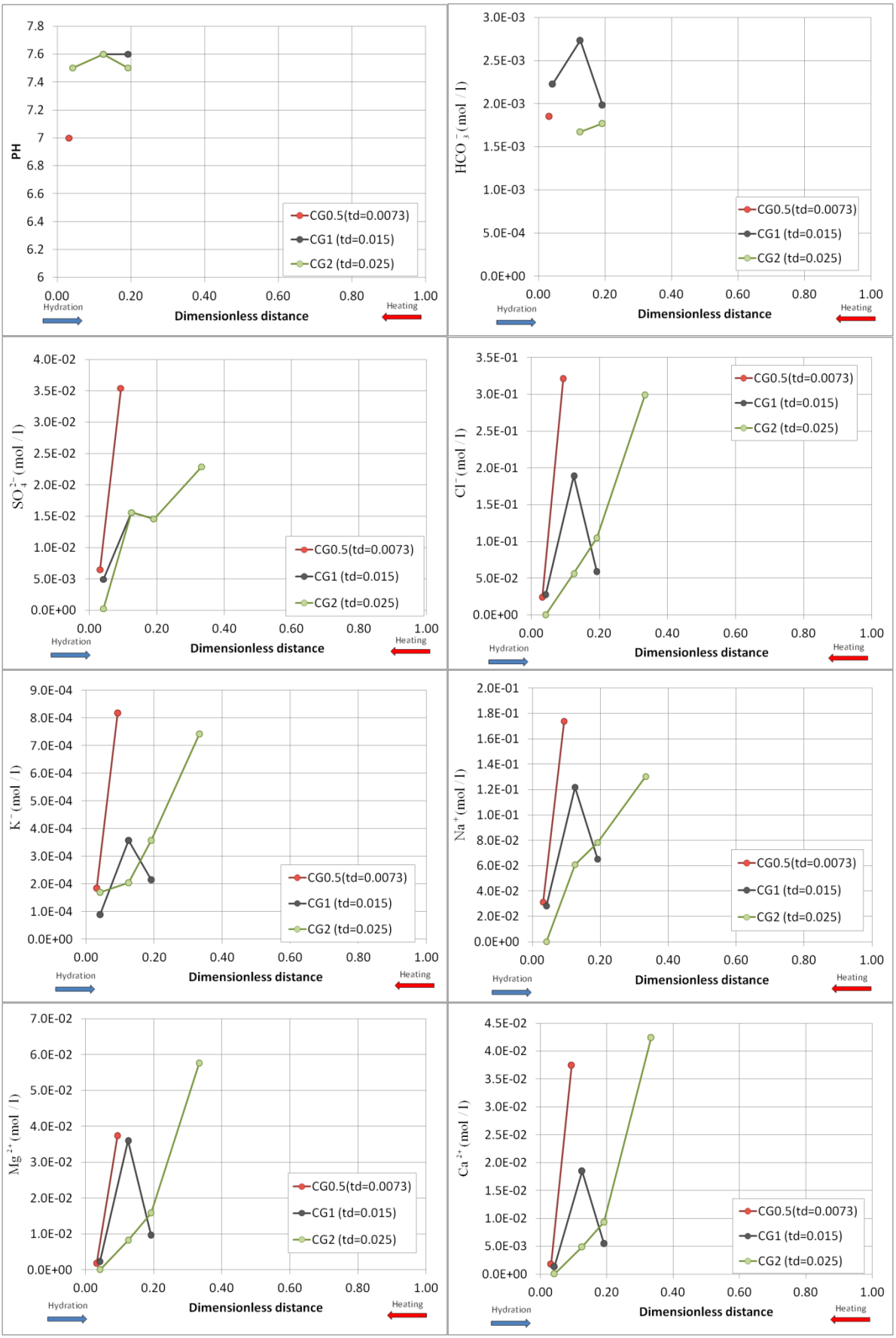

Figure 101. pH, SO_4^{2-} , HCO_3^- , K^+ , Na^+, Ca^{2+}, Mg^{2+} and Cl^- squeezing data for CG cells (Fernández and Villar , 2010).

9.2.4 Exchanged cations

Figure 102 shows the concentration of exchanged cations in meq/100g for the CG cells. The Chapman's method was used to obtain cation exchange population for the test of at 0.5, 1 and 2 years (CG1, CG4, and CG6). In this method, once the soluble salts are washed first. Then the exchanged cations of the bentonite are extracted by successive displacement with a buffered solution of 1M ammonium acetate at pH 7 (Fernández and Villar, 2010). In the longest test, cell CG3, the the exchanged cations were measured with the $CsNO_3$ method in which C_s^+ is used to displace the exchanged cations. This method is supposed to be accurate because it does not overestimate the concentration of the bivalent cations at the interlayers. The analytical error for the determination of the cation exchange population by using the ammonium acetate method is around 20%, whereas for the $CsNO_3$ method is about 10%.

Figure 103 shows the plot of the concentration of the exchanged cations in the CT23 cell measured with the Chapman's method based in successive displacement with ammonium acetate. The CT cell measured of squeezing is comparable to those CG cells measured with the same method.

Figure 104 shows the concentration of exchanged cations measured at the sections 19, 28, 29 and 31 of the in situ test. The exchanged cations were measured with the $CsNO_3$ method. The exchanged cations obtained in CG3 cell are directly comparable to those determined in the in situ test.

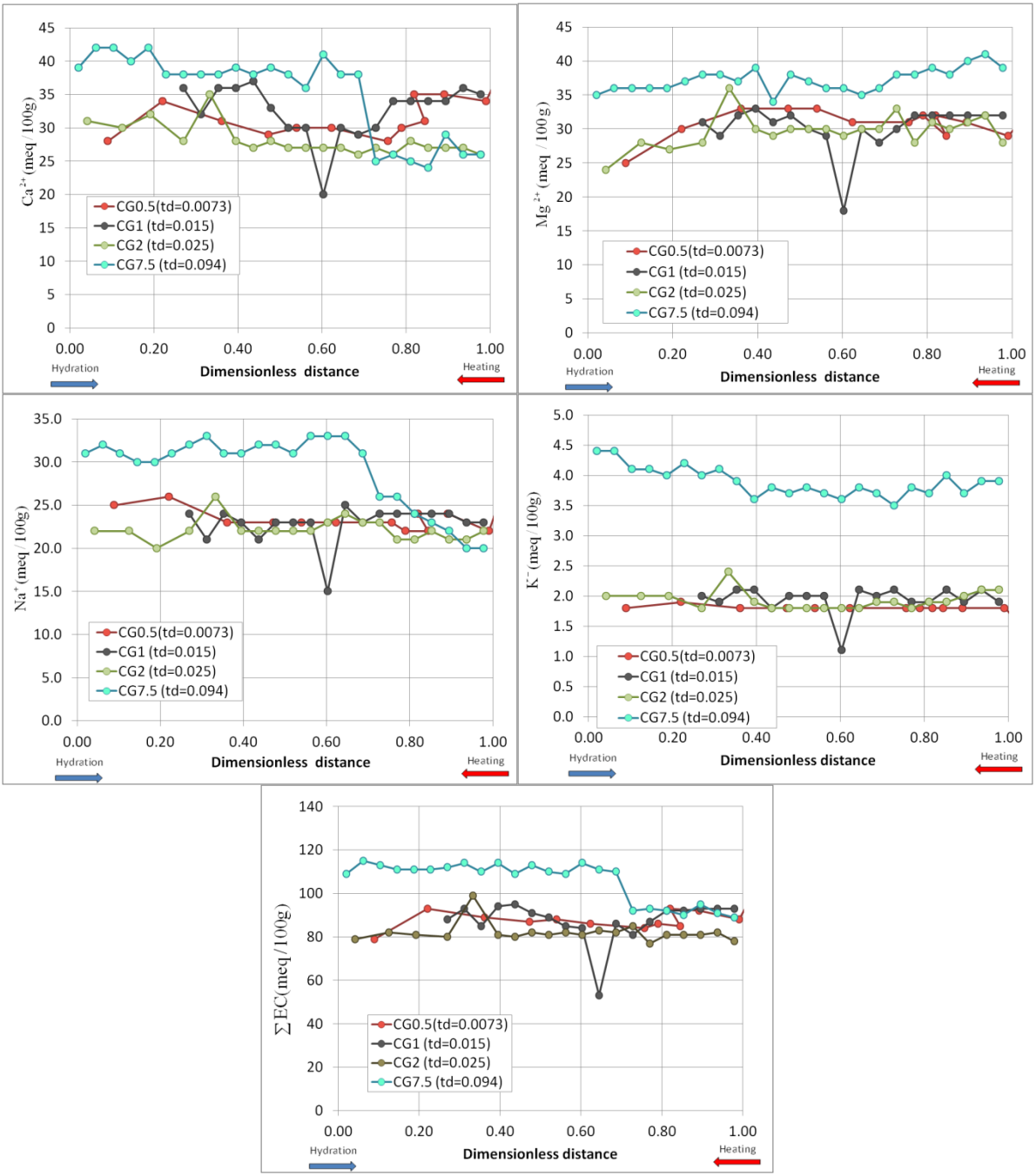

Figure 102. Measured exchanged cations in CG cells (Fernández and Villar, 2010).

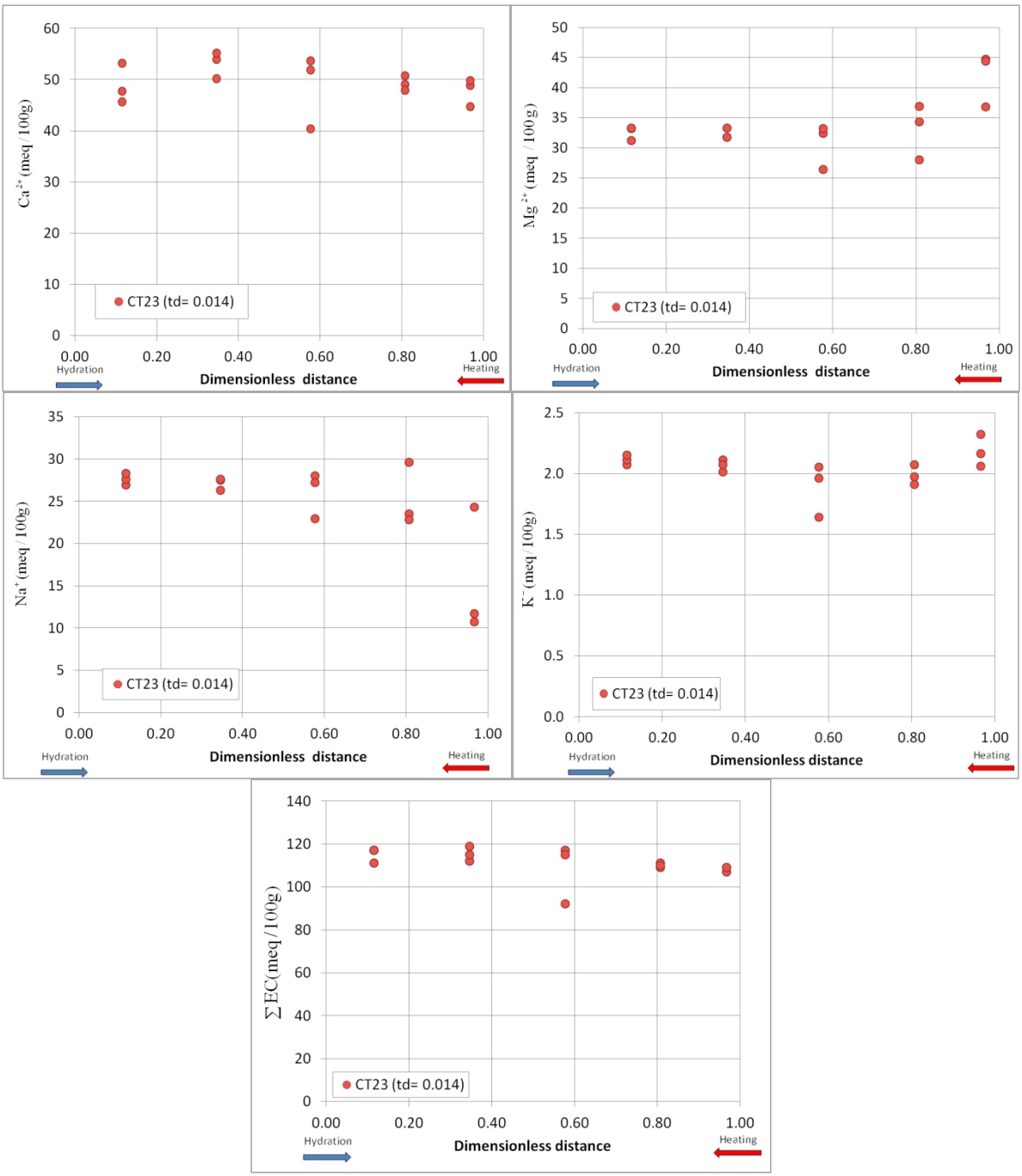

Figure 103. Measured exchanged cations in CT cells (Fernández et al., 1999).

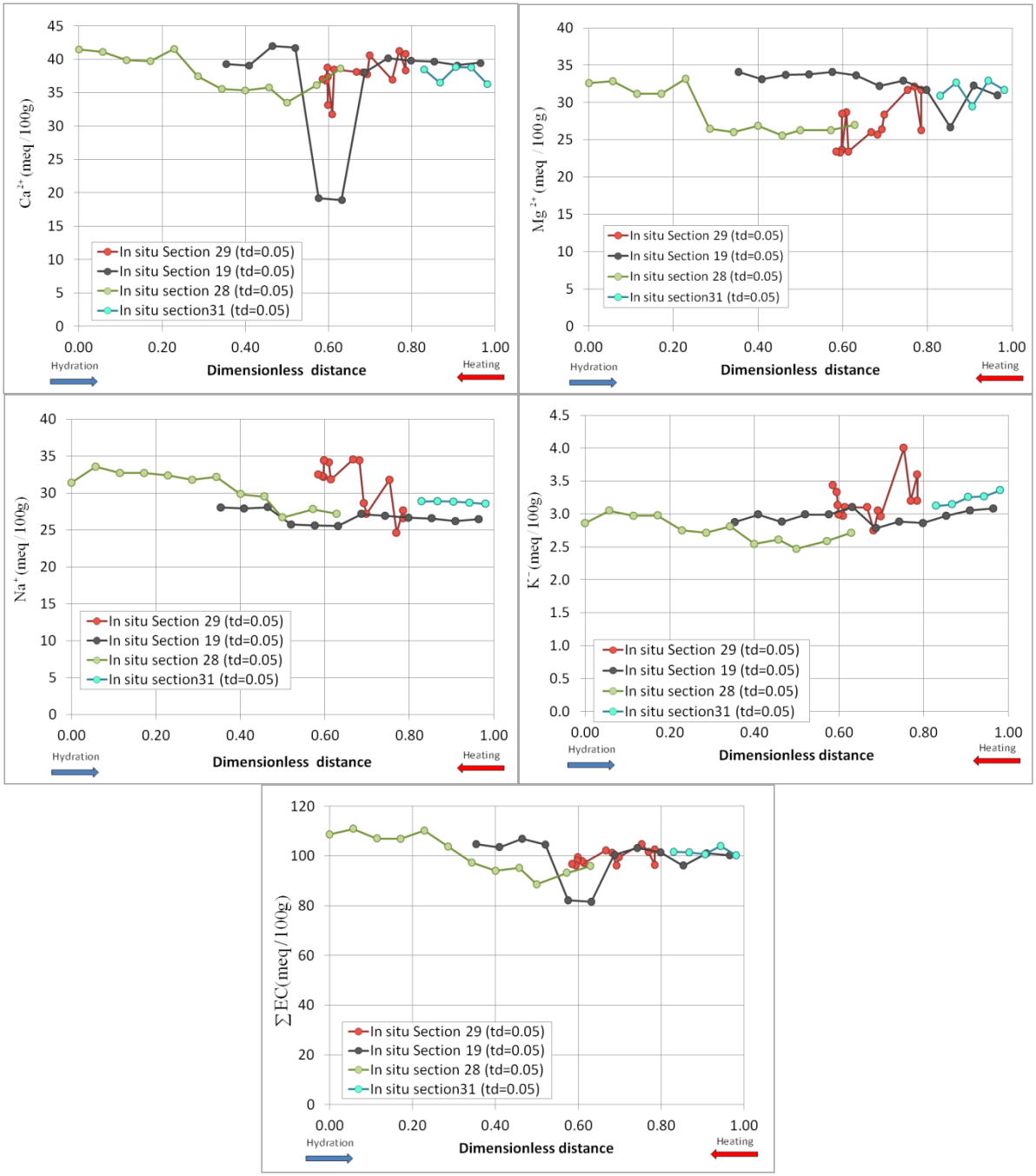

Figure 104. Measured exchanged cations for the in situ test (ENRESA, 2006).

9.2.5 Chemistry of the hydration water

The bentonite in the CT cells was hydrated with distilled water. The chemical composition of the granitic water used in hydration in the CG cells and in the in situ test is listed in Table 12.

Table 12. Chemical composition of the hydration water (mol/l).

Test	pH	Cl^-	SO_4^{2-}	HCO_3^-	Mg^{2+}	Ca^{2+}	Na^+	K^+
CG cells (Villar et al., 2008)	8.3	$3.7\cdot10^{-4}$	$1.5\cdot10^{-4}$	$2.36\cdot10^{-3}$	$3.9\cdot10^{-4}$	$1.12\cdot10^{-3}$	$4.8\cdot10^{-4}$	$2.6\cdot10^{-5}$
In situ granite porewater (Zheng et al., 2008)	9.25	$1.3\cdot10^{-5}$	$7.86\cdot10^{-5}$	$3.94\cdot10^{-4}$	$1.32\cdot10^{-6}$	$2.16\cdot10^{-4}$	$3.76\cdot10^{-4}$	$7.8\cdot10^{-6}$

9.2.6 Initial chemical composition of the bentonite

Table 13 the lists the initial composition of the bentonite as inferred by Zheng et al. (2008).

Table 13.Infered chemical composition of the bentonite (mol/l) (Zheng et al., 2008).

pH	Cl^-	SO_4^{2-}	HCO_3^-	Mg^{2+}	Ca^{2+}	Na^+	K^+
7.68	0.178	$2.12\cdot10^{-2}$	$6.65\cdot10^{-4}$	$1.44\cdot10^{-2}$	$1.14\cdot10^{-2}$	$1.88\cdot10^{-1}$	$1.68\cdot10^{-3}$

9.2.7 Integrated analysis of the chemical data

Figure 105 shows the comparison of the aqueous extract data of the CT and CG cells and the in situ test for SO_4^{2-} , HCO_3^- , K^+ , Na^+, $Ca^{2+}$and Mg^{2+}. The pH and the Cl^- are studied separately. Cl^- is a conservative species. The concentration of HCO_3^- for the CT and CG cells and in situ tests are in the range of 0.003 mol/l. The measured SO_4^{2-} data are smallest values near the hydration boundary. The range of values of the K^+, for the intermediate distances is 0.0001mol/l, except for the CT cell which has larger values. The range of values is 0.007 mol/l for the Na^+. Some Ca^{2+} and Mg^{2+} data are extremely large due to the influence of colloids. Some measured data are not representative of the bentonite pore water because some colloids are dissolved in the aqueous solution.

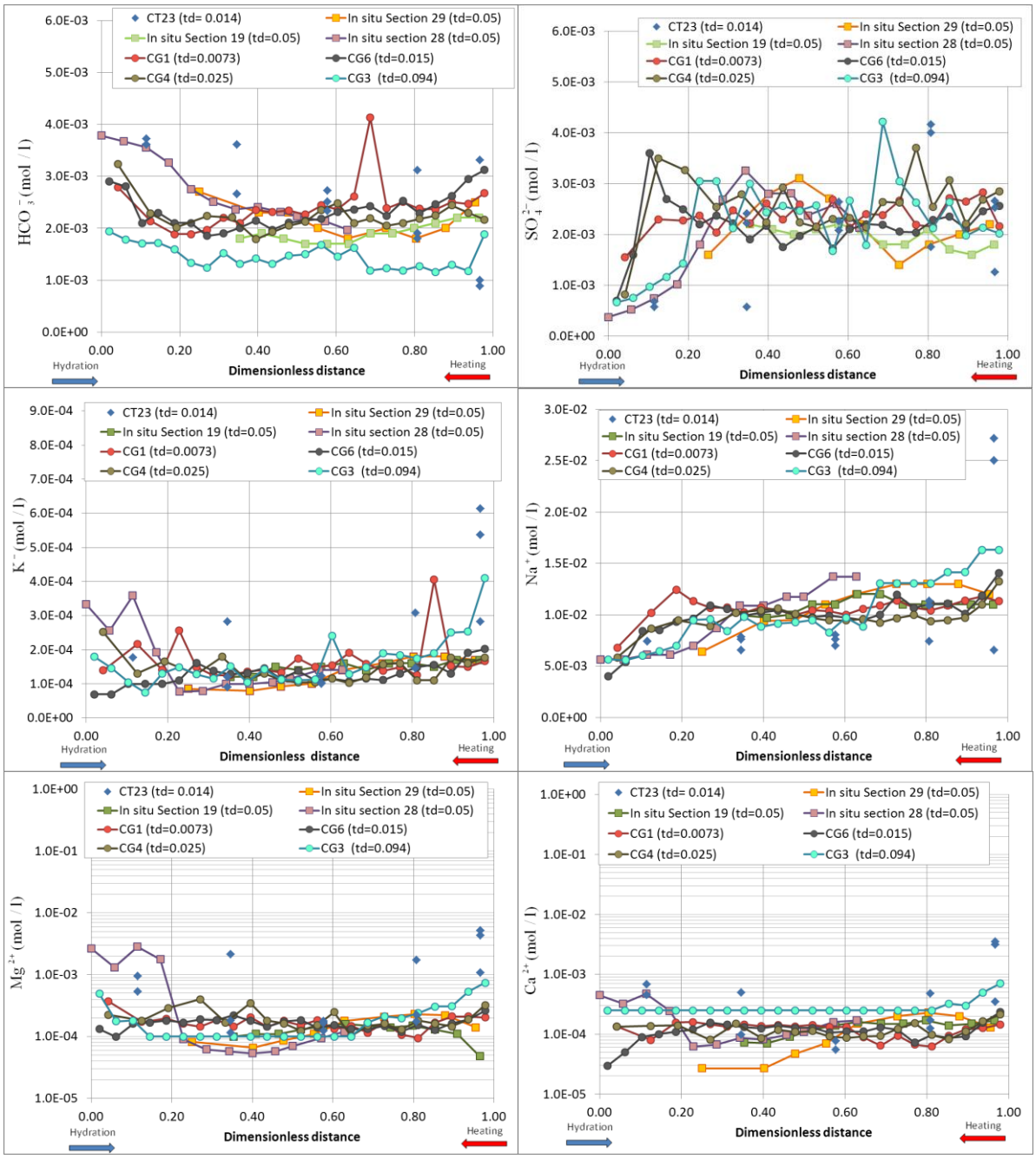

Figure 105. Spatial distribution of the aqueous extract data of CT and CG cells and the in situ test.

9.2.8 Spatial distribution of Cl^- aqueous extract data

Figure 106 shows the aqueous extract concentration of Cl^- in CT23 cell. The measured values near the heater are larger. Figure 107 shows the concentration of Cl^- of the aqueous extracts of the CG cells. The average Cl^- concentration has been computed fot the two tests having the same duration. The concentration of Cl^- aqueous extracts for CG cells decrease with dimensionless time near the hydration boundary. For the intermediate dimensionless

distances the concentration of Cl^- is similar in all tests except CG7.5. Concentration data for CG7.5 is the largest near the heater.

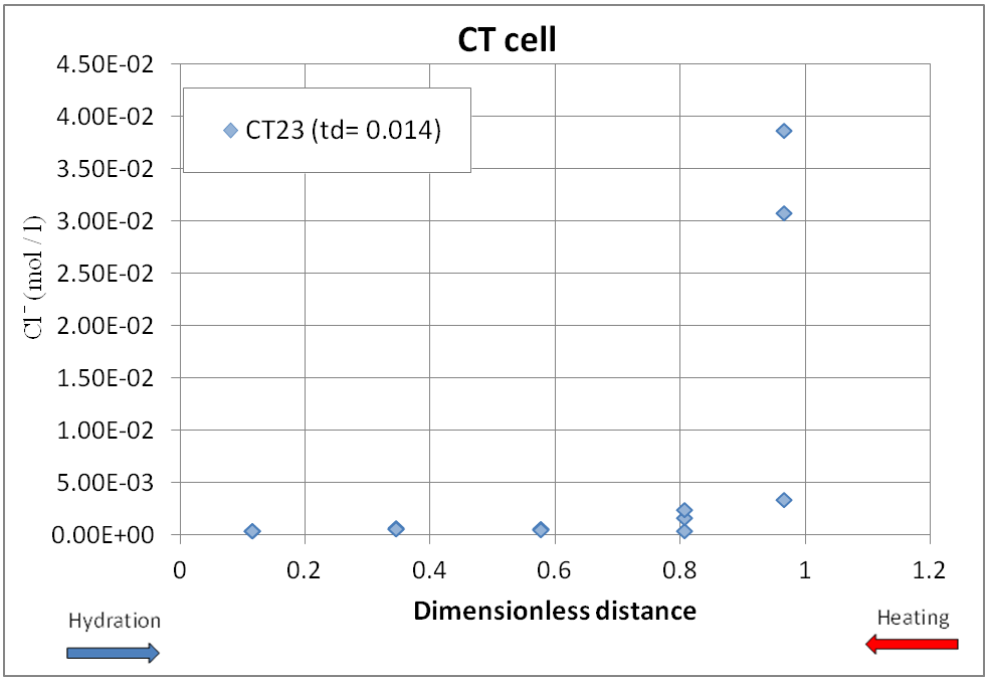

Figure 106. Concentration of Cl^- of the aqueous extracts of the CT cells versus dimensionless distance for several dimensionless times (Fernández et al., 1999).

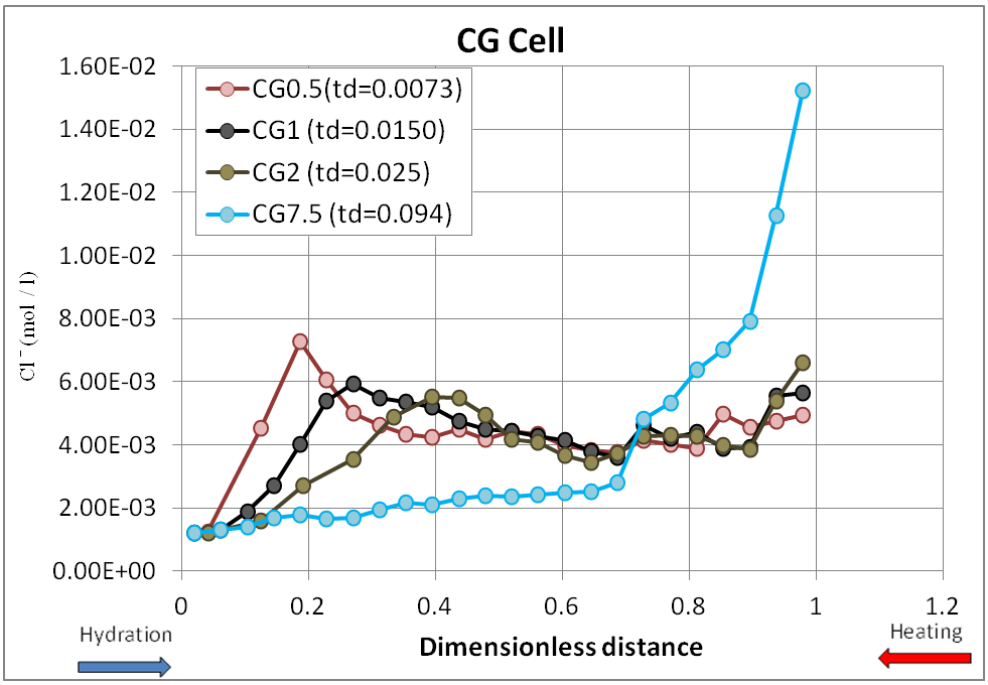

Figure 107. Concentration of Cl^- of the aqueous extracts of the CG cells versus dimensionless distance for several dimensionless times (Fernández and Villar, 2010).

Figure 108 shows the concentration of Cl^- in the aqueous extract of the sections 19, 28, 29 and 31 of the in situ test. The concentration data of Cl^- is lower in the hydration zone and larger near the heater. Figure 109 shows the comparison of the aqueous extract data concentration of Cl^- for the CT and CG cells and the in situ test. The Cl^- concentration is similar for the all the tests except the CT cells. Near the hydration boundary where there are large differences.

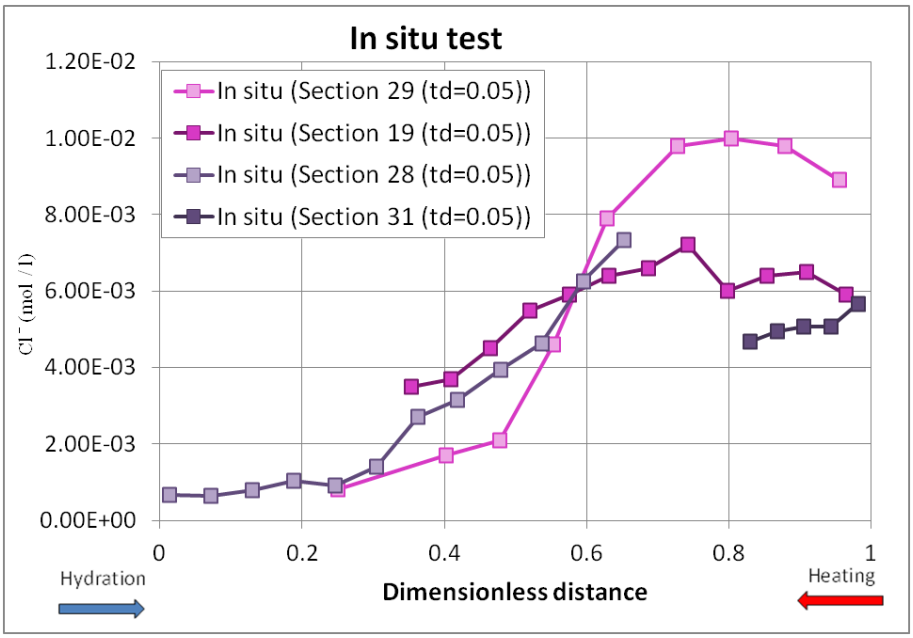

Figure 108. Concentration of Cl^- of the aqueous extracts of the in situ test versus dimensionless distance for several dimensionless times (ENRESA, 2006).

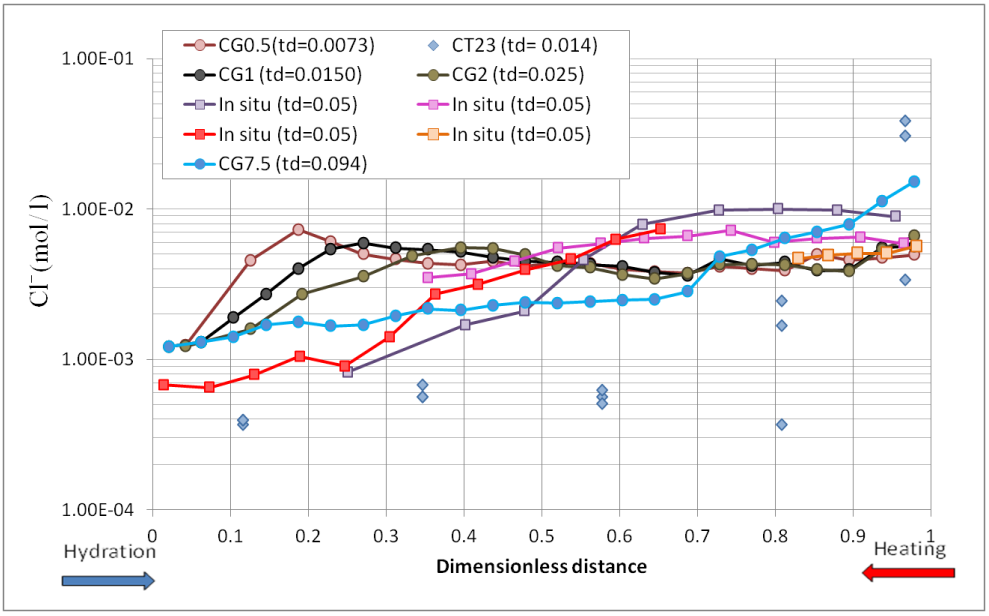

Figure 109. Aqueous extract data for Cl^- versus dimensionless distance for several dimensionless times for CT and CG cells, and in situ test.

9.2.9 Spatial distribution of inferred Cl^- concentration data using inferred data.

The concentration of conservative species in the clay pore water, c_i, can be derived from the concentration of aqueous extract, c_{ae}, performed on a clay sample of mass M_s, from the species mass balance. The gravimetric water content of aqueous extract, w_{ae}, is related to the gravimetric water content of clay sample, w_i, through:

$$w_{ae} = w_i + R(w_i + 1) \tag{39}$$

The dilution factor, F, which relates c_i to c_{ae} is given by:

$$F = \frac{c_i}{c_{ae}} = 1 + R + \frac{R}{w_i} \tag{40}$$

Using the water content measured at the end of the test, the dilution factor was calculated for each test and for each section. Figure 110 shows the spatial distribution of inferred concentrations of Cl^- of CT and CG cells. Cl^- concentration in the CT23 test are markedly different to the others.

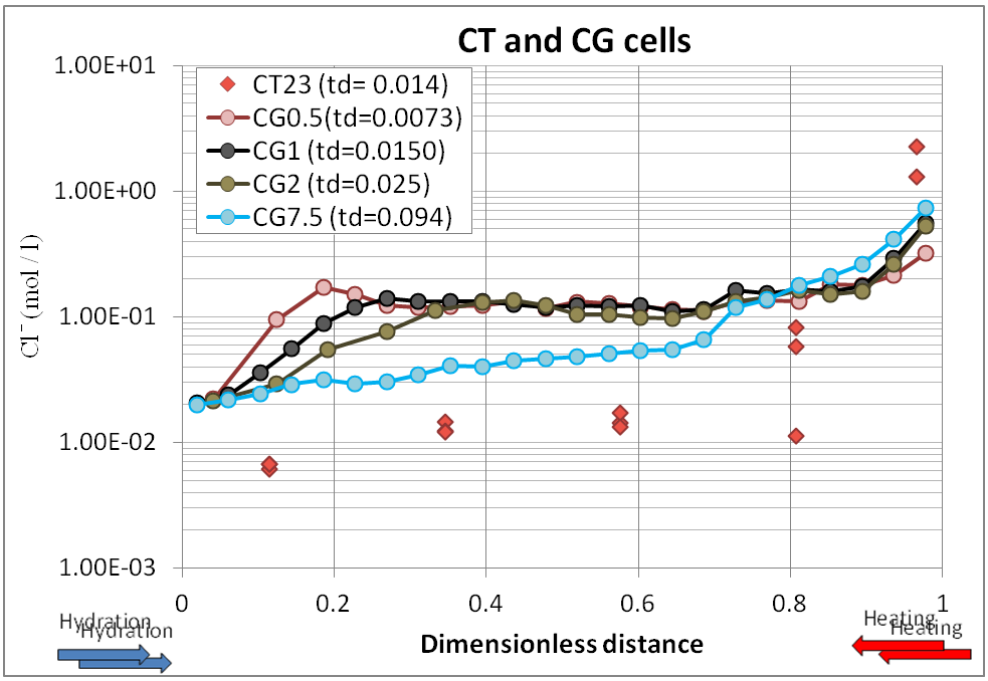

Figure 110. Inferred Cl^- concentrations for the CT and CG cells for several times.

Figure 111 shows the inferred concentration of Cl^- of the four sections of the in situ test. Figure 112 shows the inferred concentration of Cl^- for CT and CG cells and the in situ test. It

can be seen that the behaviour is similar for the in situ and the CG cells, but not the same for the CT cell. The Cl^- inferred concentrations are in the range of 2 mol/l. In the intermediate distance of the bentonite the Cl^- concentration is similar for all the tests except the CT23 cell. The largest differences became near the hydration boundary due to the dilution.

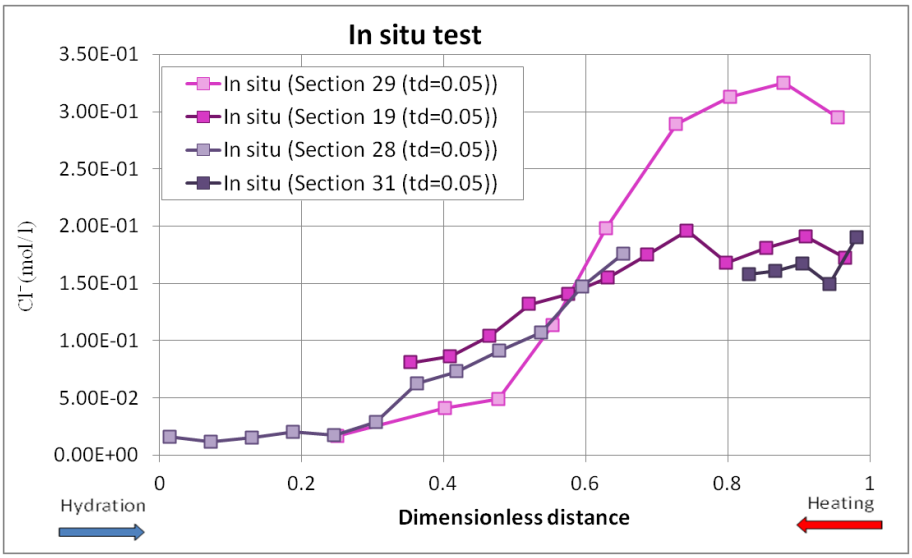

Figure 111. Inferred Cl^- concentration for several dimensionless times for the sections 19, 28, 29 and 31 of the in situ test.

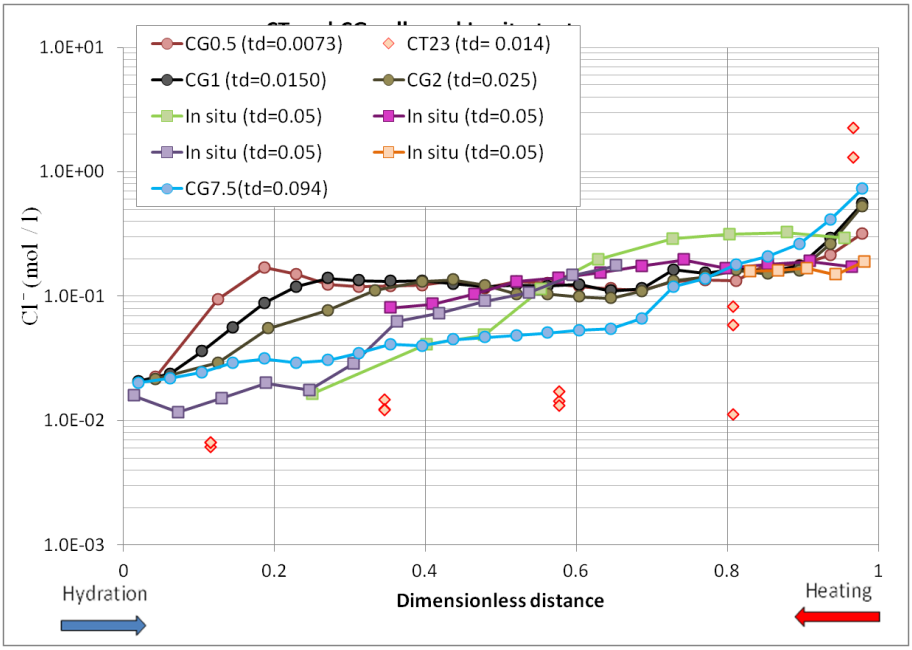

Figure 112. Inferred Cl^- concentration for the CT and CG cells and the in situ test for several dimensionless times.

9.2.10 Dimensionless inferred Cl^- concentration

Figure 113 shows the dimensionless inferred concentration of Cl^- for CT23 and CG cells and the in situ tests. Dimensionless concentrations are calculated according to Equation (23) and using the initial Cl^- concentration in the bentonite listed in Table 12, and the concentration of the hydration water of Table 13. Data for CT23 cell are markedly smaller than the data from CG cells and the in situ test.

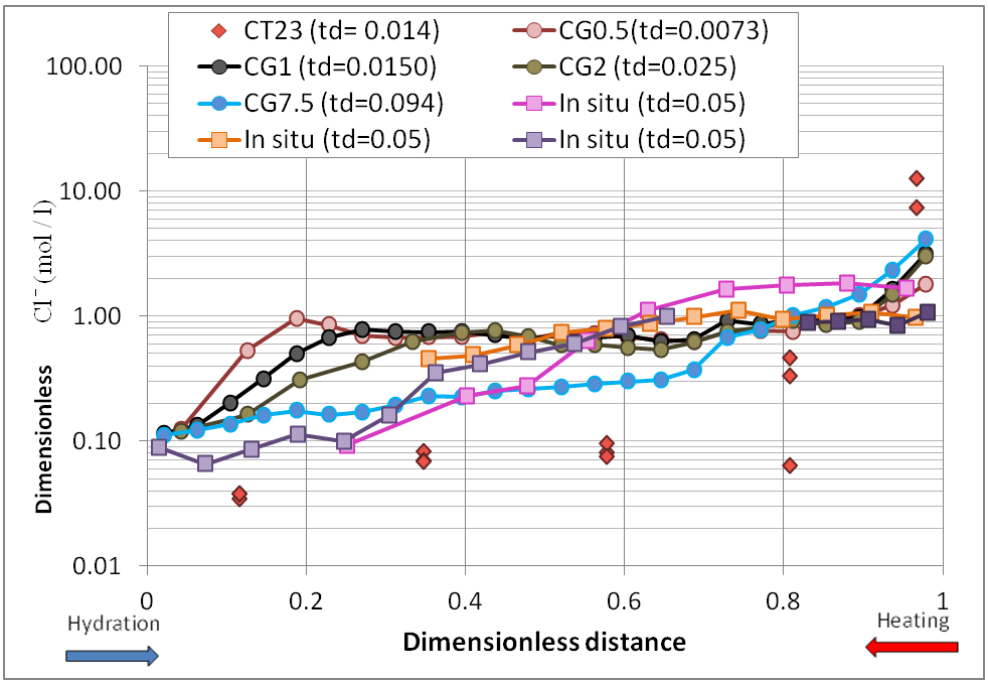

Figure 113. Dimensionless inferred Cl^- concentration for the CT and CG cells and the in situ test for several dimensionless times.

9.2.11 Inferred aqueous extract and squeezing Cl^- concentration

Figure 114 shows the comparison of the inferred aqueous extract and squeezing Cl^- concentration data for the CT23 cell. The data are the same for the measured data located near the hydration zone. Figure 115 shows the inferred aqueous extract and squeezing data for CG cells. Some squeezing data do not agree with the inferred aqueous extract data.

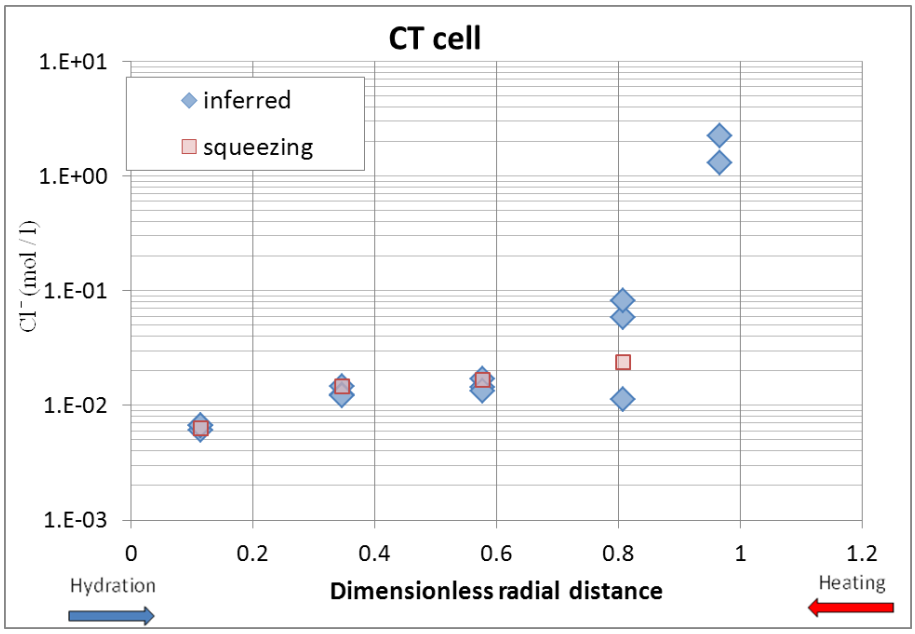

Figure 114. Inferred aqueous extract data and squeezing Cl^- data for CT cells versus dimensionless distance.

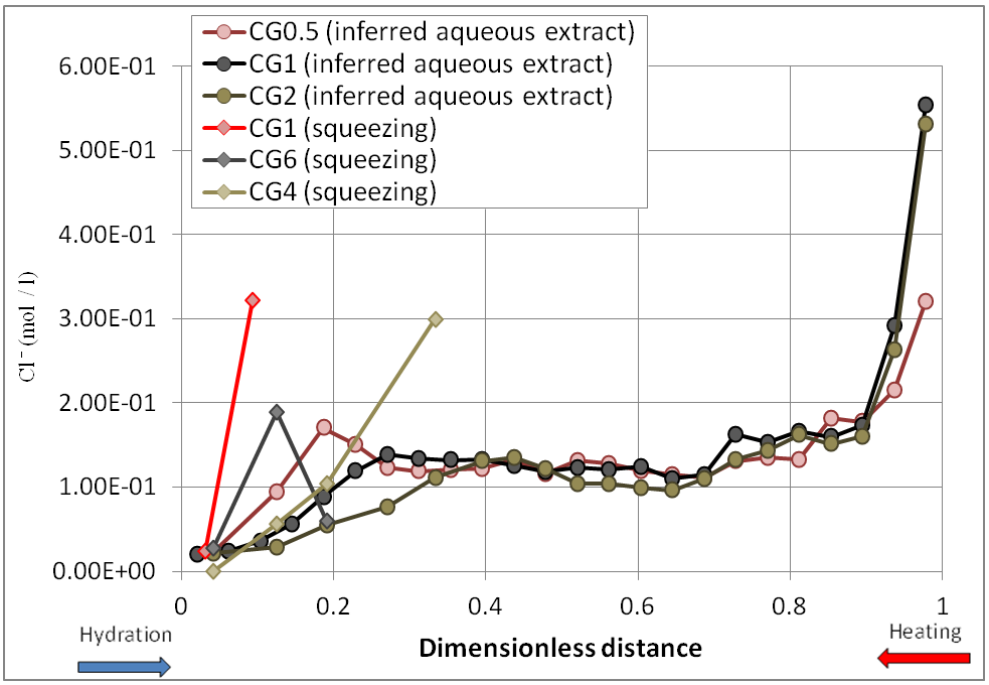

Figure 115. Inferred aqueous extract and squeezing Cl^- data for CG cells versus the dimensionless distance.

9.2.12 pH data

Figure 116 shows pH data from the aqueous extracts of CT cell. The pH data decrease with the dimensionless distance. Figure 117 shows the pH data of the aqueous extract data of CG cells. pH data range from 7 to 8.5. pH data for the in situ test is shown in Figure 118. The pH data of aqueous extract data of section 28 is larger than the pH data of the others sections. The pH data for sections 19, 29 and 31 have an average value of 8.25.

Figure 119 shows the pH data for the aqueous extracts of CT and CG cells and the in situ test. The pH is about 8 for most of the tests, except the data from section 29 of in situ test and CT cell.

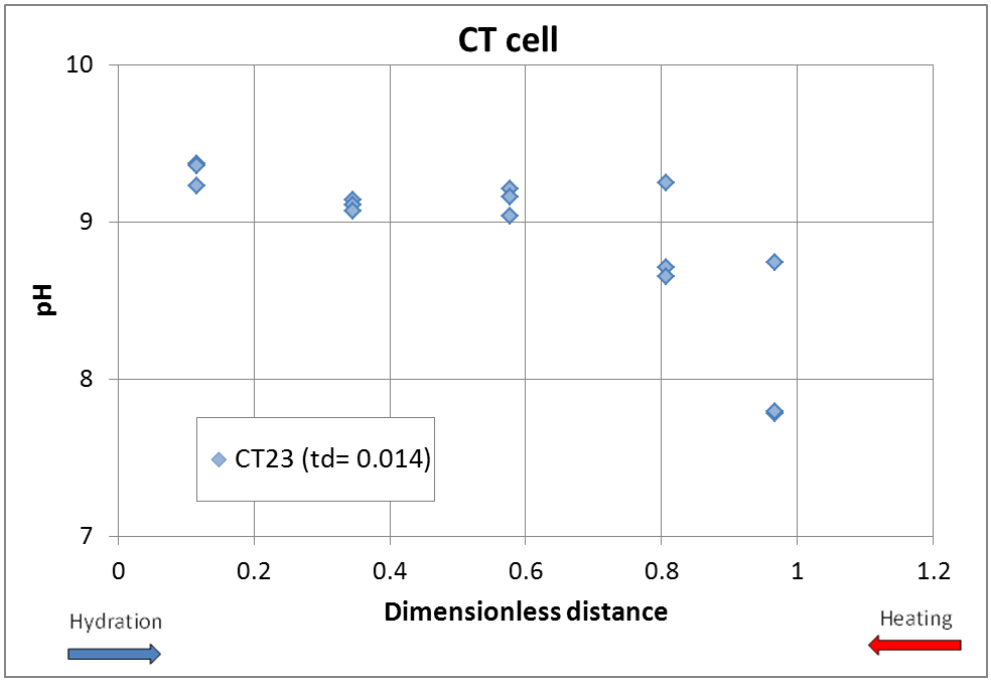

Figure 116. pH data from the aqueous extracts of the CT cells versus dimensionless distance (Fernández et al., 1999).

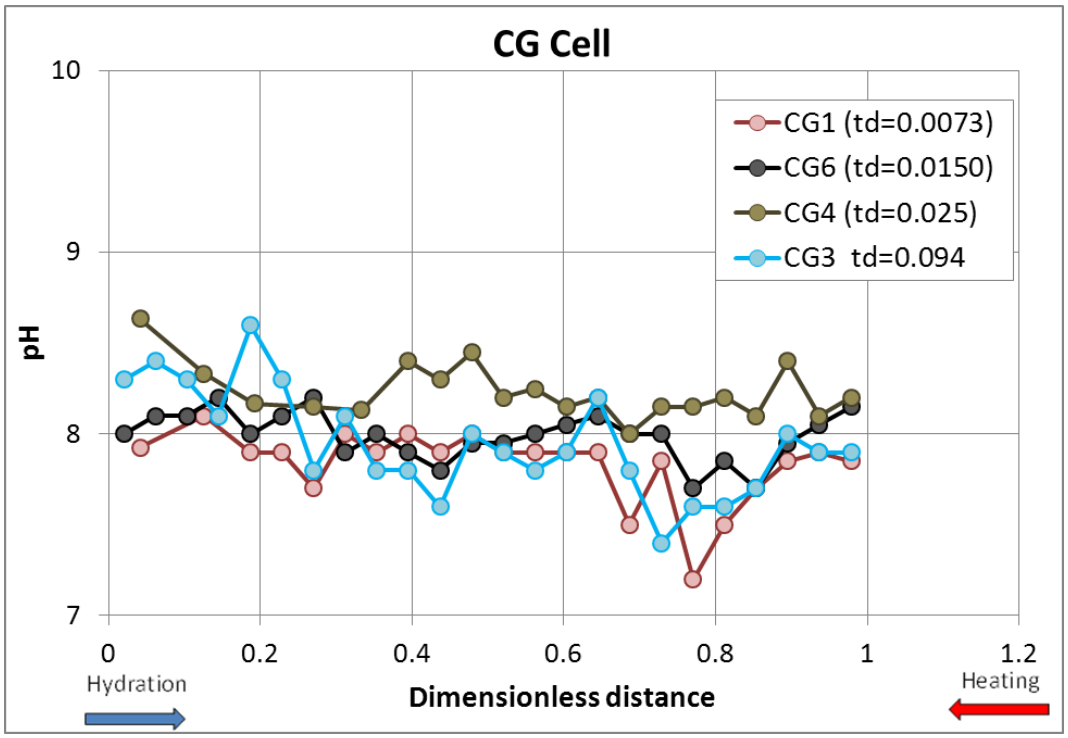

Figure 117. pH data of the aqueous extracts of the CG cells versus dimensionless distance (Fernández and Villar, 2010).

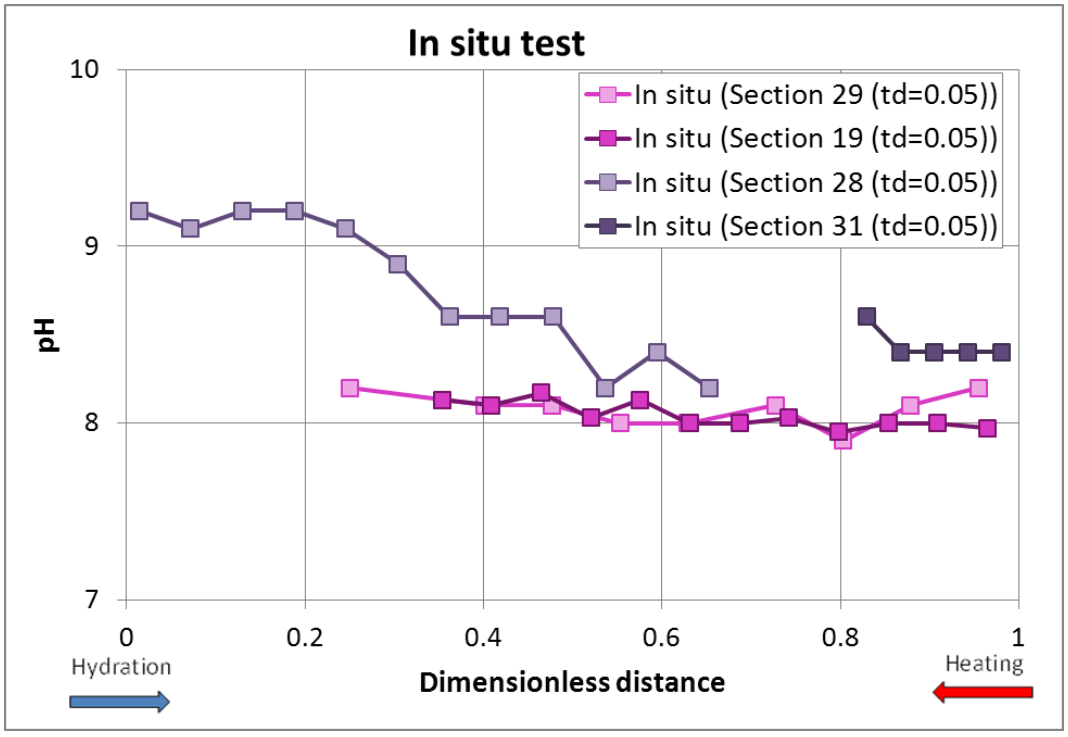

Figure 118 pH data of the aqueous extracts of the in situ test versus dimensionless distance (ENRESA 2006).

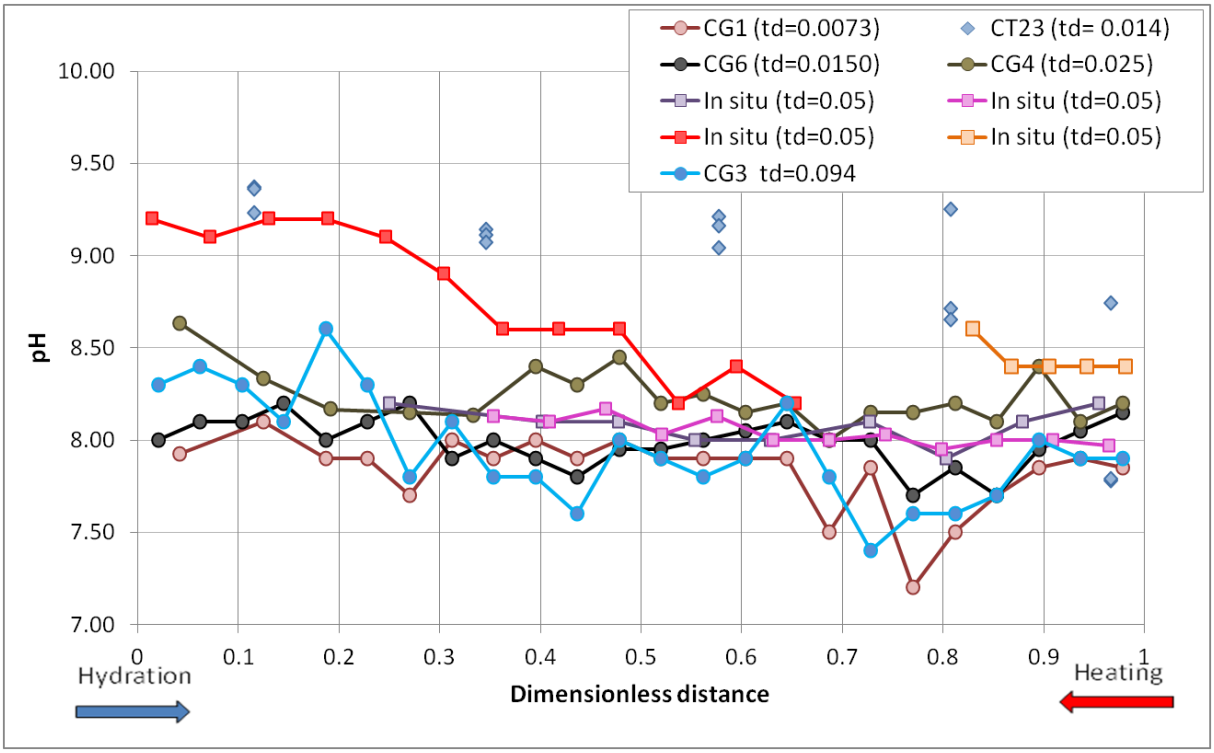

Figure 119. Integration of pH data for the aqueous extracts of the CT and CG cells and the in situ test versus dimensionless distance.

9.3. Spatial distribution of the exchanged cations

Figure 120 shows the spatial distribution of the concentrations of the exchanged cations for CG and CT cell measured of the Chapman's method. The exchange cations are similar for the CT23 and CG cells, except for the Ca^{2+}. The concentration of Ca^{2+} for the CT23 cells is larger than that of the CG cells.

Figure 121 shows the exchanged cations for CG3 cell and the in situ test. The concentration of exchanged cations shows similar ranges of values, although there are differences which are difficult to explain.

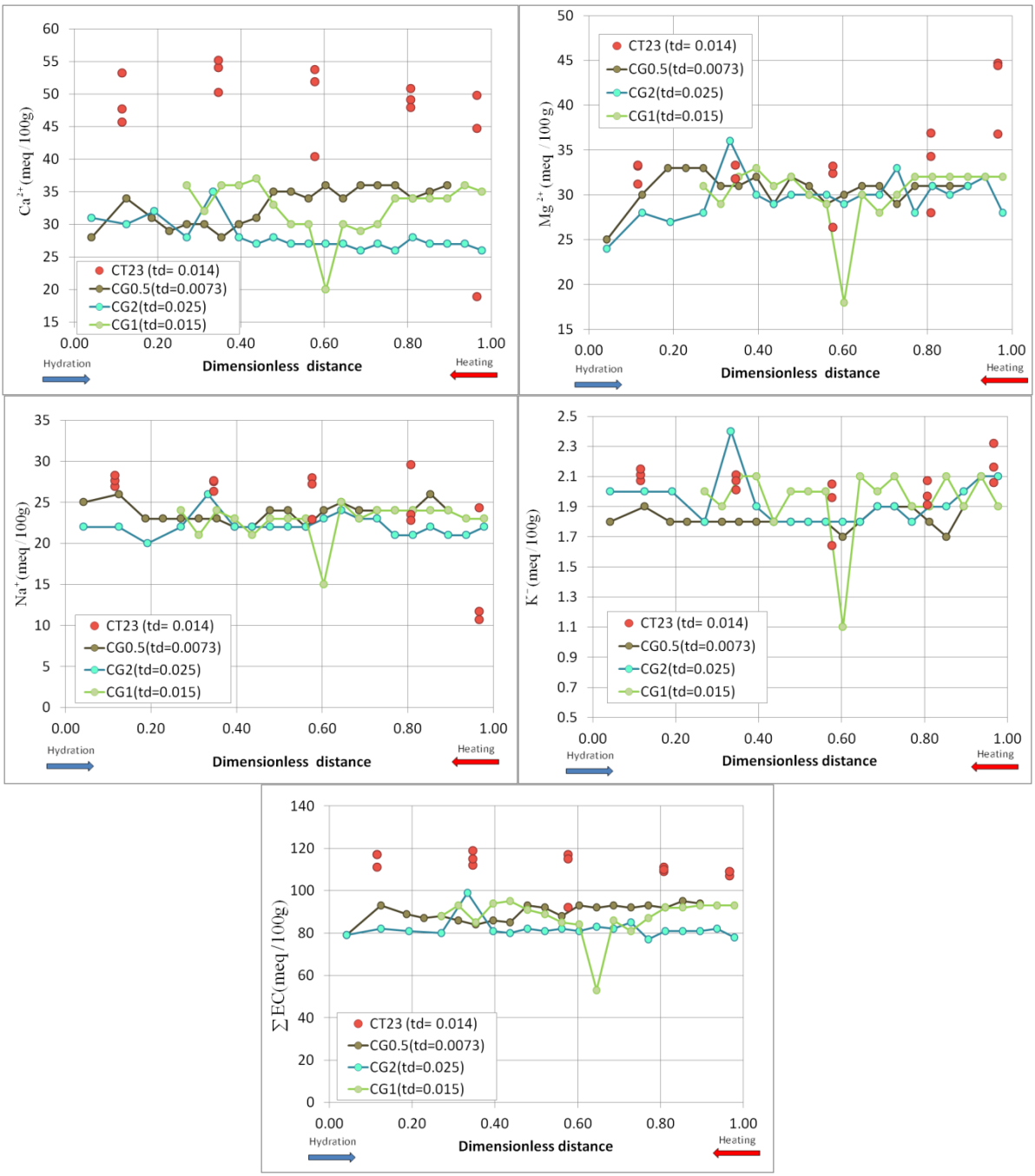

Figure 120. Exchanged cations for CT cell and CG cells measured with the Chapmam's method.

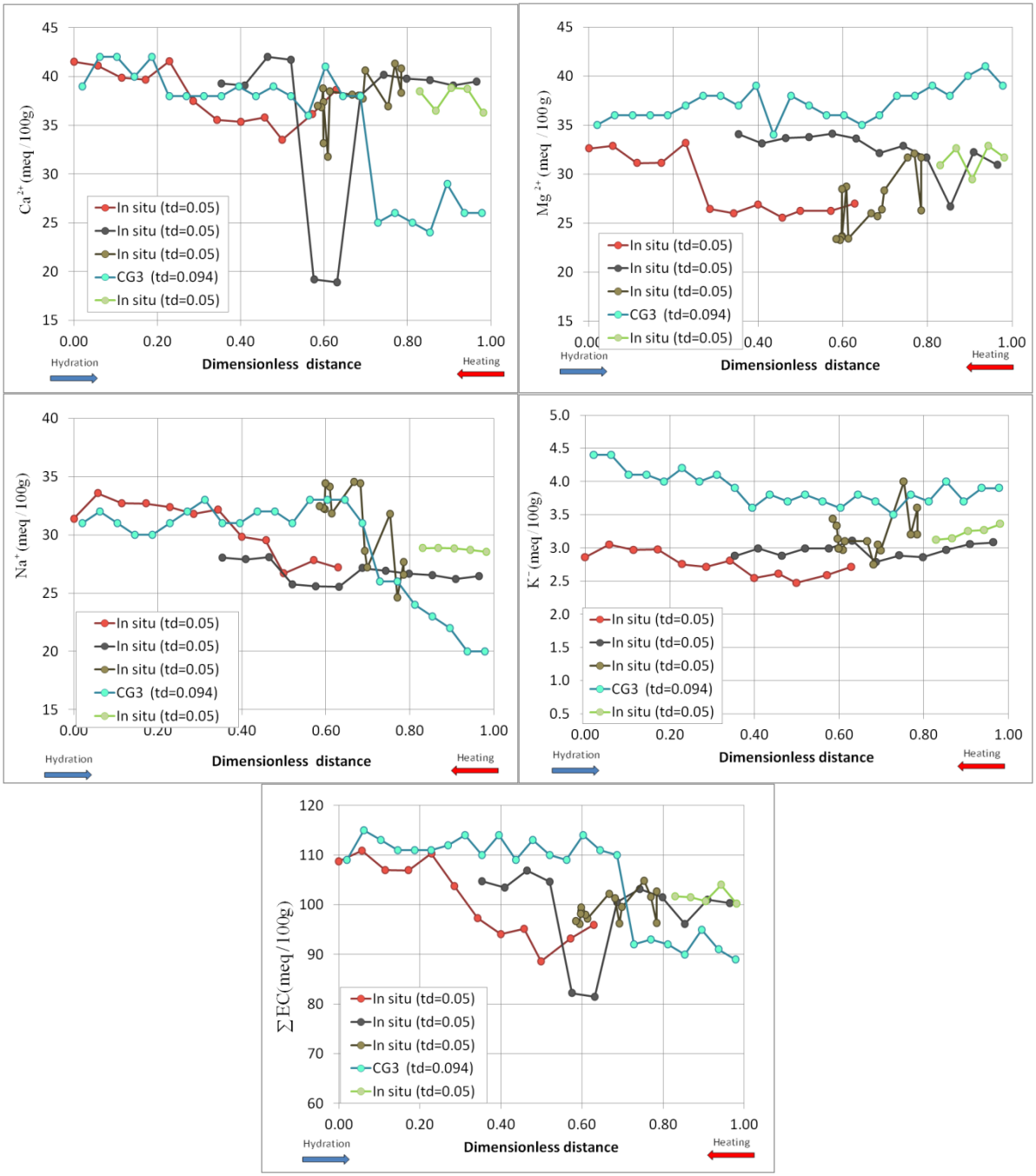

Figure 121. Exchanged cations for CG3 cell and the in situ test measured with the $CsNO_3$ method.

9.4. Conclusions

Obtaining reliable chemical data for the bentonite pore water is a difficult task. Commonly, the chemical composition of the bentonite is derived from aqueous extract data which must be interpreted numerically with inverse geochemical models. This imposes a restriction on the integrated analysis of chemical data. Here, the analysis has concentrated on chloride, Cl^-, a conservative species. Chemical data cannot be monitored in time. Most often,

they are determined at the end of the heating and hydration after the dismantling of the bentonite barrier. Therefore, the analysis of chemical data has been concentrated in the spatial distribution along the bentonite buffer of the Cl^- concentration at different times. In general, the Cl^-concentration is smallest near the hydration boundary and increases near the heater due to evaporation. In the central sections of the buffer, the concentration of Cl^- remains constant during early and intermediate times. The integrated analysis of dimensionless Cl^- concentrations show that:

1) The Cl^- concentrations in the CT cell are much smaller than those of other tests.
2) There are significant differences in the Cl^- concentrations of several sections of the dismantled heater 1 of the in situ test.

Available data do not allow drawing clear conclusions regarding the consistency between aqueous extract and squeezing data. Preliminary analyses of pH data show that data from CG cells and in situ test are consistent. However, the pH data from CT cells and from section 29 of the in situ test are markedly different from the rest of the data.

Possible reasons for the differences in chemical data among the tests include:

1) The method used to measure the chemical variables. This is the case for exchanged cations which in some tests were determined with the Chapman's method and in other tests were measured with the CsNiO3 method.
2) The chemistry of the hydration water which is different in most of the tests
3) There are also differences between the chemical composition of the hydration waters of the mock up and in situ tests
4) Geometric configuration of the flow: radial versus parallel.
5) Thermal gradient which may affect water evaporation, vapour condensation and the evapo-concentrantion near the heater.
6) Differences in the experimental conditions. In the in situ test there could be heterogeneities along the barrier and along the granitic rock.

10. Conclusions

The activities carried out include:

1) The compilation of available hydrodynamic, thermal and hydrochemical data from reported and on-going heating and hydration experiments performed on FEBEX bentonite.
2) The analysis and filtering of data.
3) The dimensional analysis of key hydrodynamic, thermal and chemical variables, including the definition of: 1) The characteristic times and volumes and 2) Dimensionless water uptake, water content, temperature and solute concentration.
4) The integrated analysis of water content, water uptake, temperatures, chemical concentrations of bentonite pore water data from experiments performed at different space-time scales by means of dimensionless variables.
5) The development of an analytical solution for bentonite hydration based on the Green-Ampt method

10.1. Integrated analysis of hydration data

The main conclusions of the integrated analyses of the water uptake data include:

1) Water hydration in CT and CG cells is mostly one dimensional and parallel to the axis of the cell. Hydration in the mock up and in situ tests, on the other hand, occurs from the outer surface and has a radial distribution. Therefore, there is a clear difference in the geometry of the hydration of the lab cells and the mock up and in situ tests.
2) Measured water uptake data contains uncertainties. For CG cells the water uptake data may have an uncertainty of about 15%. The final water uptake determined with the on line measurements (from changes in the weight of the water tank) is 15% larger than the water uptake estimated from the difference in the weight of the bentonite sample at the end and at the beginning of the test. Water uptake data from the mock up test may also contain uncertainties, especially for the most recent data because the flow rate is becoming very low.

3) The dimensionless analysis of measured water uptake data shows that the water uptake data from the CT and CG cells and the mock up test cannot be scaled up. There are large differences at early times due to spurious effects such as electric shutdown and the filling of block joints. Such differences, however, decrease with time. Measured data from most of the tests converge for dimensionless times greater than 0.04. The water uptake of the CT cell is slightly larger than that of the mock up test.

4) The computed water uptake with the numerical model for parallel flow is larger than that computed for radial flow.

Our integrated analysis assumes that the volume and density are constant. Therefore, changes in porosity, temperature and permeability are not accounted for.

10.2. Analytical solutions

The Green-Ampt analytical solution has been used to compare the water uptake for radial and parallel flow. Such comparison reveals that the analytical solutions are markedly different. Such differences should be taken into account when translating the results obtained in laboratory cells, where the conditions are of parallel flow, to the in situ test where heating and hydration are radial. The water uptake for parallel flow has been computed for the following cases: 1) Same volume and thickness; 2) Same hydration surface and thickness; 3) Same volume and hydration surface; and 4) For optimized thickness, volume and hydration surface. The best fit was obtained with the optimized values. The case of the same volume and hydration surface gives the second best approximation. It can be concluded that the water uptake of radial and parallel flow are comparable only when the dimensions and the conditions are correctly selected. Measured water uptake data from CG cells for several durations ranging from 0.5 to 7.5 years fit quite well to the Green-Ampt analytical solution for an apparent hydraulic conductivity K slightly greater than that corresponding to 25ºC and the initial bentonite porosity. The analytical Green-Ampt solution for radial and parallel flow reproduce well the numerical solutions by using an apparent hydraulic conductivity slightly larger than that corresponding to 25ºC and the initial bentonite porosity.

10.3. Integrated analysis of water content data

The main conclusions of the integrated analyses of water content data include:

1) Water content data for the small CT cell are much smaller than the water content data from other tests. Water content data for the mock up test are the largest for all the tests for dimensionless times smaller than 0.04. For large times ($t_D > 0.04$), the general slope of the water content data are similar for the CG cells, and the mock up and in situ tests.

2) Possible reasons for the differences in water content data among the tests include:

   - The initial flooding. The joints and gaps of the barrier of the mock up test were flooded at the beginning of the test. This explains why the water content data for the mock up test are the largest for all the tests small dimensionless times.
   - Geometric configuration of the flow. Water flow is radial in the mock up and in situ tests while it is parallel in CT and CG cells.
   - Thermal gradient. The temperatures at the boundaries are similar in most tests (100ºC near the heater and from 12 to 20 ºC at the hydration boundary). However, the thickness of the bentonite ranges from 10 cm (CT cells) to 75 cm in the in situ test. Water evaporates near the heater. Vapour diffuses away from the heater and condensates at some distance. This process retards the hydration of the bentonite buffer.
   - The internal boundary condition at the heater-bentonite interface. The bentonite is directly in contact with the heater in the CT and CG cells as well as in the mock up test, while in the in situ test there is metallic liner which creates a gap between the heater and the bentonite.

10.4. Integrated analysis of temperature data

Temperatures reach quasi steady values quickly. Therefore, the analysis has been concentrated in its spatial distribution along the bentonite buffer. The temperature decreases from the heater to the hydration boundary. The curves of temperature versus distance from the heater shows two mains parts: 1) Near the heater, where the thermal gradient is large and 2) Near the hydration boundary where the gradient is smaller. Dimensionless measured temperature profiles show a slope of 0.7 which is similar for all the tests. This slope is similar to that of the computed temperatures.

10.5. Integrated analysis of chemical data

Obtaining reliable chemical data for the bentonite pore water is a difficult task. Commonly, the chemical composition of the bentonite is derived from aqueous extract data which must be interpreted numerically with inverse geochemical models. This imposes a restriction on the integrated analysis of chemical data. Here, the analysis has concentrated on chloride, Cl^-, a conservative species. Chemical data cannot be monitored in time. Most often, they are determined at the end of the heating and hydration after the dismantling of the bentonite barrier. Therefore, the analysis of chemical data has been concentrated in the spatial distribution along the bentonite buffer of the Cl^- concentration at different times. In general, the Cl^-concentration is smallest near the hydration boundary and increases near the heater due to evaporation. In the central sections of the buffer, the concentration of Cl^- remains constant during early and intermediate times. The integrated analysis of dimensionless Cl^- concentrations show that:

1) The Cl^- concentrations in the CT cell are much smaller than those of other tests.
2) There are significant differences in the Cl^- concentrations of several sections of the dismantled heater 1 of the in situ test.

Available data do not allow drawing clear conclusions regarding the consistency between aqueous extract and squeezing data. Preliminary analyses of pH data show that data from CG cells and in situ test are consistent. However, the pH data from CT cells and from section 29 of the in situ test are markedly different from the rest of the data.

Possible reasons for the differences in chemical data among the tests include:

1) The method used to measure the chemical variables. This is the case for exchanged cations which in some tests were determined with the Chapman's method and in other tests were measured with the CsNiO3 method.
2) The chemistry of the hydration water which is different in most of the tests
3) There are also differences between the chemical composition of the hydration waters of the mock up and in situ tests
4) Geometric configuration of the flow: radial versus parallel.
5) Thermal gradient which may affect water evaporation, vapour condensation and the evapo-concentrantion near the heater.

6) Differences in the experimental conditions. In the in situ test there could be heterogeneities along the barrier and along the granitic rock.

10.6. Future improvements

The integrated analysis presented here could be extended by:

1) Accounting for water redistribution in the Green-Ampt solution.
2) Developing analytical solutions for other variables such as temperature and concentration of dissolved species.
3) Including laboratory tests performed on very small bentonite samples.
4) Performing the integrated analysis of chemical data for reactive species such as Ca^{2+}, Mg^{2+}, Na^{+}, K^{+}, sulfate and bicarbonate.

10.7. Global evaluation of long-term extrapolation

The main THMC processes are similar in the CT and CG cells, the mock up and the in situ tests. The differences found in the integrated analysis of the data are due to the different initial and boundary condition and the geometries. The general behaviour of the water uptake, water content, temperature and chemical concentrations is similar but there are differences due to differences in the layout of the tests. The conclusions obtained in our integrated analysis are consistent with those found by the CIEMAT team which were presented in the second annual PEBS meeting in Beijing in May 2011.

The integrated analysis of the data has been useful to: 1) Identify the differences among the tests; 2) Realize that each test requires a specific THMC model.

Data from different space-time scales cannot be integrated and therefore there is no possibility for extrapolation in time from available data. Such extrapolation is most likely to be feasible my means of coupled THMC models.

11. References

Cox, B.L. and K. Pruess, 1990. Numerical experiments on convective heat transfer in water-satured porous media at near-critical conditions. Transport in porous media 5, 299-323.

ENRESA, 2000a. Full-scale engineered barriers experiment for a deep geological repository in crystalline host rock FEBEX Project. EUR 19147 EN, European Commission.

ENRESA 2000b. Evaluación del comportamiento y de la seguridad de un almacenamiento de combustible gastado en una formación granítica. ENRESA Informe 49-1PP-M-15-01. Madrid, 2001.

ENRESA, 2006a. Full-Scale Engineered Barriers Experiment: Updated Final Report. ENRESA Tech. Publ. PT 05-02/2006, 589 pp.

ENRESA, 2006b. FEBEX: Final report on thermo-hydro-mechanical modelling. ENRESA Techn. Publ. PT 05-2/2006, 163 pp

ENRESA, 2006c. FEBEX: Final THG modelling report. ENRESA Techn. Publ. PT 05-3/2006, 155 pp

Fernández A.M., J. Cuevas, P. Rivas and P.L. Martín, 1999. THG tests in termohydraulic cells. Technical Report 70-IMA-L-0-41, CIEMAT, Madrid.

Fernández A. M., and M.V. Villar, 2010. Geochemical behaviour of bentonite barrier in the laboratory after up to 8 years of heating and hidrating. Applied Geochemistry 25 809-824

Martín, P.L., J.M. Barcala, and F.Huertas, 2006. Large-scale and long-term coupled thermo-hydro-mechanic experiements with bentonite: the FEBEX mock up test. J. Iberian Geol. 32 (2), 259-282

Navarro, V. and E.E. Alonso, 2000. Modelling swelling soils for disposal barriers. Compt. Geotech. 27,19-43.

Samper J., L.Zheng, L. Montenegro, A.M. Fernández, and P. Rivas, 2008. Coupled thermo-hydro-chemical models of compacted bentonite after FEBEX in situ test. Applied Geochemistry 23, 1186-1201.

Samper, J, JC Mayor and L Montenegro, 2010, Work Plan for Task 3.4, Technical Note 2 of the PEBS Project.

Samper J., A. Mon, L. Montenegro, B. Pisani, A. Naves, Y.i Li and J. C. Mayor, 2011, Modelos acoplados termo-hidro-mecánico-geoquímicos para los materiales arcillosos de las barreras de ingeniería en el almacenamiento de residuos En: X Jornadas de Zona no Saturada, ZNS'11, Salamanca (in press).

Villar, M.V, A.M. Fernández, P.L. Martín, J.M. Barcala, R. Gómez-Espina and P.Rivas, 2008a. Effect of heating/hydration on compacted bentonite: test in 60 cm long cells. Colección Documentos CIEMAT.

Villar, M.V., Sánchez, M., Gens, A., 2008b. Behaviour of a bentonite barrier in the laboratory:experimental results up to 8 years and numerical simulation. Physics and Chemistry of the Earth, Vol. 33, Supplement 1, pp. S476-S485.

Yu-Shu Wu and K. Pruess, 1999. Integral solution for transient fluid flow through a porous medium pressure-dependent permeability. International Journal of Rock Mechanics and Mining Scinces, 37, 51-61.

Yu-Shu Wu, H.H. Liu and G.S. Bodvarsson, 2004. A triple-continuum approach for modeling flow and transport process in fractured rocks. Journal of Contaminant Hydrology, 73, 145-179.

Zheng, L., J. Samper, L. Montenegro and A.M. Fernández, 2000. A coupled THMC model of heating and hydration laboratory experiment in unsaturated compacted FEBEX bentonite. Journal of Hydrology. 368, 80-90.

Zheng, L and J. Samper, 2005. A dual continuum coupled multiphase flow model with mixed second order water transfer term for structured soils. Jornadas de la Zona no Saturada 2005, VII, 301-306.

Zheng, L. and J. Samper, 2008. A coupled THMC model of FEBEX mock-up test. Physics and Chemistry of the Earth 33, S486-S498

Zheng, L., J. Samper and L. Montenegro, 2008. Inverse hydrochemical model of aqueous test. Physics and Chemistry of the Earth 33,1009-1018

Zheng, L., J. Samper, L. Montenegro and A.M. Fernández, 2010. A coupled model of heating and hydration laboratory experiment in unsaturated compacted FEBEX bentonite. Journal of hydrology 386, 80-94.

Zheng, L. J. Samper and L. Montenegro, 2011. A coupled THC model of FEBEX in situ test with bentonite swelling and chemical and thermal osmosis. Journal of Contaminant Hydrology (in press).